



GMe Forum 2001

PROCEEDINGS OF THE SEMINAR
AT THE VIENNA UNIVERSITY OF TECHNOLOGY

ORGANIZED BY THE SOCIETY FOR MICROELECTRONICS
(GESELLSCHAFT FÜR MIKROELEKTRONIK – GMe)

April 5 – 6, 2001



GMe Forum 2001

PROCEEDINGS OF THE SEMINAR
AT THE VIENNA UNIVERSITY OF TECHNOLOGY

ORGANIZED BY THE SOCIETY FOR MICROELECTRONICS
(GESELLSCHAFT FÜR MIKROELEKTRONIK – GMe)

April 5 – 6, 2001

SPONSORED BY:

GESELLSCHAFT FÜR MIKROELEKTRONIK
BUNDESMINISTERIUM FÜR WISSENSCHAFT UND FORSCHUNG

PROGRAM COMMITTEE:

Emmerich Bertagnolli
Karl Riedling
Friedrich Schäffler

EDITOR OF THE PROCEEDINGS:

Karl Riedling

Seminar Organization:

Karl Riedling
Claudia Benedela

Production of the Proceedings:

Claudia Benedela
Karl Riedling

ISBN: 3-901578-07-2

© 2001 Gesellschaft für Mikroelektronik (GMe)
c/o Technische Universität Wien
Institut für Industrielle Elektronik und Materialwissenschaften
Gusshausstrasse 27-29/366, A-1040 Vienna

Preface

In spring 1977, the first Austrian microelectronics technology seminar took place in Grossarl, Salzburg, under the title “*Technologie in der Mikroelektronik*” (“*Technology in Microelectronics*”), primarily intended as a workshop for Austrian university researchers in this field. A long series of biennial seminars in Grossarl followed, the first of which were organized by a group of institutes at the Technical University Vienna. Later, after the Society for Microelectronics (*Gesellschaft für Mikroelektronik*; GMe) had been founded in the mid-1980s, the GMe coordinated the seminars. This sequence of seminars continued in 1999 at a new venue, Bad Hofgastein, and with a new title, “*Current Developments of Microelectronics*”. With the change of the seminar venue from Grossarl to Bad Hofgastein the scope of the seminar shifted: Great efforts had been made particularly during the 1990s to invite guest speakers from industry or foreign universities, however, the audience consisted practically exclusively of university researchers. Beginning with the 1999 seminar in Bad Hofgastein, the seminar was designed to appeal to a more application-oriented audience. This trend continued in 2001 when we decided to hold the seminar at a more central place, i.e., at the Vienna University of Technology, thereby facilitating the participation of representatives of foreign and Austrian industry and government. To reflect more clearly the new target of the seminar, its title was changed to “*GMe Forum 2001*”. Most of the oral presentations are now review papers presented by top-level speakers from international industry and research facilities. The institutions supported by the GMe also present their results, partly as oral presentations but mostly as posters.

The main goal of the Society for Microelectronics (GMe) is to promote microelectronics research and technology at Austrian universities and to establish links to the Austrian industry. The GMe is essentially financed by the government and supports relevant microelectronics activities at Austrian universities. The relatively small budget of the GMe prohibits the full sponsoring of research projects; nevertheless, the GMe supplements other research funding sources by providing contributions for creating and maintaining laboratory infra-structure. In addition to backing other technological activities in the fields of design, sensors, and optoelectronics, the main goal of the GMe in recent years was the support of the two cleanroom centers at the Technical University Vienna and at the University Linz, respectively, where internationally competitive technological equipment has been made available to researchers and students.

We hope that the proceedings will promote the impact of the *GMe Forum 2001*, and that they may contribute to an even better international cooperation of the Austrian microelectronics researchers.

Univ.Prof. Dr. Günther BAUER
President of the GMe

Ao.Univ.Prof. Dr. Karl RIEDLING
Secretary General of the GMe

GMe Forum Program

(The titles in parentheses and page references refer to the pertinent contributions in these proceedings.)

Thursday, April 5th, 2001

9:00 – 9:40 G. BAUER – *Introduction*

P. SKALICKY – *Introduction*

N. ROZSENICH – *Introduction*

9:40 – 10:25 A. OURMAZD (IHP Frankfurt/Oder):

“*Silicon-based Technologies for Wireless*” – **page 3**

10:25 – 10:45 BREAK

10:45 – 11:30 H. NOLL (AMS Unterpremstätten):

„*Die neue AMS 200 mm Mixed Signal Foundry – Technische und ökonomische Herausforderung*“

(W. PRIBYL: “*The New AMS 200 mm Mixed Signal Foundry – Technical and Economic Challenge*” – **page 5**)

11:30 – 12:15 R. PETSCHACHER, F. KUTTNER, H. WEINBERGER, A. WIESBAUER (Infineon Villach):

„*Mixed Signal ICs auf dem Weg zu 0.1µm-Technologien*“

(“*Mixed-Signal Circuits on their Way to 0,1µm Technologies*” – **page 9**)

12:15 – 13:30 BREAK – CATERING

Components and Systems – Part I

13:30 – 14:15 U. KÖNIG (DaimlerChrysler Ulm):

“*SiGe High-Frequency Devices*” – **page 17**

14:15 – 15:00 W. KELLNER (Infineon München):

„*Mikroelektronische III-V-Bauelemente für hohe Frequenzen*“ – **page 19**

15:00 – 15:45 J. BRUGGER (EADS Ulm):

“*Module Technologies for RF Telecom Radios: Status and Trends*” – **page 27**

15:45 – 16:15 BREAK

Components and Systems – Part II

16:15 – 17:00 R. WEIGEL (DICE and Univ. Linz):

„*Hochintegrierte Schaltkreise für UMTS*“

(“*Highly-Integrated Radio Frequency Integrated Circuits (RFICs) for UMTS*” – **page 29**)

- 17:00 – 17:45 H. BALTES (ETH Zürich):
„CMOS-basierte Mikro- und Nano-Systeme“ – **page 35**
- 17:45 – 18:00 BREAK
- 18:00 – 20:00 **Panel Discussion**
„Innovationstransfer zwischen Universität und Industrie“
(“Innovation Transfer Between University and Industry”)
Moderator: E. GORNIK
Participants: N. ROZSENICH and the invited speakers of the GMe Forum

Friday, April 6th, 2001

Gallium Nitride for Optoelectronics

- 9:00 – 9:30 B. SCHINELLER, M. HEUKEN, H. JÜRGENSEN (Aixtron):
„GaN MOCVD in Forschung und Produktion“ – **page 39**
- 9:30 – 10:00 D. HOMMEL, S. EINFELDT, T. BÖTTCHER, S. FIGGE, C. KRUSE,
V. KIRCHNER, H. HEINKE (Univ. Bremen), D. RUDLOFF, J. CHRISTEN
(Univ. Magdeburg):
“Group-III Nitrides Grown By MBE And MOVPE For Optoelectronic
Applications” – **page 41**
- 10:00 – 10:30 V. HÄRLE, D. EISERT (Osram Regensburg):
“GaN-Based Devices – A Challenge in Semiconductor Lighting” –
page 43

10:30 – 10:45 BREAK

Organic Semiconductors

- 10:45 – 11:30 G. LEISING (AT&S Leoben):
„Organische Halbleiter-Bauelemente“ – **page 51**
- GMe Presentations – Invited Talks**
- 11:30 – 11:50 F. KOHL, F. KEPLINGER, R. FASCHING, P. SVASEK, J. STEURER,
A. JACHIMOWICZ (TU Wien):
„Entwicklung von und Untersuchungen an Mikrosystemkomponenten“
– **page 55**
- 11:50 – 12:10 J. SMOLINER, B. BASNAR, S. GOLKA, E. GORNIK (TU Wien),
B. LÖFFLER, M. SCHATZMAYR, H. ENICHLMAIR (AMS
Unterpremstätten):
„Rasterkapazitätsmikroskopie an Halbleiter-Bauelementen“
(“Scanning Capacitance Microscopy on Epitaxial Si Layers” –
page 61)

12:10 – 13:30 BREAK – CATERING

- 13:30 – 13:50 W. SCHRENK, N. FINGER, S. GIANORDOLI, L. HVOZDARA, E. GORNIK, G. STRASSER (TU Wien):
„Infrarot-Quantenkaskadenlaser“
(“Infrared Quantum Cascade Laser” – **page 67**)
- 13:50 – 14:10 W. HEISS, T. SCHWARZL, G. SPRINGHOLZ, T. FROMHERZ, G. BAUER (Univ. Linz), M. AIGLE, H. PASCHER (Univ. Bayreuth), K. BIERMANN, K. REIMANN (Max-Born-Institut Berlin):
„Bleisalz-Mikroresonatoren für das mittlere Infrarot“
(“Lead-Salt Microcavities for the Mid-Infrared” – **page 73**)
- 14:10 – 14:30 D. GRUBER, T. FROMHERZ, M. MÜHLBERGER, C. SCHELLING, L. PALMETSHOFER, F. SCHÄFFLER (Univ. Linz):
„SiGeC für HBT-Anwendungen“
(“Characterization of Si/SiGeC Heterostructures for Device Applications” – **page 79**)
- 14:30 – 15:50 C. DISKUS, A. STELZER (Univ. Linz):
„HF Radarsysteme“
(“RF Radar Systems” – **page 83**)
Simulation and Circuit Design
- 14:50 – 15:20 T. GRASSER (TU Wien):
„Simulation von Bauelementen und Schaltungen für hohe Frequenzen“
(“Simulation of Semiconductor Devices and Circuits at High Frequencies” – **page 91**)
- 15:20 – 15:40 P. SÖSER (TU Graz):
„Systemsimulation und Messungen an hochauflösenden Sigma-Delta-Modulatoren“ – **page 97**
- 15:40 – 16:00 N. KERÖ, T. SAUTER, G. CADEK, H. NACHTNEBEL (TU Wien):
„Wann mi des Designbüro net vermittelt hätt – Ein Erfahrungsbericht über 10 Jahre Technologietransfer“ – **page 99**
- 16:00 – 16:15 BREAK
- 16:15 – 17:30 **GMe Presentations – Posters**
- 17:30 Conclusion

Poster Presentations

Cleanroom Vienna

- B. BASNAR, S. GOLKA, E. GORNIK¹, J. SMOLINER (TU Wien), B.LÖFFLER, M.SCHATZMAYER, H.ENICHLMAIR (AMS Unterpremstätten):
„Kontrastmechanismen in der Rasterkapazitätsmikroskopie und der Einfluss der Dotierung auf die Signalgröße“ – page 105
- R. BRATSCHITSCH, T. MÜLLER, G. STRASSER, K. UNTERRAINER (TU Wien):
*„Kohärente THz-Emission von optisch gepumpten parabolischen Quantenwells“
 (“Coherent Terahertz Emission from Optically Pumped Parabolic Quantum Wells” – page 107)*
- S. HARASEK, S. GOLKA, J. SMOLINER, E. BERTAGNOLLI (TU Wien):
*„Ultradünne Siliziumdioxidschichten: Herstellung und Charakterisierung“
 (“Ultrathin Silicon Dioxide: Growth and Characterization” – page 111)*
- P.O. KELLERMANN, N. FINGER, E. GORNIK (TU Wien), M. OST, F. SCHOLZ (Univ. Stuttgart):
*„Multiwellenlängen-Laserdioden-Array basierend auf Oberflächenmodenkopplung“
 (“Multi-Wavelength Laser Diode Array Based on Surface Mode Coupling” – page 117)*
- R. KOLM, J. FOISNER, K. PIPLITS, H. HUTTER (TU Wien):
„SIMS-Analyse von GeSi-CVD-Strukturen“ – page 121
- H. LANGFISCHER, B. BASNAR, E. BERTAGNOLLI, H. HUTTER (TU Wien):
*„Ionenstrahlunterstützte lokale Wolframabscheidung“
 (“Focused Ion Beam Induced Local Tungsten Deposition” – page 123)*
- M. LITZENBERGER, C. FÜRBOCK, R. PICHLER, S. BYCHIKHIN, D. POGANY, E. GORNIK (TU Wien), K. ESMARK, G. GROOS, H. GOSSNER, M. STECHER (Infineon Munich):
“Laser-Interferometric Investigation of Triggering Behavior in CMOS and Smart Power Technology Electrostatic Discharge (ESD) Protection Structures” – page 129
- A. LUGSTEIN, C. KRANZ, E. BERTAGNOLLI (TU Wien):
*„Integrierte Ultramikroelektrode für hochaufgelöste topographische und elektrochemische Oberflächenanalysen“
 (“FIB Based Micro Fabrication Technique for a Novel Type of Scanning Electrochemical Microscopy Probes” – page 133)*
- C. PACHER, M. KAST, C. COQUELIN, G. FASCHING, G. STRASSER, E. GORNIK (TU Wien):
*„Untersuchung von quantenmechanischen Antireflexbeschichtungen für undotierte GaAs/AlGaAs-Übergitter mittels Ballistischer Elektron Spektroskopie“
 (“Ballistic Electron Spectroscopy of Quantum Mechanical Anti-reflection Coatings for GaAs/AlGaAs Superlattices” – page 137)*

D. RAKOCZY, G. STRASSER, J. SMOLINER (TU Wien):

„Ballistische Elektronen-Emissionsspektroskopie von GaAs-AlGaAs Übergittern im transversalen Magnetfeld“

(“Ballistic Electron Emission Spectroscopy on Biased GaAs-AlGaAs Superlattices in Transverse Magnetic Fields” – **page 143**)

G. STRASSER, W. SCHRENK (TU Wien):

„Epitaktisches Wachstum von gitterangepassten und verspannten III-V Verbindungen“ – **page 149**

J. ULRICH, R. ZOBL, W. SCHRENK, G. STRASSER, K. UNTERRAINER, E. GORNIK (TU Wien):

„Terahertz-Quantenkaskadenemitter: Intra- versus Interwell-Emission“

(“Band Structure Engineering for Terahertz Quantum Cascade Lasers” – **page 151**)

H. WANZENBOECK, S. GERGOV, U. GRABNER, P. PONGRATZ, H. STÖRI, H. HUTTER, B. BASNAR, J. SMOLINER, E. BERTAGNOLLI (TU Wien):

„Sublithographische Siliziumoxid-Strukturen für die Phasenshifttechnologie“ – **page 155**

Cleanroom Linz

T. BERER, G. PILLWEIN, G. BRUNTHALER (Univ. Linz), G. STRASSER (TU Wien):

„Herstellung von AlGaAs-Punktkontakten für elektrische Messungen“

(“Fabrication of AlGaAs Nanostructures” – **page 159**)

A. DANIEL, Y. ZHUANG, J. STANGL, T. ROCH, V. HOLÝ, G. BAUER (Univ. Linz):

„Dehnungsmodulation in Si unterhalb von strukturierten Oxid-Streifen“

(“Strain Modulations in Si Underneath Patterned Oxide Stripes” – **page 165**)

D. GRUBER, M. MÜHLBERGER, F. SCHÄFFLER (Univ. Linz):

„Characterization of Si/Si_{1-x-y}Ge_xC_y Heterostructures for Device Applications” –

page 171

K. HIMMELBAUER, H. SITTER, H. KRENN (Univ. Linz):

„Außergewöhnliche magnetische Eigenschaften von sehr dünnen Eisenschichten“

(“Magnetic Properties of Thin Iron Films” – **page 173**)

K. HINGERL (Univ. Linz):

„Zerstörungsfreie optische Messverfahren für die Materialcharakterisierung während der Herstellung von dünnen Halbleiterschichten“

(“Reflection Difference Spectroscopy on II- VI Semiconductors; A Tool to Investigate Surface Processes in situ During Growth” – **page 179**)

G. KOCHER, H. PRZYBYLINSKA, M. STEPIKHOVA, L. PALMETSHOFER, W. JANTSCH (Univ. Linz):

„Erbium in SiO_x-Umgebung: Möglichkeiten zur Verbesserung der Emission bei 1,54 µm“

(“Erbium in SiO_x Environment: Ways to Improve the 1.54 µm Emission” – **page 185**)

R.T. LECHNER, A. RAAB, G. SPRINGHOLZ, M. PINCZOLITS, V. HOLY, P. MAYER, G. BAUER (Univ. Linz), H. KANG, L. SALAMANCA-RIBA (Univ. Maryland)

„Molecular Beam Epitaxy of Self-Organized PbSe Quantum Dot Superlattices” – **page 189**

- W. MÄRZINGER (Upper Austrian Research GmbH Linz), H. KRENN (Univ. Linz):
„In-line Prozesskontrolle mit einem kompakten Echtzeit-FTIR-Spektrometer“ –
page 191
- N. SANDERSFELD, W. JANTSCH, Z. WILAMOWSKI, F. SCHÄFFLER (Univ. Linz):
“Conduction Electron Spin Resonance in MBE-Grown Si/SiGe Quantum Wells” –
page 193
- N. SANDERSFELD, G. LENGAUER, L. PALMETSHOFER, F. SCHÄFFLER (Univ. Linz):
“Modulation Doped Si/Si_{1-x}Ge_x-Field-Effect Transistors” – **page 195**
- T. SCHWARZL, W. HEISS, G. SPRINGHOLZ (Univ. Linz), S. GIANORDOLI, G. STRASSER
(TU Wien), M. AIGLE, H. PASCHER (Univ. Bayreuth):
„Stark verstimmte Resonanzen in IV-VI Mikroresonatoren und Mikrodisks: Mo-
denaufspaltung und Lasertätigkeit“
(“Mode Splitting and Lasing in Detuned Lead Salt Microcavity and Microdisk
Resonances” – **page 197**)
- H. SITTE, A. ANDREEV (Univ. Linz):
„Kristalline dünne Filme aus Para-Hexaphenyl hergestellt mit Hot-Wall-Epitaxie“ –
page 201
- H. SITTE, K. HINGERL, A. BONANNI, K. HIMMELBAUER, D. STIFTER (Univ. Linz):
„In situ-Kontrolle der Herstellung von Galliumnitrid-Schichten“ – **page 203**
- J. STANGL, A. DANIEL, V. HOLÝ, T. ROCH, G. BAUER (Univ. Linz):
„Nanotomographie an SiGe-Strukturen“
(“Strain and Composition of SiGe Islands on Si (001)” – **page 205**)
- K. WIESAUER, G. SPRINGHOLZ (Univ. Linz):
“Nano-Scale Dislocation Patterning in PbTe on PbSe (100) Heteroepitaxy Studied by
Scanning Tunneling Microscopy” – **page 209**

List of Participants

- Dipl.-Ing. Holger Arthaber
Institut für Elektrische Mess- und
Schaltungstechnik, TU Wien
A-1040 Wien
- Prof. Dr. Henry Baltes
ETH Zurich, Physical Electronics
Laboratory
CH-8093 Zürich
- Dr. Herwig Bangert
Institut für Angewandte und
Technische Physik, TU Wien
A-1040 Wien
- Dr. Bernhard Basnar
Institut für Festkörperelektronik, TU
Wien
A-1040 Wien
- Prof. Dr. Günther Bauer
Institut für Halbleiter- und
Festkörperphysik, JKU Linz
A-4040 Linz
- Claudia Benedela
Gesellschaft für Mikroelektronik
A-1040 Wien
- Thomas Berer
Institut für Halbleiter- und
Festkörperphysik, JKU Linz
A-4040 Linz
- Prof. Dr. Emmerich Bertagnolli
Institut für Festkörperelektronik, TU
Wien
A-1040 Wien
- Mag. Rudolf Bratschitsch
Institut für Festkörperelektronik, TU
Wien
A-1040 Wien
- Wolfgang Brezna
Institut für Festkörperelektronik, TU
Wien
A-1040 Wien
- Dr. Hans Brugger
MicroWave Factory, EADS
Deutschland GmbH
D-89077 Ulm
- Prof. Dr. Gerhard Brunthaler
Institut für Halbleiter- und
Festkörperphysik, JKU Linz
A-4040 Linz
- Dr. Burgholzer
Upper Austrian Research GmbH
A-4021 Linz
- Dr. S. Bychikhin
Institut für Festkörperelektronik, TU
Wien
A-1040 Wien
- Dipl.-Ing. Hajdin Ceric
Institut für Mikroelektronik, TU Wien
A-1040 Wien
- Univ.-Doz. Dipl.-Ing. Dr. Christian
Diskus
Institut für Mikroelektronik, JKU Linz
A-4040 Linz
- Prof. Dr. Wolfgang Fallmann
Institut für Industrielle Elektronik und
Materialwissenschaften
A-1040 Wien
- Johann Foisner
Institut für analytische Chemie, TU
Wien
A-1060 Wien
- Dr. Thomas Fromherz
Institut für Halbleiter- und
Festkörperphysik, JKU Linz
A-4040 Linz
- Katharina Gammer
Institut für analytische Chemie, TU
Wien
A-1060 Wien
- Dipl. Ing. Andreas Gehring
Institut für Mikroelektronik, TU Wien
A-1040 Wien

- Sebastian Golka**
Institut für Festkörperelektronik, TU
Wien
A-1040 Wien
- Prof. Dr. Erich Gornik**
Institut für Festkörperelektronik, TU
Wien
A-1040 Wien
- Dipl.-Ing. Dr. Klaus-Tibor Grasser**
Institut für Mikroelektronik, TU Wien
A-1040 Wien
- Dipl.-Ing. Markus Gritsch**
Institut für Mikroelektronik, TU Wien
A-1040 Wien
- Daniel Gruber**
Institut für Halbleiter- und
Festkörperphysik, JKU Linz
A-4040 Linz
- Alma Halilovic**
Institut für Halbleiter- und
Festkörperphysik, JKU Linz
A-4040 Linz
- Dipl.-Ing. Stefan Harasek**
Institut für Festkörperelektronik, TU
Wien
A-1040 Wien
- Dipl.-Ing. Christian Harlander**
Institut für Mikroelektronik, TU Wien
A-1040 Wien
- Dr. Volker Härle**
OSRAM Opto Semiconductors GmbH
& Co. OHG
D-93049 Regensburg
- Mag. Dr. Wolfgang Heiß**
Institut für Halbleiter- und
Festkörperphysik, JKU Linz
A-4040 Linz
- Dr. Kurt Hingerl**
Institut für Halbleiter- und
Festkörperphysik, JKU Linz
A-4040 Linz
- Ao.Prof. Dr. Gerhard Hobler**
Institut für Festkörperelektronik, TU
Wien
A-1040 Wien
- DI Dr. Andreas Hoessinger**
Institut für Mikroelektronik, TU Wien
A-1040 Wien
- Prof. Dr. Detlef Hommel**
Institut für Festkörperphysik, FB1,
Universität Bremen
D-28334 Bremen
- Ao.Univ.Prof. Dr. Herbert Hutter**
Institut für analytische Chemie, TU
Wien
A-1060 Wien
- Prof. Dr. Wolfgang Jantsch**
Institut für Halbleiter- und
Festkörperphysik, JKU Linz
A-4040 Linz
- Dipl.-Ing. Parviz Kamvar**
Institut für Festkörperelektronik, TU
Wien
A-1040 Wien
- Michael Kast**
Institut für Festkörperelektronik, TU
Wien
A-1040 Wien
- Dipl.-Ing. Peer Oliver Kellermann**
Institut für Festkörperelektronik, TU
Wien
A-1040 Wien
- Dr. Walter Kellner**
Infineon Technologies AG
WS TI S MWP
D-81730 München
- Dipl.-Ing. Nikolaus Kerö**
Institut für Industrielle Elektronik und
Materialwissenschaften, TU Wien
A-1040 Wien
- Dipl.-Ing. Robert Klima**
Institut für Mikroelektronik, TU Wien
A-1040 Wien
- Dipl.-Ing. Gudrun Kocher**
- Dr. Franz Kohl**
Institut für Industrielle Elektronik und
Materialwissenschaften, TU Wien
A-1040 Wien

- Ralph Kolm
Institut für analytische Chemie, TU
Wien
A-1060 Wien
- Dr. Ulf König
Daimler Chrysler
D-89013 Ulm
- Dipl.-Ing. Robert Kosik
Institut für Mikroelektronik, TU Wien
A-1040 Wien
- Dr. Hans Kosina
Institut für Mikroelektronik, TU Wien
A-1040 Wien
- Prof. Dr. Heinz Krenn
Institut für Experimentalphysik,
Universität Graz
A-8010 Graz
- Mag. Helmut Langfischer
Institut für Festkörperelektronik, TU
Wien
A-1040 Wien
- Dipl.-Ing. Rainer Lechner
Institut für Halbleiter- und
Festkörperphysik, JKU Linz
A-4040 Linz
- Prof. Dr. Günther Leising
AT&S
A-8700 Leoben-Hinterberg
- Herbert Lichtenberger
- Dipl.-Ing. Martin Litzenberger
Institut für Festkörperelektronik, TU
Wien
A-1040 Wien
- Dipl.-Ing. Dr. Alois Lugstein
Institut für Festkörperelektronik, TU
Wien
A-1040 Wien
- Harald Maier
Institut für Festkörperelektronik, TU
Wien
A-1040 Wien
- Dr. Wolfgang Märzinger
Upper Austrian Research GmbH
A-4021 Linz
- Dipl.-Ing. Markus Mayer
Institut für Elektrische Mess- und
Schaltungstechnik, TU Wien
A-1040 Wien
- Mag.rer.nat. Marcus Milnera
Institut für Grundlagen und Theorie der
Elektrotechnik, TU Wien
A-1040 Wien
- Dipl.-Ing. Michael Mühlberger
Institut für Halbleiter- und
Festkörperphysik, JKU Linz
A-4040 Linz
- Dipl.-Ing. Thomas Müller
Institut für Festkörperelektronik, TU
Wien
A-1040 Wien
- Dr. Humbert Noll
AMS Austria Mikro Systeme
International AG,
Schloß Premstätten,
A-8141 Unterpremstätten
- Prof. Dr. Abbas Ourmazd
IHP Microelectronics
D-15204 Frankfurt Oder
- Dipl.-Ing. Christoph Pacher
Institut für Festkörperelektronik, TU
Wien
A-1040 Wien
- Dr.techn. Vassil Palankovski
Institut für Mikroelektronik, TU Wien
A-1040 Wien
- Prof. Dr. Leopold Palmethofer
Institut für Halbleiter- und
Festkörperphysik, JKU Linz
A-4040 Linz
- em.Prof.Dr. Fritz Paschke
Institut für Industrielle Elektronik und
Materialwissenschaften
A-1040 Wien
- Dipl.-Ing. Reinhard Petschacher
Infineon Technologies GmbH
Microelectronic Design Centers Austria
A-9500 Villach
- Rudolf Pichler
Institut für Festkörperelektronik, TU
Wien
A-1040 Wien

- Georg Pillwein
Institut für Halbleiter- und
Festkörperphysik, JKU Linz
A-4040 Linz
- Ing. Kurt Piplits
Institut für analytische Chemie, TU
Wien
A-1060 Wien
- Dr. Dionyz Pogany
Institut für Festkörperelektronik, TU
Wien
A-1040 Wien
- Dr. Erich Prem
BIT
A-1040 Wien
- Dr. Wolfgang Pyka
Institut für Mikroelektronik, TU Wien
A-1040 Wien
- Dipl.-Ing. Anneliese Raab
Institut für Halbleiter- und
Festkörperphysik, JKU Linz
A-4040 Linz
- Christoph Raber
Bundesministerium für Wirtschaft und
Arbeit
A-1010 Wien
- Doris Rakoczy
Institut für Festkörperelektronik, TU
Wien
A-1040 Wien
- Dr. Eveline Riedling
Institut für Industrielle Elektronik und
Materialwissenschaften, TU Wien
A-1040 Wien
- Ao.Univ.Prof. Dr. Karl Riedling
Institut für Industrielle Elektronik und
Materialwissenschaften, TU Wien
A-1040 Wien
- Dipl.-Phys. Tomas Roch
Institut für Halbleiter- und
Festkörperphysik, JKU Linz
A-4040 Linz
- SC Dr. Norbert Rozsenich
BMVIT Sektion V - Innovation und
Technologie
A-1010 Wien
- Dipl.-Ing. Rainer Sabelka
Institut für Mikroelektronik, TU Wien
A-1040 Wien
- Prof. Dr. Friedrich Schäffler
Institut für Halbleiter- und
Festkörperphysik, JKU Linz
A-4040 Linz
- Dr. Robert Schawarz
Institut für Industrielle Elektronik und
Materialwissenschaften, TU Wien
A-1040 Wien
- Dr. Bernd Schineller
AIXTRON AG
D-52072 Aachen
- Dipl.-Ing. Werner Schrenk
Institut für Festkörperelektronik, TU
Wien
A-1040 Wien
- Dipl.-Ing. Robert Schürhuber
Institut für Grundlagen und Theorie der
Elektrotechnik, TU Wien
A-1040 Wien
- Dipl.-Ing. Thomas Schwarzl
Institut für Halbleiter- und
Festkörperphysik, JKU Linz
A-4040 Linz
- Prof. Dr. Siegfried Selberherr
Institut für Mikroelektronik, TU Wien
A-1040 Wien
- Dr. Helmut Sitter
Institut für Halbleiter- und
Festkörperphysik, JKU Linz
A-4040 Linz
- Prof. Peter Skalicky
TU Wien
A-1040 Wien
- Ao.Univ.Prof. Mag. Dr. Jürgen
Smoliner
Institut für Festkörperelektronik, TU
Wien
A-1040 Wien
- Dr. Peter Söser
Institut für Elektronik, TU-Graz
A-8020 Graz

A.o.Prof. Dr. Gunther Springholz

Institut für Halbleiter- und
Festkörperphysik, JKU Linz
A-4040 Linz

Dr. Julian Stangl

Institut für Halbleiter- und
Festkörperphysik, JKU Linz
A-4040 Linz

Dr. Gottfried Strasser

Institut für Festkörperelektronik, TU
Wien
A-1040 Wien

MR Dipl.-Ing. Johann Tschöllitsch

Bundesministerium für Wirtschaft und
Arbeit
A-1010 Wien

Dipl. Phys. Jochen Ulrich

Institut für Festkörperelektronik, TU
Wien
A-1040 Wien

Dr. Karl Unterrainer

Institut für Festkörperelektronik, TU
Wien
A-1040 Wien

Prof. Dr. Robert Weigel

Inst. für Nachrichten- und
Informationstechnik, JKU Linz
A-4040 Linz

Dipl.-Ing. Karin Wiesauer

Institut für Halbleiter- und
Festkörperphysik, JKU Linz
A-4040 Linz

Contents

Introduction	1
A. Ourmazd: Silicon-Based Technologies for Wireless	3
W. Pribyl: The New AMS 200 mm Mixed Signal Foundry – Technical and Economic Challenge.....	5
R. Petschacher et al.: Mixed-Signal Circuits on their Way to 0,1 μ m Technologies	9
Components and Systems	15
U. König: SiGe High-Frequency Devices.....	17
W. Kellner: Mikroelektronische III-V-Bauelemente für hohe Frequenzen	19
H. Brugger: Module Technologies for RF Telecom Radios: Status and Trends	27
R. Weigel: Highly-Integrated Radio Frequency Integrated Circuits (RFICs) for UMTS.....	29
H. Baltes: CMOS-basierte Mikro- und Nano-Systeme.....	35
Gallium Nitride for Optoelectronics	37
B. Schineller et al.: GaN MOCVD in Forschung und Produktion.....	39
D. Hommel et al.: Group-III Nitrides Grown by MOVPE and MBE for Optoelectronic Applications.....	41
V. Härle et al.: GaN-Based Devices – A Challenge in Semiconductor Lighting	43
Organic Semiconductors	49
G. Leising: Organische Halbleiter-Bauelemente	51
GMe Presentations – Invited Talks	53
F. Kohl et al.: Entwicklung von und Untersuchungen an Mikrofluidik- Systemkomponenten	55
J. Smoliner et al.: Scanning Capacitance Microscopy on Epitaxial Si Layers	61
W. Schrenk et al.: Infrared Quantum Cascade Laser	67
W. Heiss et al.: Lead-Salt Microcavities for the Mid-Infrared	73
D. Gruber et al.: Characterization of Si/SiGeC Heterostructures for Device Applications.....	79
C.G. Diskus et al.: RF Radar Systems	83

Simulation and Circuit Design	89
T. Grasser: Simulation of Semiconductor Devices and Circuits at High Frequencies.....	91
P. Söser: Systemsimulation und Messungen an hochauflösenden Sigma-Delta Modulatoren	97
N. Kerö et al.: Wann mi des Designbüro net vermittelt hätt' — Ein Erfahrungsbericht über 10 Jahre Technologietransfer	99
 GMe Presentations – Posters Cleanroom Vienna.....	 103
B. Basnar et al.: Kontrastmechanismen in der Rasterkapazitätsmikroskopie und der Einfluss der Dotierung auf die Signalgröße	105
R. Bratschitsch et al.: Coherent Terahertz Emission from Optically Pumped Parabolic Quantum Wells.....	107
S. Harasek et al.: Ultrathin Silicon Dioxide: Growth and Characterization	111
P.O. Kellermann et al.: Multi-Wavelength Laser Diode Array Based on Surface Mode Coupling.....	117
R. Kolm et al.: SIMS-Analyse von SiGe-CVD-Strukturen	121
H. Langfischer et al.: Focused Ion Beam Induced Local Tungsten Deposition	123
M. Litzenberger et al.: Laser-Interferometric Investigation of Triggering Behavior in CMOS and Smart Power ESD Protection Structures	129
A. Lugstein et al.: FIB Based Micro Fabrication Technique for a Novel Type of Scanning Electrochemical Microscopy Probes	133
C. Pacher et al.: Ballistic Electron Spectroscopy of Quantum Mechanical Anti-reflection Coatings for GaAs/AlGaAs Superlattices.....	137
D. Rakoczy et al.: Ballistic Electron Emission Spectroscopy on Biased GaAs-AlGaAs Superlattices in Transverse Magnetic Fields.....	143
G. Strasser et al: Epitaktisches Wachstum von gitterangepassten und verspannten III-V Verbindungen.....	149
J. Ulrich et al.: Band Structure Engineering for Terahertz Quantum Cascade Lasers.....	151
H. Wanzenboeck et al.: Sublithographische Siliziumoxid-Strukturen für die Phasenshifttechnologie.....	155
 GMe Presentations – Posters Cleanroom Linz	 157
T. Berer et al.: Fabrication of AlGaAs Nanostructures.....	159
A. Daniel et al.: Strain Modulations in Si Underneath Patterned Oxide Stripes	165
D. Gruber et al.: Characterization of Si/Si _{1-x-y} Ge _x C _y Heterostructures for Device Applications	171
K. Himmelbauer et al.: Magnetic Properties of Thin Iron Films.....	173
K. Hingerl: Reflection Difference Spectroscopy on II- VI Semiconductors; A Tool to Investigate Surface Processes <i>in situ</i> During Growth.....	179
G. Kocher et al.: Erbium in SiO _x Environment: Ways to Improve the 1.54 μm Emission	185

R.T. Lechner et al.: Molecular Beam Epitaxy of Self-Organized PbSe Quantum Dot Superlattices	189
W. Märzinger et al.: In-Line Prozesskontrolle mit einem kompakten Echtzeit-FTIR-Spektrometer	191
N. Sandersfeld et al.: Conduction Electron Spin Resonance in MBE-Grown Si/SiGe Quantum Wells	193
N. Sandersfeld et al.: Modulation Doped Si/Si _{1-x} Ge _x -Field Effect Transistors	195
T. Schwarzl et al.: Mode Splitting and Lasing in Detuned Lead Salt Microcavity and Microdisk Resonances	197
H. Sitter et al.: Kristalline dünne Filme aus Para-Hexaphenyl hergestellt mit Hot-Wall-Epitaxie	201
H. Sitter et al.: <i>In situ</i> -Kontrolle der Herstellung von Galliumnitrid-Schichten	203
J. Stangl et al.: Strain and Composition of SiGe Islands on Si (001)	205
K. Wiesauer et al.: Nano-Scale Dislocation Patterning in PbTe on PbSe (100) Heteroepitaxy Studied by Scanning Tunneling Microscopy	209

Introduction

Silicon-Based Technologies for Wireless

Abbas Ourmazd

IHP Microelectronics

Im Technologiepark 25, 15236 Frankfurt (Oder), Germany

Within five years, mobile communication and internet will be submerged into a technology offering location- and context-aware, person-specific information and services, “on the fly” to the mobile individual, “untethered” to the desk-bound. The “global village”, defined by today’s wired internet, will blossom into local wireless worlds, each offering the information and services available (and appropriate) at that location. At the Louvre, your “Chameleon Access Device” will download its personality from the “local ether” to purchase you a ticket as you enter, guide you to the Rubens or the da Vinci sections, and inform you about the Mona Lisa as you stroll past it. It will show you the location of the nearest Crêperie (or hamburger joint) as you leave, help you find a taxi, and, should you wish, inform your spouse of your whereabouts.

To make this possible, a \$99 device is needed, whose primary value resides in a single, or at most very few silicon chips, with broadband wireless and advanced information processing capabilities. I will present an overview some of the technical challenges associated with this ambitious goal.

The New AMS 200 mm Mixed Signal Foundry – Technical and Economic Challenge

Wolfgang Pribyl

Austria Mikro Systeme International AG
Tobelbader Strasse 30, 8141 Unterpremstätten, Austria

1. Introduction

During the last years the traditional vertical business model of the semiconductor industry has undergone many changes, and new models have evolved. The different levels of value creation in the industry have been mapped to individual companies specializing in different aspects of the semiconductor value chain. Fabless design houses could be easily established, as the high entry barriers in form of the high capital needs of an integrated company did not apply any more. Others specialized in various production tasks as mask shops, test, and assembly plants and pure play silicon foundries. Those who remained “fabbed” as new vertical semiconductor companies started to control the different value creation steps on an individual basis and such became able to benchmark themselves against the specialists in the market. This trend has strongly improved the overall efficiency of the industry and has created a large number of new semiconductor companies, many of them are very successful on the market and achieved high valuations on the stock markets.

2. New Strategy of *Austria Mikro Systeme*

About three years ago *Austria Mikro Systeme International* also had to find an answer to the question for a new strategy. It had to be decided whether to remain a vertical integrated semiconductor company with all consequences or to adopt the new fabless model. Because of its traditional strengths in production including a very high quality and reliability record demonstrated in aviation, automotive, and industrial applications, AMS selected to remain fabbed. In addition, a certain part of the production volume was and is subcontracted to foundry partners which have AMS processes implemented. Today AMS still offers all aspects of semiconductor development and production as a “one-stop-shop”, but has separated the responsibilities into individual business units. In order to measure the performance of each unit against the best in class in the world, three product oriented business units (Automotive, Communications and Industry) and a production unit (Full service foundry) have been created.

Focusing on markets, customers and special application segments got high attention, at the same time the new 200 mm wafer fab project for deep sub micron technologies was started. Key reasons for the decision to undertake this major investment of 300 MEuro into the new fab have been on the one hand the need for access to state of the art technologies in the deep sub micron range. This includes the possibility to implement AMS specialties as BiCMOS, SiGe and HV (high voltage) on top of those. The capacity requirements of dynamic markets of the customers as well as the need for an improved

cost structure have been additional reasons. The whole project is structured in a way which allows to achieve a world wide competitive position for the production.

3. The Austria Mikro Systeme 200 mm Mixed Signal Foundry

The 200-mm Fab is set up as a three level SMIF (standard mechanical interface) fab with a cleanroom of class 1.000 on a waffle table of 2.600 m² and an additional cleanroom area of 1.100 m². Meanwhile it has been proven that the vibration characteristics of the building will allow to process even very advanced technologies down to 0,13 μm structures, the overall capacity will be > 2.500 WSPW (wafer starts per week), this roughly quadruples the production capacity.

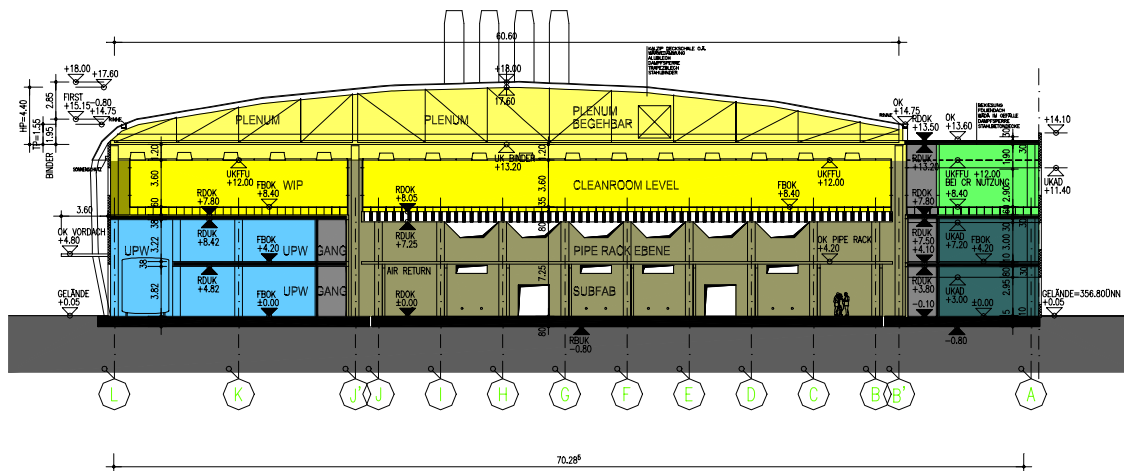


Fig. 1: Cross section of 200 mm Fab. The dark yellow (medium gray) section indicates the cleanroom area for production.

The fab will be equipped with most advanced SMIF and mini environment techniques (better than class 1) and will differentiate itself by flexibility and special process modules added on top of the base CMOS processes. These process options target high performance mixed signal and RF circuits (BiCMOS and SiGe-BiCMOS) as well as systems on chip including sensor elements (e.g. micro mechanical elements for accelerometers and hall effect sensors for various applications). For automotive and industrial applications a range of high voltage technologies are available which are exactly tailored to the existing and future business of the respective customers.

Examples for successful products using this technological base include car access systems, safety critical data transmission, and sensor applications in automotive applications as well as metering, control circuits, and bus systems in the industrial environment. For voice and data communications the RF-technologies are used for low power/high speed applications in the wired and wireless world.

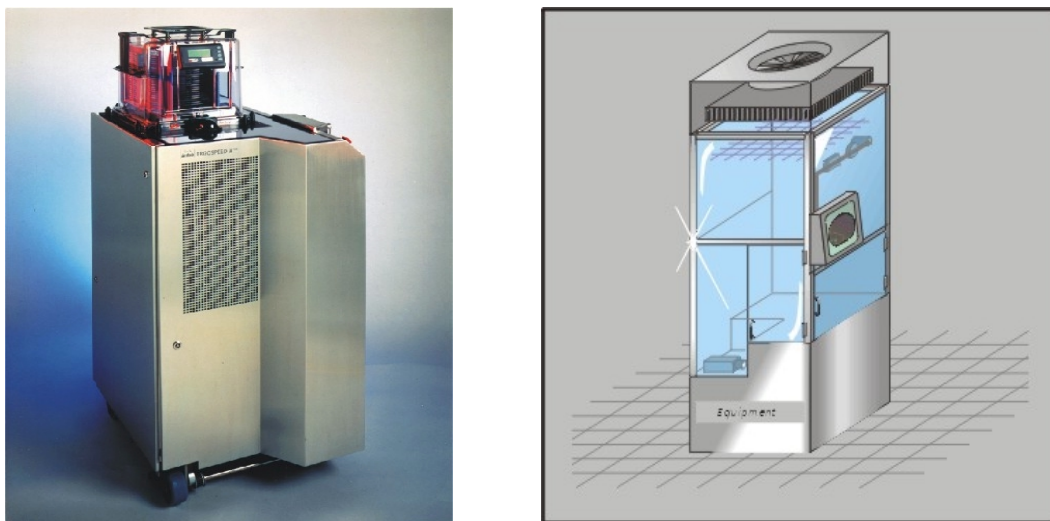


Fig. 2: SMIF robot with wafers loaded in a pod (left) and view of a ME (mini environment) which is supported from the top.

4. Technological Capabilities for the Future

In defining the technology roadmap of a semiconductor company the product portfolio and the markets served have a significant influence. In times where DRAMs and high performance processors already start to use $0,13 \mu\text{m}$ CMOS technologies produced on 300 mm wafers, other market segments can still be served well by technologies in the range of $0,6 \mu\text{m}$ to $0,25 \mu\text{m}$. Depending on the amount of analog content of a mixed signal chip, a very advanced deep sub micron technology may even not make business sense at all.

As the products of the future tend to incorporate more and more diverse functions (analog, digital, sensors, memory, NV-memory, MEMs) the set of technologies has to respond to this SoC (system on chip) trend. There is still a tradeoff to be found between integrating all functions on one chip (pure SoC solution) or combining two or more chips in a package (system in package approach), which in some cases might be the more economic one. *Austria Mikro Systeme* is committed to a technology roadmap shown in Fig. 3, which still shows several specialized technologies in $0,8$ and $0,6 \mu\text{m}$ needed for high volume business with long term commitments for automotive and industrial customers. $0,35 \mu\text{m}$ mixed signal CMOS including the BiCMOS and SiGe options will be the last true 5 V technology and the first entry point in the system level design. For BiCMOS f_t (f_{max}) of 30 (30) GHz will be available, for the SiGe Option the respective figures are 55 (75) GHz. The technologies are designed as add-ons to the CMOS base process, so a complex digital part (4+ layers of metal) can be combined with analog and RF functions. Whereas CMOS will become the mainstream technology for applications up to a range of $2 - 5 \text{ GHz}$, SiGe HBTs will generate a major competition for GaAs circuits in the frequency range up to $30 - 40 \text{ GHz}$.



Fig. 3: Technology Roadmap: green (dark gray) indicates production at AMS foundry, yellow (light gray) shows contracted production at partner foundries in AMS processes.

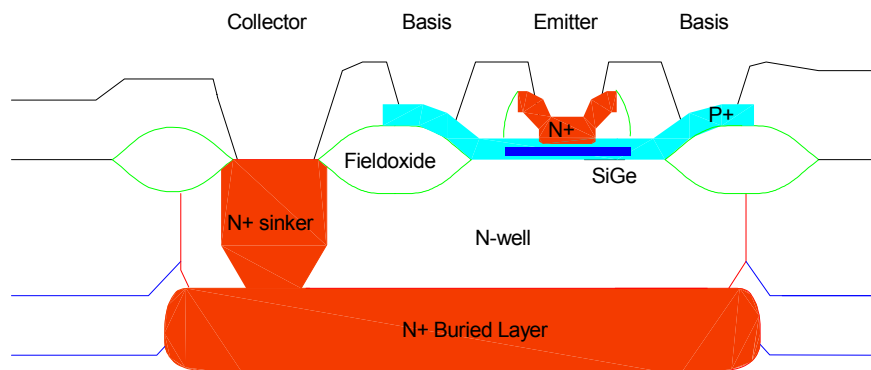


Fig. 4: Schematic cross section of a SiGe-HBT with two base contacts.

5. Summary

Having adopted the appropriate business model of individual product and production oriented business units, a mid-sized vertical semiconductor company can be successful. The individual units have to be compared to the best in class on a regular basis, and continuous learning has to be applied. It is possible to invest into state of the art production facilities and achieve a worldwide competitive cost structure even with a moderate sized fab. For a successful position on the foundry market it is necessary to offer special process enhancements, as mixed signal and RF as well as sensors and MEMs. These offers must not be restricted to the process but have to be combined with a flexible support in modeling, parameters and design support as well as support in debugging and migration to a volume production scenario.

Mixed-Signal Circuits on their Way to 0,1 μ m Technologies

R. Petschacher, F. Kuttner, H. Weinberger, A. Wiesbauer

Infineon Technologies Design Centers Austria GmbH
Siemensstraße 2, 9500 Villach, Austria

1. Introduction

Since more than 20 years the semiconductor industry enjoys the benefits of downsizing the device dimensions and thereby increasing functionality and speed of very large-scale integrated circuits. For the first time now there seem to appear some clouds on the horizon. Downscaling integrated circuits below 0.1 μ m may face over-proportional production cost due to the increase of process steps and the increase of equipment prices. While digital circuits will follow the well-known scaling laws well below 0.1 μ m [1], [2], mixed signal circuits require a differentiated analysis when reaching structure sizes in the order of 0.1 μ m and below. The reduced supply voltage affects the dynamic range as well as the noise requirements of analog circuits, and together with threshold voltages not scaling down with the same factor will force a change in circuit topologies. This paper is based on practical experiences with telecommunication circuits designed on technologies between 0.5 μ m and 0.13 μ m structure size and will describe benefits and challenges of deep sub-micron designs for mixed signal ICs.

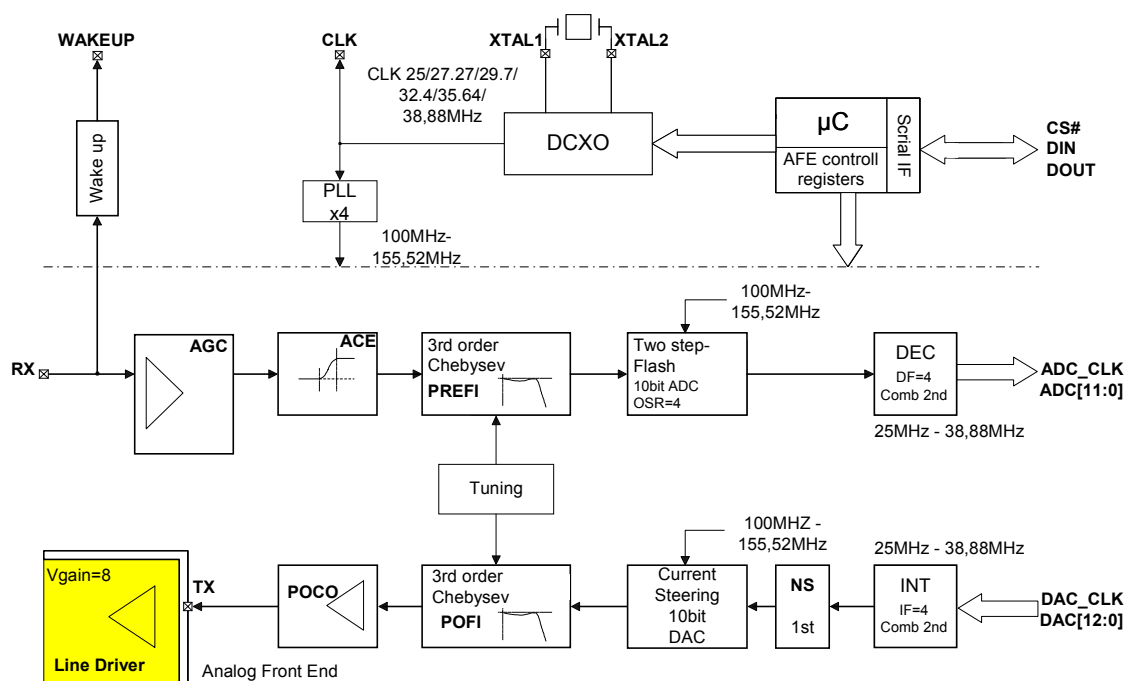
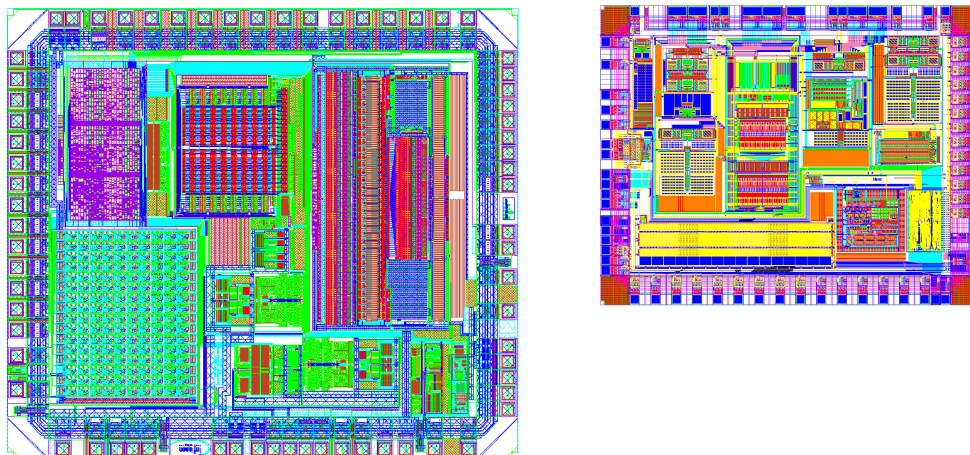


Fig. 1: Block diagram of the analog front-end IC for a VDSL-system for both symmetrical 13 Mbps and asymmetrical 26 Mbps transmission schemes.

2. Requirements Governing Scaling Benefits

In general, scaling down mixed signal circuits in the range from $0.5\ \mu\text{m}$ to $0.18\ \mu\text{m}$ offers a lot of benefits. In particular, the significant increase in bandwidth at constant power levels and the area reduction open up new possibilities in system integration of mixed signal circuits. The scaling of a VDSL analog-front-end IC (Fig. 1) illustrates these benefits. The circuit is part of a new, just unveiled 4-band VDSL solution for both symmetrical 13 Mbps and asymmetrical 26 Mbps spectral band allocation schemes, delivering data for distances of up to 1.5 km over existing telephone copper wire infrastructure.



Technology	0.6 μm BICMOS	0.18 μm CMOS
Supply Voltage	5 V	1.8 / 3.3 V
Area	14,5 mm^2	7.5 mm^2
Power consumption	710 mW	450 mW
Sampling rate	20 – 33 MSPS	100 – 155 MSPS
Bandwidth	8 MHz	12 MHz

Fig. 2: Result of scaling the VDSL analog front-end IC of Fig. 1.

Figure 2 shows the result of the shrink from a $0.5\ \mu\text{m}$ to a $0.18\ \mu\text{m}$ technology: the area was reduced by 50%, and power consumption, by 40%. The increased speed of the transistors allowed to increase the oversampling ratio of the ADC and DAC instead of increasing the moderate resolution of the modules itself. The analog filters and amplifiers also profited from the speed (e.g. the bandwidth of an op-amp increases from 300 MHz to 1 GHz), and there was no problem to enlarge the system bandwidth to 12 MHz required by the new 4-band standard. In conclusion, this example shows that mixed signal circuits with moderate dynamic range or resolution of 11 to 12 bit and higher signal bandwidth are extremely well suited for scaling, and this will continue also to the next generation with $0.13\ \mu\text{m}$ structures and 1.2 V supply.

Somewhat different are the considerations for an ADSL-system [3], [4] that serves for line lengths up to 4 km at an asymmetrical transmission rate of up to 8 Mbps. Here a line referred noise of $-140\ \text{dBm/Hz}$, a maximum receive signal of $4\ V_{\text{pp}}$ and a signal bandwidth of 1.1 MHz define a dynamic range of 100 dB (Fig. 3). When the allowed signal swing at the input scales down with the structure size of the technology also the noise level in the amplifiers and filters has to be reduced. A simple calculation (Table 1)

shows that due to the noise limitation capacitances in SC circuits increase dramatically with down-scaling. To make it worse modern wafer-processes use low-k dielectrics in order to minimize propagation delay on long and dense interconnects. This in turn increases the chip area consumed by capacitances. In this example, the 0.1 µm generation will need different circuit topologies, e.g. SI instead of SC structures. New structures exploiting the speed advantage of a 0.1 µm process will also be necessary for the 14 bit A/D-converters as shown in Table 2.

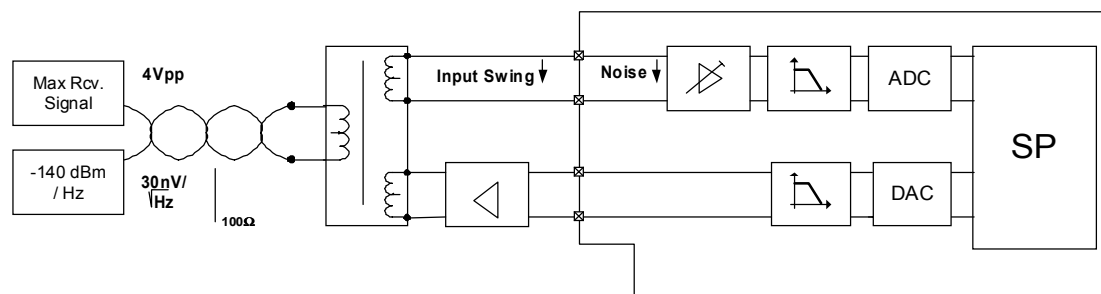


Fig. 3: Schematic input circuit of an ADSL-system. The required dynamic range is 103dB.

Min. Structure Size	Swing	Input Referred Noise	Equivalent R	C (const. RC)
0,5 µm	4 V _{pp}	10 nV√Hz	6.7 kΩ	1 pF
0,18 µm	2 V _{pp}	5 nV√Hz	1.7 kΩ	4 pF
0,1 µm	1 V _{pp}	2.5 nV√Hz	550 Ω	16 pF

Table 1: Equivalent noise resistor and corresponding capacitance calculated for constant bandwidth of a constant dynamic range of the ADSL input circuit shown in Fig. 3.

Min. Structure Size	Swing	ENOB	Quantum Noise	OSR	C _s	f _{CLK}
0.5 µm	4 V _{pp}	13 bit	13 nV√Hz	12	150 fF	26 MHz
0.18 µm	2 V _{pp}	13 bit	37 nV√Hz	12	2 pF	26 MHz
0.1 µm	1 V _{pp}	13 bit	18 nV√Hz	24	4 pF	52 MHz

New ADC concepts required!

200	0.05 pF	400 MHz
-----	---------	---------

→ Continuous time ΔΣ-ADC

Table 2: Change of requirements on the ΔΣ-ADC of the ADSL input circuit (Fig. 3) with downscaling.

Finally the conclusion is that analog processing of signals with a high dynamic range will have to deal with enlarged areas and also significantly higher currents. New circuit

topologies are required, and a careful choice has to be made which circuits can be integrated on a single chip system economically.

3. Circuit Design Considerations

The most severe limitation of analog circuit design in the 0.1 μm region is the fact that V_{th} , the threshold voltage of the MOS-transistors, does not scale linearly with the supply voltage V_{dd} , which will be as low as 1 – 1.2 V. This causes several problems [5]: Amplifier gain will suffer from the lack of cascode stages, and multi stage amplifiers with nested feedback loops might be necessary. Input and output common mode range will overlap only in a small range, thereby reducing the signal swing and so further decreasing the dynamic range. Unfortunately, different requirements for different applications lead to different transistor designs and trade-offs. So currently different threshold voltages and different gate oxide thicknesses are offered within one wafer process, which requires extra masks and lets cost and process-complexity explode.

For true system on chip applications it is consequently desirable to reduce analog circuitry to a minimum and to stick to transistors optimized for digital operation. This was done for a test structure in our newest 0.13 μm process comprising a 10 bit successive approximation ADC, a PLL circuit, a bandgap circuit, and a buffer (Fig. 4). The ADC consists of a switched capacitor array and a comparator circuit and uses only inter-metal capacitors and digital transistors.

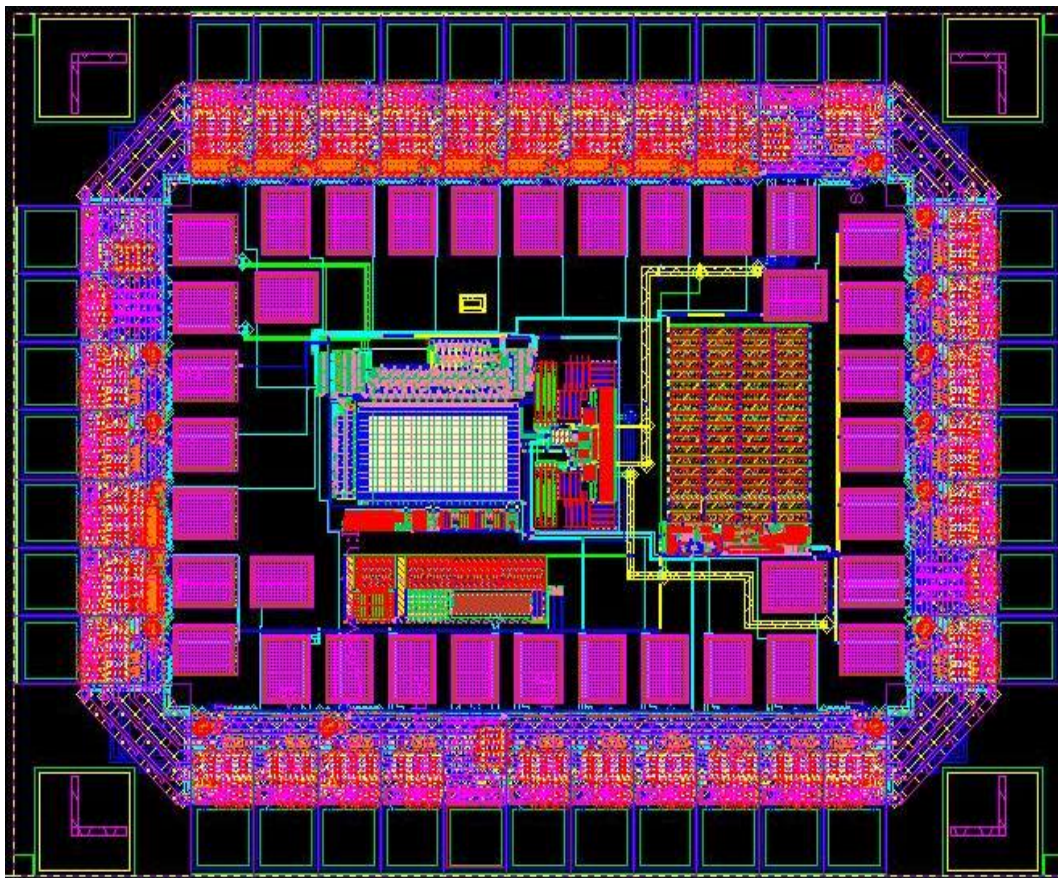


Fig. 4: Layout of a test structure built in a pure digital 0,13 μm CMOS process. It contains a 10 Bit SA-ADC, a buffer, a PLL, and a bandgap circuit.

First measurements show an extremely good performance:

Operated at 1.2 V with a sampling frequency of 16 MSPS, the ADC consumes only 2.5 mW and achieves 10 bit THD and 8.5 bit SNR over a signal frequency range of 0 – 8 MHz. The area is 0.082 mm².

4. Conclusion

Up to our current mainstream technology with a half pitch of 0,18 μ m downscaling of telecommunication ICs delivered the expected increase in performance. When focusing on simple analog structures we expect this trend to continue down to the 0.1 μ m region. This was proven by an ADC test structure in our newest 0.13 μ m process. For mixed signal circuits requiring a high dynamic range techniques like oversampling or dynamic element matching have to be further developed in order to translate accuracy requirements into speed requirements. In case this is not possible for certain high volume applications we expect to see an increase in process complexity by adding special transistors for mixed signal applications. In general, one-chip solutions for systems on silicon in 0.1 μ m processes will represent a challenge to the creativity and ingeniousness of mixed-signal designers.

References

- [1] Hiroshi Iwai, "CMOS Technology – Year 2010 and Beyond", *IEEE J. of Solid-State Circ.*, vol. 34, no. 3, pp. 357 – 366, 1999.
- [2] Siegfried Selberherr, "Die großen Herausforderungen in der Mikroelektronik in den nächsten zehn Jahren", *e&I* 115(1998), vol. 7/8, pp.344 – 348.
- [3] J. Hauptmann, et.al., "Broadband Modem IC Developments-Design and System Aspects", *Tagungsband der Austrochip 99*, Villach, Austria, 30. Sept. – 1. Oct. 99, invited paper.
- [4] A. Wiesbauer et.al., "A 13.5-Bit Cost Optimized Multi-Bit Delta-Sigma ADC for ADSL", *Proceedings of 25th ESSCIRC*, Duisburg, Germany 21 – 23 Sept. 1999, pp. 86 – 88.
- [5] Klaas Bult, "Analog Design in Deep Sub-Micron CMOS", *Proc. 26th European Solid-State Circuits Conf.*, Stockholm, 19-21 Sept. 2000.

Components and Systems

SiGe High-Frequency Devices

Ulf König

DaimlerChrysler Research
Wilhelm Runggestraße 11, 89013 Ulm, Germany

After more than 13 years of research the speed race of SiGe HBTs has arrived at 180 GHz f_{\max} and 156 GHz f_T . Even in high-volume production now are devices with around 100 GHz. The main reasons are a steadily improving epitaxy with a huge freedom in thickness and composition and the reduction of parasitics.

The main focus in this presentation is put on SiGe HFETs which are still on the research level. In SiGe HFETs the well known principle of III/V HEMTs is transferred to Si microelectronics. High mobilities up to 2900 cm²/Vs for n-channels and up to 3600 cm²/Vs for p-channels have been found, 5 to 15 times above respectively doped Si. In addition there is evidence for an increased velocity overshoot due to strain in the channels.

For Schottky- or MOS-gate devices IBM and DaimlerChrysler have reached transconductances around 300 mS/mm for depletion mode n-HFETs and around 500 mS/mm for enhancement mode. p-HFETs showed around 250 mS/mm. High currents above 600 mA/mm have been obtained for p-MOS HFETs. Cut-off frequencies for both n- and p-HFETs are for f_{\max} up to 135 GHz and for f_T around 80 GHz, which have been achieved for n-HFETs already with a gate length of 0.25 μm , for p-HFETs with 0.1 μm . Recently the performance at cryo-operation was investigated. 195 GHz was measured for n-HFETs at 50K, 180 GHz for p-HFETs at 35K. Such a pronounced frequency increase is related to the 2-dimensional electron or hole transport in the Si or Ge channels, respectively.

There is a gate length dependence visible for all frequency data reported so far, but the range below 0.2 μm is hardly exploited. Better self-aligned layouts are demanded. Simulations forecast frequencies above 200 GHz at RT assuming reduced parasitics.

Concerning noise, n- and p-type HFETs exhibit the very low noise figures of 0.3 dB at 1 – 2.5 GHz. Conservative semi-quantitative simulations for the high-frequency noise predict 0.5 dB at 10 GHz. Siemens has established outstanding low-frequency noise represented by corner frequencies below 200 Hz for p-SiGe MOSFETs.

First test circuits elucidate the potential of this novel device category. E.g., inverter delays are 22 ps for a 0.25 μm HFET, transimpedance amplifiers operate with a transimpedance above 50 dB Ω and up to a bandwidth of 2 GHz. If finally a new CMOS generation can be created, consisting of a Si-channel n-HFET and a Ge-channel p-HFET, the power-delay product can even reach values below 1fJ.

Mikroelektronische III-V-Bauelemente für hohe Frequenzen

Walter Kellner

Infineon Technologies AG, WS TI G, 81730 München, Germany

Durch HEMT (High Electron Mobility Transistor) oder HBT (Heterojunction Bipolar Transistor) lassen sich die durch das III-V-Material gegebenen Eigenschaften wie hohe Beweglichkeit und Driftgeschwindigkeit der Elektronen sowie hoher Bandabstand in attraktive Eigenschaften der Bauelemente wie hohe Grenzfrequenzen, hohe Verstärkung, niedriges Rauschen, hohe Ausgangsleistung, guter Wirkungsgrad und Linearität umsetzen. Entscheidend für den Erfolg auf dem globalen Markt ist der Preis, wobei die technische Qualität vorausgesetzt wird. Mit der Einrichtung einer 150 mm-Scheibenfertigung für GaAs in München-Perlach wurde dazu ein entscheidender Schritt getan. Im Vortrag werden die prinzipielle Funktion von HEMT und HBT sowie deren wichtigste Eigenschaften kurz beschrieben. An zwei Beispielen werden sodann erfolgreiche Entwicklungen für den Systemeinsatz demonstriert: Ein HBT-Leistungsverstärker für GSM Mobiltelefone (900 MHz) erreichte auf einer Chipfläche von nur 2 mm² eine Ausgangsleistung von 2,7 W bei einem Wirkungsgrad (PAE) von 56 % und einer Verstärkung von 32 dB sowie einem Regelbereich von 80 dB. Das zweite Beispiel beschreibt Millimeterwellenschaltungen (77 GHz) für Auto-Abstandsradar. Die vom Sensor erfassten Daten steuern Brems- und Gas, sodass das Fahrzeug automatisch den Sicherheitsabstand zum vorausfahrenden Fahrzeug einhält. Die derzeit in der Automobil-Luxusklasse angebotenen Systeme verwenden noch Gunn-Elemente in Hohlleitern. Für den Massenmarkt ist diese Technologie jedoch zu teuer. Ein Chipsatz für planaren Modulaufbau auf der Basis von HEMT-Schaltungen und einer Silizium Schottky-Diode wird vorgestellt. Das HF-Modul erwies sich in Fahrttests bei Siemens Automotive als gut geeignet für den praktischen Einsatz.

1. HEMT

Im MESFET wird der Strom zwischen Source und Drain durch die Raumladungszone unter dem Metall-Halbleiter-Übergang gesteuert, wobei die aktive Schicht meist durch Implantation der Dotierstoffe ins semiisolierende GaAs erzeugt wird. Der HEMT ist im Prinzip ein MESFET auf einer hetero-epitaktischen Schichtfolge (Fig. 1). Die Verwendung unterschiedlicher Halbleiter ermöglicht einen Potentialverlauf wie in Fig. 2, der die Elektronen im Kanal hält und somit Verluste durch Elektronenstreuung ins Substrat minimiert. Durch den dünnen Kanal nahe der Oberfläche und die hohe Beweglichkeit des InGaAs ergeben sich Verbesserungen in der Grenzfrequenz bis zum Faktor 5 im Vergleich zum MESFET. Die Auswahl der Schichtparameter und die Prozessführung ermöglichen es, die Bauelemente für verschiedene Anwendungen zu optimieren: Von Single-Heterojunction (SH)-HEMT für Low-Noise-Anwendungen (LN60) bis zu Double-Heterojunction (DH)-HEMT für Mobilkommunikation (Leistung und hoher Wirkungsgrad bei 3 V-Betrieb, M30), von Leistungsbaulementen bis 40 GHz (P60) bis zu höchsten Frequenzen bis 90 GHz (110). In SH-HEMT wird der InGaAs-Kanal begrenzt durch die dotierte AlGaAs Schicht und durch die undotierte GaAs-Pufferschicht zum Substrat. In DH-HEMT entsteht ein zweiter Hetero-Übergang durch eine AlGaAs-

Pufferschicht zum Substrat, was den Potentialtopf vertieft und die Elektronendichte erhöht - ein Vorteil für Leistungs-HEMT.

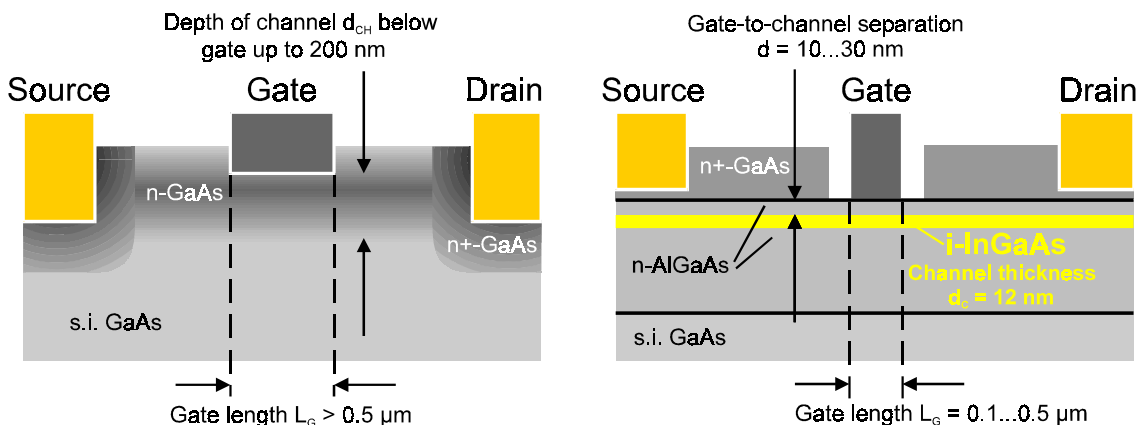


Fig. 1: Querschnitt MESFET und HEMT.

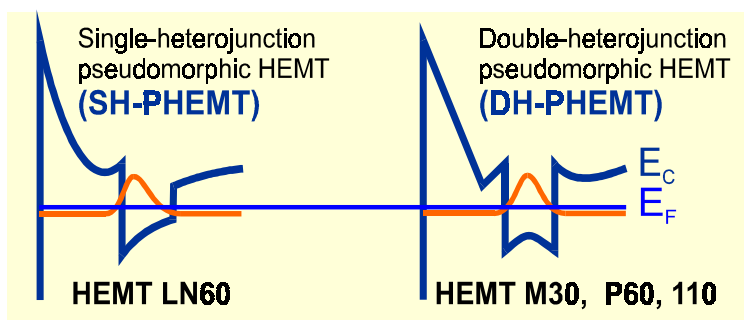


Fig. 2: Leitungsbandverlauf und Elektronendichte verschiedener HEMT-Familien, die Zahl verweist auf f_t .

Fig. 3 zeigt Rauschzahl und zugehörige Verstärkung als Funktion der Frequenz für die HEMT-Familien LN60, P60 und 110. H110 erreicht ebenso niedriges Rauschen wie LN60 und liefert mehr Verstärkung, die Prozessführung ist aber durch die kürzere Gatelänge (130 statt 180 nm) aufwändiger.

Der HEMT Prozess ist vollständig planar und durch den Einsatz optischer Lithographie sowie moderner Trockenätz- und Spacer-Prozesse kostengünstig.

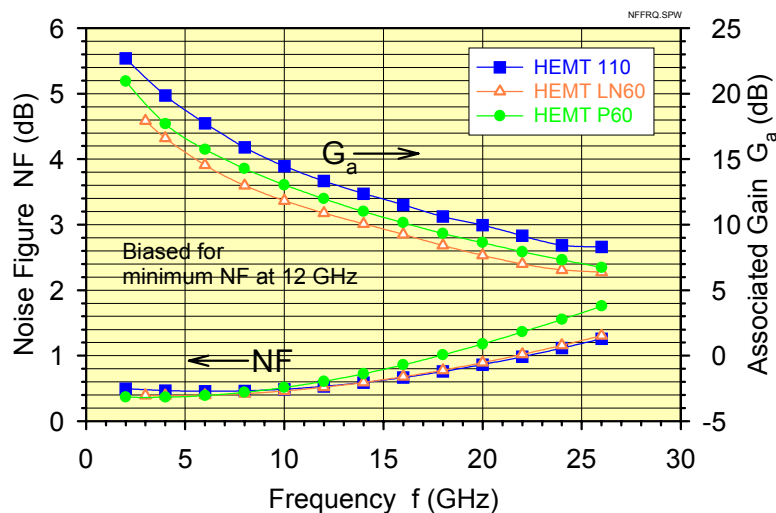


Fig. 3: Rauschzahl und zugehörige Verstärkung als Funktion der Frequenz.

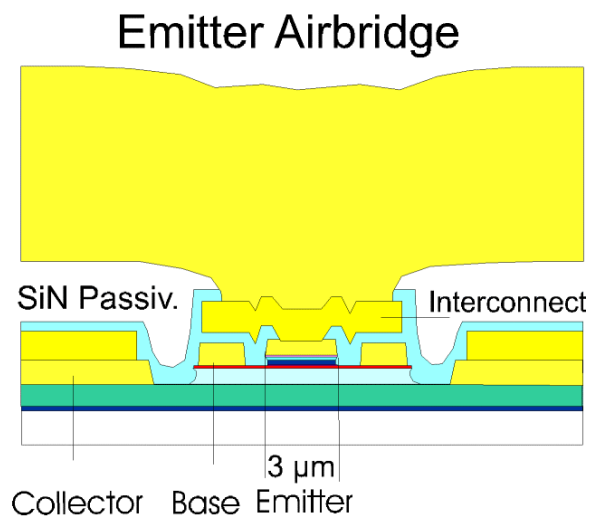


Fig. 4: Querschnitt Heterobipolar-Transistor (HBT)

2. HBT

Fig. 4 zeigt eine Querschnitt durch einen einzelnen HBT-Finger, von denen etwa 50 bis 100 parallel geschaltet werden, um einen Endstufentransistor für ein Mobiltelefon zu erhalten. Wegen der bei Leistungstransistoren erheblichen Selbsterwärmung der Transistoren sind die Finger über dicke Luftbrücken miteinander verbunden. Zwischen den Fingern entsteht so eine enge thermische Kopplung, die Temperaturunterschiede werden vermindert. Der Prozess beruht auf dem Einsatz einer Stepper-Lithographie mit 3 μm -Strukturen, wobei vertikale Höhenunterschiede von etwa 2 μm zu beherrschen sind. Trotz dieser geringen technologischen Anforderung erreicht der HBT ausgezeichnete HF-Eigenschaften und hohe Durchbruchspannung. Die Ursache hierfür liegt im Aufbau auf semiisolierendem GaAs (kleine Kapazitäten), im Material mit hoher Elektronen-Beweglichkeit und im Prinzip des Wide Gap Emitters (Shockley, 1951). Fig. 5 zeigt das

Banddiagramm im thermischen Gleichgewicht. Auf den Wide Gap Emmitter aus n-InGaP ($4 \times 10^{17} \text{ cm}^{-3}$) folgt eine hochdotierte p-GaAs-Basis ($4 \times 10^{19} \text{ cm}^{-3}$), ein n-GaAs-Kollektor ($2 \times 10^{16} \text{ cm}^{-3}$) und ein n-GaAs Subkollektor ($5 \times 10^{18} \text{ cm}^{-3}$). Beim Anlegen von positiven Spannungen an Basis und Kollektor erniedrigt sich die Barriere am EB-Übergang, wodurch Elektronen in die Basis gelangen. Durch den Wide Gap Emmitter wird eine Injektion von Löchern von der Basis in den Emmitter verhindert, sodass eine ausreichend hohe Stromverstärkung zu erzielen ist, weitgehend unabhängig von den Dotierungen von Emmitter und Basis. Zur Optimierung der HF-Eigenschaften wählt man, um den Basisbahnwiderstand zu verkleinern, die Dotierung der Basis hoch und die von Emmitter und Kollektor niedrig, um die Kapazitäten zu verkleinern. Fig. 6 zeigt die wichtigsten Kennzahlen des HBT M30 Prozesses.

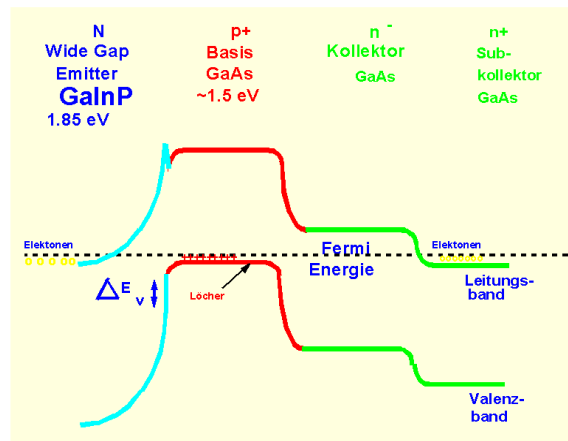


Fig. 5: Banddiagramm HBT.

Emitter Width w	3 μm
Frequencies f_t / f_{max}	30 GHz / 60 GHz
On-Resistance R_{on}	< 450 Ohm/ μm^2
Offset Voltage U_{offs}	< 0.2 V
Current Gain β	> 80
Max. Coll. Curr. Density j_{cmax}	0.2 mA/ μm^2
Coll.-Emit. Breakd. Volt. U_{ceo}	> 15 V
Outp. Pow./Emit.-Area P_{out}/A_e	0.3 mW/ μm^2

Fig. 6: Kennzahlen für HBT M30.

3. HBT-Leistungsverstärker für GSM [1]

Die Messung von HBT-Leistungszellen erforderte die Entwicklung von statischen und gepulsten Messungen im Bereich von 5 bis 10 A. Fig. 7 zeigt gepulste Ausgangskennlinien für Transistoren mit verschiedenen Emitterflächen (1440 / 4320 / 8640 μm^2), normiert auf den Strom der größten Zelle. Das gute Skalieren mit der Emitterfläche weist hin auf eine erfolgreiche Optimierung von Prozess und Zellen-Layout. Für die Großsig-

nal-Charakterisierung wurde ferner ein aktiver Load-Pull-Messplatz entwickelt, der für Ausgangsleistungen bis zu 10 W Analysen von Grund- und Oberwellen ermöglicht. Zusammen mit einem elektro-thermischen Modell für den HBT wurden die Zellen einem ausführlichen Vergleich zwischen Simulation und Messung unterzogen, womit eine Grundlage für den Entwurf künftiger Schaltungen erreicht war.

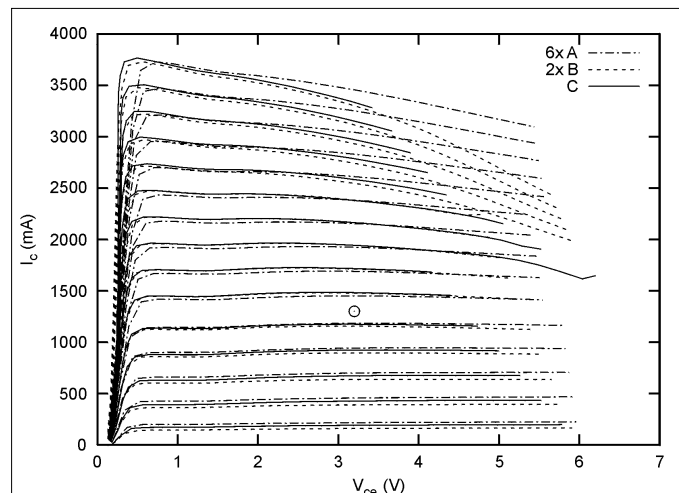


Fig. 7: Gepulste Kennlinien ($T = 0,58$ ms) für HBT- Leistungszellen mit $1440/4320/8640 \mu\text{m}^2$, A/B/C.

Die Anforderungen an lineare Verstärkung $G > 35$ dB und an Isolation im Off-Zustand (70dB) machten ein dreistufiges Design nötig. Auf der Grundlage von Load-Pull-Messungen an verfügbaren 0,5 W-Zellen wurden zunächst die Stufen mit Stromeinspeisung und die Anpasselemente zwischen den Stufen mit dem HBT-Kleinsignal-Modell entworfen. Erst danach wurde die letzte Optimierung mit dem Großsignal-Modell vorgenommen. Die Chips wurden in ein TSSOP10-Gehäuse eingebaut und in einer Testschaltung gemessen.

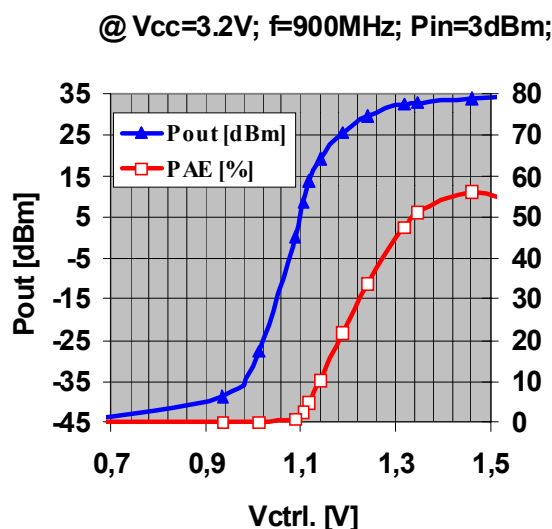


Fig. 8: Ausgangsleistung P_{out} und Wirkungsgrad PAE als Funktion der Kontrollspannung.

Fig. 8 zeigt die gemessene Ausgangsleistung (max. 2,7 W) und den Wirkungsgrad (max. 56%) als Funktion der Kontrollspannung bei $P_{in} = 3$ dB, $V_{cc} = 3,2$ V, $f = 900$ MHz. Die Großsignal-Verstärkung liegt bei 32 dB, die Leistung lässt sich über 80 dB regeln. Damit waren die Entwurfsziele erreicht.

4. Chipsatz für Autoradar [2]

Die Reduktion der Kosten auf ein für den Autokäufer erträgliches Niveau stellt derzeit die größte Herausforderung für die kommerzielle Umsetzung des Autoradars dar. Der hier vorgestellte Vorschlag beruht auf der Verwendung möglichst kleiner Standard-Komponenten, die mit hoher Ausbeute gefertigt werden können. Ein Chipsatz ermöglicht auch eine flexible und kostengünstige Realisierung unterschiedlicher Mehrstrahl-Radarkonzepte je nach Anforderung der Auto-Hersteller. Der Chipsatz für ein FMCW-Radar enthält 3 GaAs HEMT-MMICs:

- voltage controlled oscillator (VCO)
- medium power amplifier (MPA)
- active subharmonic mixer (HMIX)

sowie eine Silizium Schottky-Diode für den Empfangsmischer. Diese wurde wegen des niedrigen $1/f$ -Rauschens und der geringen Kosten gewählt. Der Konversionsverlust liegt bei 10 dB, die Rauschzahl (100kHz Zwischenfrequenz) bei 18 dB.

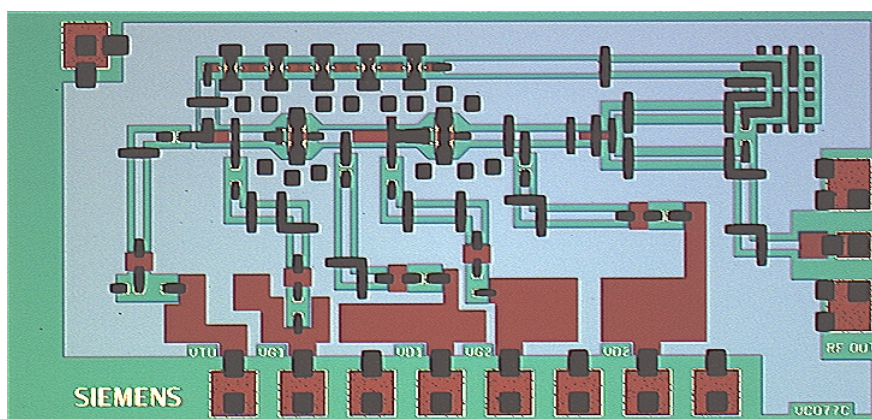


Fig. 9: HEMT-VCO 77 GHz.

Fig. 9 zeigt den VCO, der aus einem zweistufigen Verstärker, einem Wilkinson-Teiler und einem spannungsgesteuerten Phasenschieber besteht. Fig. 10 zeigt Frequenz und Ausgangsleistung als Funktion der Abstimmspannung. Eine Abstimmbandbreite von 2 GHz und eine Ausgangsleistung von 8 dBm wurden erreicht.

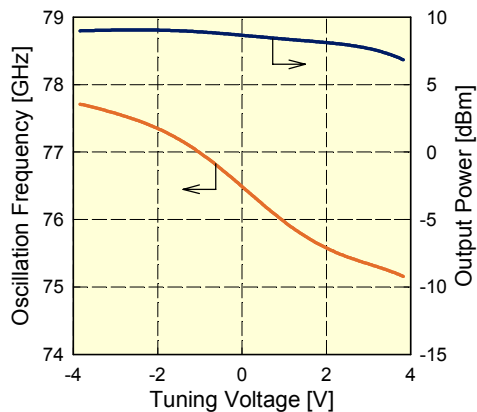


Fig. 10: VCO: Frequenz und Ausgangsleistung als Funktion der Abstimmspannung.

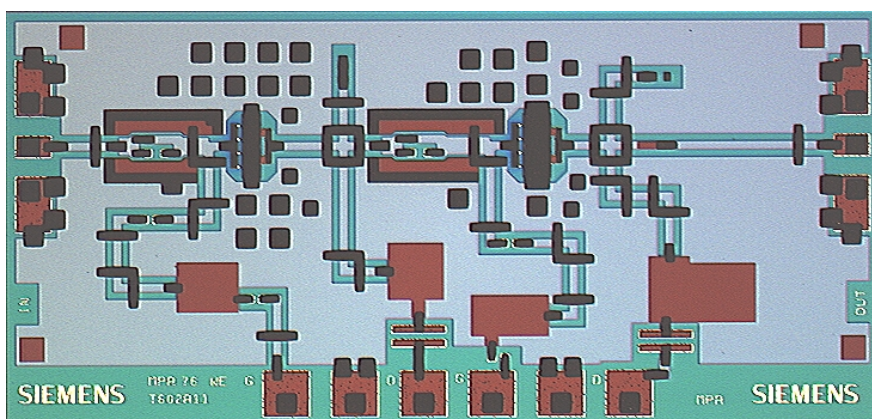


Fig. 11: HEMT-Verstärker 77 GHz.

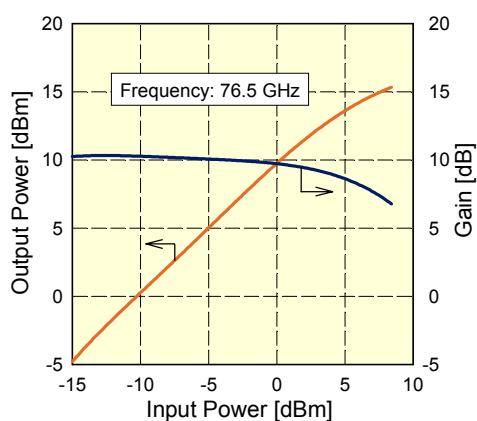


Fig. 12: Ausgangsleistung und Verstärkung über Eingangsleistung.

Fig. 11 zeigt den zweistufigen MPA, der an mehreren Stellen im FMCW-Radar eingesetzt werden kann, so z. B. nach dem VCO oder als Treiberverstärker für den Lokalos-

zillator des Empfangsmischers oder als Sendeverstärker. Fig. 12 zeigt Ausgangsleistung (> 13 dBm) und Verstärkung (10 dB) über der Eingangsleistung.

Der HMIX mischt die 5. Harmonische eines Referenzoszillators bei 15,1 GHz mit dem VCO-Signal und liefert so eine Zwischenfrequenz unterhalb von 2 GHz. Dieses dient dem Einsatz in einer PLL zur Stabilisierung des VCO, wobei Linearität und Phasenrauschen verbessert werden.

Der Chipsatz wurde bei Siemens Automobiltechnik in Fahrversuchen erfolgreich erprobt. Da die Anforderungen erfüllt wurden, ist er die Grundlage für die nächste Generation des Autoradars.

Dank

An T. Grave, J.-E. Müller, E. Pettenpaul, H. J. Siweris, P. Zwicknagl und viele Kollegen für Arbeit, Material und Diskussion. An das Bundesministerium für Forschung und Technologie für die Förderung im Rahmen der Projekte 01BM613/8, 01BM614/9 und 01BM616/0.

Literatur

- [1] J.-E. Mueller, U. Gerlach, G. L. Madonna, M. Pfof, R. Schultheis, P. Zwicknagl: A 3V small chip size GSM HBT power MMIC with 56% PAE. GAAS 2000, Paris, 2. – 3.Oct 2000, p 213 – 216.
- [2] H. J Siweris, A. Werthof, H. Tischer, T. Grave, H. Werthmann, R. H. Rasshofer, W. Kellner: A mixed Si and GaAs chip set for millimeter-wave automotive radar front-ends. RFIC Symp. 2000, Boston, 11.-13.June 2000, p 191 – 194.

Module Technologies for RF Telecom Radios: Status and Trends

Hans Brugger

MicroWave Factory, EADS Deutschland GmbH
Wörthstraße 85, 89077 Ulm, Germany

There is an overall growing demand on broadband wireless access systems and multi-media services such as LMDS, MVDS, and VSAT applications. The market for high data bit rate communication links and broadband mm-wave mobile communication network radio links is rapidly growing.

However, these emerging volume markets also force the manufacturer of RF front-ends to significantly reduce cost and react faster on market trends. The cost driver on the RF front-end is the mm-wave unit (MWU), i.e. the RF module part. Price drivers on the MWU are the GaAs MMICs (#1) and the packaging/assembly effort (#2).

Based on the proven state-of-the-art chip-by-wire ceramics substrate technology the presentation gives an overview on new trends on

- 1) advanced multichip module approaches on LTCC technology and present trends on
- 2) single packaged RF MMICs with ball grid array (BGA) and land grid array (LGA) suitable for SMD-type reflow soldering on an RF-suitable PCB carrier.

A combination of single RF packages and macro modules suitable for volume SMD fabrication will result in a near-future box-of-bricks approach for Telecom transceiver radios and innovative module designs.

Highly-Integrated Radio Frequency Integrated Circuits (RFICs) for UMTS

Robert Weigel, Senior Member IEEE

Institut für Nachrichtentechnik/Informationstechnik

Universität Linz, A-4040 Linz, Austria

&

DICE Danube Integrated Circuit Engineering GmbH & Co KG

A-4040 Linz, Austria

This paper will report on the RF-related system and radio frequency integrated circuit (RFIC) issues of 3G W-CDMA systems like UMTS, technologies that will play a major role in the future of wireless telecommunications allowing for networks which will add broadband data to support video, Internet access, and other high speed data services for untethered devices. It will also address the founding of the company DICE in Linz as an Infineon Technologies Development Center.

1. Introduction

The radio frequency integrated circuit (RFIC) market has suddenly expanded to unimaginable dimensions. Especially wireless devices such as cellular and cordless phones, pagers, global positioning system (GPS) devices, and RF identification tags are rapidly penetrating all aspects of our lives, evolving from luxury items to indispensable tools. The source for the establishment of this new RFIC market can be traced back to a technology push/market pull situation in Europe about ten years ago: at that time, (i) the semiconductor industry had developed low-cost silicon production facilities to mass-produce bipolar transistors with 10 GHz transit frequency and pushed the creation of a new market for this technology; (ii) the European telecommunication industry had just defined the dictionary and grammar for the GSM digital mobile communication system (GSM: Group Special Mobile) requiring for high-fidelity, low-cost chip solutions to produce small, light-weight mobiles at consumer prices. In the following years, both the commercial market for cellular phones and the silicon technology were growing in a harmonic environment orchestrated by the European commission and the European wireless standards organization ETSI. The European GSM story of success has played the major role in the tremendous worldwide increase of the number of subscribers and furthermore pushed the development of other mobile communication systems in the U.S. and in Japan. It is expected that the upcoming advent of the Universal Mobile Telecommunications System (UMTS) will refuel the growing RFIC market expansion.

2. RF Transceiver Architectures and RFIC Technologies

Today's pocket phones contain more than one million transistors, with only a small fraction operating in the RF range and the rest performing low-frequency baseband signal processing. In other words, the baseband section is, in terms of number of devices, yet several orders of magnitude more complex than the RF section. On the other side however, the RF section is still the design bottleneck of the entire system due to the fact

that it demands a good understanding of disciplines that are not directly related to IC design such as communication theory, microwave theory, computer-aided design, multiple access, signal propagation, theory of random signals, wireless standards, and transceiver architectures [1]. As is typical for cellular phone systems standardization, sufficient RF performance has been assumed also in the W-CDMA (Wideband Code Division Multiple Access) standardization phase for UMTS, and most efforts have been put to baseband issues. However, one has recognized meanwhile that much more attention has to be paid to the RF part of the pocket phone transceiver since it strongly influences the overall digital system performance. Thus, in the RF concept engineering of today's commercial products with their short time-to-market requirements, a prediction of the needed RF performance by using RF system simulation is meanwhile indispensable [2], [3]. This is in particular the case with the third generation (3G) W-CDMA system UMTS which, from the design point of view, is quite different from second generation (2G) systems like GSM due to the fact that the users are now separated in the power domain (using codes) rather than being separated in the time and/or frequency domain. Concerning UMTS RF transceiver architectures, complexity, cost, power dissipation, the number of external components, and, of course, the expertise of each manufacturer's RF design team are the primary criteria as is the case with any wireless system concept. As IC technologies evolve, the relative importance of each of these criteria changes, allowing approaches that once seemed impractical to return as plausible solutions. Today, the worldwide GSM RFIC market is mainly penetrated by superheterodyne I/Q receivers (80%) and homodyne I/Q receivers (15%) on the receiver (RX) side, and by, respectively, heterodyne upconversion modulation loop concepts (55%), heterodyne low IF/upconversion concepts (25%), and direct modulation concepts (10%) on the transmitter (TX) side. In the upcoming UMTS market, we will probably have a quite different market situation. Due to the results achieved by an extensive system simulation work we have done recently, it is likely that homodyne receiving combined with heterodyne transmitting will soon attain the highest market penetration although the first UMTS receivers that will appear this May on the Japanese market will be heterodyne receivers.

Today, mobile phone RFICs are mostly fabricated from BiCMOS technologies as is currently the case with RFICs for UMTS. Since the SiGe technology is now available at nearly the same wafer cost as silicon RF-bipolar technology, SiGe bipolar transistor technology combined with massive digital integration of CMOS might be the commercial solution for the next generation of UMTS RFIC's which will appear on the European market in about one year. The further roadmap is however somewhat unclear. R&D engineers and managers never stop thinking about new IC technologies such as SOI CMOS, RF CMOS, and silicon-carbide bipolar technologies associated with new technologies in the metalization and insulator arena. This plurality of technology innovations introduces extreme problems for the RFIC manufacturers since any strategic mistake made in their technology roadmaps can have severe consequences in the highly competitive market of the next RFIC product generation. Again, RF system simulation taking into account both RF architecture and IC technology aspects is becoming an important key to attack and solve this technology dilemma, at least to lower the risk when selecting a specific technology. Without system simulation we would not have been able to release the worldwide first operable RFIC's for UMTS applications [4].

3. RFICs For Heterodyne Transceiver Architectures

Reference [4] reports on our work resulting in fully integrated silicon bipolar intermediate frequency (IF) receiver and transmitter chips in various versions. All chips come in a small outline leadless package and incorporate an on-chip IF synthesizer with on-chip VCO tuning and tank as well as 6th/5th order baseband filters. The chips comply with the Japanese ARIB W-CDMA and the European UMTS standards. As an example, Fig. 1 gives the layout of one of the receiver chips.

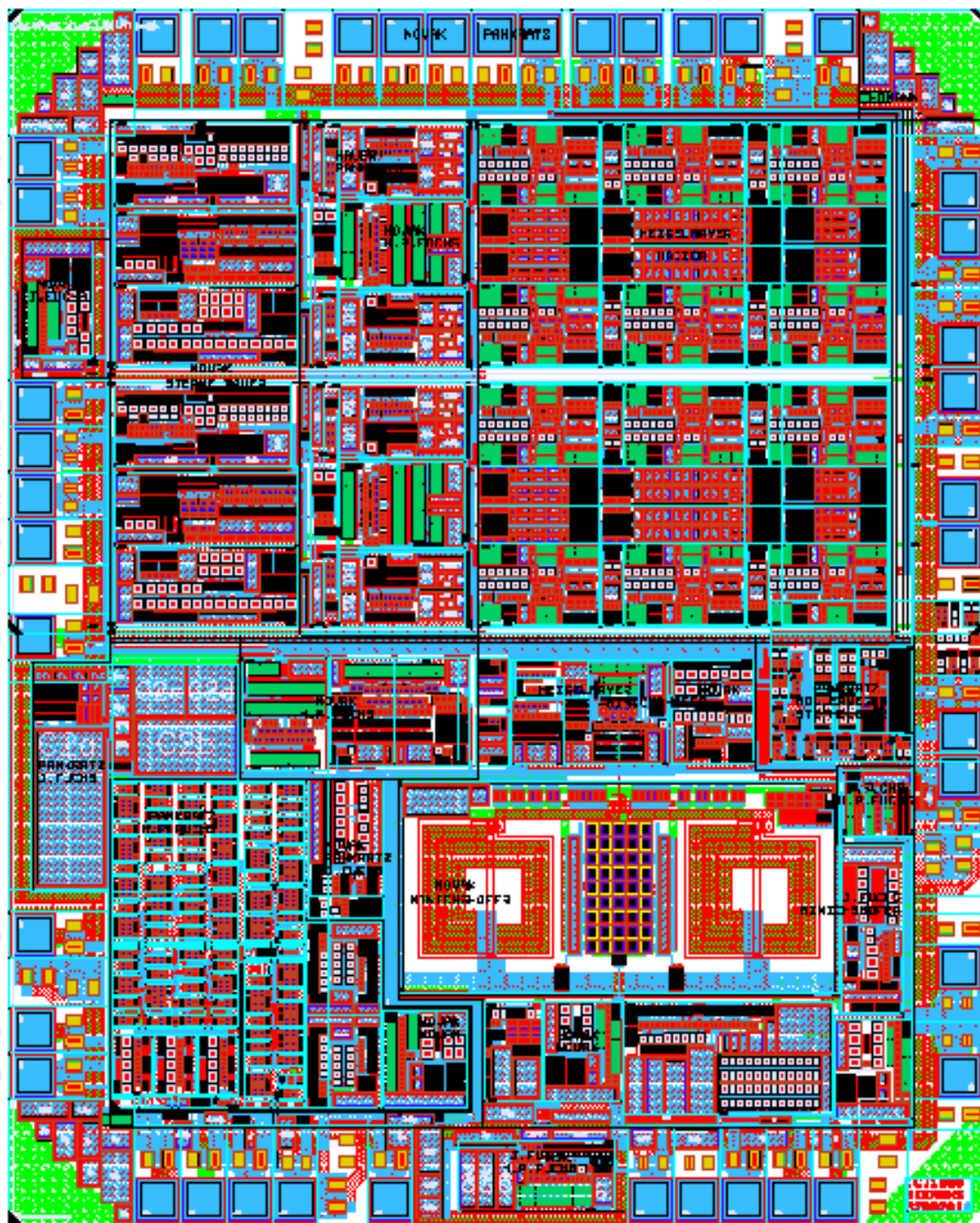


Fig. 1: Layout of a highly-integrated IF receiver RFIC.

The synthesizer is located in the lower part. The reference divider, the phase comparator and the charge pump are located in the lower left corner, and the on-chip VCO, voltage regulator and biasing in the lower right corner, respectively. VCO buffer, the LO divider and some more biasing is located just above the VCO. In the upper part two identical receiver paths are stacked vertically. The block visible far to the left is the IF variable gain amplifier, the block left to the center is the demodulator, and the block to the right contains the I/Q baseband filters. The chips are fabricated from Infineon's 0.4 μ m/25 GHz silicon bipolar process. IF receiver and IF transmitter die size is 2.33 mm x 2.9 mm. The devices are designed for low external component count and operate at 2.7 – 3.3 V supply, an ambient temperature of –30 to +85 °C, and incorporate several power-down modes for efficient use in mobiles. The receiver includes two complete IF paths for antenna diversity/service channel monitoring and a common LO generation and distribution. Any of our IF receiver and IF transmitter RFICs is a highly integrated RFIC device which completely fulfills all system requirements defined by the Japanese and European standards with sufficient reserve.

4. RFICs For Homodyne Transceiver Architectures

We have designed the heterodyne chip set reported on above in order to be able to serve the first generation UMTS market with low risk. The next generation UMTS transceivers however will rely on homodyne solutions probably using SiGe bipolar technologies. Our first design results demonstrate clearly that the many problems associated with homodyne receivers such as DC offsets, I/Q mismatch, even-order distortion, flicker noise, and LO leakage can be solved satisfactorily [5], [6], i.e. the advanced SiGe technology is mature for this approach which is extremely attractive from the techno-economic point of view since direct RF-to-baseband conversion, e.g., avoids the need for discrete surface acoustic wave (SAW) filters as external IF components.

5. Conclusion

Exchange and cross licensing of intellectual property (IP) is one key to strengthen further the European positioning in the global RFIC markets. The other key is the availability of well-trained RF designers. The latter issue has guided our initiative to start an intensive collaborative research work between the University of Linz and Infineon Technologies in July 1998 which has led to the spin-off foundation of the company DICE in Linz in August 1999; in January 2000 Infineon Technologies has joint DICE. The founding of the high-technology company DICE [<http://www.dice.at>] is an excellent example for a successful technology transfer from university to industry.

References

- [1] B. Razavi, “*RF Microelectronics*”, Prentice Hall, 1998.
- [2] R. Weigel, L. Maurer, D. Pimingsdorfer, A. Springer, “*RF Transceiver Architectures for W-CDMA Systems Like UMTS: State of the Art and Future Trends*”, Proceedings International Symposium on Acoustic Wave Devices for Future Mobile Communication Systems, Chiba, Japan, pp. 25 – 34, March 2001 (Invited Paper).

- [3] L. Maurer, M. Huemer, D. Pimingsdorfer, A. Springer, R. Weigel, “*Third Generation Wideband CDMA Systems Like UMTS*”, University of Linz Proceedings, pp. 1 – 188, January 2001 (Full-Day Tutorial).
- [4] W. Thomann, J. Fenk, R. Hagelauer, R. Weigel, “*Fully Integrated W-CDMA IF Receiver and Transmitter including IF Synthesizer and on-chip VCO for UMTS Mobiles*“, Proceedings IEEE Bipolar/BiCMOS Circuits and Technology Meeting, Minneapolis, USA, pp. 36 – 39, September 2000.
- [5] H. Pretl, W. Schelmbauer, B. Adler, L. Maurer, J. Fenk, R. Weigel, “*A Down-Conversion Mixer for a UMTS Zero-IF Receiver in 75 GHz SiGe-Bipolar Technology*“, Proceedings IEEE Bipolar/BiCMOS Circuits and Technology Meeting, Minneapolis, USA, pp. 40 – 43, September 2000.
- [6] W. Schelmbauer, H. Pretl, L. Maurer, R. Weigel, “*A Fully Integrated Analog Baseband IC for an UMTS Zero-IF Receiver*“, Proceedings Austrochip, Graz, Austria, pp. 8 – 15, October 2000.

CMOS-basierte Mikro- und Nano-Systeme

Henry Baltes

Labor für Physikalische Elektronik, ETH Zürich
Hoenggerberg, HPT-H6, 8093 Zurich, Switzerland

CMOS bedeutet hier „*Complementary Metal Oxide Silicon*“ und bezeichnet die führende industrielle Technologie zur Herstellung integrierter Schaltungen. Darüber hinaus gewinnt CMOS gegenwärtig an Bedeutung als Basistechnologie für integrierte Mikrosysteme, insbesondere Mikrosensoren, Mikroaktoren und MEMS (Micro Electro Mechanical Systems). CMOS-basierte Mikrosysteme erhalten durch ko-integrierte Schaltungen erhöhte Funktionalität, wie Kalibrierung, Selbsttest, Interface zu Computer und Telekommunikation. Die Nähe zu etablierten industriellen Fertigungsmethoden erleichtert die Umsetzung neuartiger CMOS-basierter Mikrosysteme aus der Forschung zu Produkten, nicht zuletzt durch Ausgründungen.

Der Vortrag beginnt mit einer Übersicht technologischer Methoden zur Ko-Integration von Mikrosystemfunktionen und Schaltungen auf demselben Chip, insbesondere CMOS-kompatible Mikrostrukturierung durch Ätzen und Beschichten. Es wird sowohl der industrielle Standard als auch die akademische Forschung an Hand von ausgewählten Beispielen vorgestellt. Der Vortrag schreitet von einfachen physikalischen Mikrosensoren zu komplexen chemischen Sensoren fort. Auch ein CMOS-basiertes Nanosystem wird vorgestellt, ferner ein CMOS-basiertes Mikrosystemprodukt einer Ausgründung der ETH Zürich.

Gallium Nitride for Optoelectronics

GaN MOCVD in Forschung und Produktion

B. Schineller, M. Heuken, H. Jürgensen

AIXTRON AG, D-52072 Aachen, Germany

Die vergangenen Jahre erlebten den Einzug der Halbleiter des AlGaInN Materialsystems in weite Bereiche der Optoelektronik. Grün-blaue Leuchtdioden aus InGaN bieten neue Chancen für den Einsatz als preisgünstige und stromsparende Leuchtmittel in der Anzeige- und Beleuchtungstechnik, blau-ultraviolette Laserdioden finden ihren Einsatz in optischen Speichermedien. In der Hochfrequenz- und Hochtemperaturelektronik werden Heterostruktur-Feldeffekttransistoren aus GaN-basierenden Strukturen für die Verwendung in Turbinen, Motoren und Triebwerken, sowie in strahlungsreichen Umgebungen immer interessanter.

Die metallorganische Gasphasenepitaxie (MOVPE) hat sich als die Methode der Wahl für die effiziente und kostengünstige Herstellung von Halbleiterstrukturen herauskristallisiert. Grundlagenorientierte Forschung in Universitätslabors und Forschungseinrichtungen der Industrie findet oftmals auf Einscheibenreaktoren statt (z.B. AIX 200 RF), deren Prozesse dann in der Massenproduktion auf Mehrscheibenreaktoren übertragen werden (z.B. AIX 2400 G3 HT). Hierbei werden in der MOVPE immer häufiger *in-situ*-Messmethoden eingesetzt, um die Entwicklungszeiten neuer Prozesse zu minimieren und bestehende Prozesse zu kontrollieren. In diesem Zusammenhang ist insbesondere die *in-situ*-Reflektometriemessung zu nennen, die Aufschlüsse über Wachstumsraten und Oberflächenqualitäten erlaubt.

Die Verhältnisse der Gasströmungen und Temperaturverteilungen in den Reaktortypen können heutzutage durch numerische Simulationen Aufschluss über die einzustellenden Prozessbedingungen geben. Dies ist bei der Übertragung von Prozessen von einem Reaktortyp, z.B. einem Forschungsreaktor, auf Produktionsanlagen von Vorteil.

Neben dem für die Optoelektronik überwiegend genutzten Saphirsubstrat werden eine Vielzahl alternativer Substrate untersucht. Hierzu gehört zum einen das SiC, das bereits kommerzielle Erfolge in der Nitrid-basierenden Optoelektronik feiert, zum anderen wird das aus der Halbleiterelektronik bekannte Silizium untersucht. Diese Substrate erlauben aufgrund ihrer gegenüber Saphir höheren Wärmeleitfähigkeit besonders in der Hochleistungselektronik eine bessere Verlustleistungsabfuhr.

Die AIXTRON AG arbeitet auf all diesen Gebieten eng mit industriellen und akademischen Partnern zusammen, mit dem Ziel, das AlInGaN-Materialsystem weiteren Anwendungen gegenüber zu öffnen.

Group-III Nitrides Grown by MOVPE and MBE for Optoelectronic Applications

D. Hommel, S. Einfeldt, T. Böttcher, S. Figge, C. Kruse, V. Kirchner,
H. Heinke

Institute of Solid State Physics, University of Bremen,
P.O. Box 330440, 28334 Bremen, Germany

D. Rudloff and J. Christen

Institute of Experimental Physics, Otto-von-Guericke-University
Magdeburg, Germany

Group-III nitrides are of great importance for short wavelength optoelectronic applications.

Due to a lack of lattice matched substrates growth is usually performed on sapphire or SiC using metalorganic chemical vapor phase epitaxy (MOCVD) or molecular beam epitaxy (MBE). Whereas for wide gap II-VI compounds MBE is the preferred growth method it turns out that MOVPE has certain advantages in case of nitrides. The growth start of GaN by MOVPE is studied by *in-situ* reflectometry. Depending on the conditions the grain size can vary from 150 nm to more than 4 μm . In the latter case the density of threading dislocations can be reduced to the low 10^8 cm^{-2} . A non-destructive method for determining the dislocation density by high resolution X-ray diffraction for wurzite GaN will be presented.

A comparison of quantum well structures grown by MBE on (0001) and (000-1) give clear indications that the growth on Ga-polar surfaces provides to more efficient light emitters. Nevertheless, at least for optoelectronic applications MOVPE provides to better surface morphology and structural and optical properties.

First results of light emitting structures in the violet spectral region will be discussed.

GaN-Based Devices – A Challenge in Semiconductor Lighting

V. Härle, D. Eisert

OSRAM Opto Semiconductors GmbH & Co. OHG,
Wernerwerkstr. 2, 93049 Regensburg, Germany

The rapid development of GaN-based devices since 1993 initiated a numerous amount of new, innovative applications in semiconductor lighting. In 1996 the estimated annual growth rate was about 30%. In reality the market growth rate almost tripled to about 80% for the time period from 1995 to 1999. The major markets were full color displays and automotive, mainly using green and blue LEDs. In future an even more interesting market for GaInN-LEDs will develop, the application of LEDs in general lighting. In 1999 this market had a share of only 0.5%. The general lighting market will be based mainly on white LEDs, using both three chip solutions (RGB) and single chip solutions in combination with luminous converters. The solution of choice will be defined by application, focusing on cost and performance as discussed in this paper.

1. Market Development

1.1 General GaN-Market

First light emitting devices based on GaN were presented in 1993, immediately entering the market. At that time, the market for GaN-based devices was almost zero, and production was driven by estimated market potentials. First market reports were published in 1995/1996, indicating an annual growth potential of approximately 30%, starting at 30 Million US\$ in 1995 and reaching 150-200 Million in 1999. One of the early starters was OSRAM Opto Semiconductors (former Siemens HL) strongly developing the automotive market for blue/green GaN-based LEDs.

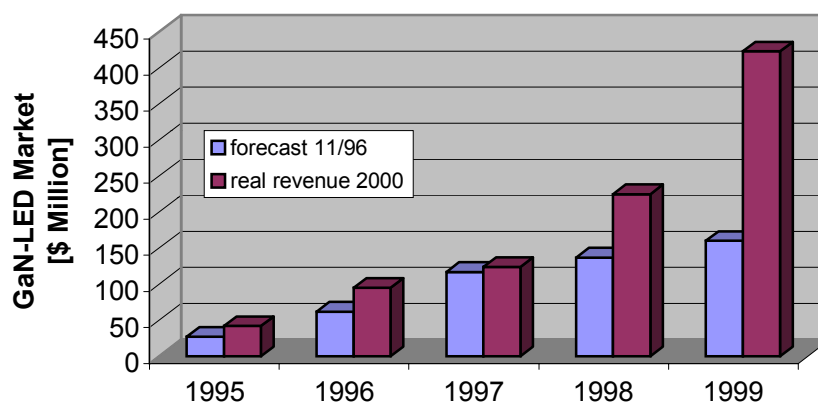


Fig. 1: Comparison of historical market forecast of 1996 and market growth by revenue reported in May 2000.

Today the automotive market with a share of about 20% developed to become one of the two major market segments. There is only one market which is bigger today. This is the segment of full color displays, taking a share of approximately 30%. These two market segments absorb about 50% of today's GaN-LED production with a total volume of more than 400 Million US\$. Comparing these numbers with the estimated numbers from 1995/96, the annual growth rate of 30% was even conservative compared to the real growth of the Nitride market, reaching an approximate growth rate of about 80% per year as indicated in Fig. 1.

Other market segments such as traffic lights or general lighting have a rather negligible market share below 1% in 1999. Yet especially general lighting is expected to become one of the major driving forces for GaN-based light emitting devices. For general lighting mainly white light emitting devices will be needed, utilizing the advantages of both technologies, three chip solutions (RGB) and single chip solutions with fluorescent converters. The preference of using single or multi chip solutions strongly depends on the application. Major driving forces for the lighting market will be energy and labor saving on one hand. On the other hand expected lifetimes exceeding 50.000 h for LED solutions will become an important issue.

1.2 White LED Market and Requirements

According to R. Haitz (Agilent Technologies) the energy consumption related with illumination is as high as 20% of the total electrical power consumption in North America. For total replacement of incandescent and fluorescent lamps in the US savings of several billion US\$ only on electrical energy are discussed, not even taking into account reduced labor costs. This rough estimate gives an indication of the market potential for solid state lighting.

Today's luminous efficiency for single chip white LEDs is in the order of 15-20 lm/W, independent of the substrate. A plug efficiency of about 20% for today's chips in a 5 mm radial housing is realistic. Corresponding converter materials show conversion efficiencies of 75 – 95%, the most. Therefrom it becomes obvious that the LED-chip shows the largest potential for improvement to achieve efficiency values of 50 – 80 lm/W and more as are reported for fluorescent lamps. Besides the increase of brightness levels, it is very important to further reduce the forward voltage. Both brightness and forward voltage requirements will lead to new vertical device structures and chip designs within the next couple of years. One possibility to reduce forward voltage is to increase chip size, reducing series resistance and thermal loss. Such large chips can be driven at higher currents combined with even lower current densities as today's devices.

Having reached device characteristics and device parameters to meet the level of conventional light sources, costs per die and costs per lm/W will be the final parameter to enter the lighting market in large volumes either using a numerous amount of today's devices with small dimensions or using only a few enlarged devices with an area of 1 mm² or more.

2. LED Technology

2.1 Light Emitting GaInN-Chips

In principle, LED technology is mainly dominated by the development of vertical LED structures for light generation and light extraction, which is determined by chip-design and packaging technology. Focusing on the chip, the design of epitaxial layers for GaN devices is based on the buffer technology, the active region, and the multi layer p-side. Most important seems to be the control of the interfaces of the active region as well as the definition of the pn junction. In order to realize highly efficient layer packages, most of the structures are grown using MOVPE. The structures contain GaInN quantum wells with well thicknesses of 2 nm to 5 nm separated by 2 nm to 10 nm barriers either of GaN or GaInN with low In content. Many devices have AlGaIn electron barriers on the p-side of the device with Al contents of about 10% to 20%, followed by p-doped GaN to form low resistance p-contacts.

For emission wavelengths between 450 nm – 470 nm carrier overflow from localized energy states within the quantum well is small due to a relatively high Indium content, minimizing the probability of carriers to reach non radiative recombination centers, e.g., threading dislocations. At the same time, the Indium content is still low enough to ensure the necessary overlap between electron and hole wavefunctions, which is affected by built-in piezoelectric fields resulting in the quantum-confined Stark effect.

At longer wavelengths two effects reduce quantum efficiency: On one hand, the high Indium content needed for long wavelengths intensifies the piezoelectric fields leading to a reduction of electron-hole wavefunction overlap. On the other hand, the quality of GaInN layers decreases with high Indium content, leading to more non-radiative recombination centers. In the short wavelength UV region, the efficiency also decreases as the confinement energy of carriers within localized states of lateral quantum well fluctuations is decreased, i.e. the probability is increased that carriers reach non-radiative recombination centers. To avoid the loss of efficiency of UV-LEDs, high band gap confinement layers containing aluminum have to be developed.

The major part of GaN-based devices is grown on sapphire substrates, only some organizations such as OSRAM-OS focus on SiC as a substrate. The advantage of sapphire is the availability and substrate costs. Not taking into account the fact of limited availability and costs, SiC has a lot of advantages as a material itself over sapphire, such as electrical and thermal conductivity, the thermal expansion coefficient as well as the reduced lattice mismatch to GaN. On top of that SiC shows additional advantages from a processing (yield, complexity, costs) as well as a manufacturing point of view.

Only recently improving the light extraction from the chips became a major topic. Since sapphire is difficult to shape due to its extreme hardness, most organizations working on sapphire try to enhance light extraction by using flip-chip or p-side down mounting techniques in combination with mirror contacts on the p-side. The generated light enters either directly into the transparent sapphire substrate or is reflected towards the sapphire side by the mirror. The efficiencies of such devices can be improved by enlarging the chip size to operate the device at lower current densities. Here the thermal saturation effects as well as band filling effects in the quantum wells do not limit the internal efficiencies. Figure 2 demonstrates the decrease of efficiency with increasing operation current density observed in a standard LED.

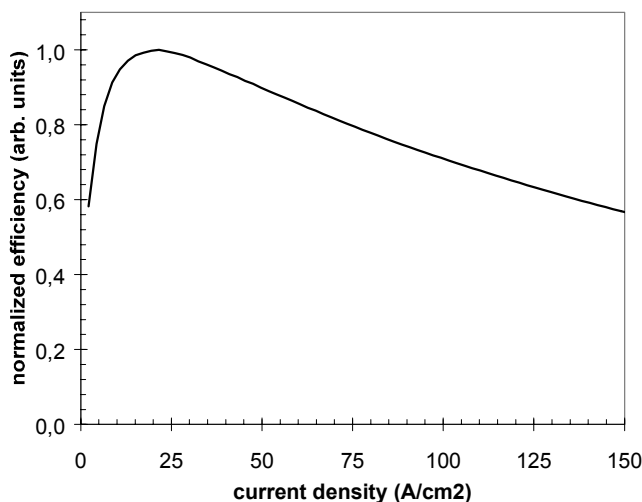


Fig. 2: External efficiency of an InGaN-LED with varying operation current density.

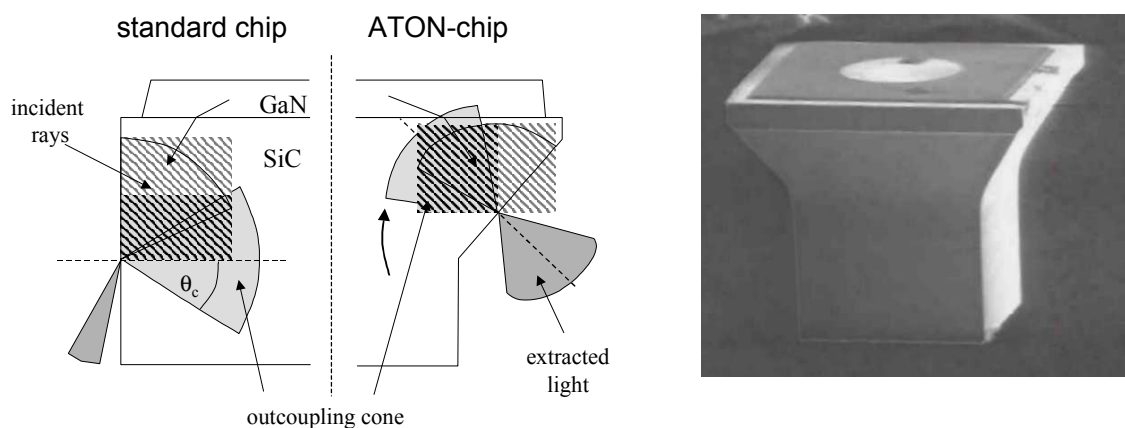


Fig. 3: Sketch of the improved light extraction conditions by the new chip design developed by OSRAM-OS, named ATON, compared to a standard GaN-LED on SiC-substrate. On the right a SEM micrograph of an ATON-chip is shown.

On SiC the situation is different. The material SiC is not as hard as sapphire and therefore can be shaped using standard processing technologies. At OSRAM-OS a technique was developed to shape devices in such a way that light extraction from the substrate is improved (Fig.3). This was achieved by designing a chip with an undercut on the side walls to generate inclined side facets. In a standard device with cubic geometry most of the light entering the substrate gets lost due to multiple total internal reflection and subsequent absorption. The limitations of geometrical optics on light extraction become clear in the sketch of the outcoupling conditions in Fig. 3. On one hand the angular range of rays entering the substrate is limited due to refraction at the GaN/SiC interface. On the other hand total reflection occurs for rays hitting the sidewall at grazing incidence, so that only a small angular range of incoming light can be coupled out. Using OSRAM's technique of shaping side walls (named ATON technology), the overlap of the incoming light cone with the outcoupling cone can be enlarged. This technique is

suitable for the entire GaInN-product line with similar brightness improvements for wavelength from UV to green and even longer wavelengths.

The use of this technology at OSRAM-OS led to an increase in brightness of about 80%. The combination of improved facet design with advances of the epitaxy lead to a brightness level of up to 8.2 mW at an emission wavelength of 470 nm.

2.2 White Light Emitting Devices

For the generation of white light, different approaches using GaInN-LEDs can be derived. Four basic combinations are demonstrated in Fig. 4. In Fig. 4A a three-chip RGB-solution is shown. The advantage of this approach is the variable color when driving each chip separately. Such diodes are used, e.g., as pixels for full color displays. Diodes based on InGaN can be used to provide the blue and green colors, whereas GaInAlP-LEDs are used for red. If just the generation of white light is intended, the Multi-LED is not well suited because of its size, multiple driving voltages, costs and last but not least color rendering.

To be competitive with other light sources it is mandatory to provide a single chip LED suitable for high volume production. Therefore luminous conversion is a very valuable technology. Today white LEDs based on single converter solutions are commercially available. Here the blue GaN-chip is embedded in a phosphor, e.g. a rare earth doped garnet. The blue light emitted by the diode partially pumps the converter, and the yellow light emitted by the phosphor in combination with the blue light of the diode adds up to white light. The spectrum of such a diode is shown in Fig. 4B. The solid line shows the complete spectrum of the LED, whereas the dashed line gives the spectrum of the converter itself and the diode without converter, respectively (the intensity loss due to conversion is not drawn to scale in this figure).

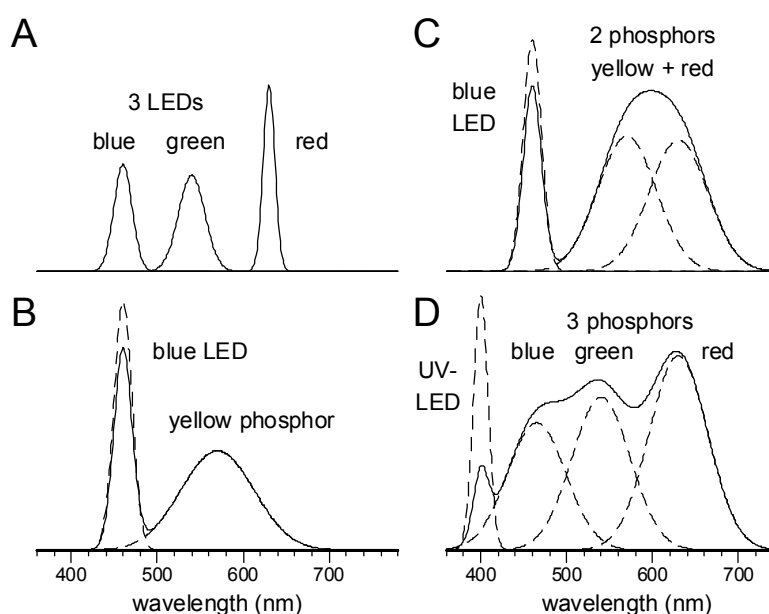


Fig. 4: Possible approaches for the fabrication of white LEDs: RGB-solution (A); blue chip combined with 1 (B) or 2 (C) converters; UV-LED with 3 converters (D).

One of the most important parameters for white light sources is color rendering. It is well known that a colored surface looks different when illuminated by an artificial light source or by daylight. With the color rendering index (CRI) a figure of merit R_a can be assigned to a light source, giving information on the color rendering of eight standard surfaces. For daylight the CRI has been normalized to $R_a = 100$. For comparison an incandescent bulb has an $R_a \approx 90$, a standard fluorescent bulb has an $R_a \approx 70 - 90$.

The CRI of the white converter LED depends of the emission wavelength of the blue LED. Using a single converter a maximum CRI of about $R_a = 80$ can be reached for an LED emitting in the wavelength range of 450 nm – 470 nm. The limitation on the CRI for the one converter solution is due to the large gap between the blue pump wavelength and the emission wavelength of the converter. Yet this gap cannot be avoided due to the laws of color mixing, where a blue source needs to be combined with a yellow source to yield white light.

The use of only a single converter imposes more or less stringent limitations on the properties of white LEDs. More flexibility can be gained by using an additional converter. So, e.g., red tones can be emphasized as shown in Fig. 4C. These diodes will give a more natural color to human skin. Yet the gap in the spectrum between the pump wavelength and the converter emission remains, because of the Stokes shift between absorption and emission of the converter.

In an even more advanced solution the visible part of the spectrum is completely generated by phosphors. With a spectral width of the converter emission between 70 nm – 120 nm a quasi-continuous spectrum can be simulated (Fig. 4D). With this technique a high color rendering index of $R_a > 90$ can be achieved for applications like photography, where a high quality of the illumination source is needed. Since in this solution visible light is generated by phosphors, the emission wavelength of the pump source can be moved into the UV spectral range. This is on one hand necessary for pumping the blue phosphor, on the other hand the choice of available converter materials is enlarged, because the pump wavelength now can be tuned to the absorption maximum of the converters. As a drawback it should be mentioned that three converters are not as efficient as the one phosphor solution from the energetic point of view, given by the down conversion of a 400 nm photon to blue 470nm, green 530nm and red 600 nm, where the photon energy is reduced down to 1/3 of the original energy.

If a white LED with high efficiency, high brightness and low costs is needed, the single chip solution with one converter will be used. By using two or three phosphors high end products can be obtained for special lighting applications.

Organic Semiconductors

Organische Halbleiter-Bauelemente

Günther Leising

Science & Technology AT&S,
Fabriksgasse 13, 8700 Leoben, Austria

Ende der siebziger Jahre demonstrierte die Gruppe A.J. Heeger, A.J. MacDiarmid und H. Shirakawa, dass das konjugierte Polymer Polyacetylen sich wie ein Halbleiter verhält und durch entsprechende „Dotierung“ p- bzw. n-leitend gemacht werden kann. Extensive „p-Dotierung“ oder besser chemische Oxidation führte zu Modifikationen von Polyacetylen mit Werten der elektrischen Leitfähigkeit im Bereich sehr gut leitender Metalle wie Kupfer. Schon in den ersten Arbeiten dieser Gruppe wurden pn-Dioden und einfache Solarzellen realisiert, die bereits damals das Potenzial der Substanzgruppe der konjugierten Systeme erkennen ließen. Etwa zwanzig Jahre später, im Jahre 2000, wurde diese Forschergruppe mit dem Nobelpreis für Chemie ausgezeichnet.



Schon in den Anfängen der Forschungsrichtung konjugierter Festkörper zeichnete sich ab, dass gravierende Fortschritte sowohl in der Grundlagenforschung um das Verständnis der physikalischen Prozesse als auch für eventuelle Anwendungen, in der reinen defektarmen Darstellung, d.h. reinen und definierten Synthese dieser neuartigen Substanzgruppe, begründet liegen. Mitte der neunziger Jahre konnte die Grazer Gruppe zeigen, dass ein konjugiertes Polymer (leiterartiges Polyparaphenylen) mit Defektkonzentrationen um 10^{15} Defekte pro cm^3 machbar ist, das wegen seiner ausgezeichneten Stabilität als Basismaterial für die Realisierung eines optisch gepumpten Polymerlasers

diente. Ende der achtziger Jahre gelang es der Gruppe um R. Friend, eine gelb-grüne Polymer-Leuchtdiode zu fertigen, und unmittelbar danach zog die Grazer Gruppe mit blauen LEDs auf der Basis von Polyparaphenylen gleich. Mit zunehmendem Verständnis um die intrinsischen Eigenschaften dieser neuartigen organischen Festkörper wurden die verschiedensten Bauelemente, wie ein elektrisch gepumpter organischer Laser und effiziente organische Solarzellen und Feldeffekttransistoren, realisierbar. Organische Festkörper haben den Vorteil, dass sie mit verschiedenen kostengünstigen Verfahren wie Aufschleudern, Tauchverfahren, Ink-Jet-Druck und Vakuumverdampfung aufgebracht werden können. Es wird ein Überblick über den internationalen Status quo präsentiert und die Aktivitäten bzw. Ergebnisse der Forschungsgruppen um den Vortragenden demonstriert.

GMe Presentations – Invited Talks

Entwicklung von und Untersuchungen an Mikrofluidik-Systemkomponenten

F. Kohl, F. Keplinger, R. Fasching, P. Svasek, J. Steurer, A. Jachimowicz
Institut für industrielle Elektronik und Materialwissenschaften, TU Wien,
Gusshausstraße 27-29, 1040 Wien, Austria

Die Erzeugung komplexer dreidimensionaler Mikrostrukturen auf einem Chip mittels planarer Beschichtungs- und Photolithographieprozesse und photovernetzbarer Epoxide wird vorgestellt. Thermische Strömungssensoren auf der Basis von Thermistoren aus amorphem Germanium, die auch in Mikrosysteme integrierbar sind, wurden über einen extrem weiten Messbereich und unter extremen dynamischen Betriebsbedingungen charakterisiert. Aus der Antwort des Sensors auf akustische Schockwellen konnte unter Freifeldbedingungen eine Kleinsignal-Ansprechzeit von weniger als 1 ms nachgewiesen werden. Bei Strömungsquerschnitten unter 1 mm^2 bietet der Sensor einen Gasflussmessbereich von mehr als fünf Größenordnungen. Grundlage der hohen Auflösung ist das geringe Stromrauschen der Thermistoren.

1. Einleitung

Um den Weg zur Lab-on-Chip-basierten medizinische Diagnostik zu ebnet, werden heute allorts Mikrosystemkomponenten und mikrotechnologischen Verfahren entwickelt. Dabei erfordert die effiziente Analytaufbereitung dreidimensionale Mikrostrukturen, deren Realisierung nun mit Hilfe einer neuen Generation von Photolacken gelungen ist. Bereits entwickelte, miniaturisierte Strömungssensoren können als Systemkomponenten zur Steuerung und Überwachung von Mikroanalysatoren dienen. Je nach Anwendungsfall werden dabei sehr unterschiedliche Eigenschaften gefordert, von empfindlicher Anzeige geringer Strömungsgeschwindigkeiten bis hin zur schnellen Reaktion auf sprunghafte Änderungen der Strömung. Die vorgestellten Untersuchungsergebnisse an einem thermischen Mikroströmungssensor demonstrieren die extrem kurze Ansprechzeit und den außergewöhnlich weiten Messbereich dieser Sensoren.

2. Experimentelle Resultate

2.1 Technologien für Mikrofluidikkomponenten

Der Negativ-Photolack EPON-SU8 auf Epoxy-Basis ist für die Fertigung von mikromechanischen Strukturen besonders geeignet, da er für bestimmte mikrotechnologische Aufgaben eine Alternative zu den bisher eingesetzten Materialien, wie Siliziumnitrid, anisotrop geätztes Silizium, geätztes Pyrex usw. darstellt und darüber hinaus völlig neue Möglichkeiten erschließt. Nach Prozessierung der Strukturen (Belichten, Entwickeln und Härten) ist dieser Photolack mechanisch und chemisch sehr belastbar.

Die Strömung durch Mikrokanäle ist generell laminar ausgebildet. Bei einfacher Zusammenführung von Kanälen fließen Flüssigkeitsströme weiterhin kompakt nebeneinander und nur die Querdiffusion sorgt für eine allmähliche Durchmischung der Reagenzien.

Zur Abhilfe wurden daher miniaturisierte Anordnungen gesucht, welche einerseits die Durchmischung zweier Reagenzien forcieren und andererseits weiterhin die Möglichkeit zur dünnschichttechnischen Herstellung und damit auch zur bequemen Miniaturisierung bieten. Simulationen ließen erwarten, dass die laterale Führung der Strömung mittels Mikrostrukturen, die vor der Vereinigungsstelle der Kanäle platziert sind, bereits eine wesentliche Verbesserung bewirken. Fig. 1 zeigt derartige Führungsstrukturen, die dafür sorgen, dass die Berührungszone der abgehenden Teilströme parallel zur großen Kanalgrenzfläche liegt.

Die Trennschicht zwischen den beiden Rippenstrukturen kann nur auf eine planare Oberfläche aufgebracht werden, weshalb die Entwicklung der tragenden Rippenstruktur erst nach der Prozessierung dieser Trennschicht erfolgen kann. Bis dahin ist die untere Lackschicht, etwa mit Hilfe einer Metall-Zwischenschicht, gegen Belichtung zu schützen. Eine elegante Variante des Verfahrens arbeitet mit einer selbsttragenden Metalllage und verzichtet so auf zusätzliche Resistschichten. Das so erreichte extreme Seitenverhältnis des abgehenden Kanals sorgt für maximale Interdiffusion und typischen Durchmischungszeiten von 100ms. Weiters ist die Zahl der Ebenen prinzipiell nicht begrenzt. Erste Versuche einer Mehrlagenlithographie sind sehr zufriedenstellend verlaufen.

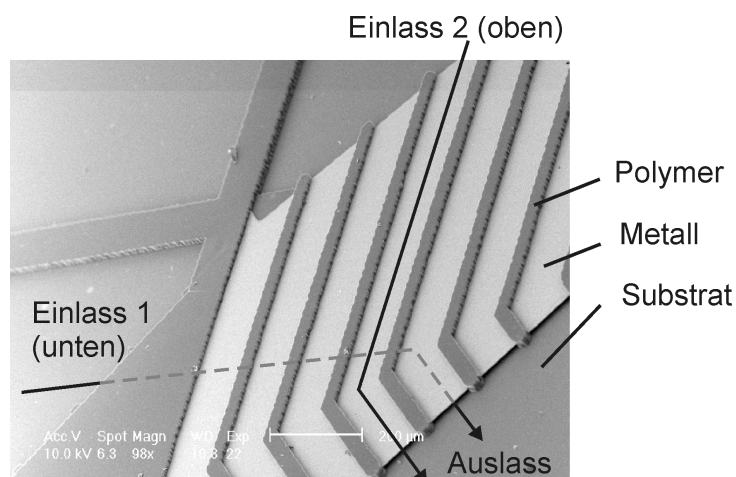


Fig. 1: REM-Aufnahme der Mikrostrukturen zur Strömungsführung (ohne Decklage).

2.2 Mikromechanischer Strömungssensor

Ein hochempfindlicher Strömungssensor basierend auf Thermistoren aus amorphem Germanium wurde mittels Silicon Micromachining realisiert [1]. Zur Bestimmung des Messbereichs als Durchflussmesser wurde der thermische Strömungssensor in die Wand eines Mikroströmungskanals integriert und sowohl mit konstanter Differenztemperatur als auch mit konstanter Betriebsleistung vermessen. Aus Fig. 2 ist ersichtlich, dass im temperaturgeregelten Betrieb ein maximaler Messbereich erzielbar ist. Geringe Ansprechzeiten sind allerdings wesentlich einfacher mit konstanter Betriebsleistung zu erreichen. Für diese Betriebsart wurden mit Hilfe von Schockwellen Ansprechzeiten von weniger als 1 ms nachgewiesen. Die vorgestellten Resultate wurden mit gasförmigen Medien gewonnen, wobei alle Erkenntnisse unter Berücksichtigung der entsprechenden Stoffkennzahlen auch auf Flüssigkeiten übertragbar sind.

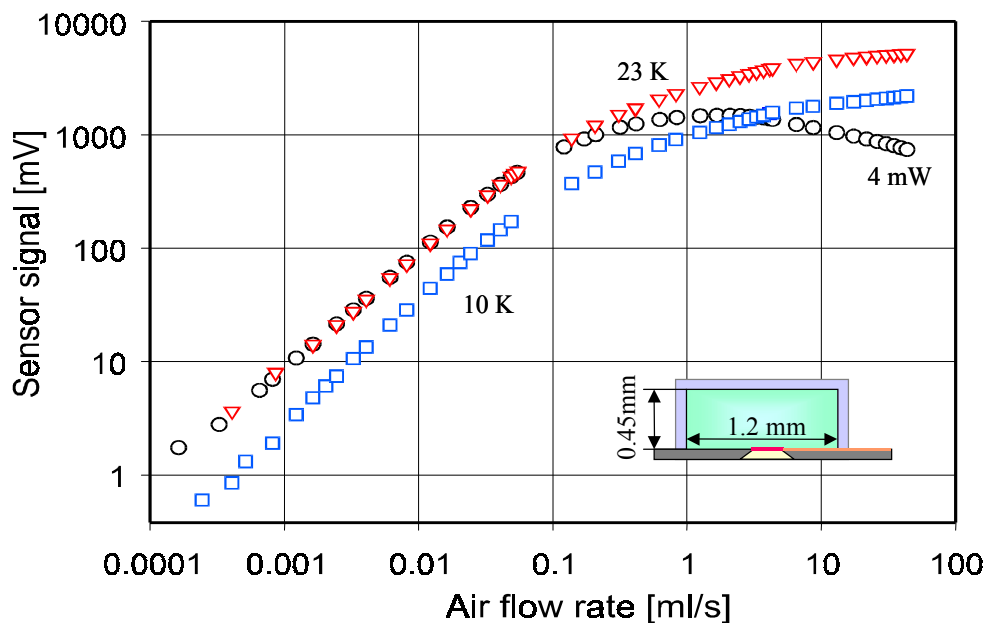


Fig. 2: Sensorsignal in Abhängigkeit vom Durchfluss. Die Resultate für konstante Übertemperatur (23 K (∇), 10 K (\circ)) und für konstante Betriebsleistung (4 mW (\square)) gelten für den skizzierten Querschnitt des Durchflusskanals.

2.3 Untersuchung Temperatursensorstabilität

Für die zuverlässige direkte Messung kleiner Schwankungen bei niedrigen Frequenzen ist ein hoher apparativer Aufwand nötig. Es sind dafür die vom Sensor bewirkten Schwankungserscheinungen von allen anderen unvermeidlichen Störungen sauber zu trennen. Fig. 3 zeigt schematisch das Prinzip der verwendeten Messmethode.

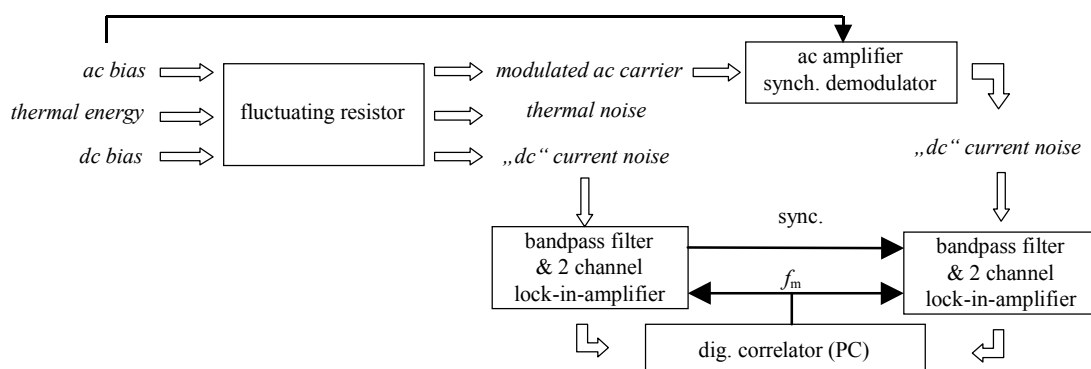


Fig. 3: Prinzip der Messung der spektralen Leistungsdichte des $1/f$ -Rauschens. Zwei Trägerfrequenzen (dc und 55 kHz) werden durch das Stromrauschen moduliert. Durch kohärente Demodulation entstehen daraus korrelierte Anteile in den digitalisierten Ausgangssignalen.

Fig. 4 gibt Resultate von Messungen an Germaniumthermistoren und an Metallfilmwiderständen wieder. Man erkennt, dass der korrelierte Anteil der Rauschleistung wie er-

wartet annähernd mit $1/f_m$ variiert. Er wächst annähernd quadratisch mit der Vorspannung an den Proben. Zur Orientierung ist in Fig. 4 auch der frequenzunabhängige Pegel des thermischen Widerstandsrauschens eingetragen. Für Messergebnisse mit ausreichender Qualität sind lange Messzeiten (typisch 30 h je Frequenzgang) und damit eine automatische Steuerung der Messung erforderlich.

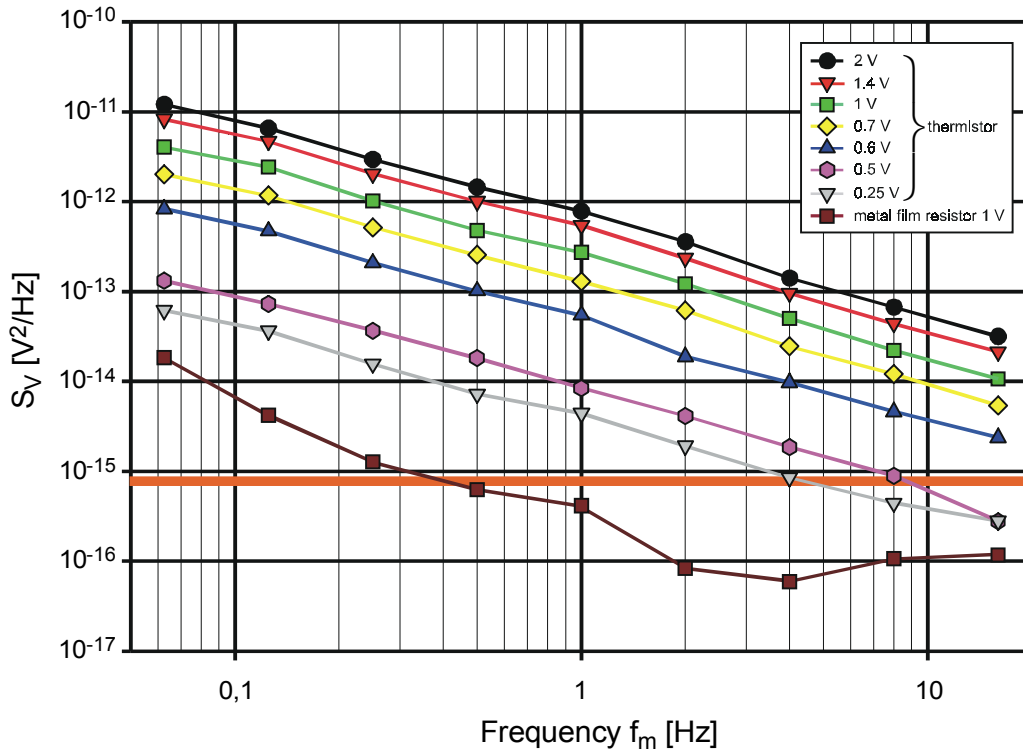


Fig. 4: Spektrale Leistungsdichte der Rauschspannung eines aGe-Thermistors und eines Metallfilmwiderstandes in Abhängigkeit von der angelegten Spannung.

Ein umfangreiches Softwarepaket, bestehend aus einem Steuer- und einem Analysemodul, wurde auf der Basis der graphischen Programmiersprache G (LabView) entwickelt. Diese Plattform bot sich durch ihr umfangreiches Angebot an Gerätetreibern und Analyse- und Darstellungsfunktionen für die Signalbearbeitung an.

3. Zusammenfassung

Es ist gelungen, eine Technologie zur Herstellung dreidimensionaler Strukturen zu entwickeln, welche die Integration von unterschiedlichsten Sensoren und Mikrofluidikkomponenten entscheidend erleichtert. Mit Hilfe der neuen Photoresisttechnologie lassen sich Verbindungskanäle, Reaktoren, Mischer und dergleichen, wie sie für das *Lab on Chip*-Konzept benötigt werden, realisieren, wobei weitgehende Freiheit in der Dimensionierung der Mikrofluidikkomponenten gegeben ist. Die Charakterisierung von thermischen Strömungssensoren hat gezeigt, dass in Mikrofluidiksystemen außergewöhnlich große Messspannen bei hoher Dynamik erreichbar sind. Die vorgestellte Methode zur Untersuchung der Stabilität von Germaniumthermistoren stellt eine wesentliche Verbesserung für die Qualitätskontrolle resistiver Bauelemente dar. Mit Hilfe dieses Messaufbaus kann beispielsweise die Qualität der in Biosensorsystemen integrierten

thermischen Messfühler quantitativ erfasst werden und so die Verbesserung der Integrationstechnologien weiter vorangetrieben werden.

Referenzen

- [1] A. Glaninger, A. Jachimowicz, F. Kohl, R. Chabicovsky, G. Urban, "Wide Range Semiconductor Flow Sensors", *Sensors & Actuators A, Physical*, Vol. 85/1–3, 2000, p139 – 146.

Scanning Capacitance Microscopy on Epitaxial Si Layers

J. Smoliner¹, B. Basnar¹, S. Golka¹, E. Gornik¹, B. Löffler², M. Schatzmayr²,
H. Enichlmair²

¹ Institut für Festkörperelektronik, TU Wien,
Floragasse 7, 1040 Wien, Austria

² Austria Mikro Systeme International AG,
Tobelbader Strasse 30, 8141 Unterpremstätten, Austria

In this work, the physical processes leading to contrast in Scanning Capacitance microscopy (SCM) are investigated both experimentally and theoretically. Using a p-type silicon epitaxial staircase structure we show that a monotonic dependence of the SCM signal on the doping level is only obtained if the tip bias is adjusted in a way that the sample is either in accumulation or depletion. In the transition region, the SCM signal is non monotonic because depending on bias, any doping concentration can yield a maximum SCM signal size. We also show that this behavior is in excellent agreement with the conventional model of a metal-oxide-semiconductor junction.

1. Introduction

Scanning Capacitance Microscopy [1] (SCM), an extension of conventional Atomic Force Microscopy (AFM), is a promising tool for semiconductor device characterization. The main application of this method is two-dimensional carrier profiling for failure analysis or process control especially on cross-sectional samples. The current state of the art of this technique can be found in the review articles [2] – [4]. However, SCM is not an easy and straightforward to use technique. In detail, quantitatively reproducible measurements are a serious problem, since sample preparation has a dramatic influence on the results especially in cross-sectional measurements. According to the literature, best results are obtained on samples polished with silica slurry [5], [6], followed by a low temperature oxidation in an oven [7], [8]. Usually temperatures below 350 °C are used to avoid diffusion processes which would lead to a broadening of the investigated doping profiles. Alternatively, irradiation with UV light and simultaneous oxidation through *in-situ* generated ozone [9], or a combination of these two approaches [10], [11] is employed.

In addition to these technical problems, the physical processes leading to contrast in SCM images are not fully understood. Recently, a non-monotonic behavior of the SCM signal for large dynamic range samples was observed, and the influence of the applied DC bias [12] was studied qualitatively. Further an influence of light on the SCM signal [13] was found. Apart from this, the influence of adsorbed water on the sample surface on the resolution has been published [14], [15].

To obtain quantitative results, calibration samples such as epitaxial staircase structures [16], [17] are often used. However, simple calibration attempts immediately fail when the investigated structure size reaches the order of the depletion length in the semiconductor, or the diameter of the AFM-tip. Thus, intensive simulations were carried out to

study the limitations of the calibration curve method for determining doping profiles [18]. In general it turns out that quantitative 2D doping measurements on small structures are obviously impossible without inverse modeling [19] or detailed simulations using empirical databases [20] – [22].

2. Experimental

In this work, we investigate the physical processes leading to SCM contrast both experimentally and theoretically. Using conventional Metal-Oxide-Semiconductor (MOS) theory [23], [24] and epitaxial staircase structures we show that the maximum SCM signal strongly depends both on doping and the applied bias. The sample we used was a CVD-grown doping staircase prepared by AMS (*Austria Mikro Systeme International AG*) and consists of five nominally 400 nm thick p-type Si-layers having doping concentrations of 2.1×10^{15} , 2.0×10^{16} , 1.7×10^{17} , 2.2×10^{18} and $9.1 \times 10^{18} \text{ cm}^{-3}$, respectively. The highest concentration is located at the sample surface. The substrate is p-doped silicon with a concentration below $1 \times 10^{15} \text{ cm}^{-3}$. The dopant concentrations were determined by a SIMS measurement the result of which is shown in Fig. 1. To avoid the usual problems related to sawing and polishing procedures in sample preparation for cross-sectional AFM/SCM measurements the samples were cleaved and subsequently oxidized in UV-light [9] – [11]. For the back contact, sputtered aluminum was employed. The capacitance measurements were performed using the Dimension-3100 system with integrated SCM sensor (Digital Instruments, USA). The probes implemented for the investigations were conducting diamond tips (Nanonsensors, Germany) which turned out to be superior to metal coated tips due to their high resistance against abrasion. Space charge effects in such tips can be neglected as long as the dopant concentration in the tip (10^{20} at/cm^3) is much higher than in the sample.

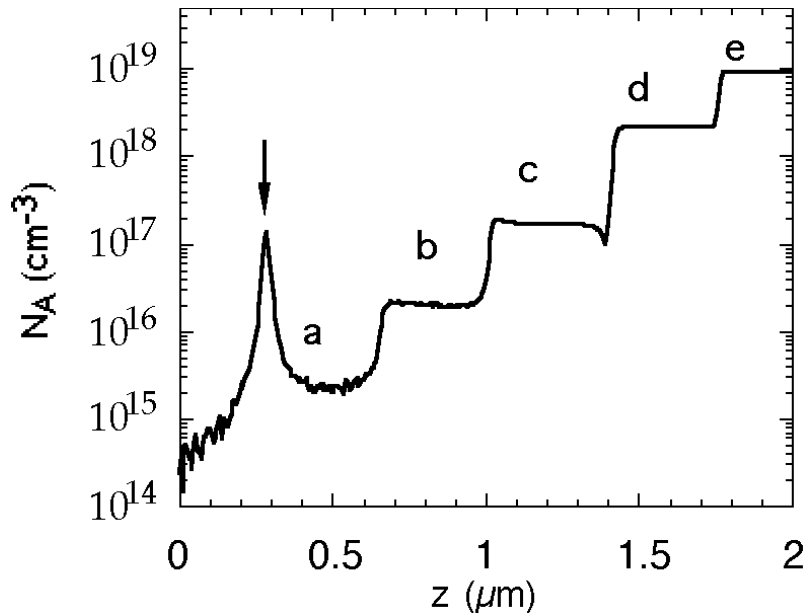


Fig. 1: Doping profile of our epitaxial staircase structure determined by SIMS. The sample surface is on the right hand side. The peak at $z = 0.25 \mu\text{m}$ is an unintentional artifact of the epitaxial process.

Before we discuss our SCM data, we have to introduce the following important convention concerning the bias polarity: In analogy to textbooks on conventional MOS theory [23], [24], the bias in this work is always plotted in a way as if it would be applied to the AFM tip. In reality this is not the case, since in the DI-3100 SCM the bias is applied to the substrate for technical reasons. Finally, it needs to be mentioned that the SCM only measures the derivative of the capacitance, dC/dV , and not the capacitance itself.

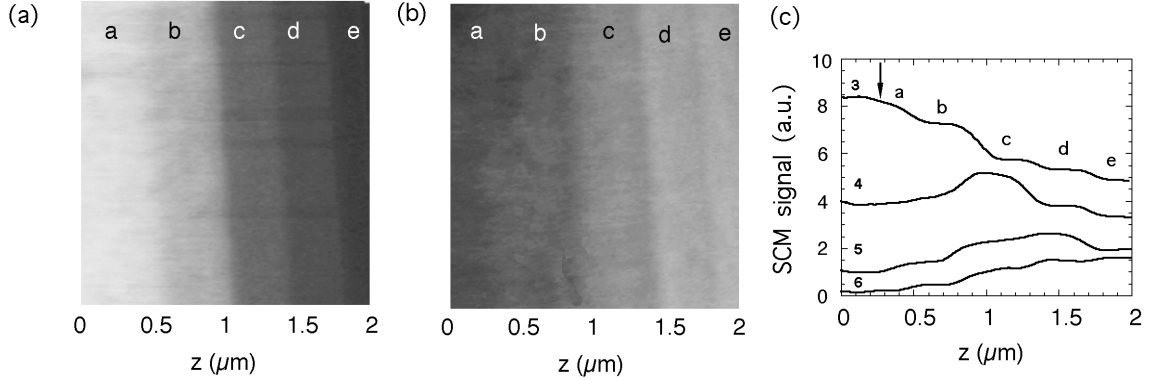


Fig. 2: (a) SCM image of our sample taken at a bias of -1.9 V. Image (b) was recorded at $+0.8$ V. The regions (a), (b), (c), (d) and (e) have doping concentrations 2.1×10^{15} , 2.0×10^{16} , 1.7×10^{17} , 2.2×10^{18} and 9.1×10^{18} cm^{-3} , respectively. (c): Sections through SCM images taken at a bias of $+0.8$ V, 0 V, -0.5 V and -1.9 V (curves 3-6). The numbering of the curves corresponds to the numbering in Figure 3.

Figure 2 shows cross sectional SCM images of our sample measured at two different bias values. The sample surface is on the right hand side. Figure 2(a) was measured at a tip bias of -1.9 V and Fig. 2(b) at $V = +0.8$ V. As one can see, the contrast between these two images is reversed. Figure 2(c) shows sections through SCM images perpendicular to the growth direction and measured at four different bias values. Two features are evident: First, the 400 nm wide differently doped layers are clearly visible as well defined steps in the SCM signal (see curve (3) e.g.). As a consequence we conclude that geometry effects of the tip can be neglected otherwise the steps would be washed out. This washout, however is nicely seen for the doping spike at the substrate interface, the position of which is marked by an arrow both in curve (3) and the SIMS data (Fig. 1). As the spike is much narrower than the steps and already in the same order as the radius of the tip (100 nm), only a small dip is observed in curve (3) instead of the expected well pronounced minimum.

As second feature in Fig. 2(c), the contrast dependence as a function of bias, can be seen in detail. At -1.9 V (curve 3), the SCM signal decreases with increasing doping. At $+0.8$ V (curve 6), however, this behavior is reversed and the SCM signal increases monotonically with increasing doping concentration. For bias values of -0.5 V and 0 V the behavior is non monotonic, and the maximum of the SCM signal is observed in regions (c) and (d), respectively.

Although the bias induced contrast reversal was already reported in the literature [12], a detailed study of this behavior was not carried out up to now. To explain the origin of this behavior, we consider an ideal p-Si/SiO₂/Al junction as model system and use conventional MOS theory. Figure 3 (a) shows the corresponding $C(V)$ and dC/dV curves,

where the y -axis of the dC/dV was flipped for better comparison with the experimental data. For the calculation an acceptor concentration of $N_A = 1 \times 10^{16} \text{ cm}^{-3}$, an oxide thickness of 3 nm (a typical thickness for SCM), and no traps or surface charges were assumed. Other parameters could also be chosen, but have no qualitative influence on the obtained result. At low bias, the sample is in accumulation, which means that the capacitance is high, because it is mainly determined by the oxide thickness. The dC/dV peak marks flatband conditions, and above 0.9V, the area under the gate becomes depleted. To explain the non-monotonic behavior of the SCM contrast, we simply calculate dC/dV as a function of the acceptor concentration N_A at various constant bias values both in the accumulation and the depletion regime. As our considerations apply for n- and p-type samples and the sign of the SCM output depends on the phase adjustment of the built in lock-in amplifier, we consider the absolute value of dC/dV for convenience. The result of this calculation is shown in Fig. 3 (b) where the curve numbers correspond to the bias values marked by arrows in Fig. 3 (a). In accumulation (curves 1 – 3), the SCM signal always decreases exponentially with increasing doping. Further, the signal increases when the bias approaches the region of the maximum in the dC/dV curve. Under depletion conditions (curves 4 – 6), the situation is complex. For bias values close to the dC/dV maximum, the SCM signal shows a clear maximum for doping concentrations around $N_A = 1 \times 10^{16} \text{ cm}^{-3}$ (curve 4). This maximum shifts to higher concentrations when the sample goes deeper into depletion (curves 5, 6). In addition, the signal size decreases. At a bias of 1.1 V (curve 6) a situation is achieved where the maximum is close to $N_A = 1 \times 10^{19} \text{ cm}^{-3}$. Above that bias, the SCM signal becomes very small but monotonically increases in the whole regime between $N_A = 1 \times 10^{15} \text{ cm}^{-3}$ and $N_A = 1 \times 10^{19} \text{ cm}^{-3}$.

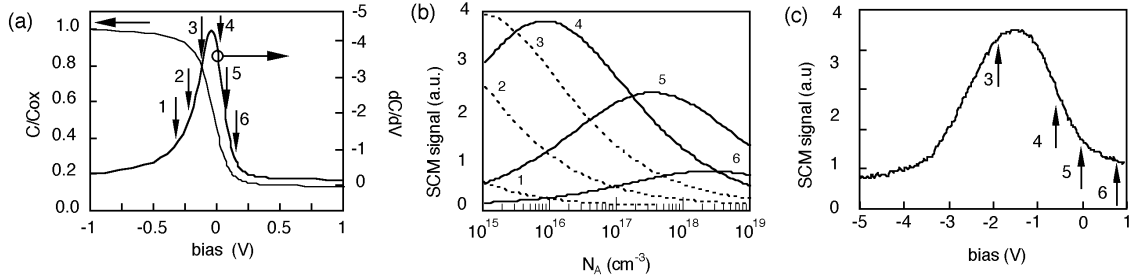


Fig. 3: (a) calculated $C(V)$ and dC/dV curves of an ideal p-Si/SiO₂/Al junction. The y -axis of the dC/dV plot was flipped for better comparison with the experimental data. (b): SCM signal plotted as a function of N_A for different constant bias values as labeled in Figure 3(a). (c) typical dC/dV curve measured with our SCM. The arrows labeled with (3-6) indicate those bias values at which curves (3 – 6) in Fig. 2 (c) were taken.

If we now compare the measured SCM signal in the differently doped areas with the calculated behavior in Fig. 3(b), one can see that the experimental curves (3 – 6) in Fig. 2(c) clearly correspond to the calculated curves (3 – 6) of Fig. 3(b). Thus, it becomes clear why the SCM signal decreases with increasing doping concentration in accumulation and vice versa in depletion. In the transition regime, any doping concentration can yield highest contrast depending on bias.

To verify this further, we also measured dC/dV curves using our SCM. Figure 3(c) shows typical data. Again, the absolute value of the SCM signal is plotted for conven-

ience. Compared to the calculated dC/dV curve of an ideal p-Si/SiO₂/Al junction (see Fig. 3(a)), the position of the peak is shifted to negative bias, which is due to surface charges and the use of a diamond tip having a different surface barrier height than aluminum. In addition, the peak is much broader, which is mainly due to the tip geometry [25]. The arrows (3 – 6) indicate the bias positions where curves (3 – 6) of Fig. 2(c) were measured. As one can see, bias positions (4 – 6) are located on the right hand side of the dC/dV peak, which is the bias regime where the sample moves from accumulation into depletion. At bias position (3) the sample is still completely in the accumulation regime. This good agreement nicely shows that the experimental situation indeed qualitatively corresponds to our idealized model system.

For practical SCM applications some conclusions can now be drawn: To obtain unambiguous results, the bias position of the maximum in dC/dV has to be known. Then, the bias should be chosen in a way that the sample is either in accumulation or depletion. According to our experience, the accumulation region yields more reproducible results, probably due to the fact that deep depletion is difficult to achieve because of the influence of the laser beam necessary for the AFM feedback control. Note that the dC/dV maximum shifts with doping concentration so that one has to stay in a safe distance from the dC/dV maximum in order to avoid to enter the transition regime between accumulation and depletion by accident. Finally, care should be taken on samples where both p-type and n-type regions exist. If the bias is adjusted in a way that the sample is in accumulation in the p-type regions, it will be in depletion in the n-type regions. As a consequence, the contrast is reversed in the n-type region and also the signal will be small. Moreover, measurements at zero bias, as often found in the literature on pn-junction imaging, might yield unpredictable contrast behavior.

3. Conclusion

In summary, we have investigated the bias dependent SCM contrast on a p-type silicon doping staircase. We have found, that a monotonic behavior of the SCM signal as a function of doping is only obtained if the sample is either in sufficient accumulation or depletion. In the transition region, the behavior is non-monotonic, and the maximum SCM signal size depends both on doping concentration and applied bias. The observed behavior is in good agreement with conventional MOS theory and theoretically applies for p- and n-type samples.

Acknowledgements

This work was sponsored by: *Österreichisches Bundesministerium für Verkehr, Innovation und Technologie, Fonds für innovative Projekte an der TU Wien, Gesellschaft für Mikroelektronik (GMe) and Fonds zur Förderung der wissenschaftlichen Forschung (FWF) project No. Z24-TPH.*

References

- [1] D.D.Bugg, P.J.King, J.Phys. E21, 147 (1988)
- [2] V.V. Zavyalov, J.S. McMurray, C.C. Williams, Rev. Sci. Instr. 7, 158 (1999)
- [3] P. De Wolf, R. Stephenson, T. Trenkler, T. Clarysse, T. Hantschel, W. Vandervorst, J.Vac. Sci. Technol. B18, 361 (2000)

-
- [4] R. Stephenson, P. DeWolf, T. Trenkler, T. Hantschel, T. Clarysse, P. Jansen, W. Vandervorst, *Vac. Sci. Technol.* B18, 555 (2000)
 - [5] F. Giannazzo, F. Priolo, V. Raineri, V. Privitera, *Appl. Phys. Lett.* 76, 2565 (2000)
 - [6] J.S. McMurray, J. Kim, C.C. Williams, *J. Vac. Sci. Technol.* B15, 1011 (1997)
 - [7] G.H. Buh, H.J. Chung, C.K. Kim, J.H. Yi, I.T. Yoon, Y. Kuk, *Appl. Phys. Lett.* 77, 106 (2000)
 - [8] J. Schmidt, D.H. Paoport, G. Behme, H.-J. Fröhlich, *J. Appl. Phys.* 86, 7094 (1999)
 - [9] J.J. Kopanski, J.F. Marchiando, B.G. Rennex, *J. Vac. Sci. Technol.* B18, 409 (2000)
 - [10] V. A. Ukraintsev, F.R. Potts, R.M. Wallace, L.K. Magel, H. Edwards, M.-C. Chang, *AIP Conf. Proc.* 449, 736-740 (1998)
 - [11] V.V. Zavyalov, J.S. McMurray, S.D. Stirling, C.C. Williams, H. Smith, *J. Vac. Sci. Technol.* B18, 549 (2000)
 - [12] R. Stephenson, A. Verhulst, P. DeWolf, M. Caymax, W. Vandervorst, *Vac. Sci. Technol.* B18, 405 (2000)
 - [13] C.C. Williams, J. Slinkman, W.P. Hough, K. Wickramasinghe, *Vac. Sci. Technol.* A8, 895 (1990)
 - [14] N. Nakagiri, T. Yamamoto, H. Sugimura, Y. Suzuki, *Vac. Sci. Technol.* B14, 887 (1996)
 - [15] S. Lany, *Surf. Interface Anal.* 27, 348 (1999)
 - [16] T. Clarysse, M. Caymax, P. DeWolf, T. Trenkler, W. Vandervorst, J.S. McMurray, J. Kim, C.C. Williams, J.G. Clark, G. Neubauer, *Vac. Sci. Technol.* B16, 394 (1998)
 - [17] J.S. McMurray, J. Kim, C.C. Williams, *Vac. Sci. Technol.* B15, 1011, (1997)
 - [18] J.F. Marchiando, J.J. Kopanski, J. Albers, *J. Vac. Sci. Technol.* B18, 414 (2000)
 - [19] Y. Huang, C.C. Williams, J. Slinkman, *Appl. Phys. Lett.* 66, 344 (1995)
 - [20] J.F. Marchiando, J.J. Kopanski, J.R. Lowney, *J. Vac. Sci. Technol.* B16, 463 (1998)
 - [21] L. Ciampolini, M. Ciappa, P. Malberti, W. Fichtner, V. Ranieri, (preprint, submitted)
 - [22] J.J. Kopanski, J.F. Marchiando, J.R. Lowney, *J. Vac. Sci. Technol.* B14, 242 (1996)
 - [23] S.M. Sze, *Physics of Semiconductor Devices*, John Wiley & Sons Ltd, New York, 1981
 - [24] E.H. Nicollian, J.R. Brews, *MOS (metal oxide semiconductor) physics and technology*, John Wiley & Sons Ltd, New York 1982
 - [25] L. Ciampolini, private communication

Infrared Quantum Cascade Laser

W. Schrenk, N. Finger, S. Gianordoli, L. Hvozdar, E. Gornik, G. Strasser

Institut für Festkörperelektronik, Technische Universität Wien
Floragasse 7, 1040 Wien, Austria

We report on quantum cascade lasers in the AlGaAs material system grown on GaAs. The emission wavelength is in the range of $\lambda \sim 9.5 - 13 \mu\text{m}$. Both, first and second order distributed feedback laser have been fabricated. A metallized surface-relief grating is used for feedback to achieve single-mode emission. The emission wavelength is continuously tunable with the heat sink temperature. The second order distributed feedback lasers are efficient surface emitters with low beam divergence. Further, continuous wave operation at cryogenic temperatures has been achieved for a chirped superlattice active region.

1. Introduction

A quantum cascade laser (QCL) is a semiconductor laser involving only one type of carrier and which is based on two fundamental phenomena of quantum mechanics, namely, tunneling and quantum confinement. In conventional semiconductor diode lasers (as used, e.g., in compact disk players), the light originates from the recombination of electrons and holes, and the emission wavelength is determined by the bandgap. However, in QCLs the light generation is based on intersubband transitions within the conduction band (or valence band). So far, QCLs are demonstrated only in two material systems, the InGaAs/InAlAs material system grown on InP [1] and the AlGaAs/GaAs grown on GaAs [2]. Spontaneous emission from quantum cascade structures has been achieved in some other materials [3], [4]. Recently, room temperature operation of AlGaAs based QCL [5] has been demonstrated for Fabry Perot lasers, which is an important step towards commercial applications. Up to this, room temperature operation was a privilege for QCL grown on InP. Continuous wave operation of QCL is so far restricted to low temperatures [6], also for QCL grown on InP [7] – [9]. However, for absorption measurements like gas sensing, single mode lasers are favored. Therefore, distributed feedback (DFB) QCL [10] – [13] have been realized soon after the invention of QCLs. Some demonstration of infrared spectroscopy of gases [14] – [16] (single- or multiple pass absorption), liquids [17] or photoacoustic spectroscopy [18] show the potential for commercial applications. In this letter, we report on distributed feedback quantum cascade lasers in the AlGaAs material system grown on GaAs.

2. Experimental

The energy band diagram (conduction band) of a typical QCL is shown in Fig. 1. The electrons are injected into the upper laser level 3 by an electron funnel (injector). Inversion is achieved by fast depopulation of level 2 by LO-phonon emission (lifetime ~ 0.3 ps). Therefore the energy spacing of level 2 and level 1 is designed close to the LO-phonon energy of GaAs (36 meV). The lifetime of the upper laser level is in the range of 2 ps, allowing fast direct modulation.

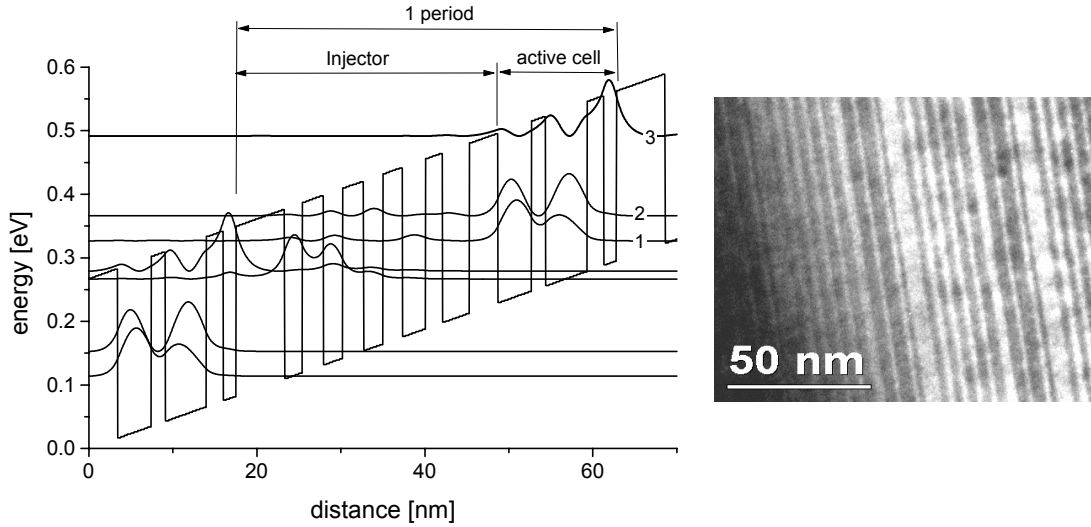


Fig. 1: Left: Energy band structure and moduli square of the most relevant wave functions of a QCL. The laser transition is the transition 3–2, and the energy separation of the level 2 and 1 is close to the LO-phonon energy. Right: Transmission electron microscope picture of a MBE grown QCL.

We have used $\text{Al}_{0.33}\text{Ga}_{0.67}\text{As}$ or AlAs as barrier material and GaAs or $\text{In}_{0.04}\text{Ga}_{0.96}\text{As}$ as well material for our lasers. The active cell is formed by three quantum wells or by a chirped superlattice. The superlattice is chirped in order to get flat minibands for the design field. The conduction band discontinuity and the energy of the upper laser level determines the leakage current into the continuum, which restricted the very first $\text{Al}_{0.33}\text{Ga}_{0.67}\text{As}/\text{GaAs}$ based QCL to low operation temperatures as the upper laser level is close to the barrier energy (Fig. 1). In the first structures we used $\text{Al}_{0.33}\text{Ga}_{0.67}\text{As}$ as barrier material, where the X-valley is higher in energy than the Γ -valley in order to get rid of multi valley effects as the crossover from a direct to an indirect semiconductor occurs for $\text{Al}_x\text{Ga}_{1-x}\text{As}$ at $x \sim 0.45$. We have also investigated InGaAs as well material, which increased the band offset in respect to $\text{Al}_{0.33}\text{Ga}_{0.67}\text{As}$ [19]. The lattice mismatch of $\text{In}_x\text{Ga}_{1-x}\text{As}$ grown on GaAs allowed only low In contents. Then we used AlAs as barrier material, where the overall Al concentration is small and the AlAs layers are very thin (down to 2 monolayers) so that the electrons remain around the Γ -valley. In this case, the lowest energy levels for the X-valleys (GaAs and AlAs) are higher than for the Γ -valley. An AlAs/GaAs chirped superlattice laser material showed the first time continuous wave operation for GaAs based QCL.

Our laser material is grown by solid source molecular beam epitaxy on n-doped GaAs (100). A double plasmon enhanced waveguide is used for all lasers. 30 to 40 periods of active cell/injector are cascaded and embedded into low doped GaAs (Si , $4 \times 10^{16} \text{ cm}^{-3}$, $d \sim 3.5 \mu\text{m}$) layers, forming the low loss waveguide core. The cladding layers are formed by highly doped GaAs (Si , $4 \times 10^{18} \text{ cm}^{-3}$, $d \sim 1.0 \mu\text{m}$).

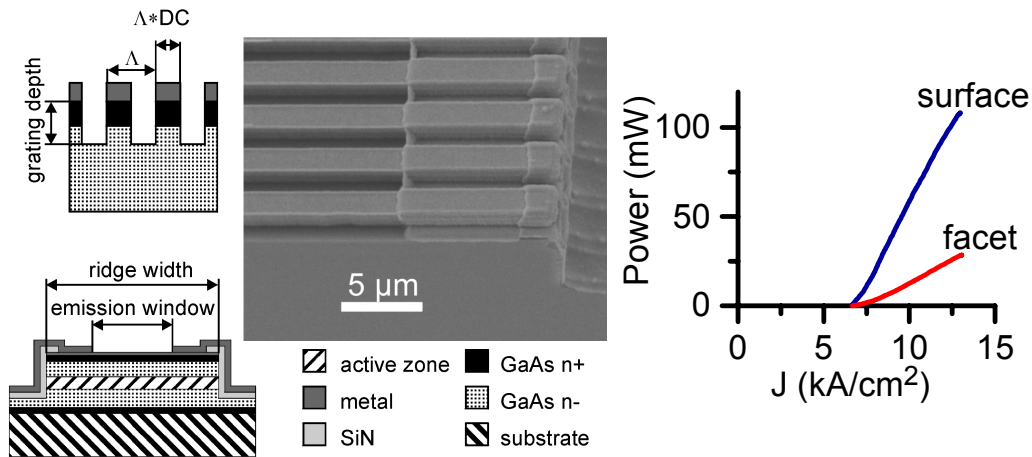


Fig. 2: Left: Schematic cross section of the grating region and the ridge waveguide, and a SEM picture of a fabricated laser. Λ denotes the grating period and DC is the duty cycle of the grating. Right: Emitted power via surface and one facet for a 2.99 mm long and 45 μm wide laser in pulsed mode operation (100 ns, 5 kHz).

We have fabricated DFB laser from several laser materials [6], [13], [20]. A metallized surface relief grating is used for feedback, resulting in a large contact area and avoiding the need of regrowth. The coupling coefficients and losses are calculated based on Floquet Bloch analysis [21]. The Floquet Bloch fields are rigorously calculated at resonance and a connection to the coupled mode theory is made by a perturbation method, as the optical intensity in the grating region is small. In the case of first order DFB laser the whole grating is covered with metal whereas in the case of the second order DFB laser only the grating peaks (Fig. 2) are covered with metal allowing efficient transmission of the TM polarized light through the metal stripe structure. We have fabricated ridge waveguides where we etched through the active region. The lateral light confinement is almost unity whereas the vertical light confinement by the plasmon enhanced waveguide (in growth direction) is in the range of 0.3 – 0.5.

The absolute average power is measured with a slow thermopile detector. The pulse peak power in pulsed mode operation (pulse length 100 ns) is in the several 100 mW range (Fig. 2). Spectral measurements were performed with a Fourier transform infrared (FTIR) spectrometer equipped with a mercury-cadmium-telluride (MCT) detector. As the current heats the active region, the emission wavelength is shifted to longer wavelengths during a pulse causing a broadening of the emission in pulsed mode operation. The current heating can be neglected for short pulses and low pulse repetition rates. The emission wavelength is in this case only a function of the heat sink temperature. The emission wavelength shifts according to the Bragg wavelength and the temperature dependence of the refractive index at a rate of $(d\lambda/dT)/\lambda \sim 1 \times 10^{-5}/\text{K}$ (Fig. 3). In continuous wave operation the emission tunes with the current (Fig. 3) corresponding to temperature within the laser cavity.

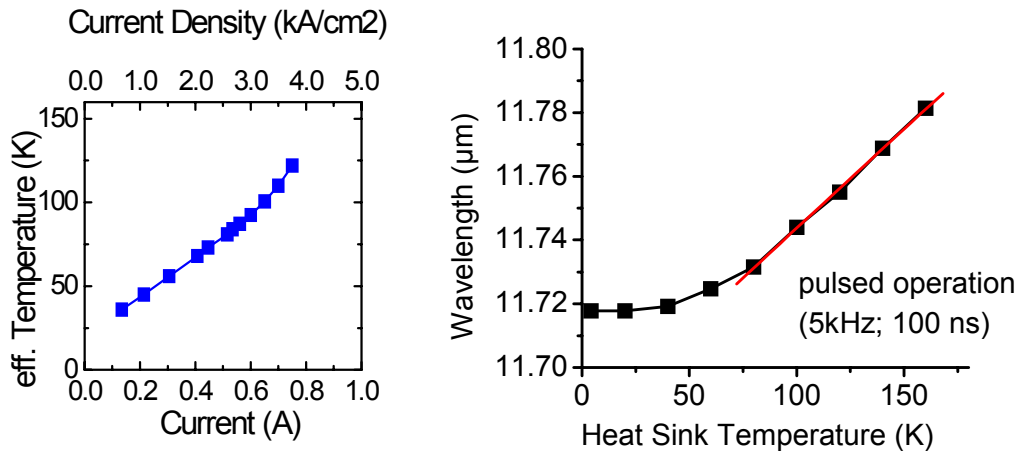


Fig. 3: Left: Effective temperature in the laser cavity for continuous wave operation as obtained from the emission wavelength (heat sink temperature 4.2 K). Right: Emission wavelength in pulsed mode operation (100 ns, 5 kHz) as a function of the heat sink temperature for the same laser.

3. Conclusion

In conclusion, we have achieved single mode emission in the mid-infrared from quantum cascade lasers grown on GaAs. The emission wavelength is continuously tunable by the temperature. We have developed an analysis which allows the accurate prediction of the coupling coefficient and the losses of the waveguide grating structure, including the surface emission of second order DFB lasers. Further, continuous wave operation at low temperatures has been achieved for a DFB laser emitting at 11.7 μm .

Acknowledgements

This work was partly supported by the European Community by the research projects SUPERSMILE IST-1999-1493 and UNISEL (Brite Euram III) BE97-4072 and the FWF Austria.

References

- [1] J. Faist, F. Capasso, D. L. Sivco, C. Sirtori, A. L. Hutchinson, and A. Y. Cho, “Quantum Cascade Laser”, *Science* **264**, 1994, pp. 553.
- [2] C. Sirtori, P. Kruck, S. Barbieri, P. Collot, J. Nagle, M. Beck, J. Faist, and U. Oesterle, “GaAs/Al_xGa_{1-x}As quantum cascade lasers”, *Appl. Phys. Lett.* **73**, 1998, pp. 3486.
- [3] G. Dehlinger, L. Diehl, U. Gennser, H. Sigg, J. Faist, K. Ensslin, D. Grützmacher, and E. Müller, “Intersubband Electroluminescence from Silicon-Based Quantum Cascade Structures”, *Science* **290**, 2277 (2000).

- [4] C. Becker, I. Prevot, X. Marcadet, B. Vinter, and C. Sirtori, "InAs/AlSb quantum-cascade light-emitting devices in the 3-5 μm wavelength region", *Appl. Phys. Lett.* **78**, 2001, pp. 1029.
- [5] H. Page, C. Becker, A. Robertson, G. Glastre, V. Ortiz, and C. Sirtori, "300 K Operation of a GaAs based Quantum Cascade Laser at $\lambda = 9 \mu\text{m}$ ", *Appl. Phys. Lett.*, in print.
- [6] W. Schrenk, N. Finger, S. Gianordoli, E. Gornik, and G. Strasser, "Continuous-wave operation of distributed feedback AlAs/GaAs superlattice quantum-cascade lasers", *Appl. Phys. Lett.* **77**, 2000, pp. 3328.
- [7] J. Faist, F. Capasso, C. Sirtori, D. L. Sivco, A. L. Hutchinson, and A. Y. Cho, "Continuous wave operation of a vertical transition quantum cascade laser above $T=80 \text{ K}$ ", *Appl. Phys. Lett.* **67**, 1995, pp. 3057.
- [8] R. Köhler, C. Gmachl, A. Tredicucci, F. Capasso, D. L. Sivco, S. N. G. Chu, and A. Y. Cho, "Single-Mode Tunable Quantum Cascade Lasers in the Spectral Range of the CO_2 Laser at $\lambda = 9.5\text{-}10.5 \mu\text{m}$ ", *Appl. Phys. Lett.* **76**, 2000, pp. 1092.
- [9] A. Tahraoui, A. Matlis, S. Slivken, J. Diaz, and M. Razeghi, "High-performance quantum cascade lasers ($\lambda \sim 11 \mu\text{m}$) operating at high temperature ($T \geq 425 \text{ K}$)", *Appl. Phys. Lett.* **78**, 2001, pp. 416.
- [10] C. Gmachl, J. Faist, J. N. Baillargeon, F. Capasso, C. Sirtori, D. L. Sivco, S. N. G. Chu, and A. Y. Cho, "Complex-Coupled Quantum Cascade Distributed-Feedback Laser", *IEEE Photonics Technol. Lett.* **9**, 1997, pp. 1090.
- [11] J. Faist, C. Gmachl, F. Capasso, C. Sirtori, D. L. Sivco, J. N. Baillargeon, and A. Y. Cho, "Distributed feedback quantum cascade lasers", *Appl. Phys. Lett.* **70**, 1997, pp. 2670.
- [12] D. Hofstetter, M. Beck, T. Aellen, and J. Faist, "High-temperature operation of distributed feedback quantum-cascade lasers at $5.3 \mu\text{m}$ ", *Appl. Phys. Lett.* **78**, 2001, pp. 396 – 398.
- [13] W. Schrenk, N. Finger, S. Gianordoli, L. Hvozdar, G. Strasser, and E. Gornik, "GaAs/AlGaAs distributed feedback quantum cascade lasers", *Appl. Phys. Lett.* **76**, 2000, pp. 253.
- [14] C. R. Webster, G. J. Flesch, D. C. Scott, J. E. Swanson, R. D. May, W. S. Woodward, C. Gmachl, F. Capasso, D. L. Sivco, J. N. Baillargeon, A. L. Hutchinson, and A. Y. Cho, "Quantum-cascade laser measurements of stratospheric methane and nitrous oxide" *Appl. Optics* **40**, 2001, pp. 321.
- [15] L. Hvozdar, S. Gianordoli, G. Strasser, W. Schrenk, K. Unterrainer, E. Gornik, C. S. S. S. Murthy, M. Kraft, V. Pustogow, B. Mizaikoff, A. Inberg, N. Croitoru, "Spectroscopy in the Gas Phase with GaAs/AlGaAs Quantum-Cascade Lasers", *Appl. Optics* **39**, 2000, pp. 6926 – 6930.
- [16] A. A. Kosterev, F. K. Tittel, C. Gmachl, F. Capasso, D. L. Sivco, J. N. Baillargeon, A. L. Hutchinson, A. Y. Cho, "Trace-gas detection in ambient air with an thermoelectrically cooled, pulsed quantum-cascade distributed feedback laser" *Appl. Optics* **39**, 2000, pp. 6866 – 6872.

-
- [17] B. Lendl, J. Frank, R. Schindler, A. Müller, M. Beck, and J. Faist, "Mid-Infrared Quantum Cascade Lasers for Flow Injection Analysis", *Analytical Chemistry* **72**, 2000, pp. 1645 – 1648.
- [18] B. A. Paldus, T. G. Spence, R. N. Zare, J. Oomens, F. J. M. Harren, D. H. Parker, C. Gmachl, F. Capasso, D. L. Sivco, J. N. Baillargeon, A. L. Hutchinson, A. Y. Cho, " Photoacoustic spectroscopy using quantum-cascade lasers ", *Optics Lett.* **24**, 1999, pp. 178 – 180.
- [19] S. Gianordoli, W. Schrenk, L. Hvozdar, N. Finger, G. Strasser, and E. Gornik, "Strained InGaAs/AlGaAs/GaAs-quantum cascade lasers", *Appl. Phys. Lett.* **76**, 2000, pp. 3361.
- [20] W. Schrenk, N. Finger, S. Gianordoli, L. Hvozdar, G. Strasser, and E. Gornik, "Surface-emitting distributed feedback quantum-cascade lasers", *Appl. Phys. Lett.* **77**, 2000, pp. 2086.
- [21] N. Finger, W. Schrenk, and E. Gornik, "Analysis of TM-Polarized DFB Laser Structures with Metal Surface Gratings", *IEEE J. Quant. Electron.* **36**, 2000, pp. 773.

Lead-Salt Microcavities for the Mid-Infrared

W. Heiss¹, T. Schwarzl¹, G. Springholz¹, T. Fromherz¹, G. Bauer¹, M. Aigle²,
H. Pascher², K. Biermann³, K. Reimann³

¹Institut für Halbleiter- u. Festkörperphysik, Johannes Kepler Universität,
Altenbergerstraße 69, 4040 Linz, Austria

²Experimentalphysik I, Universität Bayreuth, 95447 Bayreuth, Germany

³Max-Born-Institut für Nichtlineare Optik und Kurzzeitspektroskopie,
12489 Berlin, Germany

Operation of optically pumped IV-VI vertical-cavity surface emitting lasers is reported. The microcavity structures were grown by molecular beam epitaxy on BaF₂ (111) substrates. High reflectivity Pb_{1-x}Eu_xTe/EuTe multilayers are used as Bragg interference mirrors of the cavity. Stimulated emission at wavelengths between 3 and 4.5 μm is generated either in PbTe quantum wells embedded at the antinode positions of the microcavity or in correlated, self-organized PbSe quantum dots.

1. Introduction

Narrow band gap IV-VI semiconductor compounds (lead salts) are important materials for optoelectronic devices for the mid-infrared (MIR) spectral region (3 – 30 μm). As a result of their favorable band structure, lead salt diode lasers were obtained with cw operation temperatures up to 223 K [1] and up to 60 °C in pulsed mode [2]. This represents the highest cw operation temperature for electrically pumped MIR diode lasers. The major application for such lasers is high resolution and high sensitivity chemical gas analysis as well as atmospheric pollution monitoring. This is due to numerous absorption lines of many gaseous molecules in the MIR range.

Apart from the conventional edge emitting lasers, very recently, surface emitting lead-salt mid-infrared microcavity lasers were demonstrated for the first time [3]. These vertical cavity surface emitting lasers (VCSELs) offer several advantages like a circular output beam with small divergence, single mode operation, and the possibility of high monolithic integration. In addition, VCSELs offer the possibility for reducing the threshold currents and increasing operation temperatures.

In this work, lead-salt VCSELs working in the wavelength range between 3 and 4.5 μm are presented. With optical pumping, pulsed laser operation is demonstrated up to a temperature of 65 °C. In addition, stimulated emission from correlated, self organized PbSe quantum dots, embedded between PbEuTe/EuTe Bragg interference mirrors is shown. This is of high interest since quantum dot lasers have been predicted to yield strongly increased material gain and differential gain, lower threshold currents, higher modulation band widths and better temperature stability as compared to quantum well lasers.

2. Sample details

The microcavity structures were grown by molecular beam epitaxy (MBE) on (111) oriented BaF_2 substrates. Sample 1 consists of a $\text{Pb}_{0.94}\text{Eu}_{0.06}\text{Te}$ cavity with a thickness corresponding to two times the optical wavelength (λ) with nine inserted PbTe quantum wells (QWs). The cavity is embedded between two dielectric Bragg mirrors. The bottom mirror consists of three periods of $\text{Pb}_{0.95}\text{Eu}_{0.05}\text{Te}/\text{EuTe}$ $\lambda/4$ layer pairs. Because of the very high refractive index contrast of the layers of more than 80 %, this yields a mirror reflectivity of more than 99 %. To enable optical pumping, the top mirror has to be transparent at the pump wavelength. Therefore, the Eu content in the ternary layers of the top mirror was increased to 20 %. This leads to a reduced refractive index contrast, so that four layer pairs had to be used to obtain a reflectivity of 98 %. As active laser material, nine 20 nm wide PbTe QWs were inserted in the cavity close to the five anti-node positions of the electric field.

Sample 2 contains a superlattice of correlated, self-organized PbSe quantum dots between the two dielectric Bragg mirrors. These are formed during heteroepitaxial growth of PbSe on $\text{Pb}_{1-x}\text{Eu}_x\text{Te}$ (111) due to the 5.4 % lattice mismatch [4]. Due to the strong increase of the $\text{Pb}_{1-x}\text{Eu}_x\text{Te}$ energy band gap with Eu content ($\Delta E_g/\Delta x_{\text{Eu}} = 4.48$ eV at 4 K), a quantum confinement of the free carriers in the PbSe dots is achieved already for Eu concentrations of a few percent. We have chosen $x_{\text{Eu}} = 5\%$, the same concentration as used for the growth of the mirrors. To obtain PbSe dots with an areal dot density of about $5 \times 10^{10} \text{ cm}^{-2}$, an average dot height of 120 Å, a width of 300 Å, and a size dispersion of typically around $\pm 15\%$, 5 monolayers PbSe were deposited at a substrate temperature of 360°C whereas the mirrors were grown at 260°C . Fig. 1 shows a cross section of the sample 2, by a sketch in (a), a SEM micrograph of the complete VCSEL structure in (b), and the PbSe dot arrangement in the superlattice by the TEM images of a reference sample grown under identical conditions in (c).

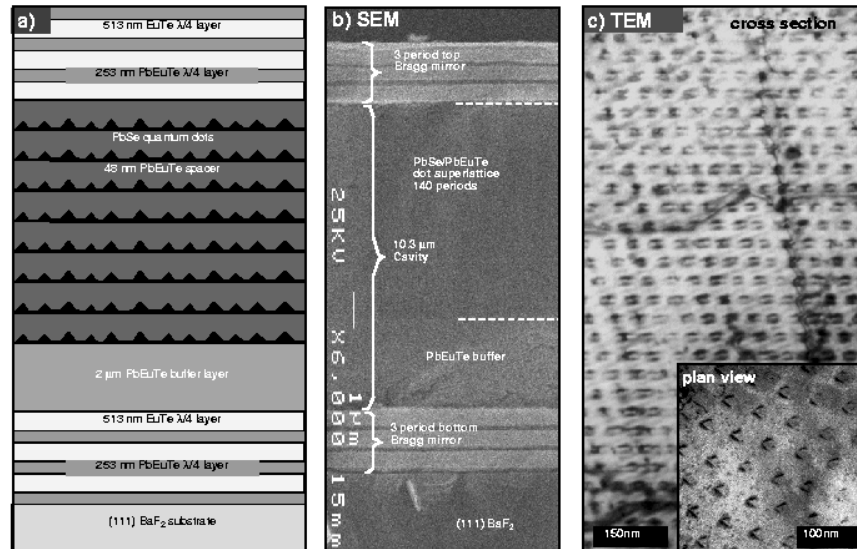


Fig. 1: Schematic representation (a) and cross sectional SEM micrograph (b) of the PbSe quantum dot VCSEL structure. (c) Cross sectional and plan-view TEM micrographs of a $\text{PbSe}/\text{Pb}_{1-x}\text{Eu}_x\text{Te}$ dot superlattice reference sample with 5 ML PbSe and 480 Å $\text{Pb}_{1-x}\text{Eu}_x\text{Te}$.

3. Experimental Results

For optical pumping of sample 1, we used 100 fs long pulses at a wavelength of $1.97 \mu\text{m}$ with a repetition rate of 1 kHz. For sample 1 MIR emission can be observed at room temperature. Below laser threshold, the emission spectrum shows a Lorentzian shaped line centered at 3200 cm^{-1} with a width of 160 cm^{-1} . Increasing the excitation density to 1 mJ/cm^2 results in a considerable narrowing of the emission spectrum and a drastic rise of the luminescence intensity. Both effects indicate the onset of stimulated emission. For excitation powers above 1 mJ/cm^2 the line width becomes larger again and the integrated emission intensity of the sample linearly increases with rising pump power. Such a linear dependence is expected for laser emission, and it is shown in detail in Fig. 2(a) giving a laser threshold energy density of 0.83 mJ/cm^2 .

The temperature dependence of the emission spectra of sample S1 excited with an energy density of 8 mJ/cm^2 is demonstrated in Fig. 2(b). With increasing sample temperature the laser output intensity at first only slowly decreases until about 55°C above which the intensity rapidly decreases and completely quenches at 70°C . As shown in Fig. 2 (a), with rising temperature also the laser threshold increases slightly from 0.83 mJ/cm^2 at room temperature to 1 mJ/cm^2 at 50°C .

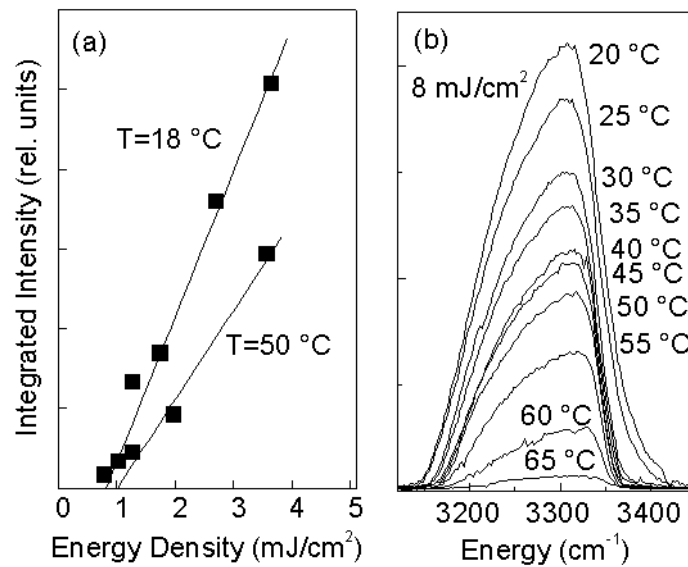


Fig. 2: Dependence of the stimulated emission of sample 1 on excitation intensity (a) and on sample temperature (b). Laser operation is obtained up to 65°C .

In the following, emission measurements on a superlattice of self-assembled PbSe Stranski-Krastanow islands embedded in a vertical cavity are presented. Because of the large total cavity length of sample 2 a large number of cavity resonance modes are observed within the stop band region. The central $m = 28^{\text{th}}$ cavity mode is located at 290 meV ($\lambda = 4.27 \mu\text{m}$), corresponding to the low temperature onset of quantum dot absorption measured on PbSe/Pb $_{1-x}$ Eu $_x$ Te reference samples. The stimulated emission spectra of the VCSEL structure induced by optical pumping with a pulsed Nd:YAG laser is shown in Fig. 3. At 1.5 K, simultaneous emission at the $m = 28$ and 29^{th} order cavity modes at $\lambda = 4.24$ and $4.09 \mu\text{m}$ occurs, with a line width of only $700 \mu\text{eV}$. This two-mode laser operation is a result of the inhomogeneous broadening of the quantum dot gain spectrum to dot size fluctuations. Measurements of the integrated output inten-

sity as a function of pump power indicates an external threshold of $P_{\text{th}} = 510 \text{ kW/cm}^2$. As shown in Fig. 3, with increasing temperature, the intensity of the 29th mode increases whereas that of the central 28th mode decreases and eventually disappears at a temperature of 40 K. As the temperature is further increased, the 29th emission in turn decreases and at 60 K the next higher laser mode turns on. At 70 K, the 29th mode completely disappears, whereas the 30th mode emission persists up to 90 K. This successive switching of the laser emission is explained by the increase of the PbSe band gap with increasing temperature. The envelope of the emission lines is given by the inhomogeneously broadened dot gain spectrum with a width of about 18 meV. Similar as in PbTe quantum well VCSELs, the upper limit of operation temperature is caused by the detuning between the gain spectrum and the central cavity modes at higher temperatures. This indicates that much higher operation temperatures can be achieved for the dot lasers by appropriate tuning of the optical cavity modes to the dot emission at higher temperatures.

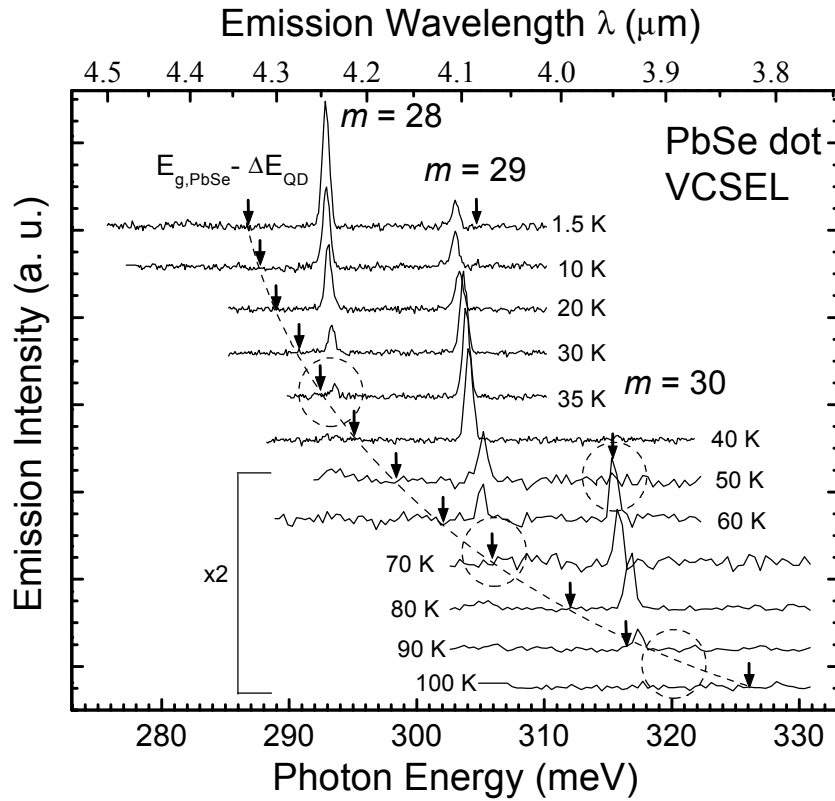


Fig. 3: VCSEL emission spectra at temperatures between 1.5 and 100 K showing the switching of the laser emission to higher cavity modes as the temperature increases. The arrows and dashed line indicate the low energy edge of the quantum dot gain spectrum.

Acknowledgements

This work is supported by the FWF, the Austrian Academy of Sciences, and the Deutsche Forschungsgemeinschaft.

References

- [1] Z. Feit, M. Mc Donald, R. J Woods, V. Archambault, P. Mak, *Appl. Phys. Lett.* **68**, 738 (1996).
- [2] P. Schießl, J. Rohr, *Infrared Physics. Technol.* **40**, 325 (1999).
- [3] T. Schwarzl, W. Heiss, G. Springholz, M. Aigle, H. Pascher, *Electron. Lett.* **36**, 322 (2000).
- [4] G. Springholz, V. Holy, M. Piczoliths, G. Bauer, *Science* **282**, 734 (1998).

Characterization of Si/SiGeC Heterostructures for Device Applications

D. Gruber, T. Fromherz, M. Mühlberger, C. Schelling, L. Palmetshofer, F. Schäffler

Institut für Halbleiter- und Festkörperphysik, Johannes Kepler Universität, Altenbergerstraße 69, 4040 Linz, Austria

1. Introduction

With the commercial introduction of the Si/SiGe hetero bipolar transistor (HBT) into mainstream integration technologies, process incompatibilities become an important issue. A basic problem is, for example, the transient enhanced diffusion (TED) of boron out of the SiGe base layer upon thermal activation of the poly-emitter implant. As a remedy, the use of a carbon co-doped base has been proposed, in which a carbon concentration of a few tenths of an atomic percent have been shown to very effectively suppress TED. On the other hand, great effort has been dedicated in the past to reduce the carbon concentration in Si ingots as far as possible, because of the propensity of C to form complexes and β -SiC precipitates. In contrast to substitutional C, some of these complexes are known to introduce electrically active states in the band gap. It is therefore important to characterize the microscopic configuration in which C is present after processing of SiGe:C HBTs. In this work, we address this problem with a combination of Fourier Transform Spectroscopy (FTIR), x-ray diffraction (XRD) and SIMS studies.

With the FTIR technique, one is able to probe the local surroundings of carbon atoms in the silicon crystal. In order to detect the absorption from carbon, a silicon reference spectrum has to be subtracted because of the strong Si phonon absorption in the interesting spectral region. The process of subtraction of the Si background is very sensitive to differences in thickness between sample and Si reference, making numerical correction necessary. This is done by measuring the thicknesses by Fabry-Perot interference fringes.

2. Measurement of Substitutional Carbon / Silicon Carbide

FTIR is the standard method for the measurement of substitutional C in bulk-Si. Despite the high concentrations in epitaxially grown $\text{Si}_{1-y}\text{C}_y$ layers, the integrated amount of C is small compared to bulk material. With a method for correction of differences in thickness between sample and Si reference, quantitative measurements on thin layers are possible as shown in Fig. 1.

It is also possible to measure the β -SiC concentration by FTIR. A defined amount of C was deposited on a Si substrate followed by a thin Si cap layer. During an annealing step at 1000 °C, the carbon forms β -SiC, which can be identified by its characteristic phonon absorption.

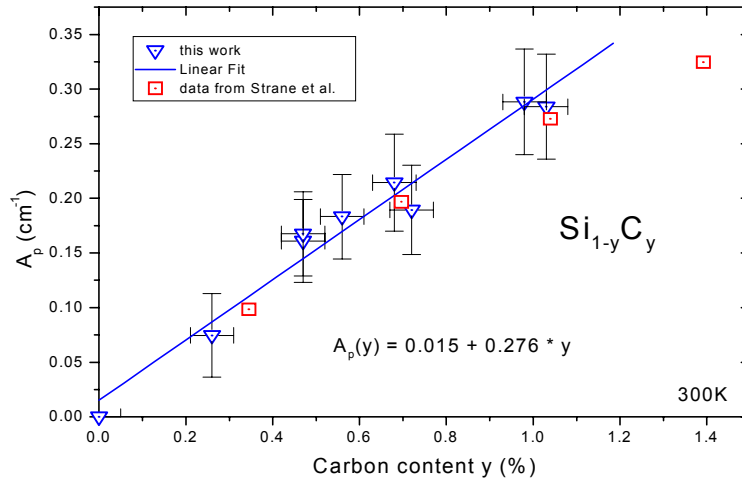


Fig. 1: Dependence of the integrated peak for substitutional carbon from the FTIR measurement as a function of carbon content measured by XRD. The layers are MBE grown with a thickness of 1000 Å.

3. Precipitation Behavior

Since the solid solubility of C in Si is about 0.0001%, the epitaxially grown layers are metastable and tend to relax their strain by forming β -SiC precipitates. The process can be studied by FTIR spectroscopy. Substitutional carbon (607 cm^{-1}) leaves the lattice and forms small precipitates which are coherently bound to the Si crystal (750 cm^{-1}).

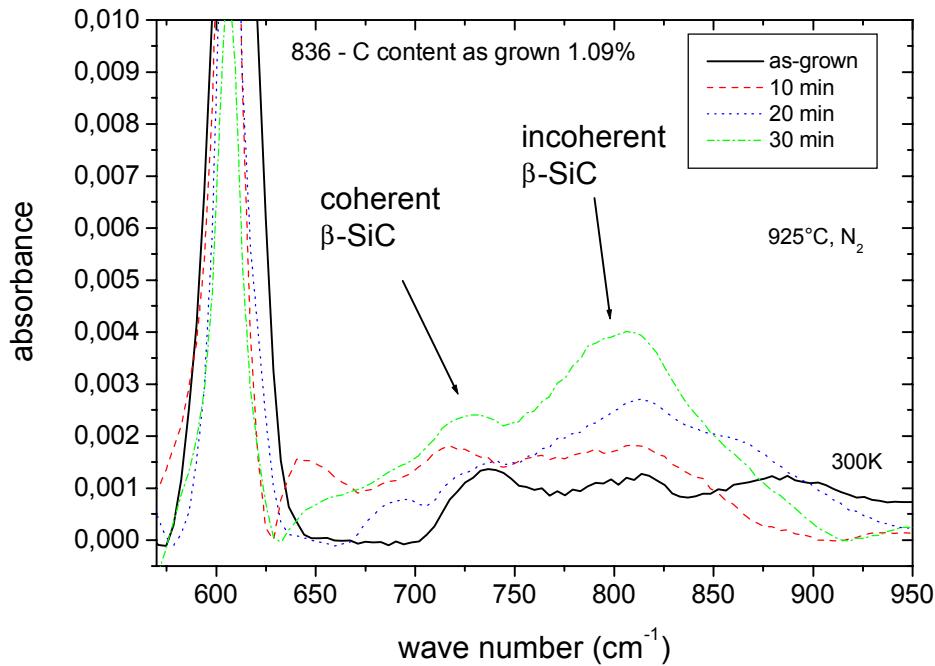


Fig. 2: Time evolution of the different peaks for a 1000 Å thick $\text{Si}_{0.99}\text{C}_{0.01}$ layer which has been annealed at a temperature of 925 °C for different amounts of time.

If the temperature is high enough, more strain can be relaxed, if the bonds between Si atoms and precipitate break up and the coherence with the neighboring Si atoms is lost. Phonon absorption from β -SiC can then be seen at 820 cm^{-1} .

The precipitation process is very sensitive to the as-grown situation. The above figure shows the time evolution of spectra from a $\text{Si}_{1-y}\text{C}_y$ sample annealed at $925\text{ }^\circ\text{C}$ for different periods of time. At the same time, the expansion of the vertical lattice constant can be monitored by XRD.

4. Impact of C on TED in a SiGeC: HBT

The influence of C on TED of B was studied for an HBT structure with graded Ge base. Pieces of two samples, one with (0.2%) and one without C doping in the base have been annealed at different RTA temperatures. The slope for the sample with C doping is, within the accuracy of the measurement, constant. TED of B is completely suppressed in this structure. Electrical measurements suggest no negative influence of carbon on device characteristics.

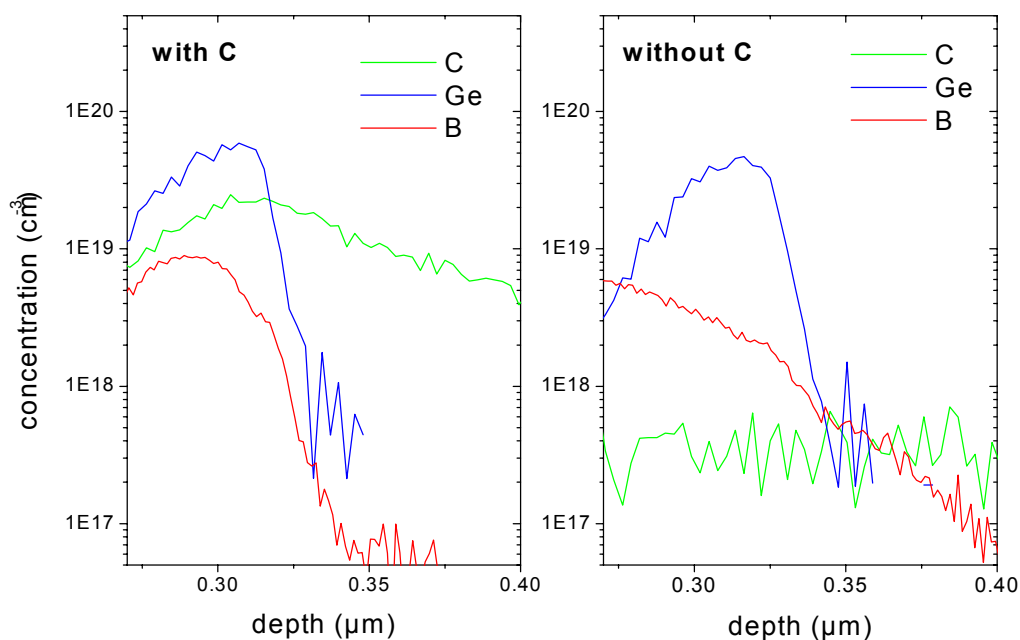


Fig. 3: Comparison of the B profile at the base-collector junction for a SiGe drift-HBT with and without carbon co-doping of the base.

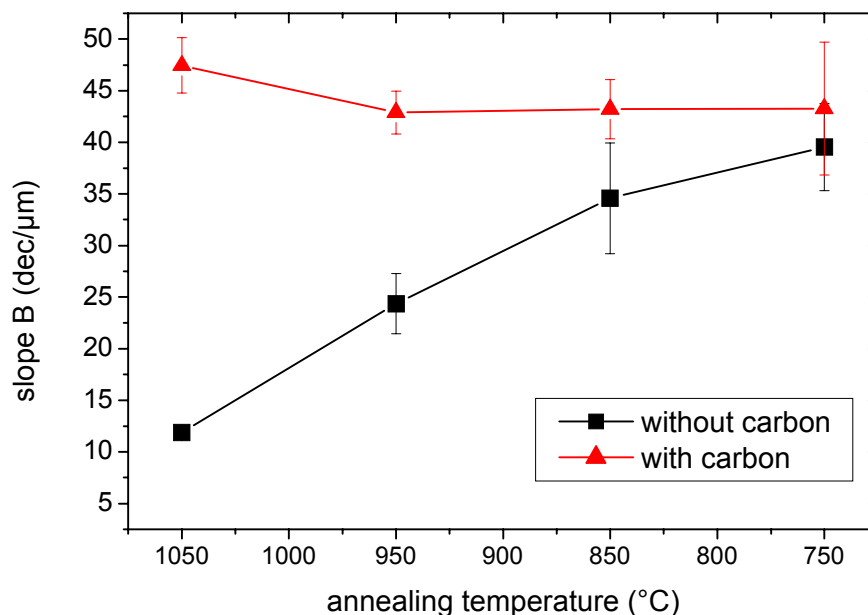


Fig. 4: Slope of the boron profile as a function of annealing temperature for the sample with and without C doping.

5. Conclusions

Quantitative measurements of substitutional carbon and SiC were performed on MBE grown $\text{Si}_{1-y}\text{C}_y$ layers. In the IR transmission spectra, optical absorption from coherent and incoherent β -SiC was observed. The precipitation behavior of C to β -SiC in $\text{Si}_{1-y}\text{C}_y$ layers was then studied with the FTIR technique.

As a second experiment, the impact of carbon in a SiGeC HBT structure with a poly-Si emitter was studied. Complete suppression of TED of B was obtained by carbon doping of the base with 0.2% subst. C.

References

- [1] P A Stolk, H-J Gossmann, D J Eaglesham, and J M Poate, *Mat. Sci. Eng. B* **36** (1996), no. 1 – 3, p. 275.
- [2] J W Strane, H J Stein, S R Lee, S T Picraux, J K Watanabe, and J W Mayer, *J. Appl. Phys.* **76**, no. 6, p. 3656.
- [3] R Scholz, U Gösele, J-Y Huh, and T Y Tan, *Appl. Phys. Lett.* **72** (1998), no. 2, 200.

RF Radar Systems

C. G. Diskus¹, A. Stelzer²

¹ **Microelectronics Institute, Johannes Kepler University,
Altenberger Straße 69, 4040 Linz, Austria**

² **Institute for Communications and Information Engineering
Johannes Kepler University, Altenberger Straße 69, 4040 Linz, Austria**

After a treatment of standard radar techniques the development of a radar sensor capable of measuring distance with 0.1 mm accuracy is presented. The operating frequency of the front-end is 34 – 36 GHz. The proposed prototype sensor makes use of some new techniques such as direct homodyne receiving and direct frequency measurement.

1. Introduction

The driving force in the field of radar technology has always been the development of military equipment. Especially during the Second World War the existence of operational radar sensors was crucial and fostered research. But the same is true for today's military R&D. Nevertheless, the end of the Cold War had a strong impact on the financial situation of the microwave industry forcing the opening of commercial markets.

Another reason for the rapid growth of the commercial radar market is the availability of microelectronic devices. A radar front-end is no longer a clumsy waveguide device but can be realized in a rather compact way. In addition, new manufacturing processes reduced the cost of such sensors significantly.

1.1 Frequency Allocation

One fundamental problem of every industrial radar application is the limited bandwidth. The resolution of a radar sensor is inversely proportional to the bandwidth. The frequencies that can be used by industrial sensors are restricted to the so called ISM-bands (industrial, scientific, medical). Table 1 shows the allocation of these frequencies.

1.2 Resolution and Accuracy

In contrast to the commonly used nomenclature the word resolution has a different meaning when used in connection with radar techniques. Converting a voltage to a number using an A/D-converter quantizes the information with the least significant digit being the resolution.

The resolution of a radar sensor is defined similar to the resolution of an optical microscope. It quantifies the minimum distance between two resolvable targets. For this reason, the accuracy of a radar measurement of a single target is usually much better than the resolution.

ISM-Band	Frequency range	Bandwidth	Resolution
1	26,957 – 27,283 MHz	326 kHz	460 m
2	40,660 – 40,700 MHz	40 kHz	3750 m
3	433,050 – 434,790 MHz	1,74 MHz	86 m
4	868,000 – 870,000 MHz	2 MHz	75 m
5	2,400 – 2,483 GHz	83 MHz	1,8 m
6	5,725 – 5,875 GHz	150 MHz	1 m
7	24,000 – 24,250 GHz	250 MHz	600 mm
8	61,000 – 61,500 GHz	500 MHz	300 mm
9	122,000 – 123,000 GHz	1 GHz	150 mm
10	244,000 – 246,000 GHz	2 GHz	75 mm

Table 1: ISM-Bands [1] and corresponding radar resolution.

2. Radar Principles

The two physical effects mainly used for measurements are (1) the Doppler effect, which allows the determination of the speed of a target, and (2) the propagation time of a wave for determining the distance to a target. Additional information can be obtained by evaluating other physical effects as attenuation, phase change, or rotation of the polarization plane.

Two different sensors were built at the Microelectronics Institute. A low cost speed sensor [2] using a microwave oscillator [3] and an InGaAs/GaAs detector diode [4] both developed in-house and a high end distance radar capable of measuring distance with an accuracy of 0.1 mm.

3. High Accuracy Distance Radar

On the initiative of the VOEST Alpine Stahl AG a highly accurate level sensor was developed. Due to the rather harsh environment in a steel plant laser sensors do not work satisfactorily, so applying microwaves was the technology of choice. This distance radar should be part of a closed loop control guaranteeing a constant level of liquid steel in a crucible.

3.1 Specifications

Not only the high temperature and the existence of fumes make the design of such a sensor challenging but also the demand for fast measurement cycles. The distance range is 0.5 to 1 m, the accuracy specification 0.1 mm. The sensor will be placed inside a metallic enclosure which allows sweeping the frequency over a larger bandwidth than specified in the ISM-bands.

3.2 Sensor Prototype

As a trade-off between accuracy and costs the frequency of operation was chosen to be 34 to 36 GHz. In this range most devices are commercially available with the exception of direct frequency counters.

To achieve the high accuracy the combination of two modes of operation is necessary: (1) a phase evaluation of the reflected wave at a constant frequency and (2) an analysis of a linear sweep (FM-CW ... frequency modulated continuous wave). The phase measurement, which is unambiguous within a quarter of a wavelength, supplies the high accuracy while the coarse FM-CW measurement gives an absolute distance reading.

There are two possibilities of realizing a radar front-end: The conventional way is the application of a highly stable and, hence, expensive signal source. It is not only the stability of the frequency which is an issue but also the possibility of producing a very linear frequency sweep. This is essential for obtaining an accurate distance value using the FM-CW mode. By contrast, the signal source of the presented prototype sensor is a cost-effective varactor tuned Gunn oscillator (VCO ... voltage controlled oscillator). The controlling bias of the varactor is provided via a digital/analog converter by a digital signal processor (DSP). After characterizing the control characteristic of the VCO by means of sweeping through the full bandwidth and recording the actual frequency, the generation of a precisely linear sweep is possible. Details of the direct frequency counter were published in [5]. A photograph of the whole radar set-up is shown in Fig. 1.

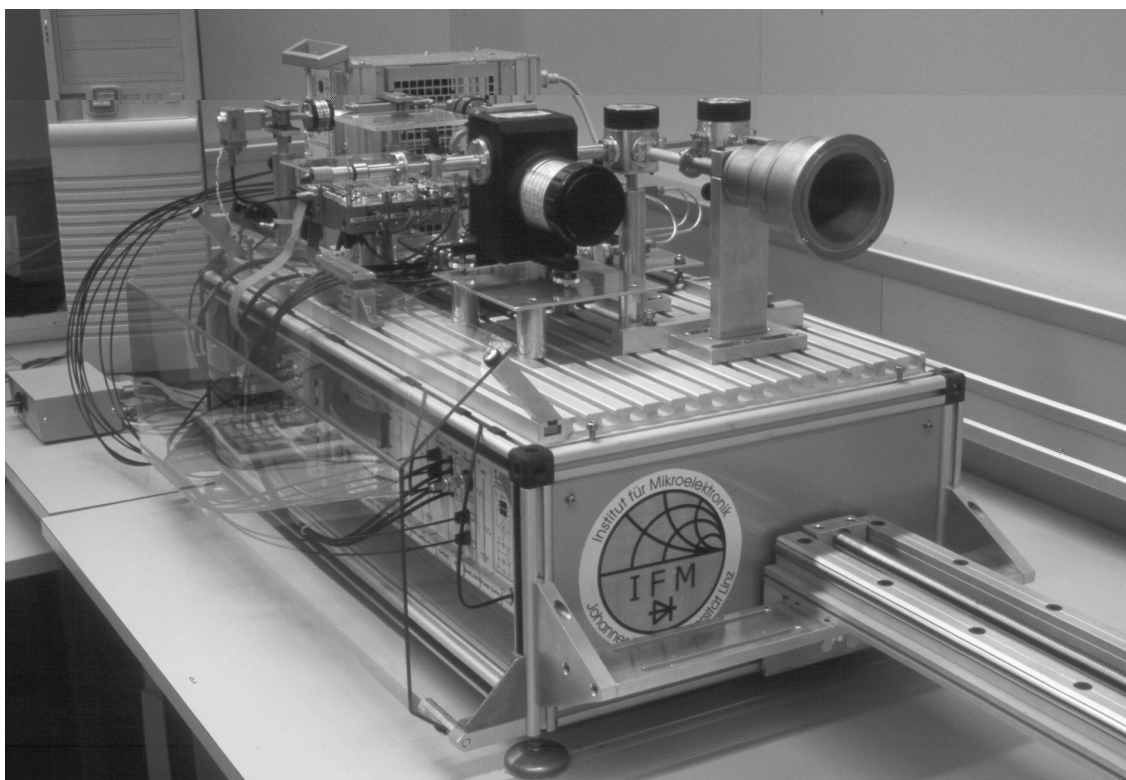


Fig. 1: Radar prototype consisting of waveguide and coaxial components.

The receiving part of the radar front-end is a so called six-port. This device has been used more and more since the early 1970's [6] in laboratories and research establishments and represents an attractive alternative to a conventional heterodyne receiver. The six-port technique is primarily used for measuring magnitude and phase of a received wave. In the proposed sensor the six-port allows measuring the phase of the reflected wave with respect to the incident wave with an accuracy of ± 3 degrees which corresponds to about one hundredth of a wavelength.

3.3 Results

The distance measurement is accomplished in two steps. Firstly, a linear frequency sweep is applied yielding the absolute distance with an accuracy of ± 1 mm. Note that the resolution of an FM-CW measurement with 2 GHz bandwidth is about 75 mm. Secondly, a constant 35.1 GHz signal is transmitted and the phase of the reflected wave is evaluated. This enhances the accuracy of the distance measurement to ± 0.1 mm. The stability of the distance reading is one order of magnitude better [7].

Due to the application of a direct frequency counter the measurement cycle of a 20 bit frequency measurement is 120 μ s. These time steps are only necessary for calibrating the VCO. The cycle time during the FM sweep (open loop control) is 6 μ s.

4. Conclusion and Outlook

The proposed prototype sensor makes use of some new techniques such as direct homodyne receiving and direct frequency measurement. With these features the sensor operating in the 34 – 36 GHz range is capable of measuring distance with ± 0.1 mm accuracy. Future work will concentrate on shrinking the sensor set-up by integrating the six-port and the detector diodes on GaAs.

Acknowledgements

The authors would like to thank K. Lübke and E. Kolmhofer for their support. The technical assistance of J. Katzenmayer and M. Hinterreiter is also greatly acknowledged. The presented projects were supported in part by the Austrian Science Foundation (FWF) and the Upper Austrian Government.

References

- [1] A. Heuberger, V. Gehrman: „Störsichere Übertragung in den ISM-Bändern“, *Elektronik*, Nr. 19, 1999, pp. 74 – 79.
- [2] A. A. Efanov, C. G. Diskus, A. Stelzer, H. W. Thim, K. Lübke, and A. L. Springer: “Development of a Low-Cost 35 GHz Radar Sensor”, *Annales des Télécommunications / Annals of Telecommunications*, Special Issue to the International Workshop on Millimeter Waves, Vol. 52, Nr. 3-4, March-April 1997, pp. 219 – 224.
- [3] K. Lübke, H. Scheiber, H. Thim: “A Voltage Tunable 35 GHz Monolithic GaAs FECTED Oscillator”, *IEEE Microwave and Guided Wave Letters*, Vol. 1, No. 2, Feb. 1991, pp. 35 – 37.
- [4] C. G. Diskus, A. Stelzer, K. Lübke, H. W. Thim: “A Ka-Band Detector Diode with High Sensitivity”, Proceedings of the Seminar *Current Developments of Microelectronics 1999*, GMe, March 3 – 6, 1999, Bad Hofgastein, pp. 29 – 33.
- [5] A. Stelzer, C. G. Diskus, K. Lübke: “Fast Frequency Measurement Applied to a Microwave Distance Sensor”, The Society for Microelectronics (Gesellschaft für Mikroelektronik - GMe), *Annual Report 1999*, Vienna, May 2000, pp. 103 – 106.

-
- [6] G. F. Engen: "Application of an Arbitrary 6-Port Junction to Power-Measurement Problems", *IEEE Transactions on Instrumentation and Measurement*, Vol. IM-21, No. 4, Nov. 1972, pp. 470 – 474.
 - [7] A. Stelzer, C. G. Diskus: "A Ka-Band Distance Sensor with 0.1 Millimeter Accuracy", *Proceedings of 2000 Asia Pacific Microwave Conference (APMC 2000)*, Dec. 3 – 6, 2000, Sydney, Australia, Vol. 1, pp. 465 – 468.

Simulation and Circuit Design

Simulation of Semiconductor Devices and Circuits at High Frequencies

Tibor Grasser

Institute for Microelectronics, TU Wien
Gusshausstraße 27–29, 1040 Wien, Austria

Due to the rapid progress in semiconductor technology, device sizes could be continually decreased during the last decades. This reduction allows for a higher package density which in turn increases the demands on modern simulation tools. This article covers some of the recent advances on the fields of device, circuit, and interconnect simulation which are fundamental requirements for accurate simulation of state-of-the-art circuits.

1. Introduction

With shrinking device dimensions device and circuit simulations with distributed devices need to be carried out by state-of-the-art tools, accounting for physical effects on a microscopic level. Several questions during device fabrication, such as device optimization and process control, can today be addressed by device simulation. For circuits operated in the GHz regime the influence of the interconnect structure becomes very important, and accurate simulation of the resulting parasitics is a must.

2. Device Simulation

To enable predictive simulation of semiconductor devices proper models describing carrier transport are required. The classic drift-diffusion transport model [1] is by now the most popular model used for device simulation. However, with down-scaling of the feature size, non-local effects become more pronounced and must be accounted for by using energy-transport or hydrodynamic models [2].

2.1 Mainstream Silicon CMOS Technology

As the driving force of today's semiconductor industry, mainstream silicon CMOS technology has attracted large attention during the last decades. The bulk of papers in the TCAD field were devoted to this subject and the behavior of the devices for not too small gate lengths is pretty well understood nowadays. For deep submicron devices with $L_g < 0.25 \mu\text{m}$, however, several second-order effects increase in importance and can no longer be neglected in an accurate simulation. Among these effects are quantum mechanical effects (quantization in the channel and tunneling through the oxide) and hot-carrier effects (non-local behavior and impact ionization) which further complicate the simulation.

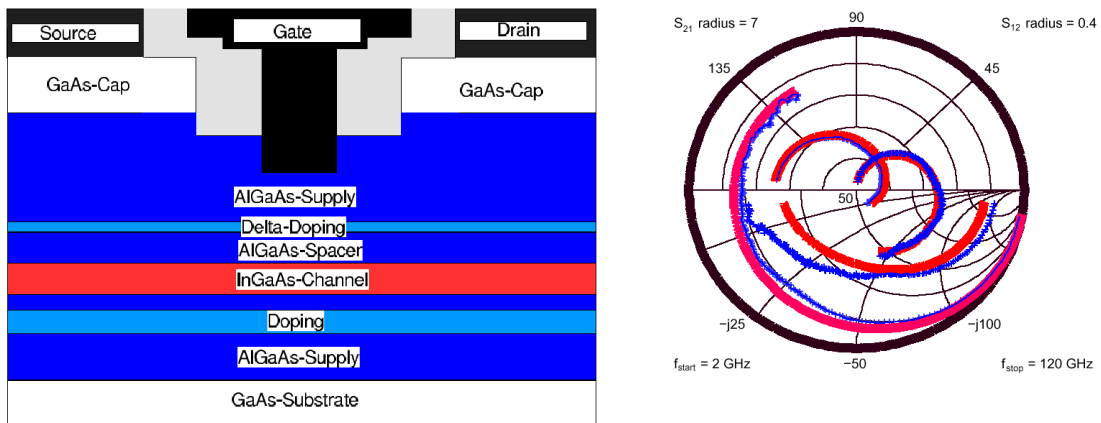


Fig. 1: Geometry of a HEMT and simulated (red / light gray) and measured (blue / dark gray) S-parameters ($L_g = 140$ nm).

2.2 High-Frequency Devices

Especially for high-frequency applications, SiGe and III-V heterostructure bipolar transistors (HBTs) and GaAs based high-electron mobility transistors (HEMTs) are being considered. The simulation of these devices is a challenging task with many issues still not satisfactorily solved. An important issue remains the proper modeling of heterostructure interfaces which can only be adequately dealt with when the quantum mechanical nature of the carriers is considered. A typical pseudomorphic InGaAs/AlGaAs HEMT on GaAs substrate with $L_g = 140$ nm is shown in Fig. 1 together with a comparison of the simulated and measured S-parameters at $T_L = 373$ K. These devices gain increasing importance for low noise applications like 77 GHz automotive collision avoidance radar. The parasitic elements were extracted from the measurements, and no fitting on device-level was employed. To obtain such an excellent agreement, many effects like energy relaxation, impact ionization, gate currents and self-heating must be modeled carefully.

3. Circuit Simulation

Circuit simulation has been traditionally performed using compact models of the individual devices. The most prominent program based on compact models is definitely SPICE which is being widely used. However, development of a compact model is a very complex task and requires permanent refinement to keep pace with modern technology developments. Even standard devices like MOS transistors are often only poorly described using these compact models. One of the most elaborate models is the BSIM3v3 [3] model which has been under continuous development throughout the last decade. While calibrating the model to measured data we found that the model failed for a device with $L_g = 0.13$ μm , even though accurate results have been obtained for $L_g = 0.25$ μm . Simulation results obtained by the compact model and a realistic device simulation are shown in Fig. 2 for the $L_g = 0.13$ μm device. As can be seen, the sub-threshold region is only poorly reproduced by the compact model but poses no problems to the device simulation. This region is very critical for low-power applications, and an accurate description is therefore mandatory.

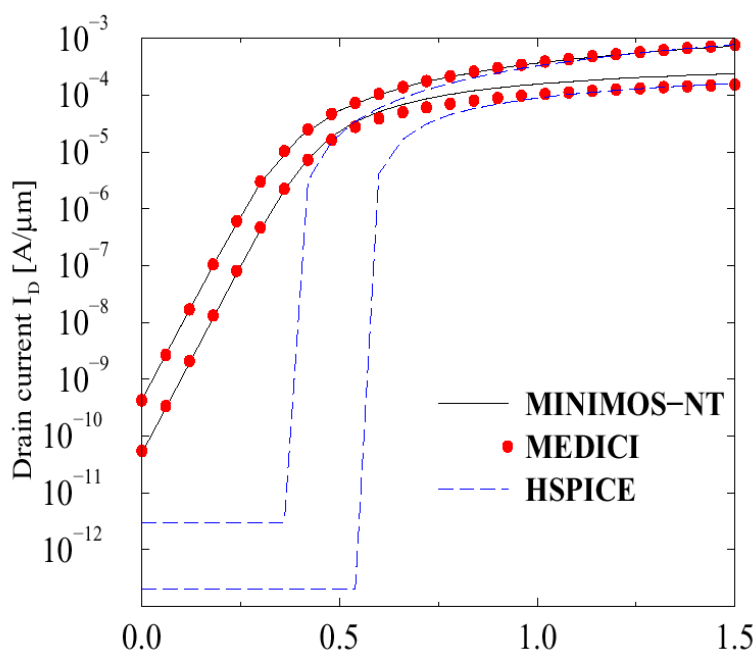


Fig. 2: Comparative simulation of a 0.13 μm NMOS I_d - V_g characteristics at $V_{DS} = 0.1$ V and $V_{DS} = 1.5$ V.

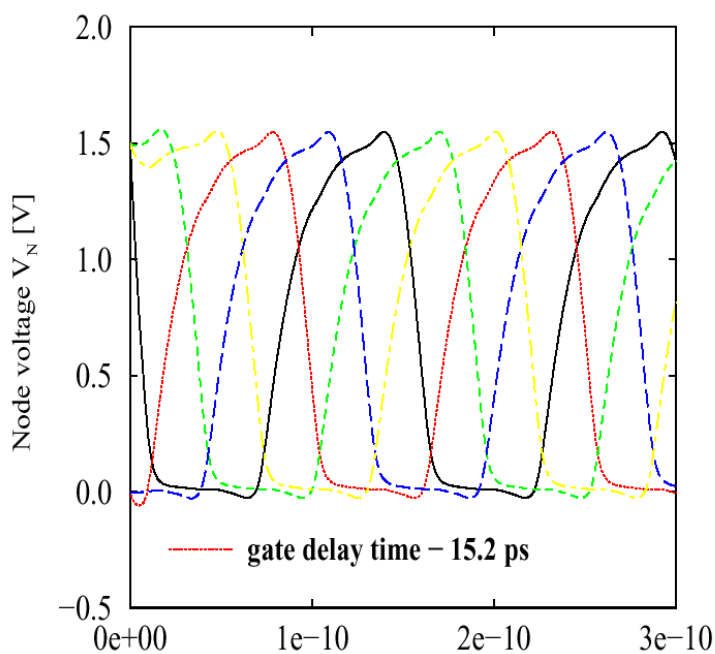


Fig. 3: The simulated node voltages of a five stage ring oscillator created with 0.13 μm technology

Mixed-mode device/circuit simulation provides a solution for this problem for up to medium-sized circuits. A typical example is the simulation of ring-oscillators which are commonly fabricated on test-wafers to investigate the high-frequency performance of the devices. Simulated node voltages of such a ring-oscillators are shown in Fig. 3 for the circuit of Fig. 4. The device simulator has been calibrated for a 0.25 μm technology

and used for a predictive simulation of $0.13\ \mu\text{m}$, a feature not offered by compact models. The simulated inverter delay time of $15.2\ \text{ps}$ is well within the scattering range of the measured data.

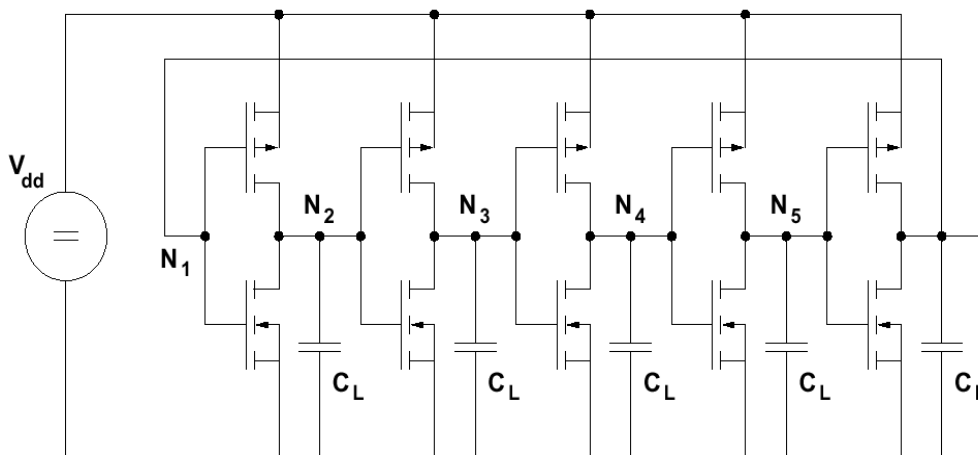


Fig. 4: Schematics of a five stage ring oscillator.

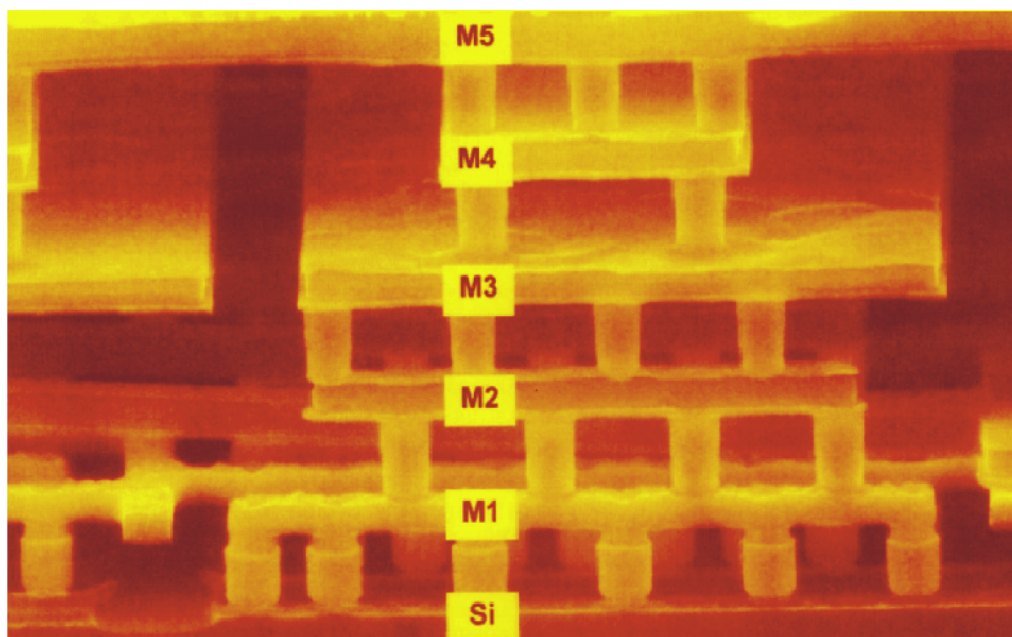


Fig. 5: Typical interconnect structure

4. Interconnect Simulation

Down-scaling of integrated circuits to the deep sub-micron regime increases the influence of interconnects on circuit behavior [4]. As devices are getting faster and line widths get smaller parasitic effects of the interconnects become the limiting factor for

further improvements in circuit speed. With clock frequencies in the GHz regime, integrated circuits will behave more and more like microwave circuits [5]. During the design phase care must be taken on various parasitic effects, like attenuation caused by resistive voltage drops, self-heating due to losses, delay times, crosstalk (caused by capacitive or inductive coupling or by the substrate), reflections incurred by discontinuities, skin-effect and eddy currents (e.g. in on-chip spiral inductors). A typical interconnect structure is shown in Fig. 5 which utilizes five metal layers. Extraction of the parasitic elements by means of simple analytical models yields rather unsatisfactory results, and a numerical simulation should be used instead. Highly satisfactory results for the generally very complex structures have been obtained using the finite element method. Simulated isopotential surfaces together with the extracted capacitances are shown in Fig. 6. A fully-coupled three-dimensional interconnect/device simulation would require too large amounts of computer memory and CPU time to be feasible from an engineering point of view. Thus, the parasitic elements are extracted and used for a mixed-mode device/circuit simulation.

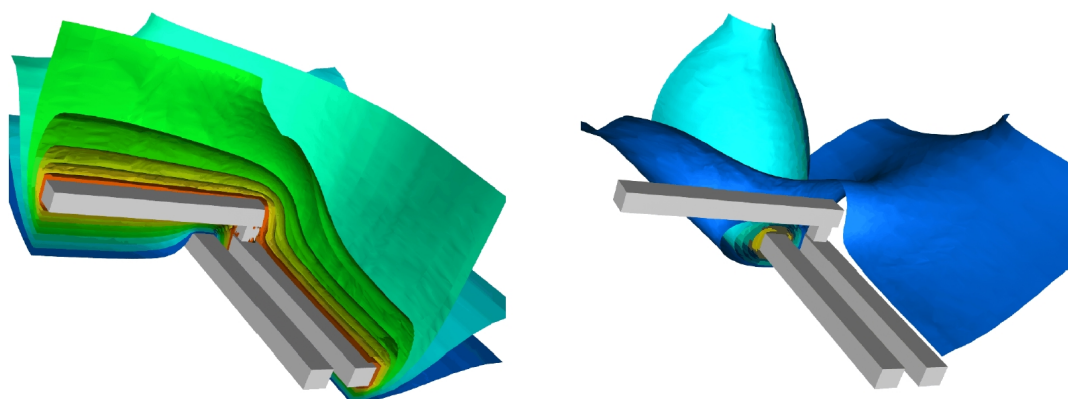


Fig. 6: Simulated isopotential surfaces of a typical interconnect structure ($C_{1,2} = 0.52$ fF, $C_{1,GND} = 1.04$ fF, $C_{2,GND} = 1.15$ fF).

Acknowledgements

The work is supported by Infineon Technologies AG, Munich, Germany, by LSI Logic Corporation, Santa Clara, USA, by the Fraunhofer Institute of Applied Solid-State Physics, Freiburg, Germany and by the “Christian Doppler Forschungsgesellschaft”, Vienna, Austria.

References

- [1] S. Selberherr, "Analysis and Simulation of Semiconductor Devices", Springer, Wien – New York, 1984.
- [2] W. Hänsch, "The Drift Diffusion Equation and its Application in MOSFET Modeling", Springer, Wien – New York, 1991.
- [3] Y. Cheng, M.-C. Jeng, Z. Liu, J. Huang, M. Chan, K. Chen, P.K. Ko, and C. Hu, "A Physical and Scalable I-V Model in BSIM3v3 for Analog/Digital Circuit Simulation", *IEEE Trans. Electron Devices*, vol. 44, no. 2, pp. 277 – 287, 1997.

- [4] A.K. Goel, "High-Speed VLSI Interconnections", *John Wiley & Sons*, New York, 1994.
- [5] N. P. van der Meijs and T. Smedes, "Accurate interconnect modeling: Towards multi-million transistor chips as microwave circuits", in *Proc. Intl. Conf. Computer Aided Design*, San Jose, CA, USA, Nov. 1996, pp. 244 – 251, IEEE.

Systemsimulation und Messungen an hochauflösenden Sigma-Delta Modulatoren

Peter Söser

Institut für Elektronik, TU-Graz
Inffeldgasse 12, 8020 Graz, Austria

Sigma-Delta (SD) Modulatoren stellen den wesentlichen Bestandteil von monolithisch integrierten SD-Analog/Digital-Umsetzern (SD-ADU) dar. Es gibt eine Vielfalt von Realisierungsvarianten für solche Modulatoren. Kriterien für die Auswahl sind neben der Komplexität vor allem die gewünschte Auflösung und die maximal umsetzbare Signalfrequenz. Eine Erhöhung der Auflösung erfordert eine Erhöhung der Ordnung des SD-Modulators. Mit einfachen Mitteln kann für eine derartige Architektur aber keine Aussage über die tatsächlichen Eigenschaften gemacht werden. Es bedarf einer Simulation auf Systemebene, um eine Charakterisierung vornehmen zu können. Dabei ist es notwendig, die in der Realität vorhandenen Nichtidealitäten der verwendeten Funktionsblöcke (Kondensatoren, Schalter, Operationsverstärker, Komparatoren etc.) mit zu berücksichtigen.

Am Institut für Elektronik der TU Graz wurde in einer Diplomarbeit, die in Zusammenarbeit mit der Firma *Austria Mikro Systeme International AG*. durchgeführt wurde, eine Modellierung dieser Nichtidealitäten erarbeitet. Sie wurde in der Simulationsumgebung MATLAB[®]/SIMULINK[®] implementiert, womit vernünftige Simulationszeiten und eine praktikable Auswertung der Ergebnisse möglich waren.

Um die Brauchbarkeit der Modellierung zu untersuchen wurde ein in 0,6 μm CMOS-Technologie realisierter Modulator 4-ter Ordnung mit einer nominellen SINAD (signal-to-noise and distortion) von 120 dB (entspricht einer Auflösung von 19,64 bit) auf Systemebene simuliert und diese Ergebnisse mit Messungen verglichen, die ebenfalls im Rahmen dieser Diplomarbeit durchgeführt wurden. Dabei konnte eine gute Übereinstimmung zwischen Simulation und Messung nachgewiesen werden.

Wann mi des Designbüro net vermittelt hätt' — Ein Erfahrungsbericht über 10 Jahre Technologietransfer

N. Kerö¹, T. Sauter², G. Cadek¹, H. Nachtnebel¹

¹ Institut für Industrielle Elektronik und Materialwissenschaften, ASIC-Design, TU Wien

² Institut für Computertechnik, TU Wien
Gusshausstraße 27–29, 1040 Wien, Austria

Obwohl zahlreiche nationale und europäische Förderprogramme den industriellen Einsatz von Integrationstechnologien und damit verbunden neue Entwurfsmethoden stimulieren sollten, blieb der Erfolg in Österreich bisher hinter den Erwartungen zurück. Dieser Artikel analysiert die Gründe dafür und schlägt neue Strukturen vor, um die Situation in Zukunft zu verbessern.

1. Was bisher geschah

Bei der Verfassung von Förderungs-Anträgen wird oft und gerne eine zentrale Motivation zitiert: Der Einsatz von Integrationstechnologien (ASICs – Application Specific Integrated Circuits, MCMs – Multi Chip Module, Mikrosysteme) in österreichischen Klein- und Mittelbetrieben bleibt weit hinter den technischen Möglichkeiten, aber auch Erwartungen sowohl von Experten als auch fördernden Stellen zurück. Vorschnell werden für dieses Problem immer wieder dieselben Gründe genannt:

- Mangelnde Ausbildung an Fachhochschulen und Universitäten;
- Mangelnde Weiterbildungsmöglichkeiten für die Industrie;
- Zu wenig Information über neue Technologien, deren Einsatzmöglichkeiten und Entwurfsmethoden;
- Mangelnde unabhängige Beratungsangebote;
- Der Einsatz moderner Technologien lohnt sich auf Grund der hohen Investitionskosten und der geringen Produktionsstückzahlen nicht.

Noch vor fünf bis zehn Jahren waren diese Argumente größtenteils berechtigt und gültig. Nationale und europäische Förderprogramme haben seither aber wesentliche Verbesserungen gebracht. An allen namhaften österreichischen Universitäten (TU Wien, TU Graz, Universität Linz) und Fachhochschulen (FH Villach, FH Wien 22 und andere) werden seit einigen Jahren moderne Ausbildungsmöglichkeiten auf dem Gebiet des computerunterstützten Entwurfs elektronischer Schaltungen und Systeme angeboten.

Losgelöst von der akademischen Grundausbildung bieten einige Gruppen zusätzlich praxisnahe Weiterbildungskurse für die Industrie zu allen relevanten Themen (Entwurf und Verifikation elektronischer Schaltungen mit den Hochsprachen VHDL und Verilog, ASIC-Projektmanagement, FPGA-Design, Analoges ASIC-Design).

Auch das Argument der mangelnden Information und Beratung ist längst nicht mehr anwendbar. High-Tech-Beratung – durch regionale Wifis gefördert – wird allen Unternehmen regelmäßig angeboten. Diese Beratungen werden zumeist von Universitäten durchgeführt und bieten damit ein Höchstmaß an Unabhängigkeit. Die Erfahrung zeigt allerdings, dass derartige Angebote trotz großer Werbeanstrengungen oft nur zögerlich angenommen werden.

Am schwierigsten ist dem letzten Argument, der Unwirtschaftlichkeit von ASICs für KMUs, zu begegnen. Die von den Autoren mehrfach mit Erfolg gewählte und bewährte Vorgangsweise bei der Initiierung von Designprojekten besteht aus mehreren Stufen:

- Halb- bis ganztägiges technisches Consulting (meist vollständig gefördert), mit dem Ziel, vorwiegend Entwicklungsingenieure über die Möglichkeiten und technischen Randbedingungen von Integrationstechnologien zu informieren, aber auch aktuelle Probleme und Fragen (Möglichkeiten moderner Simulationswerkzeuge, Leistungsfähigkeit programmierbarer Logikbausteine ...) zu beantworten.,
- Vorstellung neuer Technologien, um namentlich den Entscheidungsträgern einen Überblick über den Stand der Technik zu geben und sie besser in die folgenden Prozesse einbinden zu können,
- Analyse des Produkt-Portfolios der Firma auf den möglichen Einsatz von Integrationstechnologien im Hinblick auf technische Machbarkeit, aber auch unter Einbeziehung aller wirtschaftlichen Randbedingungen (Hard- und Softwareinvestitionen, Training der Ingenieure, Zeitplan für die Entwicklung, erforderliche Partnerschaften mit externen Designhäusern und ASIC-Herstellern, Kosten für die Prototypenherstellung, Zeit- und Kostenplan für die Überführung in die Serie etc.).

Firmen, die bislang noch keine Erfahrungen im Einsatz von Integrationstechnologien hatten, sind mit dem komplexen und teils langwierigen Ablauf solcher Projekte oft überfordert. Insbesondere gilt das für die Koordination der unterschiedlichen involvierten Partner (internes und externes Designteam, Hersteller, ev. Testzentrum). Für ein erfolgreiches Projekt ist daher von entscheidender Bedeutung, dass ein erfahrener Ansprechpartner zusammen mit der Firma das Projekt koordiniert und begleitet. Der Know-how-Transfer ergibt sich dann im Idealfall zwangsläufig aus dem „Learning by Doing“.

Die eben beschriebene Vorgangsweise ist zwar sicherlich die aufwendigste Form des Technologie-Transfers, aber wie die Teilnahme an zwei erfolgreichen EU-Projekten (EURO-FORM-TTI, EUROFORM-ETI, beide im Leonardo-Programm) eindrucksvoll gezeigt hat, der einzig erfolgversprechende Weg.

Auf keinen Fall unerwähnt bleiben darf die Tatsache, dass erfolgreicher Technologietransfer auf dem Gebiet der Mikroelektronik nur durch industriell erfahrene Entwicklungsingenieure durchgeführt werden kann, die ihr Wissen durch die ständige Nutzung aller relevanten CAD-Werkzeuge auf den neusten Stand der Technik halten. Auf Grund der hohen Investitions- und Betriebskosten können solche Zentren nicht von universitären Ausbildungsstellen alleine getragen werden. Es sind daher langfristige Förderaktivitäten zwingend erforderlich. In Österreich wurden Gruppen an der TU Wien, der TU Graz, der Universität Linz und der FH Villach in den letzten Jahren großzügig durch Bund, Länder und Gemeinden unterstützt. Allen Förderern sei an dieser Stelle herzlich gedankt.

2. Was zukünftig geschehen sollte

In den letzten Jahren wurden zwar alle wesentlichen Voraussetzungen für österreichische Betriebe geschaffen, moderne Integrationstechnologien in Produkte umzusetzen: kompetente, unabhängige Beratung, umfangreiche Fortbildungsmöglichkeiten, Zugang zu kostengünstiger Prototypen- und Kleinserienfertigung über das EU-Projekt EURO-PRACTICE; dennoch konnten sich ASICs nur unzureichend als etablierte Standardtechnologie durchsetzen.

Das letzte verbleibende Hindernis stellen sicherlich die für den Entwurf zwingend erforderlichen CAD-Werkzeuge dar. Diese Programmpakete werden zwar immer leistungsfähiger, damit verbunden aber auch immer teurer und aufwendiger zu beherrschen. Nachhaltige Produktentwicklung ist damit zwangsläufig mit sehr hohen Eigeninvestitionen und vom Unternehmen selbst schwer einschätzbaren Aus- und Weiterbildungskosten verbunden. Für KMUs, die erstmalig vor der Entscheidung stehen, ein Designprojekt mit solchen Werkzeugen durchzuführen, sind diese hohen Einstiegskosten extrem abschreckend. Daher schlagen wir eine Struktur vor, wie sie in Abb. 1 gezeigt wird. Im Mittelpunkt der Beziehungen unterschiedlicher, an einem Designprojekt beteiligter Partner steht ein Technologie-Transfer-Zentrum, das während des gesamten Projekts als einziger, zentraler Ansprechpartner für das Unternehmen agiert, wodurch komplizierte Kommunikationsabläufe und Verantwortlichkeiten in einem für das Unternehmen ungewohnten Gebiet entfallen. Das Transferzentrum unterstützt das Unternehmen bis zur Überleitung in die Serienproduktion, die jedoch in direkter Kommunikation mit dem IC-Hersteller erfolgt.

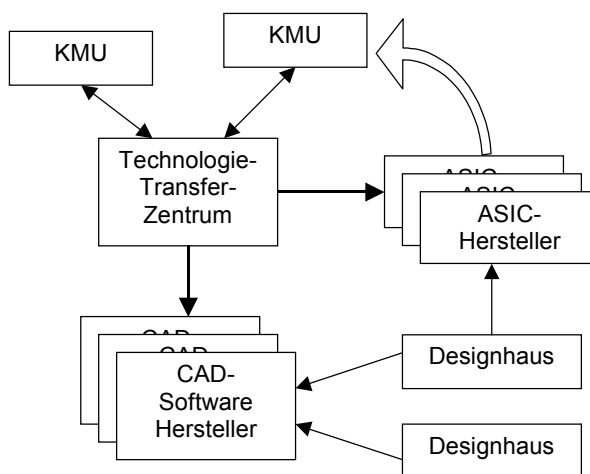


Abb. 1: Ein Technologie-Transfer-Zentrum als Mittelpunkt unterschiedlicher, an einem Designprojekt beteiligter Partner.

Für einen erfolgreichen Technologie-Transfer reichen die oben bereits angeführten Maßnahmen jedoch nicht aus. Seitens des Technologie-Transfer-Zentrums ist auch der ständige Betrieb eines eigenen Design-Zentrums erforderlich, das KMUs besonders in der ersten Phase eines Projekts die gesamte Entwicklungs-Infrastruktur (Hard- und vor allem Software, sowie erfahrene ASIC-Designer) zur Verfügung stellt. Dadurch werden mögliche Einstiegshürden (aufwendige Installation der Software, langwierige und teure Schulung) abgebaut. Zwingende Voraussetzung ist jedoch eine Förderung dieser Aktivität durch die öffentliche Hand, da die notwendige Infrastruktur allein durch Consulting-Aktivitäten nicht finanzierbar ist. Die zweite Bedingung ist eine aktive Beteiligung

großer EDA-Softwarehersteller durch eine neue, für KMUs und Start-Ups attraktive Preisgestaltung für die Durchführung des tatsächlichen Designs.

Kommerzielle Designhäuser ohne aktive Beteiligung an Technologie-Transfer-Förderprogrammen sehen wir im vorgestellten Modell nicht als Konkurrenten, sie werden vielmehr vom Transferzentrum bei Bedarf als externer Partner zur professionellen Bearbeitung spezieller Aufgaben eingebunden (Entwurf analoger Module, Smart-Power, RF-Design etc.).

Das Funktionieren eines solchen "One-Stop-Shops" für ASIC-Design wurde anhand konkreter Projekte bereits nachgewiesen. Der zukünftige Erfolg hängt aber letztlich von neuen, flexiblen Lizenzmodellen der CAD-Software-Hersteller ab, deren traditionelle Hauptkunden größere Betriebe mit entsprechend hohen Budgets für EDV-Infrastruktur sind. Sofern große Software-Hersteller von dieser Initiative überzeugt werden können, wäre der Einsatz von Integrationstechnologien für KMUs eine attraktive Alternative mit zuverlässig abschätzbarem Investitionsrisiko und kalkulierbarer Entwicklungszeit.

GMe Presentations – Posters Cleanroom Vienna

Kontrastmechanismen in der Rasterkapazitätsmikroskopie und der Einfluss der Dotierung auf die Signalgröße

B. Basnar¹, S. Golka¹, E. Gornik¹, B.Löffler², M.Schatzmayer²,
H.Enichlmair², J. Smoliner¹

¹ Institut für Festkörperelektronik, TU Wien,
Floragasse 7, 1040 Wien, Austria

² Austria Mikro Systeme International AG,
Schloss Premstätten, 8141 Unterpremstätten, Austria

Die Rasterkapazitätsmikroskopie (Scanning Capacitance Microscopy, SCM) ist eine Abart der Rasterkraftmikroskopie, bei der die Probe mit einer feinen metallisch leitfähigen Nadel abgetastet und simultan die Topographie und die lokale Kapazität gemessen wird. Aus der lokalen Kapazität zwischen Nadel und Probe kann die lokale Dotierstoffkonzentration im Halbleiter bestimmt werden.

In dieser Arbeit werden die physikalischen Prozesse untersucht, welche für den dotierungsabhängigen Kontrast in der Rasterkapazitätsmikroskopie verantwortlich sind. Auf mittels CVD hergestellten stufenförmigen Dotierprofilen in Silizium konnte gezeigt werden, dass nur dann ein monotonen Verhalten des SCM Signals in Abhängigkeit von der Dotierung besteht, wenn die äußere Spannung so eingestellt wird, dass sich die Probe in „accumulation“ oder „depletion“ befindet. Im Übergangsbereich ist das Verhalten nicht monoton, sodass je nach angelegter Spannung jede beliebige Dotierung das maximale SCM-Signal erzeugen kann. Es konnte weiterhin gezeigt werden, dass das beobachtete Verhalten in guter Übereinstimmung mit der konventionellen Theorie des Metall-Oxid-Halbleiterübergangs erklärt werden kann.

Coherent Terahertz Emission from Optically Pumped Parabolic Quantum Wells

R. Bratschitsch, T. Müller, G. Strasser, K. Unterrainer

Institut für Festkörperelektronik, TU Wien,
Floragasse 7, 1040 Wien, Austria

We report on few-cycle terahertz (THz) emission from modulation-doped parabolic quantum wells. The quantum wells are optically excited by near-infrared femtosecond laser pulses. The observed THz emission corresponds to the intersubband plasmon of the parabolic quantum well. The emission frequency is independent of the number of optically generated carriers. We identify the excitation mechanism of the intersubband plasmon and hence THz emission to be ultrafast field screening. This mechanism allows for an optically driven THz emission from a completely symmetric nanostructure, in contrast to quantum beats which require a broken symmetry for their excitation.

1. Introduction

Recently, Sekine et al. [1] reported on the optically pumped emission of THz radiation from grating-coupled *intrasubband* plasmons in a doped single quantum well. We present experiments which show that *modulation doped* parabolic quantum wells (PQWs) emit coherent THz radiation corresponding to the *intersubband* plasmon when excited by near infrared femtosecond laser pulses.

2. Experimental

The samples used in the experiments are modulation doped GaAs/AlGaAs PQWs, with widths in the range of 1200 – 2000 Å and carrier sheet densities of 1.7×10^{11} – 5×10^{11} cm⁻². We perform THz autocorrelation (AC) measurements where two temporarily delayed visible femtosecond laser pulses hit the sample. The emitted THz radiation is collected by parabolic mirrors and detected by a bolometer. The Fourier transform of the recorded AC signal then gives the spectrum of the coherent radiation emitted by the source. The samples are mounted in a continuous flow cryostat to cool them to approximately 5 K, and the whole setup is purged with nitrogen gas to avoid absorption of the THz radiation by water vapor.

Figure 1 shows an AC trace of a modulation doped PQW ($W=1400$ Å, $n_{2D} = 5 \times 10^{11}$ cm⁻²) excited by 780 nm ($\tau_{FWHM} = 80$ fs) laser pulses. The density of the optically generated carriers is kept well below the carrier density inside the PQW due to the modulation doping.

The spectrum of the emitted THz radiation (inset of Fig. 1) consists of two components, a broad one around 0.8 THz and a narrow one (FWHM: 0.3 THz) with a center frequency of 2.55 THz. These two emission peaks can be observed within a wide range of excitation wavelengths (815 – 760 nm).

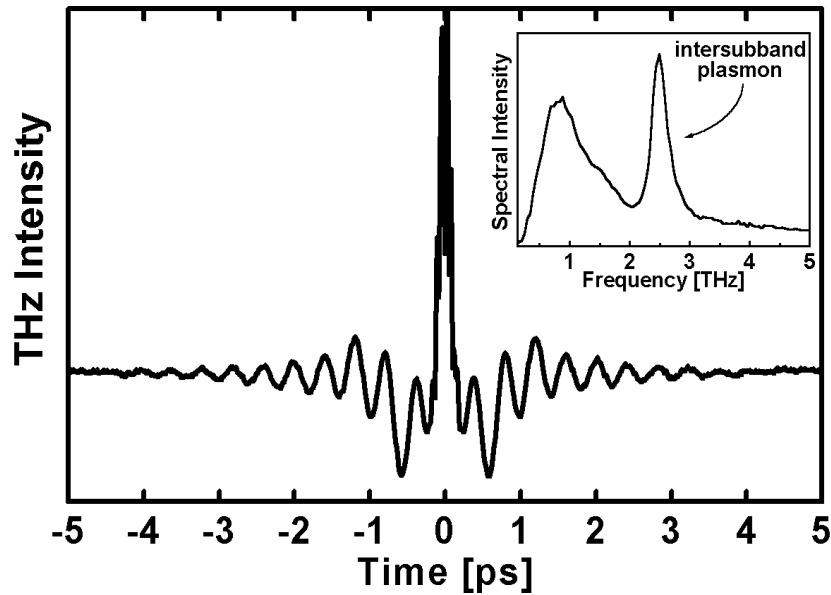


Fig. 1: THz autocorrelation signal of the 1400 Å PQW excited by 780 nm laser pulses ($T = 5$ K). Inset: Fourier transform of the recorded AC.

While the broadband component varies in frequency, the emission at 2.55 THz doesn't change. The low frequency broadband component is found with all the different PQW samples and shows roughly the same frequency dependence, i.e. it is independent of the PQW sample structure. The origin of the broadband component is due to THz generation at the surface of the sample [2].

The narrowband emission results from the oscillation of the carriers inside the PQW [3]. FTIR absorption and THz-Time Domain Spectroscopy measurements [4] show nearly the same resonance frequency of 2.2 THz which is the characteristic frequency of the intersubband plasmon of this PQW. The width of the THz emission line is as narrow as 0.2 THz for the 2000 Å PQW sample.

The excitation mechanism for the intersubband plasmon is due to screening of the surface depletion field by the electron-hole pairs injected by the ultrafast laser pulse [5]. In this way the electrons inside the quantum well experience a kick and begin to oscillate with their *eigenfrequency* (Fig. 2).

This is supported by the fact that the oscillation can be excited over a large wavelength range of the femtosecond pulses (815 – 760 nm). This large range implies that the excitation mechanism is clearly a non-resonant phenomenon, in contrast to THz quantum beat experiments. The difference between the two excitation mechanisms — quantum beats and ultrafast field screening — is also discernible when we perform THz emission experiments on an *undoped* PQW of the same width ($L = 1400$ Å). In this case no THz emission associated with the PQW can be observed, i.e. no quantum beats can be excited.

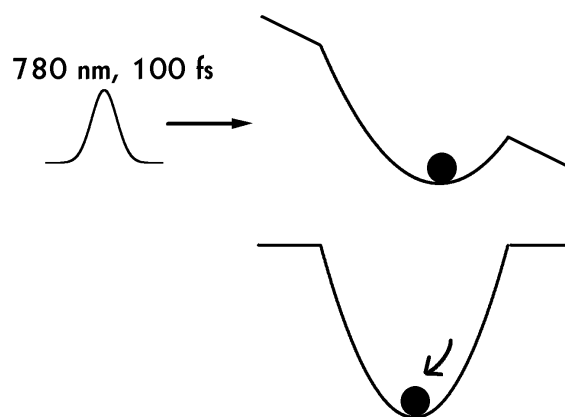


Fig. 2: Schematic drawing of the excitation mechanism: An oscillation of the carriers in the parabolic potential is initiated by ultrafast field screening.

3. Conclusion

We have demonstrated optically driven THz emission from intersubband plasmons in modulation-doped parabolic quantum wells. The excitation mechanism is due to screening of the surface depletion field by electron-hole pairs injected by an ultrafast laser pulse. Due to this non-resonant excitation mechanism, a completely symmetric nanostructure can emit optically driven THz radiation. THz emission due to quantum beats can be excluded since we observe no THz radiation from an identical but undoped PQW. The combination of the designability of the transition frequency, the narrowband emission, and the absence of any processing of the sample make modulation-doped PQWs attractive and easy-to-use THz emitters.

Acknowledgements

This work has been supported by the *Fond zur Förderung der Wissenschaftlichen Forschung* (START-Y47).

References

- [1] N. Sekine, K. Yamanaka, K. Hirakawa, M. Voßbürger, P. Haring-Bolivar, and H. Kurz: “Observation of terahertz radiation from higher-order two-dimensional plasmon modes in GaAs/AlGaAs single quantum wells”, *Appl. Phys. Lett.*, Vol. 74, 1999, 1006 – 1008.
- [2] X.-C. Zhang, B. B. Hu, J. T. Darrow, and D. H. Auston: “Generation of femtosecond electromagnetic pulses from semiconductor surfaces”, *Appl. Phys. Lett.*, Vol. 56, 1990, 1011 – 1013.
- [3] R. Bratschitsch, T. Müller, R. Kersting, and K. Unterrainer: “Coherent terahertz emission from optically pumped intersubband plasmons in parabolic quantum wells”, *Appl. Phys. Lett.*, Vol. 76, 2000, 3501 – 3503.

-
- [4] R. Kersting, R. Bratschitsch, G. Strasser, K. Unterrainer, and J. N. Heyman: “Sampling a terahertz dipole transition with subcycle time resolution”, *Opt. Lett.*, Vol. 25, 2000, 272 – 274.
 - [5] R. Kersting, K. Unterrainer, G. Strasser, H. F. Kauffmann, and E. Gornik: “Few-cycle THz emission from cold plasma oscillations”, *Phys. Rev. Lett.*, Vol. 79, 1997, 3038 – 3041.

Ultrathin Silicon Dioxide: Growth and Characterization

S. Harasek, S. Golka, J. Smoliner, E. Bertagnolli

Institute for Solid State Electronics, TU Wien,
Floragasse 7, 1040 Wien, Austria

The technology of ultrathin solid films represents a key issue in microelectronic manufacturing. The continued shrinking of lateral dimensions has to be accompanied by an appropriate reduction of vertical dimensions to control short channel effects. As far as dielectric layers are concerned, silicon dioxide remains in the center of interest. In this work we investigate silicon dioxide layers of a few nanometers thickness grown by thermal oxidation. Electrical characterization of the oxide layers is performed by capacitance-voltage and current-voltage measurements. Comparison of the measured C-V curves with simulated curves shows that the simple MOS-capacitor model used for the simulation is well applicable within the ultrathin regime.

1. Introduction

The formation and characterization of ultrathin dielectric layers is of major importance in microelectronics. Due to the continuing reduction of lateral device dimensions, scaling of the vertical dimensions is required to maintain an appropriate gate control over the channel. In the field of dielectrics silicon dioxide still is the most important material. The gate oxide thickness of MOSFET devices is about to enter the ultrathin layer regime by now. Therefore the electrical properties of ultrathin layers with a thickness of only a few nanometers are of immanent technological interest. These properties are influenced by the growth process itself and post-oxidation processing steps. In this work, ultrathin oxides were thermally grown at intermediate temperatures. The oxidized substrates were integrated into a metal-oxide-semiconductor (MOS) capacitor scheme. Electrical characteristics of ultrathin silicon dioxide were investigated by capacitance-voltage (C-V) and current-voltage (I-V) measurements. The measured C-V characteristics were compared to curves resulting from simulation based on a simple analytical MOS model.

2. Experimental

P-type silicon ($\rho = 14 \text{ } \Omega\text{cm}$) wafers were oxidized by dry thermal oxidation in pure oxygen after a thorough RCA-clean. To investigate the influence of the oxidation temperature, oxidations were carried out at temperatures from 700 to 800 °C. Oxidation times were adjusted to yield the same oxide thickness (2.8 nm) in each experiment. The oxidized substrates were covered with aluminum by thermal evaporation and patterned using optical lithography and wet etching to form gate electrodes with an area of $1.2 \times 10^{-4} \text{ cm}^2$. Al was sputtered for good backside contacts. The samples were subjected to a pre-metallization anneal at the temperature of the previous oxidation process in an inert atmosphere (N_2). The patterned samples were annealed in forming gas (post-metallization anneal) at 400 °C. Annealing times were varied from zero to a maximum

of 30 minutes. A HP 4156B semiconductor parameter analyzer and a HP 4284A LCR meter were used for electrical testing. Oxide thickness was determined from C-V curves at strong accumulation region without any correction and showed good agreement with ellipsometric thickness evaluation.

3. Simulation

In order to simulate the C-V characteristics of a MOS capacitor, the device is modeled as a series connection of a constant capacitance caused by the insulator (C_{Ox}) and the variable capacitance of the semiconductor depletion layer (C_D) [1]. C_D is accessible from (1):

$$C_D = \frac{\partial Q_S}{\partial \psi_S} \quad (1)$$

Q_S space charge
 ψ_S surface potential

The space charge is related to the electric field at the surface of the semiconductor (\mathfrak{E}_S) by (2):

$$Q_S = -\epsilon_S \mathfrak{E}_S \quad (2)$$

ϵ_S dielectric constant
of the semiconductor

Finally equation (3) describes the ideal relation between the electric field \mathfrak{E} and the potential ψ of the material:

$$\mathfrak{E}^2 = \left(-\frac{d\psi}{dx} \right)^2 = \left(\frac{2kT}{q} \right)^2 \left(\frac{qp_{p0}\beta}{2\epsilon_S} \right) \left[\left(e^{-\beta\psi} + \beta\psi - 1 \right) + \frac{n_{p0}}{p_{p0}} \left(e^{\beta\psi} - \beta\psi - 1 \right) \right] \quad (3)$$

ψ potential
 x distance from surface
 k Boltzmann's constant
 T absolute temperature
 ϵ_S dielectric constant of the semiconductor
 q elementary charge
 p_{p0} equ. density of holes
 n_{p0} equ. density of electrons
 $\beta = q/kT$

Knowing the values of C_D and C_{Ox} the overall capacitance and the voltage between gate and bulk is easily computed in dependence of the surface potential ψ_S . The exact position of the calculated curve along the voltage axis is determined from the difference in the work function of the gate metal and the silicon substrate. Since the areas of the stacked capacitors are relatively large, rim induced effects may be neglected in the simulation of the C-V characteristics.

4. Results and Discussion

The variation of the oxidation temperature shows that the C-V characteristic of the gate oxide is drastically improved if the oxidation temperature is increased. Fig. 1 shows the C-V curves of oxide layers grown at 700°C and 800°C respectively. Apart from this both samples underwent the same procedures including pre- and post-metallization anneal. The higher oxidation temperature leads to a well-behaved C-V curve with striking correspondence to the simulated characteristic (dashed line) thereby suggesting that the

simulated curve is valid as a measure of oxide quality. The oxide grown at 700°C on the other hand displays several imperfections like a shifted position along the voltage axis and a nearly constant capacitance from weak to strong accumulation which can be interpreted as a consequence of insulator leakage [2]. The shift of the curve from the ideal position, however, is due to a fixed charge (N_f) of about $1 \cdot 10^{12} \text{ cm}^{-2}$ in the oxide layer. This charge is obviously nearly totally absent when the oxidation is carried out at the higher temperature. Also the post-oxidation annealing procedures were found to be of major influence on the device behavior (Fig. 2).

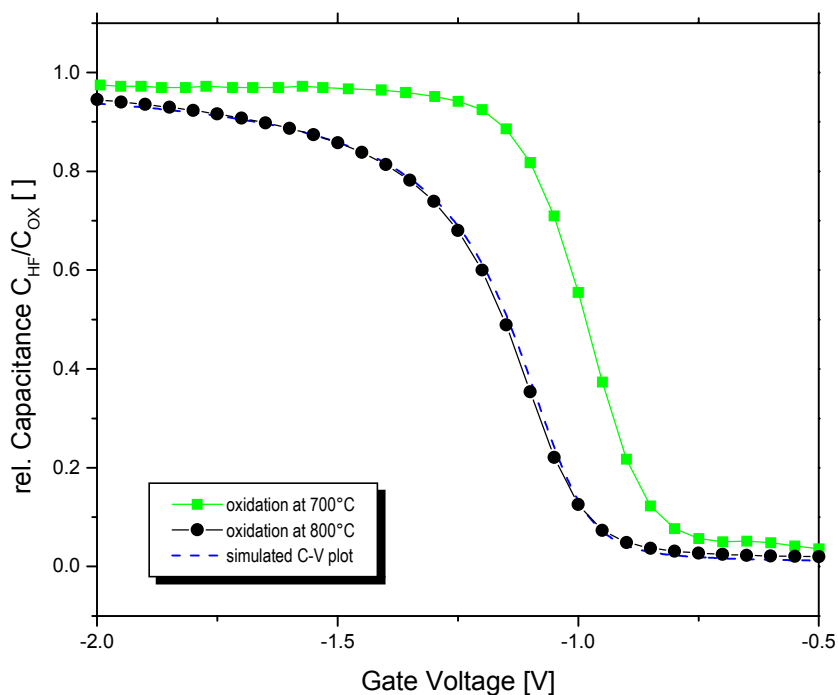


Fig. 1: Typical C-V characteristics showing the effect of different oxidation temperatures.

Without any further temperature treatment after the oxidation, the C-V plot displays a relatively large amount of fixed charge as well as a high density of interface traps which cause the typical stretch-out of the plot (squares). These defects are reduced by a pre-metallization anneal of 30 minutes (circles). Further improvement of the curve to almost the ideal shape of the simulation is achieved by a post-metallization anneal of 10 minutes. Longer heating times are of no desired effect since they in some cases lead to strongly increased gate leakage likely due to metal diffusion through the oxide. Fig. 3 displays a typical current-voltage plot recorded using a sample grown at 800 °C and annealed before and after metallization. The measured current densities are well within the expected range. The much smaller gate currents at positive voltage are due to formation of the depletion layer.

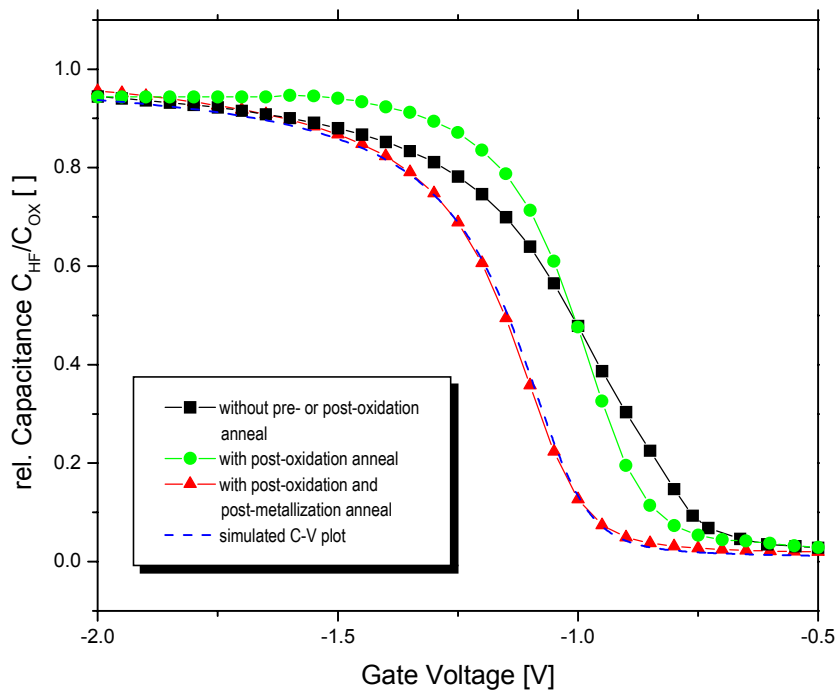


Fig. 2: The effect of annealing processes on C-V characteristics.

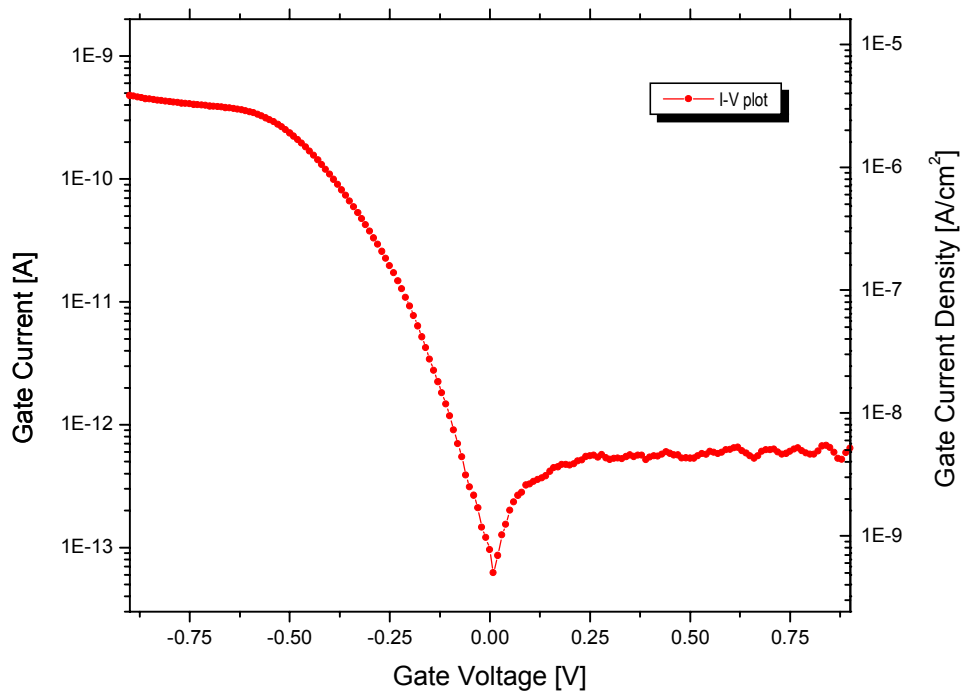


Fig. 3: I-V curve measured on a fully annealed sample grown at 800°C.

5. Conclusion

Ultrathin silicon dioxide films were thermally grown on p-type silicon at intermediate temperatures ranging from 700 °C to 800 °C and subjected to different pre- and post-metallization annealing steps. Electrical characterizations were performed by capacitance-voltage and current-voltage measurements and compared with simulated curves based on a simple MOS-capacitor model. Excellent agreement of simulation and measurements proved high predictability of electrical behavior and demonstrated applicability to the ultrathin regime. Thus these films are well suited for and have already facilitated pioneering work in demanding applications like scanning capacitance microscopy (SCM) [3].

References

- [1] S.M. Sze: "Physics of Semiconductor Devices", John Wiley, New York, 1981.
- [2] W.K. Henson, K.Z. Ahmed, E.M. Vogel, J.R. Hauser, J.J. Wortman, R.D. Venables, M. Xu and D. Venables: "Estimating Oxide Thickness of Tunnel Oxides Down to 1.4 nm Using Conventional Capacitance-Voltage Measurements on MOS Capacitors", *IEEE Electron Device Lett.*, vol. 20, 1999, 179 – 181.
- [3] B. Basnar, S. Golka, E. Gornik, S. Harasek, E. Bertagnolli, M. Schatzmayer and J. Smoliner: "Quantitative Scanning Capacitance Microscopy Investigations on p-doped Si-Multilayers", *J. Vac. Sci. Technol. B*, accepted for publication.

Multi-Wavelength Laser Diode Array Based on Surface Mode Coupling

P.O. Kellermann, N. Finger, E. Gornik

Institut für Festkörperelektronik, Mikrostrukturzentrum, TU Wien,
Floragasse 7, 1040 Wien, Austria

M. Ost, F. Scholz

4. Physik. Institut, Univ. Stuttgart,
Pfaffenwaldring 57, 70550 Stuttgart, Germany

Multi-wavelength emission from a visible red GaInP/AlGaInP laser diode array has been achieved with the contradirectional surface mode coupling technique. The wavelength control is attained by postgrowth adjustment of the thickness of a surface waveguide. The horizontal cavity lasers show both edge and surface emission (beam divergence $0.1^\circ \times 10^\circ$). The individual elements show single-mode emission with a spectral linewidth of less than 0.1 nm and a sidemode suppression ratio up to 30 dB. The wavelength spacing between the elements is 0.76 ± 0.08 nm yielding a total range across the array of 5.4 nm (from 681.5 nm to 686.9 nm). The thermal red-shift of the wavelength is 0.028 ± 0.002 nm/K.

1. Introduction

The *wavelength division multiplexing* (WDM) scheme is utilized to increase significantly the transmission rate of optical communication systems. Monolithic arrays of multi-wavelength laser diodes are considered as a compact choice for WDM light sources. Lasers in the visible regime are suitable to be used as emitters in optical short-range data transmission since the attenuation minimum of *polymethylmethacrylate* (PMMA) fibers lies near 650 nm.

Wavelength shift in *distributed feedback* (DFB) laser arrays is achieved by changing the grating period of the individual elements requiring a very precise definition of the grating period [1]. Also, arrays of multi-wavelength *vertical cavity surface emitting laser* (VCSEL) diodes have been attained. The optical thickness of their layers is varying in the lateral direction on the wafer. The resonance wavelength of the microcavity can be adjusted after the epitaxial growth by oxidation of an AlGaAs adjustment layer [2] or the local growth rate of all the epilayers is controlled with the help of a topographically patterned substrate [3].

2. Experimental

We have developed a multi-wavelength surface emitting laser array with horizontal cavities. The wavelength of single array elements can be adjusted after the processing by just changing the optical thickness of a *surface waveguide* (SWG). If the Fabry-Perot mirrors are etched (not cleaved) the wavelength of laser groups can be monitored and adjusted automatically on the chip. The principle of the laser diodes is based on *surface mode coupling* (SMC). Phase matching of the surface mode (propagating in the dielec-

tric SWG) and the laser mode is achieved by a surface relief grating in the top cladding of the laser waveguide. The grating causes radiation losses of the laser mode (dominated by the emission into the substrate). The losses are reduced significantly in a narrow spectral range by the excitation and feedback process of the surface mode. The linewidth of this resonance is comparable to the longitudinal Fabry-Perot mode spacing of the laser cavity, thus providing an effective mode selection mechanism, which leads to single-mode emission. By adapting the thickness of the SWG phase matching of the surface and the laser mode is achieved at another emission wavelength. By choosing the appropriate grating period either co- (the laser and surface mode propagating in the same direction are coupled) or contradirectional (the counterpropagating modes are coupled) coupling is achieved. The surface mode couples both to the active region and into the vacuum light cone resulting in surface emission.

Recently, we have shown that a SMC laser exploiting contradirectional coupling leads to an increased SMSR [4]. This can be explained by the fact that the slopes of the intersecting dispersion curves differ much more and hence the resonance is five times narrower than for the codirectional SMC concept. The wavelength shift induced by a change of the SWG thickness is five times smaller for contradirectional SMC. This eases the wavelength adjustment and improves the insusceptibility against longitudinal variations of the SWG thickness. In this work, we realized for the first time a multi-wavelength laser array with the contradirectional SMC concept. The adjusting span was increased from 1.2 nm in Ref. 4 to 5.4 nm, the SMSR from 26 dB to 30 dB.

The GaInP/AlGaInP-lasers were grown by low-pressure metalorganic vapour-phase epitaxy (MOVPE). Asymmetric cladding layers (by the aspect of thickness and refractive index) shift the electric field distribution of the laser mode towards the surface to achieve sufficient coupling. The second-order grating for the SMC is defined by holographic exposure of a spin-coated photoresist on the p-side of the laser structure. The pattern is etched into the top layers by ion milling ($\Lambda = 270$ nm, height 100 nm). The evaporation of semitransparent Au/Zn/Au stripes (5/5/20 nm, orientated perpendicularly to the surface grating) with a width of 10 μm defines the stripe-contacts of the lasers.

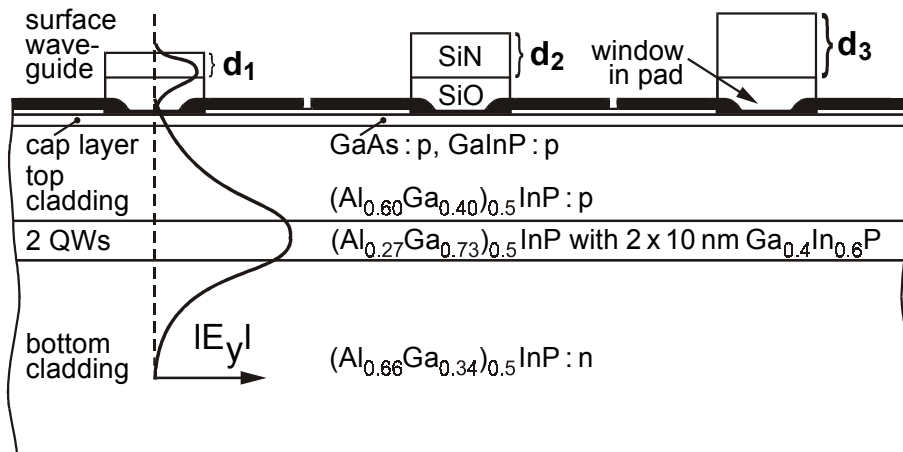


Fig. 1: Cross-sectional sample structure of three array elements. The semiconductor layers, surface waveguides (with different thicknesses), contact pads, windows, and optical mode profiles are indicated. The stripe-contacts are orientated perpendicular to the plane of the drawing. Different SiN-layer thicknesses of the surface waveguides result in different emission wavelengths.

Contact pads are evaporated on a polyimide isolation and on the stripe contacts leaving a $5\ \mu\text{m}$ wide window in the center of the contacts. Next the lasers are coated with $\sim 170\ \text{nm}$ SiO_x below $\sim 335\ \text{nm}$ SiN_x forming the SWG, which supports the TE_0 surface mode. The combination of one low- (SiO_x) and one high-index (SiN_x) dielectric layer avoids excessive leakage losses into the high-index substrate. The SWG thickness of individual lasers is adjusted by ion milling and photolithography. Thicknesses descending from ~ 505 to $\sim 450\ \text{nm}$ in steps of $\sim 8\ \text{nm}$ are realized on the finally cleaved laser bars. In Fig. 1 the cross-sectional sample structure of three array elements is sketched. The semiconductor layers, surface waveguides (with different thicknesses), contact pads, windows, and optical mode profiles are indicated. The stripe-contacts are orientated perpendicular to the plane of the drawing.

Single-mode edge emission is observed both in pulsed driven (AC) and continuous wave (CW) operation. The SMC laser diodes showed a threshold current density of $1\ \text{kA}/\text{cm}^2$ at a temperature of 10°C in AC and at -5°C in CW operation. Spectra of an array with seven wavelengths due to seven different thicknesses of the SWG are shown in Fig. 2 (CW, $1.6\ \text{kA}/\text{cm}^2$, 0°C). In the spectral center of the array the SMC-resonance (and thus the wavelength of the laser) falls together with the maximum of the active layer gain spectrum ($\sim 684.2\ \text{nm}$). This leads to a SMSR up to $30\ \text{dB}$ as shown in the inset on the right side. With increasing distance to the gain maximum the light output intensity and the SMSR decrease. The smallest SMSR of $19\ \text{dB}$ is depicted in the inset on the left side. The spectral linewidth achieved is $<0.1\ \text{nm}$.

An average wavelength spacing between neighbored lasers of $0.76 \pm 0.08\ \text{nm}$ is found yielding a total range across the array of $5.4\ \text{nm}$ (from 681.5 to $686.9\ \text{nm}$). The SWG thickness increases in small steps of $7.9 \pm 0.3\ \text{nm}$ from 450 to $505\ \text{nm}$ (as measured with a profilometer).

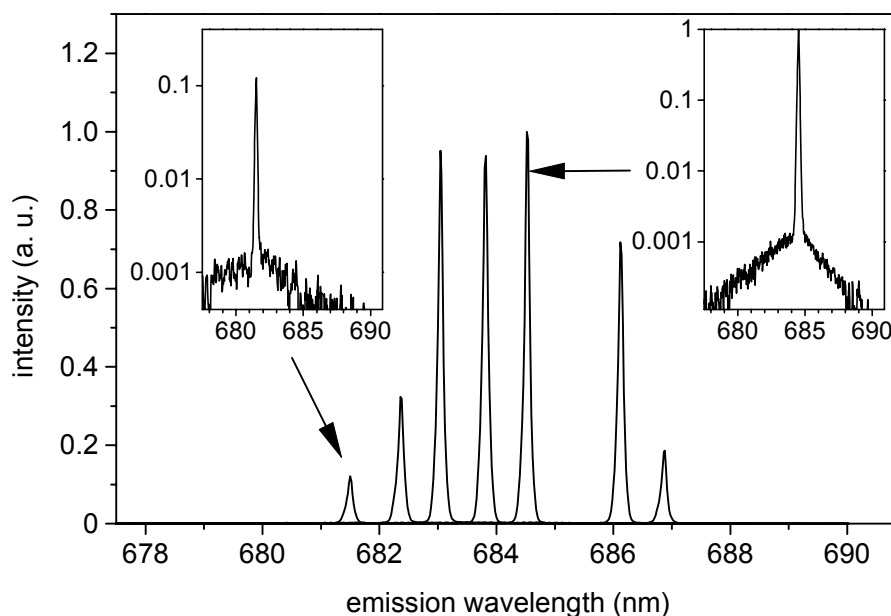


Fig. 2: Emission spectra of seven SMC lasers with seven different thicknesses of the SWG all joining the same array (CW, $1.6\ \text{kA}/\text{cm}^2$, 0°C). Spectra with the smallest ($19\ \text{dB}$) and highest ($30\ \text{dB}$) SMSR are shown with a logarithmic scale in the insets.

The far-field pattern of the lasers was measured by scanning from one cleaved facet along the stripe contact to the other facet. The surface emission for a laser that emits at 683.7 nm is observed at $\alpha = \pm 47.5^\circ$ with a beam divergence of 0.12° . The divergence in the azimuthal direction is 10° . The other array elements show a shift in α due to their different wavelengths. The shift in α between neighbored lasers is $\sim 0.25^\circ$. The intensity emitted per solid angle via the surface beam is five times larger than the one at the edges. Presently a fraction of 2% of the whole light output power (7 mW at 1.6 kA/cm^2 , 0°C , CW) is emitted via the surface.

The thermal behavior $\partial\lambda/\partial T$ of an SMC-laser was compared with a Fabry-Perot laser, which was prepared on the same array. The wavelength of the SMC-laser increases with $0.028 \pm 0.002 \text{ nm/K}$. The Fabry-Perot laser shifts with $0.12 \pm 0.01 \text{ nm/K}$ according to the bandgap shift. The small red-shift of the SMC-lasers is due to the fact that the wavelength is "locked" to the SMC resonance.

3. Conclusion

In conclusion, the contradirectional SMC technique for obtaining a multi-wavelength surface emitting single-mode laser array has been demonstrated with visible red GaInP/AlGaInP lasers. The wavelength control is achieved by postgrowth adjustment of the thickness of a surface waveguide. The wavelength spacing between the individual lasers is $0.76 \pm 0.08 \text{ nm}$ yielding a total range across the array of 5.4 nm. A SMSR up to 30 dB is reached.

An optimization of the red SMC laser array with the help of index- instead of gain-guiding is under progress. Increased surface emitted power, increased SMSR and a wider wavelength span are expected.

Acknowledgements

This work is partly supported by the Volkswagen-Stiftung (Germany).

References

- [1] Y. Muroya, T. Nakamura, H. Yamada, and T. Torikai: "Precise wavelength control for DFB laser diodes by novel corrugation delineation method", *IEEE Photon. Technol. Lett.*, vol. 9, 1997, pp. 288 – 290.
- [2] A. Fiore, Y. A. Akulova, J. Ko, V. Hegblom, and L. A. Coldren: "Postgrowth tuning of semiconductor vertical cavities for multiple-wavelength laser arrays", *IEEE J. Quantum Electron.*, vol. 35, 1999, pp. 616 – 623.
- [3] S. Q. Luong, G. G. Ortiz, Y. Zhou, Jun Lu, C. P. Hains, J. Cheng, H. Q. Hou, and G. A. Vawter: "Monolithic wavelength-graded VCSEL and resonance-enhanced photodetector arrays for parallel optical interconnects", *IEEE Photon. Technol. Lett.*, vol. 10, 1998, pp. 642 – 644.
- [4] P.O. Kellermann, N. Finger, W. Schrenk, E. Gornik; R. Winterhoff, H. Schweizer and F. Scholz: "Wavelength adjustable surface-emitting single-mode laser diodes with contradirectional surface-mode coupling", *Appl. Phys. Lett.*, vol. 75, 1999, pp. 3748 – 3750.

SIMS-Analyse von SiGe-CVD-Strukturen

R. Kolm, J. Foisner, K. Piplits, H. Hutter

Institut für Analytische Chemie, TU Wien,
Getreidemarkt 9/151, 1060 Wien, Austria

Um mittels CVD Strukturen herzustellen, ist eine Kalibrierung der Flüsse der zur Synthese verwendeten Gase gegen die Konzentration der Elemente in der Probe vorzunehmen. Des Weiteren ist die auf den unterschiedlichen Gasflüssen abhängige Wachstumsgeschwindigkeit zu bestimmen. Dazu wurden Proben zur Multi-Parameter Kalibrierung hergestellt. Jedes dieser Schichtsysteme wurde mittels CVD aus SiH_4 , GeH_4 und B_2H_6 epitaktisch auf Silizium hergestellt. Die Gasflüsse von GeH_4 und B_2H_6 wurden von Schicht zu Schicht geändert. Von dieser Kalibrierung ausgehend ließ man eine Schicht, in der die Germanium-Konzentration linear ansteigt, epitaktisch auf Silizium aufwachsen. Darüber brachte man eine Schicht mit konstanter Bor-Konzentration auf. Dann wurde die Probe einem RTA Schritt unterworfen, wobei Bor in die Germanium enthaltende Schicht diffundierte.

Die SIMS Messungen zeigten, dass die Konzentration von Bor in den Schichten nicht linear vom Gasfluss abhängt. Es konnte eine Kalibrationskurve erstellt werden. Mit Hilfe dieser Kalibrierung ließ sich die mittels CVD hergestellte Germanium-Struktur optimieren. Die Struktur zeigt den erwarteten linearen Anstieg der Germanium-Konzentration. Die Diffusion von Bor in die 50nm breite Germanium-Schicht konnte dokumentiert werden.

Focused Ion Beam Induced Local Tungsten Deposition

H. Langfischer, B. Basnar, E. Bertagnolli

Institute for Solid State Electronics, Vienna University of Technology,
Floragasse 7, 1040 Wien, Austria

H. Hutter

Institute of Analytical Chemistry, Vienna University of Technology
Getreidemarkt 9, 1060 Wien, Austria

Direct writing of metal lines is a widely used approach to interconnect prototype circuits and to rewire defective circuits at the very backend of the process line. However, the application of these direct written metal structures to contact devices is actually an open topic. In the presented metallization process a metal organic compound is decomposed by a focused ion beam (FIB) to form metal layers on several substrates. A variety of test structures allows the application of analytical methods and to quantify electrical properties. In addition, the detection of secondary electrons gives rise to time resolved *in situ* surface imaging of deposited metal layers. A direct characterization of the layers is obtained by atomic force microscopy (AFM).

1. Introduction

A widely used approach to interconnect prototype circuits and to rewire defective circuits is direct writing of metal lines at the very backend of the process line by means of FIB induced deposition. Primary beam related contaminations, intermixing effects, and unintentional local charging are the most important issues to be overcome if an application of FIB is viable close to the frontend. In this work we investigate the ion beam induced metallization process focusing on nucleation, intermixing, and growth, involving *in situ* characterization, AFM topography, SIMS, and electrical measurements.

2. Experimental

2.1 Layer Formation and Characterization

Based on a volatile metal organic tungsten compound ($W(CO)_6$) W-layers were deposited on thermal oxide layers by a Ga^+ ion beam [1]. Time resolved *in situ* surface imaging of the growth process addressing the primary steps in layer formation including nucleation and nuclei coalescence are involved. Characterization of the surface topography of the layers is done by atomic force microscopy (AFM). The chemical composition of the layers and the intermixing effects are both evaluated by secondary ion mass spectroscopy (SIMS) measurements.

2.2 Electrical Characterization

Electrical measurements are issuing the onset of the electrical conductivity, the specific resistance, and the maximum current densities the deposited material is capable to carry.

To quantify the ohmic resistivity and maximum current densities in the metal, specific test structures were developed. Figure 1 shows a typical van der Pauw test structure for measuring sheet resistances. In the left viewgraph, the structure is already crosssectioned by FIB to determine the associated layer thickness.

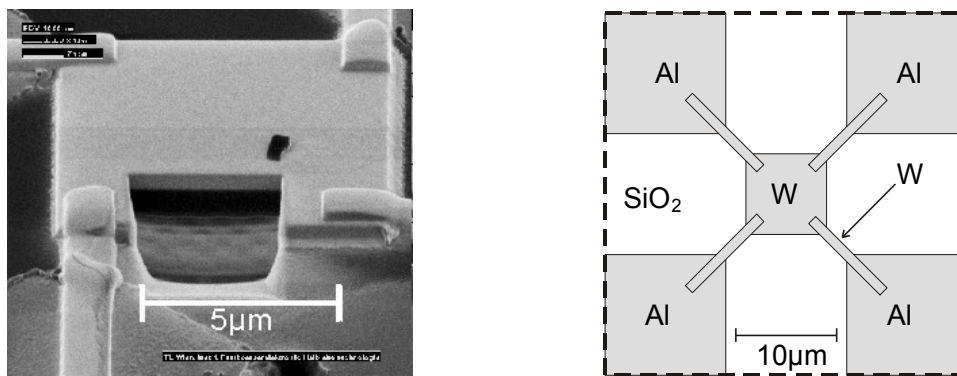


Fig. 1: Van der Pauw structure with FIB cross-sectional view and schematic illustration.

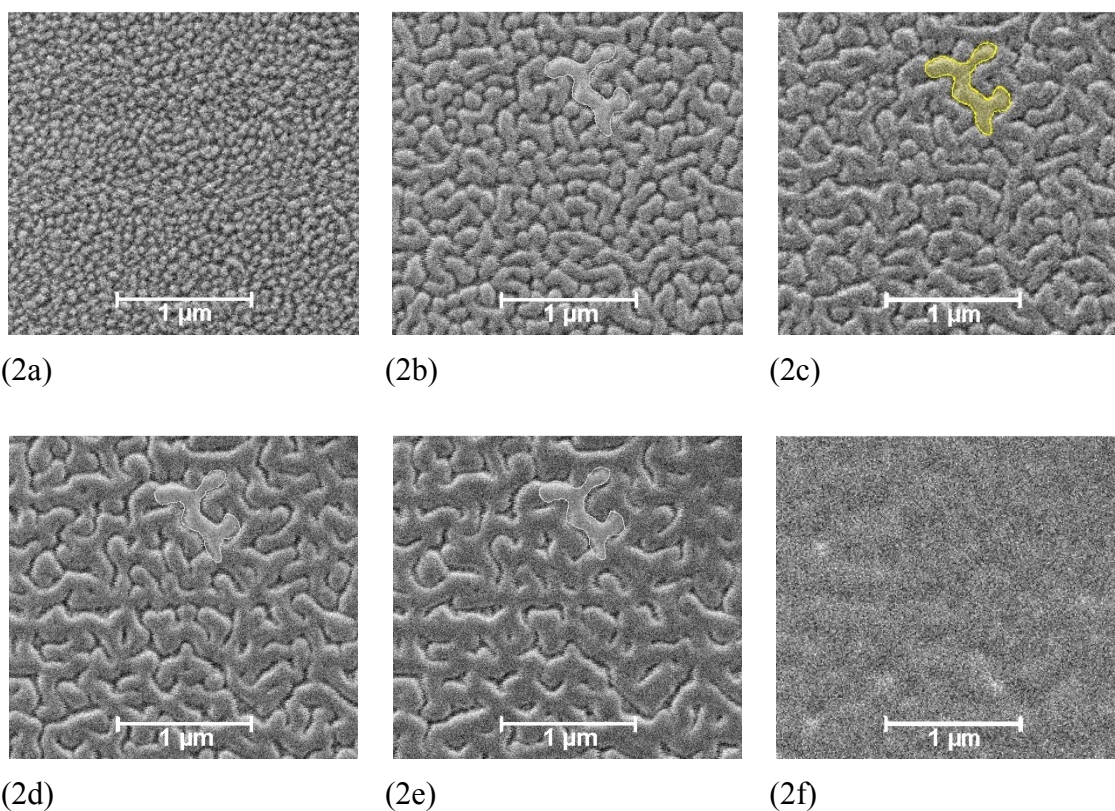


Fig. 2: Evolution of an ion beam induced CVD tungsten process on thermal silicon dioxide.

3. Results and Discussion

3.1 FIB Induced Growth Process

In order to determine the evolution of the tungsten deposition process, *in situ* observations of the developing nanoscale structures are done by detecting the secondary charges (electrons or ions) emitted from the surface during focused ion beam irradiation. After each ion induced deposition step, an image scan over the same sample region is done. By the way, time resolved *in situ* surface images of the evolving metal layers are obtained. Figures 2a to 2f are a sequence of images showing how the process of tungsten layer formation proceeds.

At the beginning of the deposition process (Fig. 2a) the time resolved investigation shows nucleation at spots that are stochastically but homogeneously distributed over the area exposed to the ion beam. Then the nuclei grow during the deposition and start to collapse to form larger connected structures. Its remarkable that the formations grown in the early deposition steps are preserved in their shape during the consecutively following steps. They are not destroyed by the ion beam. This can be verified observing the weakly enlightened region in the upper part of Figs. 2b – 2e. After the exposure to an accumulated ion dose of about $1.7 \cdot 10^{16}$ ions/cm² the merging process of formerly separated “islands” results in a closed metal surface (Fig. 2f).

3.2 Topography

Direct characterizations of the surface topography of the layers are obtained by atomic force microscopy (AFM). Figure 3 shows a three dimensional plot of the AFM data corresponding to a tungsten layer deposited with the same ion dose as the one in Fig. 2c. As seen in this figure, the topographic view is in close correspondence with the FIB imaging.

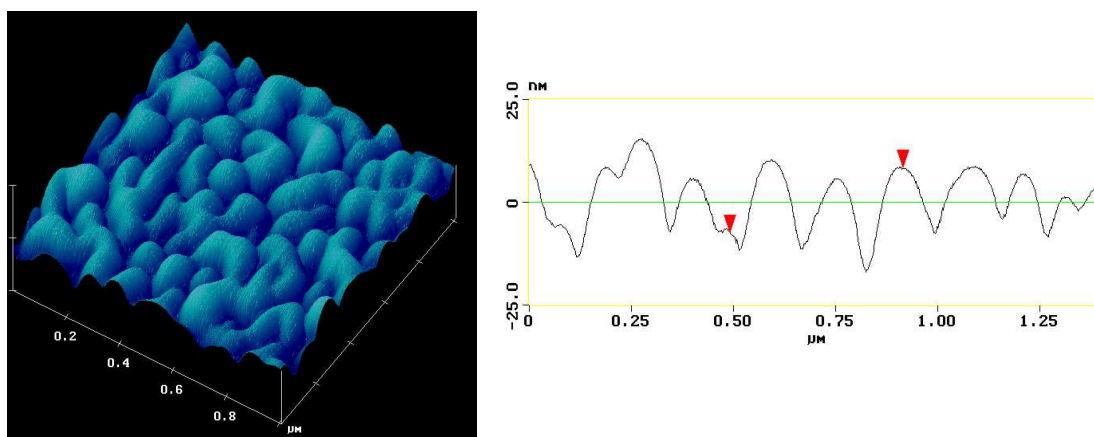


Fig. 3: Three dimensional plot of AFM surface scan (left). AFM analysis of the as grown tungsten surface (right).

The AFM section analysis of a tungsten surface in Fig. 3 exhibits a surface roughness value of up to 40 nm peak to peak.

3.2.1 Chemical

A SIMS based chemical analysis confirms a tungsten layer on the top of the substrate. In addition, however, to the direct observation, SIMS evidences, that no sharp interface to the substrate is formed. The exposure to the Ga beam leads to an intermixing region. Approaching the interface a clear pile up in the WSi concentration is seen, demonstrating the presence of a 50 nm interface layer between the tungsten layer and the substrate (Fig. 4).

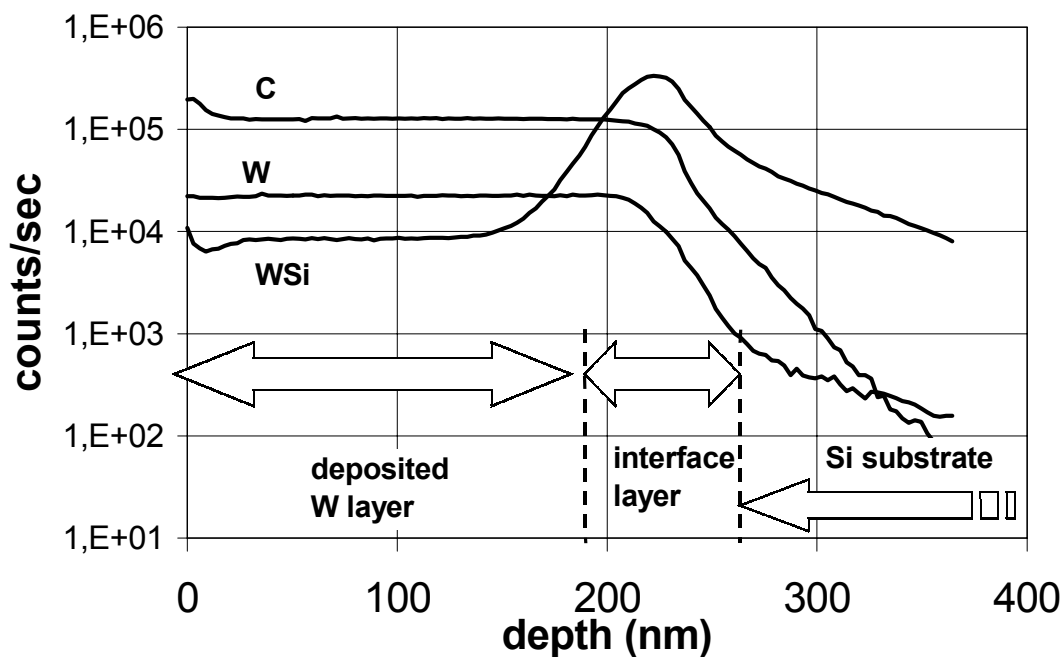


Fig. 4: SIMS profiles of C, W and WSi.

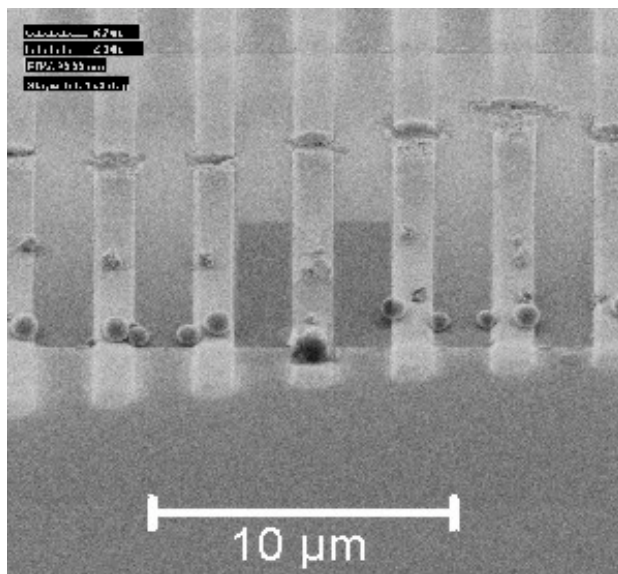


Fig. 5: Current stressed tungsten lines.

3.2.2 Electrical

The sheet resistance of a 280 nm layer is typically 3 Ω /square. The resistivity of the metal was calculated to be in a typical range of 200 – 300 $\mu\Omega\text{cm}$. The maximum current densities, indicating the robustness of the material were estimated using arrays of identical parallel W-lines (1 μm wide, 280 nm thick) connecting two contact pads. Maximum current densities up to $3.5 \cdot 10^6 \text{ A/cm}^2$ were obtained. The array of current stressed tungsten lines is depicted in Fig. 5. A remarkable feature are the spherical hillocks visible at the lower ends of the lines because they give a strong indication for the fact that electromigration took place before the lines broke down due to the local ohmic heating.

4. Summary and Conclusion

Direct writing of metal lines is a suitable approach to interconnect prototype circuits and to rewire defective circuits at the very backend of line. The application of these direct written metal structures to contact devices is actually an open topic. In the presented metallization process a metal organic compound is decomposed by a focused ion beam (FIB) to form metal layers on several substrates. A variety of test structures allows the application of analytical methods and to quantify electrical properties. In addition, the detection of secondary electrons gives rise to time resolved *in situ* surface imaging of deposited metal layers. A direct characterization of the layers is obtained by atomic force microscopy (AFM).

References

- [1] T. Kodas, M. Hampden-Smith, *The Chemistry of Metal, CVD*, VCH, Weinheim (1994).

Laser-Interferometric Investigation of Triggering Behavior in CMOS and Smart Power ESD Protection Structures

M. Litzenberger, C. Fürböck, R. Pichler, S. Bychikhin, D. Pogany, E. Gornik

Institute for Solid State Electronics, Vienna University of Technology,
Floragasse 7, 1040 Wien, Austria,

K. Esmark, G. Groos, H. Gossner, M. Stecher

Infineon Technologies, Munich, Germany

We report on noninvasive laser-interferometric thermal and free carrier mapping in electrostatic discharge (ESD) protection devices during a high current stress. The method is based on monitoring the changes in the silicon refractive index due to thermo-optical and plasma-optical effects. We study the homogeneity of bipolar transistor triggering along the device width in CMOS and smart power technology devices. The measured optical phase shift due to temperature and concentration changes is in a good agreement with the results of device simulation.

1. Introduction

Protection of electronic circuits against electrostatic discharge (ESD) is becoming a more and more important issue with the scaling down of technologies [1] and using the electronics in steadily harsher environment as e.g. in automotive applications [2]. Due to the high energy dissipated during the ESD pulse, the self-heating effect is a dominant failure cause in the ESD protection devices [1]. Due to non-linearities in bipolar conduction, the current flow in the device may be inhomogeneous leading to destructive hot spots. Therefore, thermal mapping is of great importance for hot spot identification and for experimental verification of simulation models [2] – [4]. We have recently developed a laser-interferometric thermal mapping technique for non-invasive investigation of thermal distribution and free carrier concentration changes in ESD protection devices under high current stress [5] – [7]. In this contribution we present the study of triggering homogeneity, thermal and free carrier distribution, and dynamics in CMOS and smart power technology ESD protection devices.

2. Results and Discussion

Devices studied are grounded gate- (gg) n-MOSFETs of 0.35 μm process (gate width is 100 μm) [3] and smart power ESD bipolar transistor protection devices [2] (see Fig. 1). The thermal energy distribution and free carrier concentration changes in devices are studied using a heterodyne interferometric technique [5], [6]. The temperature or carrier concentration change during a high current stress causes a modulation of the silicon refractive index which results in a phase shift of an infrared laser beam probing the device from the polished backside. The phase shift is a superposition of thermal and free carrier contributions. They can be distinguished by sign and different time evolution of the phase signal [6]. The devices were stressed by rectangular current pulses using a

transmission line pulser or a DMOS high-current switch. All measurements are performed under the snapback operation where the bipolar conduction occurs in the device.

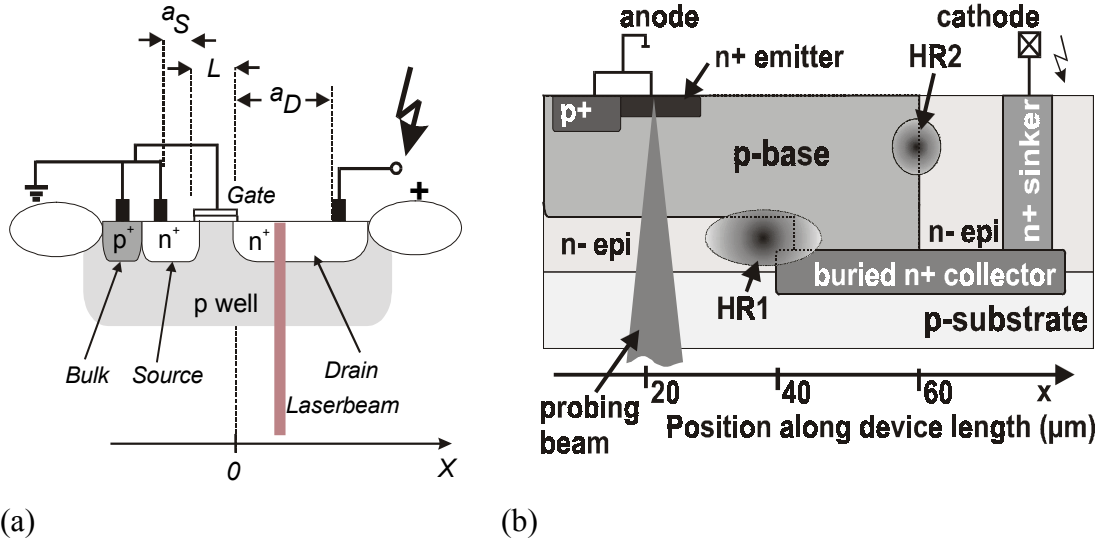


Fig. 1: Cross section of (a) gg-n-MOSFET and (b) smart power ESD protection devices. Probing beam is indicated. HR1 and HR2 in (b) indicate the location of regions with dominant heating.

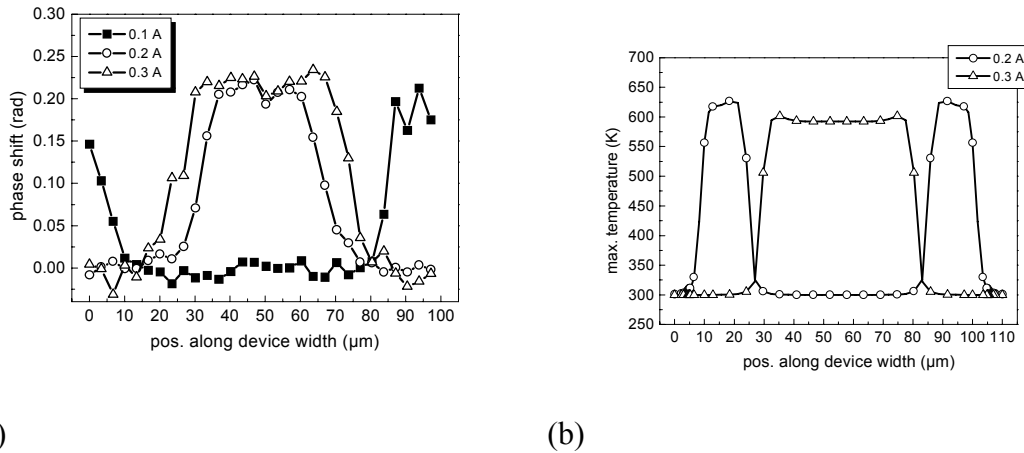


Fig. 2: (a) Phase shift distribution at the end of 100ns ESD pulse along the width of a gg-n-MOSFET with the stress current as parameter. (b) Simulated current density distribution in the same device.

The trigger homogeneity along the gate width in gg-n-MOS devices is studied at low stress currents. The probe beam is located on position where heat dissipation along the device length is maximal (i.e. at the drain edge of the channel, see Fig. 1(a)). Figure 2(a) shows the measured phase shift distribution along the device width as a function of the stress current. As the holding voltage is nearly current independent, the phase shift represents, in the first approximation, the current density (current per unit of device width). At low stress currents ($I_S = 0.1$ A) the device triggers preferentially at corners. This is due to a high electric field at the drain/bulk junction curvature at the corners, and consequently higher hole base current density, which promotes the transistor triggering at the

corners. When I_S increases, the triggered place switches to the middle of the device. With a further increase in I_S the triggered width increases, until the device is completely triggered. The change of triggering place from the corner is caused by a lower distributed drain resistance in the device middle, which makes the current conduction in the center energetically more favorable. This trigger behavior can qualitatively be reproduced by an isothermal three-dimensional device simulation using DESSIS^{ISE} (see Fig. 2(b)). At even higher stress currents, when the device is completely triggered, the current conduction along the width is homogeneous until the stress level ($I_S > 1$ A) where the device fails due to a formation of destructive current filaments [8].

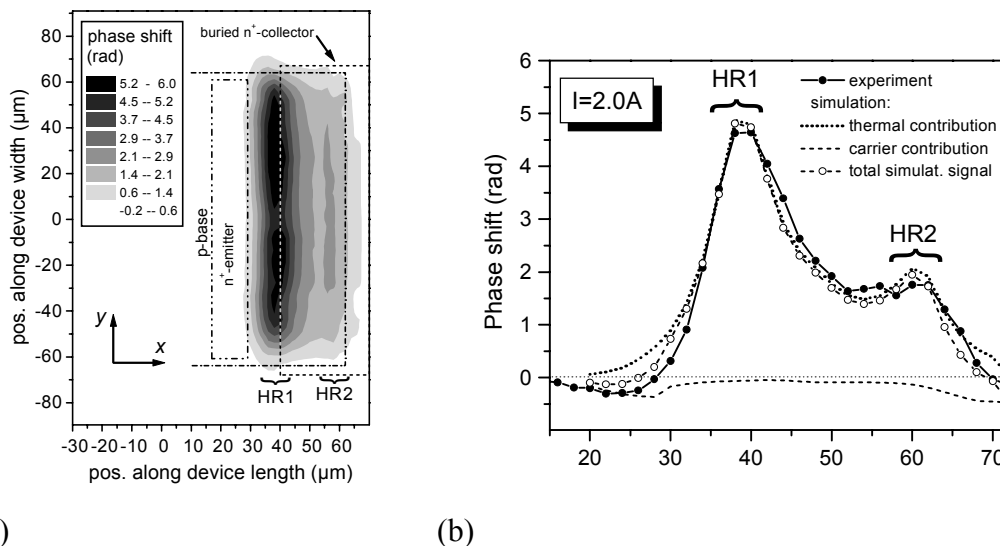


Fig. 3: 2D distribution (a) and a cross section (b) of phase shift at the end of a current pulse of 170ns duration and $I_S = 2$ A in a smart power ESD protection device (cf. Fig.1(b)).

Because of a larger characteristic feature size in smart power ESD devices, the trigger homogeneity in these devices is studied by performing two-dimensional phase shift mapping in lateral directions. The phase shift distribution along the device length at the end of the stress pulse of $I_S = 2$ A shows one dominant heat dissipated region (HR 1) and a region with a smaller local temperature maximum (HR 2), see Fig. 3(a). The temperature distribution along the device width is nearly homogeneous, with a slight temperature increase at device corners, probably due to lateral current crowding effect (Fig. 3(a)). Figure 3(b) shows a phase shift distribution along the device length in the middle of the device ($y = 0$, cf. Fig. 3(a)). The two hot regions HR1 and HR2 can clearly be distinguished. In addition, a region with a negative phase shift can be found under the emitter region. The latter is attributed to a negative phase shift contribution caused by electron injection from the emitter to the base. The electro-thermal two-dimensional device simulation using DESSIS has revealed that the region HR1 (HR2) is related to the heat dissipation due to a vertical current flow from the emitter to the buried layer (due to a subsurface lateral current flow between the p-base and n-sinker), see Fig. 1(b). As the devices at this stress current level trigger homogeneously, the experimental phase shift can be compared to a simulated phase shift. The latter was calculated as a sum of thermal and free carrier contributions, using the integrals of simulated temperature and free carrier distribution along the optical beam path. The agreement between the simulation and experiment is excellent (see Fig. 3(b)). For better distinction of the

free carrier and thermal contributions to the total phase shift, these are also given in the figure.

3. Conclusion

The laser interferometric method is a useful characterization tool for study of thermal and free carrier distribution and dynamics in ESD protection devices in ns time domain. An inhomogeneous triggering at low stress currents has been found and explained in gg-n-MOSFET devices. Two hot spots due to a lateral and vertical current path have been revealed in the smart power ESD protection devices. The results are in good agreement with the simulation.

References

- [1] Amerasekera A and Duvvury D. ESD in silicon integrated circuits. J Wiley & Sons, 1995.
- [2] Gossner H, Müller-Lynch T, Esmark K and Stecher M, "Wide range control of the sustaining voltage of ESD protection elements realized in a smart power technology. *Proc. EOS/ESD Symp.*, 1999, pp. 19 – 27.
- [3] K. Esmark, W. Stadler, M. Wendel, H. Gossner, X. Guggenmos, W. Fichtner: "Advanced 2D/3D ESD device simulation- A powerful tool already used in a pre Si Stage", *Proc. EOS/ESD Symp.*, 2000, pp. 420 – 429.
- [4] K. Esmark, C. Fürböck, H. Gossner, G. Groos, M. Litzenberger, D. Pogany, R. Zelsacher, M. Stecher, and E. Gornik, "Simulation and experimental study of temperature distribution during ESD stress in smart-power technology ESD protection devices", *Proc. Int. Reliab. Phys. Symp. (IRPS'2000)*, San Jose, California, April 10 – 13, (2000), pp.304 – 309.
- [5] C. Fürböck, D. Pogany, M. Litzenberger, E. Gornik, N. Seliger, H. Gossner, T. Müller-Lynch, M. Stecher, and W. Werner, "Interferometric temperature mapping during ESD stress and failure analysis of smart power technology ESD protection devices", *J. Electrostatics*, Vol. 49, 2000, pp.195 – 213.
- [6] C. Fürböck, K. Esmark, M. Litzenberger, D. Pogany, G. Groos, R. Zelsacher, M. Stecher, and E. Gornik, "Thermal and free carrier concentration mapping during ESD event in smart power ESD protection devices using an improved laser interferometric technique", *Microel. Reliab.*, Vol.40, 2000, pp. 1365 – 1370.
- [7] M. Litzenberger, K. Esmark, D. Pogany, C. Fürböck, H. Gossner, E. Gornik, and W. Fichtner, "Study of triggering inhomogeneities in gg-nMOS ESD protection devices via thermal mapping using backside laser interferometry", *Microel. Reliab.*, vol 40, 2000, pp.1359 – 1364.
- [8] D. Pogany, K. Esmark, M. Litzenberger, C. Fürböck, H. Gossner and E. Gornik, "Bulk and surface degradation mode in 0.35 μ m technology gg-nMOS ESD protection devices", *Microel. Reliab.*, Vol. 40, 2000, pp. 1467 – 1472 (2000).

FIB Based Micro Fabrication Technique for a Novel Type of Scanning Electrochemical Microscopy Probes

A. Lugstein¹, C. Kranz², E. Bertagnolli¹

¹ Institute for Solid State Electronics, TU Wien,
Floragasse 7, 1040 Vienna, Austria

² Institute for Analytical Chemistry, TU Wien,
Getreidemarkt 9, 1060 Vienna, Austria

Scanning Electrochemical Microscopy is a powerful technique to obtain *in situ* information of a wide range of processes occurring at interfaces. However, one major drawback of this technique is the lack of high spatial resolution compared with AFM or STM, due to the interference of the currents originated by the topographical and the electrochemical effects, respectively. Hence, a simultaneous but independent sensing of both, the topographical and the electrochemical information with high spatial resolution is a major issue in the field of scanning electrochemical microscopy (SECM). In this paper, we present a Focused Ion Beam (FIB) based technology, which, for the first time, enables the realization of an independent, simultaneous sensing of both the topography and the electrochemically active interface [1]. By remodeling an AFM-cantilever, an isolated ring-shaped electroactive metallic surface was integrated in the probe, whereas the residual AFM-tip was applied to gain the topographic information.

1. Introduction

Miniaturization of electrodes and electrochemical transducers by microfabrication processes is one of the fundamentals in modern electroanalytical chemistry [2]. Laterally resolved information on a sub-micrometer scale was added to electroanalytical chemistry with the invention of Scanning Electrochemical Microscopy (SECM) [3], [4]. This analytical method provides spatially resolved information on interface processes, which can be obtained by the possibility to use all common electrochemical methods, such as amperometry, potentiometry or cyclic voltammetry. The changes of the diffusion limited Faraday current at the microelectrode due to hemispherical diffusion of a redox mediator is recorded while scanning in constant height in the x,y-plane within a distance of a few electrode radii above the sample surface. The current response as a function of the microelectrode position is mainly influenced by the morphology and the reactivity of the investigated surface and the distance between microelectrode and sample. One major drawback of this technique is the lack of sufficient spatial resolution compared to AFM or STM, as long as a current dependent mode for positioning of the microelectrode is used. Any further progress in information quantification and qualification has to address (i) sub-micrometer to nanometer-sized electrodes (nanoelectrodes) for improved lateral resolution, (ii) the integration of current independent height information and (iii) the precise knowledge of the distance between the electrode tip and the sample surface. Consequently, the combination of SECM with other scanning probe techniques such as Scanning Tunneling Microscopy (STM), Atomic Force Microscopy

(AFM), Scanning Nearfield Optical Microscopy (SNOM), etc. is of particular interest in order to overcome the current limitations and to obtain complementary surface information. Several approaches have been reported so far to overcome the “fixed height problem in conventional SECM experiments”. A constant current mode combined with a vertical tip position modulation was already described in 1992 [5], [6]. A second approach based on electrochemical signaling uses convective effects when the microelectrode is moved with high speed perpendicular to the sample surface [7]. However, both methods do not provide current independent information on the tip-to-sample distance. Though, this approach is restricted to a few practical applications. An innovative possibility to circumvent this drawback is to integrate an electroactive area within a defined distance to the sample surface in a conventional AFM tip. In the present paper we discuss this novel approach applying a Focused Ion Beam (FIB) technique to produce a microelectrode integrated in a standard AFM tip. Thus, for the first time a precisely defined and constant held distance between the microelectrode and the sample surface can be obtained, thus allowing a simultaneous independent recording of the topographic and electrochemical information.

2. Experimental

The formation of the SECM electrode comprises coating of the AFM cantilever with thin conductive and insulating layers by RF sputtering respectively plasma enhanced chemical vapor deposition (PECVD) and the modeling of the integrated ultramicroelectrode by FIB cutting.

Conventional silicon nitride cantilevers were initially subjected to a RF-sputter coat forming a 5 nm chromium layer to ensure good adhesion of the subsequently deposited metal layer. The electrode material in form of a thin gold layer (100 nm to 400 nm) was then sputtered onto the cantilever. Finally a thin insulating and chemically inert $\text{SiO}_2/\text{Si}_3\text{N}_4$ sandwich layer was deposited (PECVD) onto the metal coated cantilever (Fig. 1). In order to produce homogeneous, dense films without pinholes the cantilever had to be annealed at 300 °C.

The well-defined microelectrode integrated in an AFM tip at a certain distance above the apex of the tip was generated by a FIB pattern process as shown in Fig. 1. The electrode formation includes several diametrically opposed cuttings, which are repeated several times in order obtain the demonstrated tip geometry. A major prerequisite for a simultaneous electrochemical and high resolution topographical imaging is the quality and stability of the re-modeled AFM tip. In order to ensure high resolution imaging, the original tip is re-established by FIB. Even smaller curvatures than usual for conventional Si_3N_4 tips are achieved and thereby the quality of the AFM image after the entire modification procedure could be improved. As a final step, re-deposited material was removed from the electrically active part of the tip.

The electrical contact was provided by an insulated copper wire (diameter: 0.2 mm) glued with a conducting silver epoxy resin to a small exposed area of gold layer at the end of the cantilever mount.

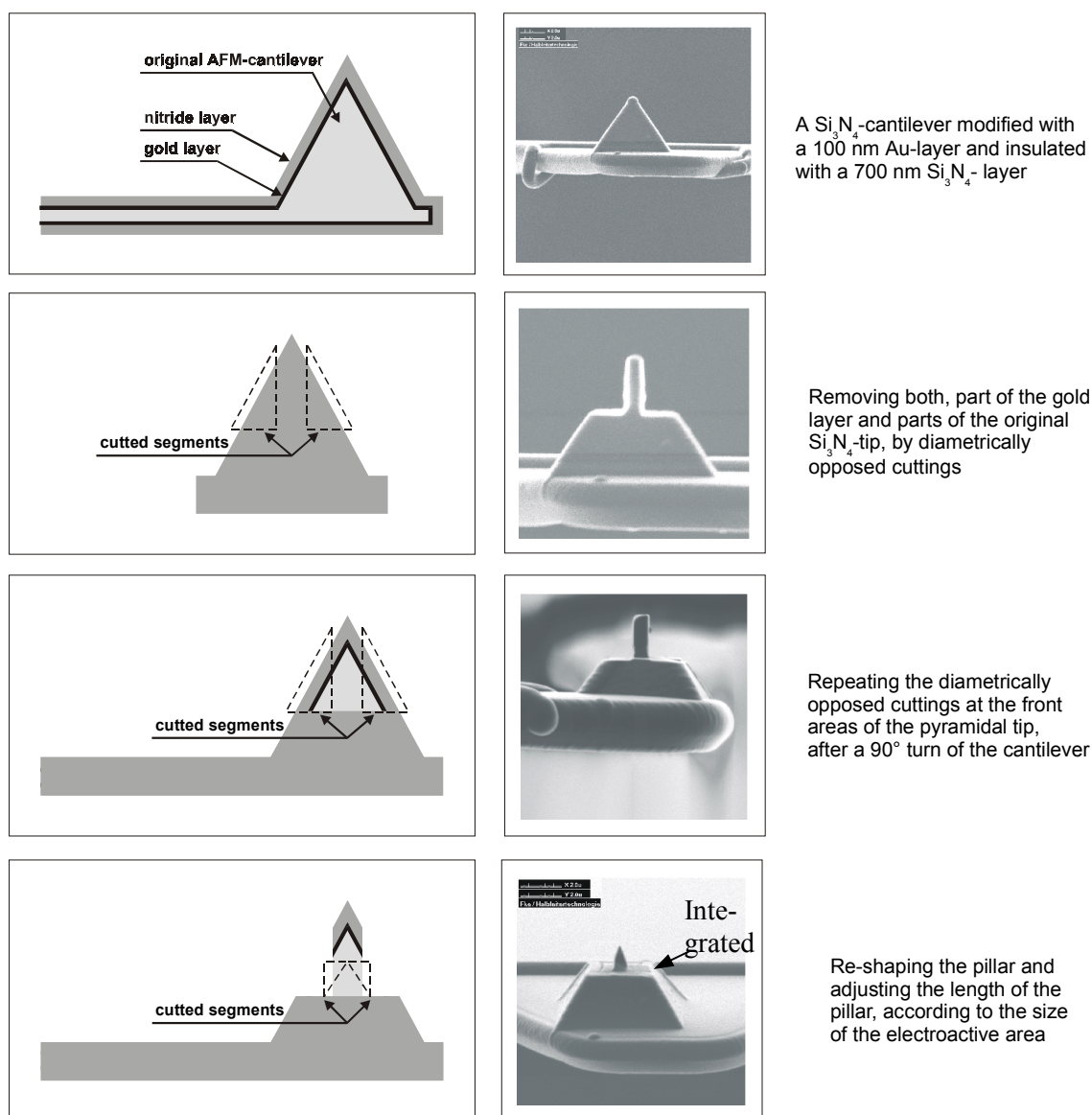


Fig. 1: Ion beam assisted modification of the AFM-tip. Schematic view of the processing steps (left) and the corresponding FIB-images (right).

AFM imaging was performed using a Nanoscope III atomic force microscope. The electrochemical investigations were performed in a fluid cell using an NPI VA10 potentiostat. All images were obtained in contact mode operation. The electrochemical setup was located in a Faraday cage. First results of simultaneous topographical and electrochemical measurement are shown in Fig. 2. A micromachined gold grating on gallium arsenide with a periodicity of $4.2 \mu\text{m}$ and a height of $0.45 \mu\text{m}$ was used as a model surface.

3. Conclusion

We present a novel technique which enables for the first time the integration of a microelectrode into an conventional AFM tip using an ion beam assisted approach, allowing simultaneous mapping of topographical and laterally resolved electrochemical information. This development allows to position the electroactive area in a precisely defined

and deliberately chosen distance to the very end of a scanning probe tip. Based on the opportunity to exactly adjust the distance of the electroactive area to the sample surface by adapting the length of the topographical probe with a micromachining technique like FIB, an optimized and defined working distance is ensured without theoretical fitting of current/distance approach curves. This procedure ensures high resolution topographical imaging and a precisely defined and constant distance between the integrated electrode and the sample surface within the working distance for electrochemical mapping. The demonstrated design is not limited to amperometric electrodes but can be extended to potentiometric electrodes or integrated electrochemical sensors, which are particularly difficult to position in a defined distance above a sample surface.

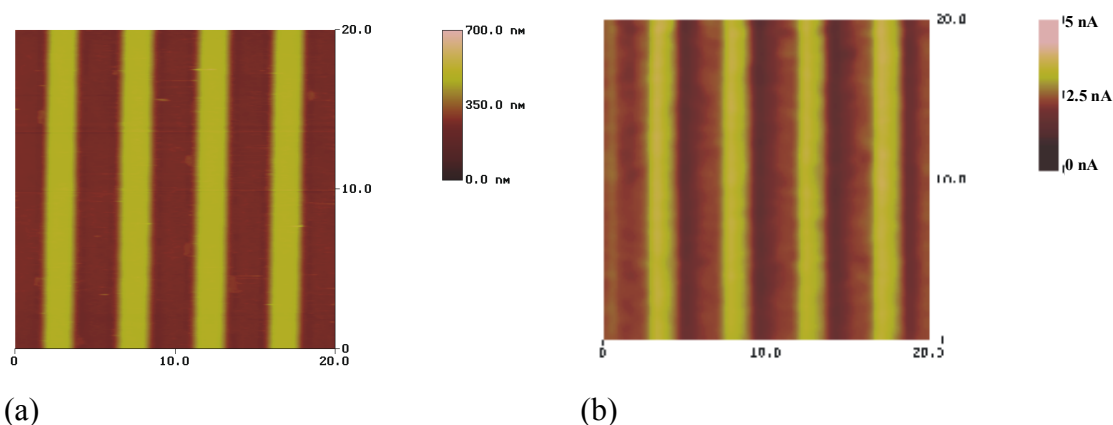


Fig. 2: Imaging of a gold grating (periodicity 4,2 μm). Simultaneously recorded AFM image (a) and corresponding SECM signal (b).

Acknowledgements

The authors thank Gernot Friedbacher (Institute of Analytical Chemistry, Vienna University of Technology) for the possibility to use the AFM-SECM facilities.

References

- [1] Patents pending, A 1011/2000 G01N, June 09, 2000; A 1012/2000 G01N, Jun. 09, 2000.
- [2] M.I. Montenegro, A.A. Queiros, J.D. Daschbach, *Microelectrodes: Theory and Applications*, Kluwer: Dordrecht, NL, 1990.
- [3] H.Y. Liu, F.-R.F. Fan, C.W. Lin, A.J. Bard, *J. Am. Chem. Soc.* 1986, 108, 3838.
- [4] R.C. Engstrom, M. Webber, D.J. Wunder, R. Burgess, S. Winquist, *Anal. Chem.* 1986, 58, 844.
- [5] D.O. Wipf, A.J. Bard, *Anal. Chem.* 1992, 64, 1362.
- [6] D.O. Wipf, A.J. Bard, D.E. Thallman, *Anal. Chem.* 1993, 65, 1373.
- [7] K. Borgwarth, D.G. Ebling, J. Heinze, *Ber. Bunsen-Ges. Phys. Chem.* 1994, 98, 1317.

Ballistic Electron Spectroscopy of Quantum Mechanical Anti-reflection Coatings for GaAs/AlGaAs Superlattices

C. Pacher, M. Kast, C. Coquelin, G. Fasching, G. Strasser, E. Gornik
Institut für Festkörperelektronik, TU Wien,
Floragasse 7, 1040 Wien, Austria

It is demonstrated that a standard concept for optics, anti-reflection coatings, can be transferred to ballistic electron transport in semiconductor superlattices. This constitutes a further manifestation of the electronic wave nature in nanoscale devices. We demonstrated the counter-intuitive effect that the transmission through a superlattice is increased by a factor of 2.4 if two further barriers are added at both sides of the structure. Additionally we designed a new injector for ballistic electrons which increases the energy resolution of ballistic electron spectroscopy to approx. 10 meV for further studies.

1. Introduction

Ballistic electron spectroscopy is a suitable method to investigate both semiconductor bulk and heterostructure material properties. In Fig. 1 the scheme of a typical application, the spectroscopy of superlattice minibands [1], is shown.

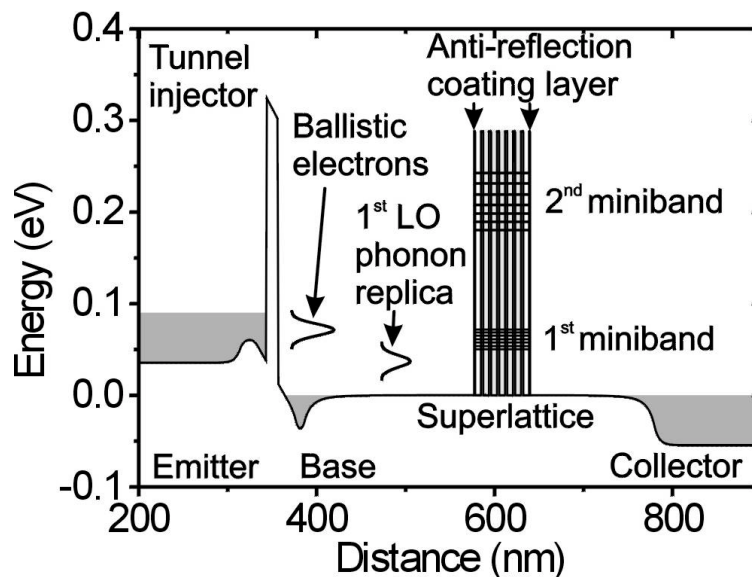


Fig. 1: Schematic bandstructure of a three-terminal device for ballistic electron spectroscopy.

By applying a DC voltage between the emitter and the base contact of a three-terminal device (3TD) hot electrons with a tunable energy are injected through a tunnel barrier into a first drift region. This drift region serves the purpose to reduce quantum-

confinement effects originating from the well formed by the injector barrier and the superlattice structure. After traversing the drift region the hot electrons hit the superlattice. In a third contact the electrons which have been transmitted through the superlattice are detected as collector current. From the ratio $\alpha = I_C/I_E$ of the measured currents at $T = 4.2$ K an energy-resolved spectrum of the superlattice transmission is obtained. The measured transfer ratio $\alpha(V_{BE})$ corresponds to the transmission function $T(E)$ but peaks of $T(E)$ get broadened due to the injected electron distribution, thus limiting the energy resolution of the spectrum.

2. Quantum Mechanical Anti-Reflection Coating

2.1 Theory

A quantum mechanical anti-reflection coating (ARC) for a superlattice (SL) consists in the simplest case of two additional barriers, one in front and one after the superlattice separated from the superlattice by a quantum well. In order to increase the transmission through the superlattice minibands these additional barriers have to be thinner than the barriers forming the superlattice. Using the transfer-matrix method in envelope function approximation including non-parabolicity we studied the transmission through a GaAs/Al_{0.3}Ga_{0.7}As-superlattice with five periods (barrier width 25 Å, well width 65 Å) while varying the width of the additional barrier and the distance to the superlattice. As a measure for the transmission we integrate the transmission $T(E)$ over the width of the first superlattice miniband: $T_I = \int T(E)dE$. For the case where the well width between the superlattice and the ARC equals one superlattice well width (65 Å) the maximum of the transmission T_I is achieved when the barrier width equals *half* the width of the barriers constituting the superlattice (12.5 Å). From the calculations of $T(E)$ for both samples shown in Fig. 2, a very strong enhancement of the integrated transmission for the first miniband (by a factor of 3.1) and a significant enhancement for the second miniband (+79 %) due to the additional barriers can be seen.

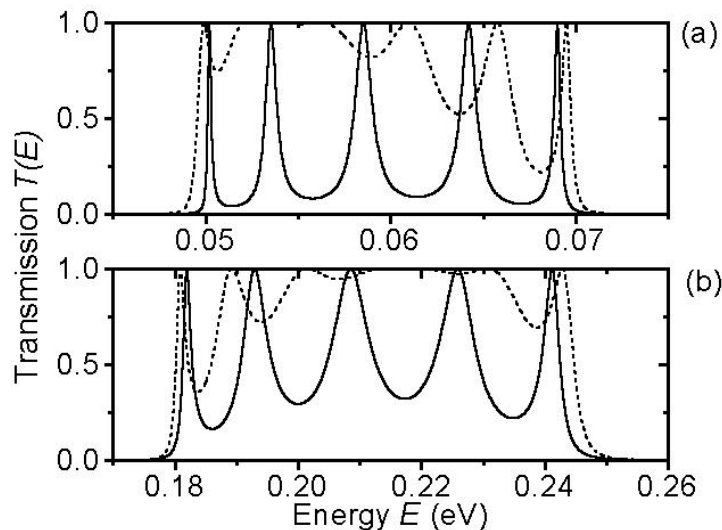


Fig. 2: Calculated transmission $T(E)$ through a superlattice with (dotted line) and without (full line) anti-reflection coating. (a) first miniband, (b) second miniband.

2.2 Experiment

In Fig. 3 the measured transfer ratio α at $T = 4.2$ K as a function of the applied base-emitter voltage V_{BE} , which specifies the injection energy, is plotted for both structures. In both samples the first peak from the left corresponds to ballistic transport through the first miniband whereas the following peak originates from electrons that have emitted one LO phonon in the drift region in front of the superlattice structure. From the shape of the first peak we deduce that the miniband width and position are not influenced by the anti-reflection coating as is predicted by our calculations. From the peak values an increase of the transfer ratio by a factor of 2.4 is found. This agrees quite well with the average increase of 3.1 estimated from the envelope function calculation, thus showing the validity of the concept of anti-reflection coating for superlattice transport. For the second miniband we measured an increase in the transmission by a factor of 1.35 as can be seen in Fig. 3(b).

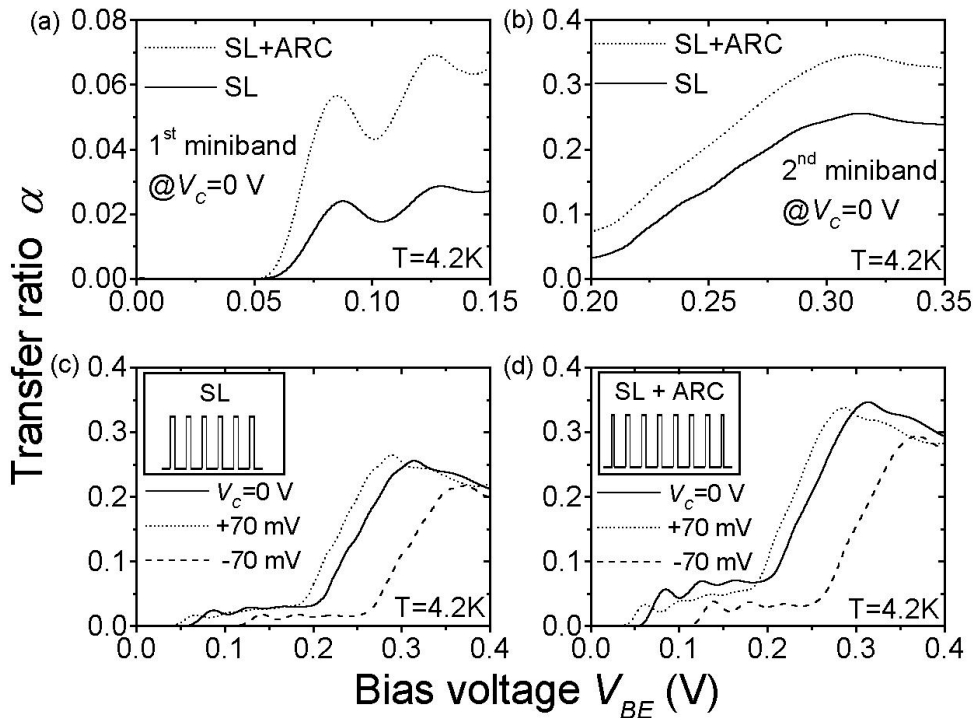


Fig. 3: Measured transfer ratios vs. bias voltage for superlattices with and without anti-reflection coating.

By applying a positive or negative voltage to the collector, the influence of an electric field on the electron transport has been studied. Fig. 3(c) and (d), show the transmission of both samples at collector bias voltages of $+70$ mV (dotted line), 0 mV (full line), and -70 mV (dashed line), respectively. The absolute value of the transmission of the first miniband ($\Delta_1 = 20$ meV) does not depend on the direction of the applied electric field since the transmission time is much shorter than the dominant interface roughness scattering time ($\tau_1 \approx 1$ ps). This situation is different for the second miniband. Since the miniband width ($\Delta_2 = 65$ meV) exceeds the energy of an LO phonon ($\hbar\omega_{LO} = 36$ meV), LO phonon scattering becomes the dominant scattering mechanism. For a positively biased superlattice LO phonon enhanced transport leads to an additional current in forward direction. This is the reason for the asymmetric transmission in the second mini-

band with respect to the applied electric field (peak maximum in the positive bias case is larger than in the negative bias case) as can be seen in Fig. 3 (c) and (d). This effect can be observed in both samples, but is weaker in the sample with anti-reflection coating, although the superlattice is about 33% longer. The LO phonon scattering inside the second miniband leads to a phase loss of the electrons and is therefore the reason why the effect of the anti-reflection coating is reduced for the second miniband.

3. Injector Improvements

The aim of this work is to reduce the width of the ballistic electron distribution by optimizing the layer structure of the electron injector. This was achieved by a special doping profile in the injector. To measure the energetic width of the ballistic electron beam, a three terminal device was designed using a special triple barrier RTD as a narrow energy filter between base and collector. It consists of three $\text{Al}_{0.3}\text{Ga}_{0.7}\text{As}$ barriers and two GaAs wells. To get a transmission of the analyzer that forms a sharp energy filter with a FWHM of 1 meV at 100 meV we choose both well widths to be 4.2 nm and the center barrier (8 nm) twice as thick as the neighboring barriers (4 nm). The complete conduction band structure of the three terminal device is shown in the left part of Fig. 4.

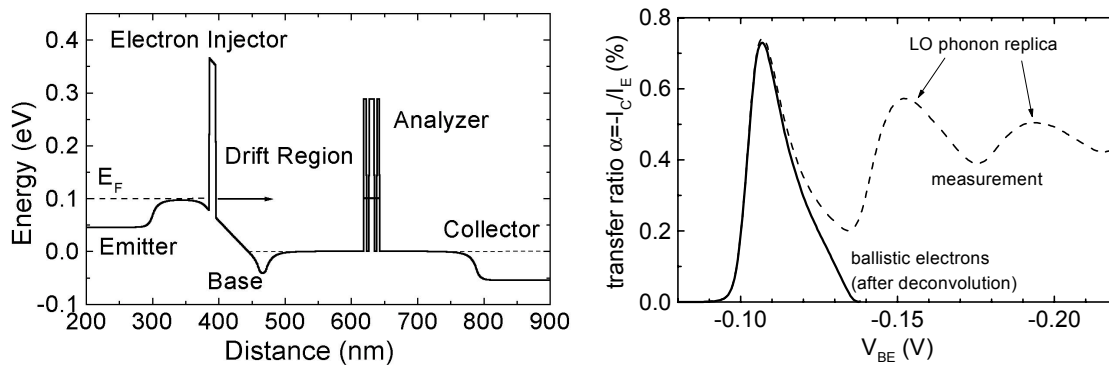


Fig. 4: Schematic bandstructure and transfer ratio for a three-terminal device with optimized injector and analyzer.

The transfer ratio vs. emitter bias is shown in the right part of Fig. 4. Due to the nearly δ -shaped transmission $T(E)$ of the analyzer the first peak of the transfer ratio reflects almost directly the energy distribution of the ballistic electrons. The following peaks in the transfer ratio are due to electrons which are scattered by LO-phonons while traversing the drift region and which have lost 36 meV during the scattering processes. After deconvoluting [2] (thus removing the LO phonon replica) the transfer ratio and estimating the broadening due to the analyzer (≈ 3 meV) we get a full width at half maximum (FWHM) of the injected electrons of 10 meV.

4. Conclusion

In conclusion, we have demonstrated that the optical concept of anti-reflection coatings is of relevance for electron transport in semiconductor superlattices as well. We have shown that an increase of the transmission by a factor of 2.4 is possible by adding additional barriers of suitable width on both sides of the structure. These concepts will allow

for a better design of various devices such as the quantum cascade lasers [3], where the introduction of such anti-reflection coatings may increase the transmission through the injectors significantly. We developed an injector with an ballistic electron distribution with a FWHM of 10 meV to increase the energy resolution for further experiments.

References

- [1] C. Rauch et al., “Transition Between Coherent and Incoherent Electron Transport in GaAs/GaAlAs Superlattices”, *Phys. Rev. Lett.* vol. 81, pp. 3495 – 8, Oct. 1998.
- [2] W. S. M. Werner, “Slowing down of medium energy electrons in solids”, *Phys. Rev. B*, vol. 55, pp. 14925 – 34, June 1997.
- [3] J. Faist et al., “Quantum cascade laser”, *Science*, vol. 264, pp. 553 – 6, April 1994.

Ballistic Electron Emission Spectroscopy on Biased GaAs-AlGaAs Superlattices in Transverse Magnetic Fields

D. Rakoczy, G. Strasser, J. Smoliner

Institut für Festkörperelektronik, TU-Wien,
Floragasse 7, 1040 Wien, Austria

In this work, we introduce a metal-insulator-metal (MIM) injector structure as a solid-state version of ballistic electron emission spectroscopy (BEES) and utilize this structure for the investigation of the lowest miniband of a biased GaAs-AlGaAs superlattice in a transverse magnetic field. The ballistic electron current measured as a function of the collector bias shows a peak at flatband condition indicating coherent transport through the superlattice miniband. With increasing transverse magnetic field, the coherent transport decreases, i.e. the peak is quenched. Using an extended transfer matrix method, the observed effects are explained quantitatively.

1. Introduction

Ballistic electron emission spectroscopy (BEES) is a method to probe metal-semiconductor interfaces as well as the band structure of semiconductor heterostructures. In the form of a three-terminal extension of scanning tunneling microscopy (STM) [1], [2], BEES was initially used to determine Schottky barrier heights [3] – [6]. Later BEES was also applied to study subsurface structures, such as buried GaAs-AlGaAs double barrier resonant tunneling diodes [7], superlattices [8], [9], and self-assembled InAs quantum dots [10], [11]. The main advantage of STM-based BEES is an excellent spatial resolution, which can also be used for imaging nanostructures with ballistic electrons (BEEM). However, in some experimental environments, e.g. high transverse magnetic fields or temperatures in the mK range, conventional STM equipment is difficult to use. To avoid these obstacles one can replace the STM tip by a solid-state injector which is directly integrated on the sample under investigation. As spatial resolution is usually not required for purely spectroscopic applications, device based BEES is a useful supplement to STM-based BEES. In the literature there are several reports on devices for BEES, such as hot electron transistors on the basis of GaAs-AlGaAs heterostructures [12] or the injector structures introduced by Rauch et al. [13]. Yet one has to keep in mind that all these experiments were carried out on highly specialized molecular beam epitaxy (MBE) grown structures and, in addition, required an advanced sample processing. Therefore, we were looking for a versatile, robust and easy-to-produce solid-state emitter for ballistic electrons. A very promising candidate is a metal-insulator-metal (MIM) injector based on Al-Al₂O₃-Al, which can be used on virtually any substrate material, provided the quality of the Schottky contact between the aluminum base layer and the semiconductor is good enough. The first MIM injector for ballistic electrons was realized on bulk germanium by Spratt et al. [14], whose device proved to be suitable for operation as a hot electron transistor. First tests of our MIM injector [15] were carried out on various heterostructures, which we had previously investigated with STM-based BEES. After proving that this type of injector is a suitable

tool for BEES, we applied it to a sample with a superlattice and investigated its behavior in a transverse magnetic field.

2. Sample Preparation and Experimental Setup

To test our new emitter concept we compared two different types of MBE-grown GaAs–AlGaAs samples. The first consisted of GaAs only, while the other one had a single, 10 nm thick AlGaAs barrier 30 nm below the surface. All samples (also the superlattices) were grown with a very thin region of highly p-doped GaAs (" δ -doping") in the otherwise nominally undoped GaAs to provide a "flatband" condition at the surface. The pattern of our injector structure was defined by optical lithography and is shown in Fig. 1(a). To process the MBE grown samples, first ohmic contacts to the n^+ collector region were established using a standard Ge–Au–Ni–Au metallization. Prior to the evaporation of the Al base layer, the native surface oxide was removed by dipping the samples in a 1:1 solution of HCl (35%) and de-ionized water. Then a 150 Å thick Al layer was evaporated onto the sample, which serves both as a base electrode and for the growth of the Al_2O_3 tunneling barrier. The base metallization was oxidized at ambient conditions (cleanroom environment) for 30 min at 50 °C to form a protective layer on the Al base layer for the subsequent lithography step. To fabricate the tunneling barrier, a second oxidation step of 3 min duration at 100 °C was carried out after the lithography for the emitter pattern. As a last step, a 600 Å thick Al emitter electrode was sputtered on top of the sample. For the measurements the samples were cooled down to $T = 4.2$ K and, in case of the superlattices, exposed to transverse magnetic fields of up to 8 T (see Fig. 1(b)). In the following, V_E denotes the voltage between emitter and base, I_t the corresponding tunneling current, and I_c the collector current. V_c , the bias voltage between base and collector, causes a tilt in the conduction band profile.

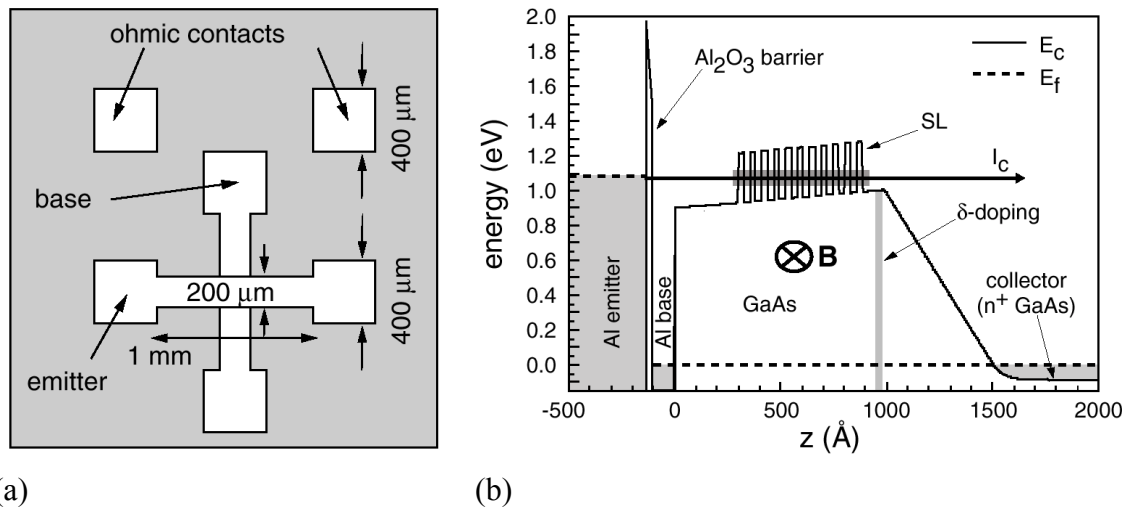


Fig. 1: (a) Sample layout. (b) Schematic conduction band profile of our device applied to a sample with a superlattice. Below the AlGaAs barrier height only ballistic electrons with the proper energy to pass through the miniband (indicated by the gray area in the superlattice) contribute to the collector current I_c .

3. Experimental Results

For all samples the BEE spectra ($\alpha = I_c/I_t$ vs. V_E) show that the transfer ratio α is negligible up to a certain threshold in V_E and increases rapidly after this onset. The measured onset voltages agree very well with the values expected from the band profile parameters. For $V_c = 0$ V we obtain $V_{\text{onset}} = -0.803$ V for the sample without any barrier and $V_{\text{onset}} = -1.113$ V for the sample with one AlGaAs barrier [15]. The measured height of the AlGaAs barrier (i.e. the difference of the two onset voltages) is thus 310 meV, in good agreement with the results obtained by STM-based BEES on the same samples. The onset voltages and the shape of the BEE spectra were reproduced on several samples and also agree excellently with the calculated results. On the other hand the total amount of the ballistic current shows large deviations when measured on different samples. This seems to originate from variations of the quality of the Al_2O_3 barrier.

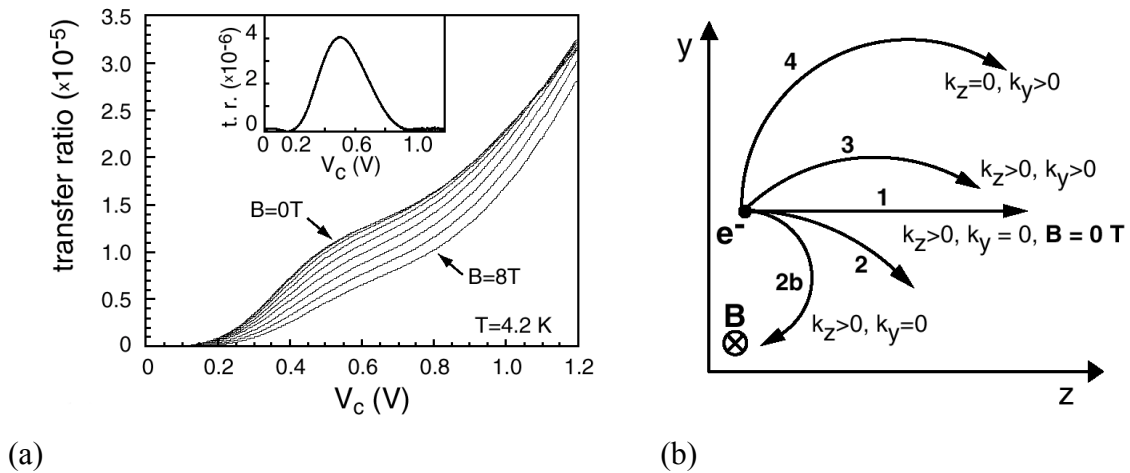


Fig. 2: (a) Measured transfer ratios vs. V_c for $V_E = -1.06$ V. The curves are measured at various B-fields from $B = 0$ T to 8 T in steps of 1 T (from left to right). At $B = 0$ T a peak at flatband condition is observed, which is quenched with increasing field. The inset shows the data for $B = 0$ T after background subtraction.

(b) Classical trajectories of electrons in a transverse magnetic field. Curve 1 shows a path without any B-field, the other trajectories are influenced by a B-field parallel to the x-axis. k_y, k_z denote the initial values of the momentum components. Curves 2 and 2b have identical initial momenta, but for 2b the B-field is higher.

Applying a positive voltage to the collector of the sample with the single barrier shifts the onset to smaller absolute values in V_E , just as expected from the band profile: $V_c > 0$ V means a lowering of the collector Fermi level which leads to a tilt of the band profile and therefore reduces the effective height of the AlGaAs barrier. The measured decrease in V_{onset} agrees very well with results from self-consistent calculations [15]. We also tested the behavior of the superlattice samples under bias before putting them into the magnetic field. These tests revealed that at zero bias the band structure of the superlattice is in fact slightly tilted, and an external collector voltage of $V_c \approx 500$ mV is needed to provide genuine flatband condition. This can also be seen directly in the measurement of the transfer ratio α in dependence of V_c for a constant emitter voltage (in the miniband regime, e.g. $V_E = -1.06$ V). After subtraction of a roughly exponential

background these curves exhibit a peak at flatband condition (see inset of Fig. 2(a)), indicating the transport through the miniband (the structure was designed in such a way that only one miniband exists below the AlGaAs barrier height). For flatband condition the onset voltage in the BEE spectra for this type of sample corresponds very well with the calculated lower edge of the miniband. A detailed description of the BEE spectra as well as a comparison with STM based BEES data can be found in [16].

The next step was to investigate the influence of the transverse magnetic field on the ballistic current. As one can already clearly see from the raw data in Fig. 2(a), the peak height in $\alpha(V_c)$ decreases with increasing magnetic field. This can already be explained by using the simple classical model of a charged particle in a transverse magnetic field (see Fig. 2(b)). The Lorentz force couples the k_y (parallel to the interface) and k_z (orthogonal to the interface) components of the electron momentum, whereas k_x , the component parallel to the B-field, stays unaffected. Due to the B-field, an electron can therefore lose k_z and gain k_y (and vice versa). Whether an electron is able to go through the superlattice or not depends on its kinetic energy associated with k_z , i.e. E_z . Electrons with an initial value of $k_y > 0$ can gain E_z via this mechanism, while all other electrons will always lose E_z . This diminishes the number of electrons with the right energy to pass the superlattice and leads to the observed change in the transmission.

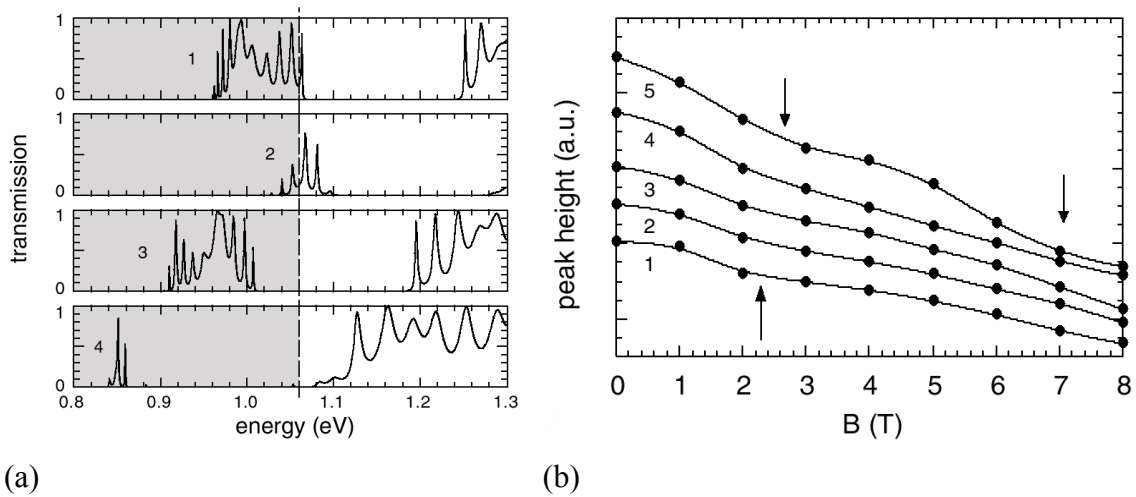


Fig. 3: (a) Transmission coefficient of the superlattice for several parameter sets. **1:** $B = 0$ T, $E_y = 0$ meV; **2:** $B = 3$ T, $E_y = 0$ meV; **3:** $B = 3$ T, $E_y = 60$ meV; **4:** $B = 8.2$ T, $E_y = 210$ meV. The dashed line indicates the position of the Fermi energy in the emitter for $V_E = -1.06$ V. (b) $\alpha(V_c)$ peak amplitude vs. B-field. The solid line is just a guide for the eye. Curves 1–5 correspond to $V_E = -1.04$, -1.05 , -1.06 , -1.07 , and -1.08 V respectively. The phonon associated features are marked by arrows.

In the quantum mechanic treatment the B field results in an additional term in the Schrödinger equation, which can be treated as a magnetic field induced potential. With this, the transmission can be calculated using conventional transfer matrix methods [16]. Fig. 3(a) shows the transmission coefficient of our superlattice structure at flatband condition as a function of E_z , calculated for different magnetic fields and different initial values of k_y . Curve 1 was calculated for $B = 0$ T and $k_y = 0$. As one can see, the miniband is located between 0.96 and 1.07 eV. If B is increased the transmissive regime for electrons with $k_y = 0$ is shifted to higher energy and becomes smaller (curve 2). How-

ever, in our experiment also electrons with positive and negative initial k_y values are injected. Electrons with $k_y < 0$ will be reflected back already at small B fields. On the other hand, electrons with positive k_y will gain E_z , which means that the transmissive range is shifted to lower values of E_z (curve 3). Despite this fact, more and more electrons are reflected back. Thus, the coherent current decreases, as it is observed experimentally. Curve 4 shows the situation for $B = 8.2$ T, $E_y = 210$ meV, and $E_z = V_b$, where V_b is the Schottky barrier height. Note that this is the highest possible E_y for $V_E = -1.06$ eV. For this case only a narrow transmission range exists just above V_b . If B is increased further ($B > 8.5$ T), the transmission is inhibited for all electrons below $e \cdot V_e = 1.06$ eV.

Plotting the peak height in $\alpha(V_c)$ (after background subtraction, see inset in Fig. 2(a)) vs. B, we observe a decrease for all emitter voltages (see Fig. 3(b)). This decrease is not completely linear, but exhibits one or two kinks, which can be interpreted as a result of sequential LO-phonon emission inside the superlattice. Simple classical estimations show that without magnetic field, the electron transfer time through our superlattice structure (≈ 100 fs) is just somewhat smaller than the LO-phonon emission time (≈ 150 fs). In a transverse magnetic field, the transfer time increases, since the average z component of the electron velocity decreases. If the LO-phonon scattering time is exceeded, scattering will occur and the scattered electrons will no longer contribute to the coherent current. Thus, the peak amplitude decreases faster than normal. If B is increased further, a second scattering can occur, provided the electron energy is still high enough. The miniband is about 100 meV broad, therefore in principle allowing the emission of 3 phonons. At $V_E = -1.08$ V, where the Fermi energy in the emitter is approximately aligned with the top of the miniband, we see two kinks in the data, while for the other curves the second kink is not observable. The second peak at low emitter bias does probably not occur because at high B-field and low injection energy most of the electrons are already below the LO-phonon energy after the first scattering. The third peak is probably missing even at higher energies, since at 8 T the transfer time might still be too small for three sequential phonon emissions.

4. Conclusion

We have developed a MIM injector structure for BEES and used it to investigate the ballistic transport through a superlattice in a transverse magnetic field. We explained the observed behavior quantitatively with an extended transfer matrix method. Furthermore, indications for sequential LO-phonon scattering inside the superlattice, facilitated by the magnetic field via increased transfer times, can be observed.

Acknowledgements

This work was sponsored by the “*Fonds zur Förderung der wissenschaftlichen Forschung*” as project No. P12925-TPH and by the “*Gesellschaft für Mikroelektronik*”.

References

- [1] W. J. Kaiser and L. D. Bell, *Phys. Rev. Lett.*, **60**, 1406 (1988).
- [2] L. D. Bell and W. J. Kaiser, *Phys. Rev. Lett.*, **61**, 2368 (1988).
- [3] W. J. Kaiser et al., *Phys. Rev. B*, **48**, 18324 (1993).

-
- [4] H. Sirringhaus, E. Y. Lee, and H. von Känel, *Phys. Rev. Lett.*, **73**, 577 (1994).
 - [5] R. Ludeke, M. Prietsch, and A. Samsavar, *J. Vac. Sci. Technol. B*, **9**, 2342 (1991).
 - [6] M. Prietsch and R. Ludeke, *Phys. Rev. Lett.*, **66**, 2511 (1991).
 - [7] T. Sajoto et al., *Phys. Rev. Lett.*, **74**, 3427 (1995).
 - [8] J. Smoliner, R. Heer, C. Eder, and G. Strasser, *Phys. Rev. B*, **58**, 7516 (1998).
 - [9] R. Heer, J. Smoliner, G. Strasser, and E. Gornik, *Appl. Phys. Lett.*, **73**, 3138 (1998).
 - [10] M. E. Rubin et al., *Phys. Rev. Lett.*, **77**, 5268 (1996).
 - [11] W. Wu, J. R. Tucker, G. S. Solomon, J. S. Harris, Jr., *Appl. Phys. Lett.*, **71**, 1083 (1997).
 - [12] M. Heiblum et al., *Phys. Rev. Lett.*, **55**, 2200 (1985).
 - [13] C. Rauch et al., *Phys. Rev. Lett.*, **81**, 3495 (1998).
 - [14] J. P. Spratt, R. F. Schwarz, and W. M. Kane, *Phys. Rev. Lett.*, **6**, 341 (1961).
 - [15] R. Heer, et al., *Appl. Phys. Lett.*, **73**, 3138 (1998).
 - [16] D. Rakoczy, J. Smoliner, R. Heer, and G. Strasser, *J. Appl. Phys.*, **88**, 3495 (2000).

Epitaktisches Wachstum von gitterangepassten und verspannten III-V Verbindungen

G. Strasser, W. Schrenk

**Institut für Festkörperelektronik & Mikrostrukturzentrum der TU Wien
Floragasse 7, 1040 Wien, Austria**

Eine funktionierende Wachstumstechnologie stellt die Grundlage für die Herstellung niedrigdimensionaler Systeme und neuartiger optoelektronischer Bauelemente dar. GaAs Schichten, AlGaAs/InGaAs/GaAs-Vielschichtsysteme (Heterostrukturen), hochbewegliche zweidimensionale Elektronengasstrukturen (2DEGs), resonante Tunneldioden (RTDs), Quantumwell- und Minibandstrukturen, Halbleiterdiodenlaser, Quantum Cascade-Laserstrukturen, Bragg-Spiegel, saturierbare Absorber, und InAs-Quantumdot-Systeme werden am Institut für Festkörperelektronik im Mikrostrukturzentrum epitaktisch hergestellt. Diese Molekularstrahlepitaxieschichten mit Einzeldicken von einzelnen Monolagen bis zu einigen Mikrometern kommen vor allem den Projekten zugute, die mit der Herstellung und Weiterentwicklung neuartiger kohärenter Strahlungsquellen beschäftigt sind. Weiters werden alle Gruppen, die niedrigdimensionale Systeme durch nasschemisches oder reaktives Ionenätzen oder Elektronenstrahlolithographie herstellen und untersuchen, sowie Gruppen die Transportuntersuchungen an GaAs-Verbindungen durchführen, versorgt. Diese Arbeit soll diese Technik einem breiteren Publikum zugänglich machen und einige Beispiele für epitaktisches Wachstum darstellen.

Band Structure Engineering for Terahertz Quantum Cascade Lasers

J. Ulrich, R. Zobl, W. Schrenk, G. Strasser, K. Unterrainer, E. Gornik

Institut für Festkörperelektronik, TU Wien,
Floragasse 7, 1040 Wien, Austria

We have investigated intra- and interwell transition schemes in magnetotransport and intersubband electroluminescence experiments regarding their potential as a central part of a terahertz quantum cascade laser. The conductivity of the interwell structure is smaller, indicating a reduced nonradiative scattering rate compared to the intrawell structure. The interwell transition exhibits a Stark shift, as expected. The intrawell transition shows a smaller shift which agrees with band structure calculations.

1. Introduction

The need of compact sources of coherent radiation in the frequency regime between 1 and 10 THz has stimulated the development of a terahertz (or far-infrared) quantum cascade (QC) laser [1] – [3]. A simple scaling of successful band structure concepts of mid-infrared QC-lasers [4] is impracticable because resonant emission of longitudinal optical (LO) phonons (in GaAs at 8.7 THz, 36 meV) cannot be utilized likewise, and fast non-radiative intersubband relaxation counteracts population inversion [1]. The relaxation rate decreases as initial and final subband of the laser transition are spatially separated by a barrier. Two band structure schemes (emission around 18 meV, 4.4 THz) have been compared, one based on an intrawell transition between the second and the first subband of one quantum well, the other based on an interwell transition between the first subbands of two adjacent quantum wells separated by a barrier [5].

2. Experimental

The samples consist of 50 periods of a 3-well system with GaAs wells and $\text{Al}_{0.15}\text{Ga}_{0.85}\text{As}$ barriers grown on n+-doped GaAs substrates employing molecular beam epitaxy. The central well of each period is lightly n-doped ($1 \times 10^{16} \text{ cm}^{-3}$). On top of the layer system is a 100 nm thick n+-doped GaAs contact layer. Calculated conduction band profiles of the two samples are shown in Fig. 1. The structures were designed for emission between the subbands denominated as $|i\rangle$ (initial) and $|f\rangle$ (final). The narrower quantum wells serve as an energy filter to extract electrons from $|f\rangle$ and inject them into the subband $|i\rangle$ of the adjacent period. We processed emission samples as 4 (intrawell) or 32 (interwell) parallel ridge mesas, each of the dimensions $25 \mu\text{m} \times 1000 \mu\text{m}$, with $25 \mu\text{m}$ distance between them. These ridges are connected on both ends with two perpendicular mesas of $175 \mu\text{m} \times 80 \mu\text{m}$ (intrawell) or $1575 \mu\text{m} \times 80 \mu\text{m}$ (interwell), which serve as bond pads. The total surface of the mesas is 0.112 mm^2 (intrawell) or 0.924 mm^2 (interwell). The mesas were shaped by $4.3 \mu\text{m}$ deep reactive ion etching through the whole layer system into the substrate. Ohmic AuGe contacts were then produced on top of the mesa structure and on the backside of the substrate.

The magnetotransport- and electroluminescence measurements were performed in the same set-up [2]. The spectral response of an InSb cyclotron resonance photodetector was tuned in the magnetic field B of a superconducting magnet from 8.7 meV ($B = 1$ T) up to 26 meV ($B = 3.4$ T). The detector and the sample were located in a closed waveguide immersed in liquid He. A second magnet controlled the magnetic field oriented perpendicular to the epitaxial layers at the position of the sample. In all measurements we applied 22 μ s long voltage pulses at 23 kHz repetition rate between the top and the back contact.

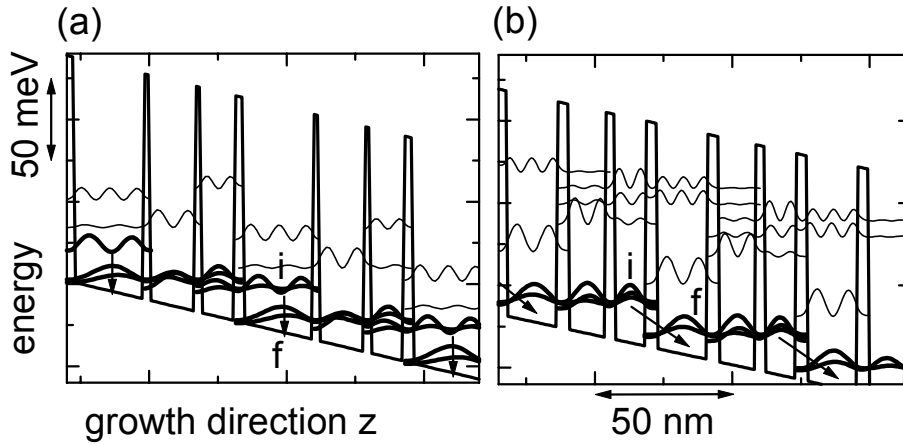


Fig. 1: Band structure calculation for $2\frac{1}{2}$ periods of (a) the intrawell and (b) the interwell structure at an electric bias of 3.6 kV/cm. The moduli squared of the envelope wavefunctions of the involved subbands (thick lines) and of higher subbands (thin lines) are plotted at their energies. The radiative $|i\rangle \rightarrow |f\rangle$ -transitions are marked with arrows. The well- and barrier (underlined) widths in nm are: (a) 25.0 / 2.7 / 16.0 / 2.5 / 12.4 / 2.8 and (b) 18.5 / 4.0 / 13.5 / 3.3 / 11.4 / 4.0.

The conductivity of the two samples is remarkably different, for example, the current densities at a bias of 5 kV/cm are 419 A/cm² in the intrawell sample and 31 A/cm² in the interwell sample. This is a direct consequence of the different spatial overlaps between the $|i\rangle$ and $|f\rangle$ subbands. We conclude that the $|i\rangle \rightarrow |f\rangle$ -transition rate governs the transport through the whole structure. In a magnetic field the current is quenched in an oscillatory manner as depicted in Fig. 2(a). The quenching originates from a suppression of intersubband scattering caused by Landau quantization of the in-plane electron motion. The maxima in the current resemble magneto-intersubband resonances [6]. The knowledge of the resonance positions allows a determination of the subband energy difference. Identifying the current maxima with a change of Landau index of $M = 2, 3, 4, 5$ and using the GaAs effective mass $m^* = 0.0667 m_e$, we derived the transition energies plotted in Fig. 2(c) versus the electric field. The data should be compared with the center frequency of the electroluminescence peak (solid circles). Some original spectra are given in Fig. 2(b). For a pure intrawell transition no first order Stark shift is expected since the centers of charge of $|i\rangle$ and $|f\rangle$ are at the same position. In the high bias region ($F > 6$ kV/cm) the energy of the transition is fairly field-independent (left panel of Fig. 2), whereas at low biases it changes from 17 meV (at 2 kV/cm) to 20 meV (at 6 kV/cm). The transition energy was calculated (Fig. 2(c), line) solving Poisson's and Schrödinger's equations. Apart from an offset of 1.8 meV the experimental data are well

described by the calculation. The energy of the interwell transition (right panel of Fig. 2) suffers a clear Stark shift, visible in the magnetotransport as well as in the electroluminescence data. The linewidth is on the average 0.4 meV broader than that of the intrawell transition. This is consistent with the argument of alloy scattering in the barrier. The slope of the measured Stark shift is somewhat smaller than the one predicted by the calculation under the assumption of a homogeneous electric field.

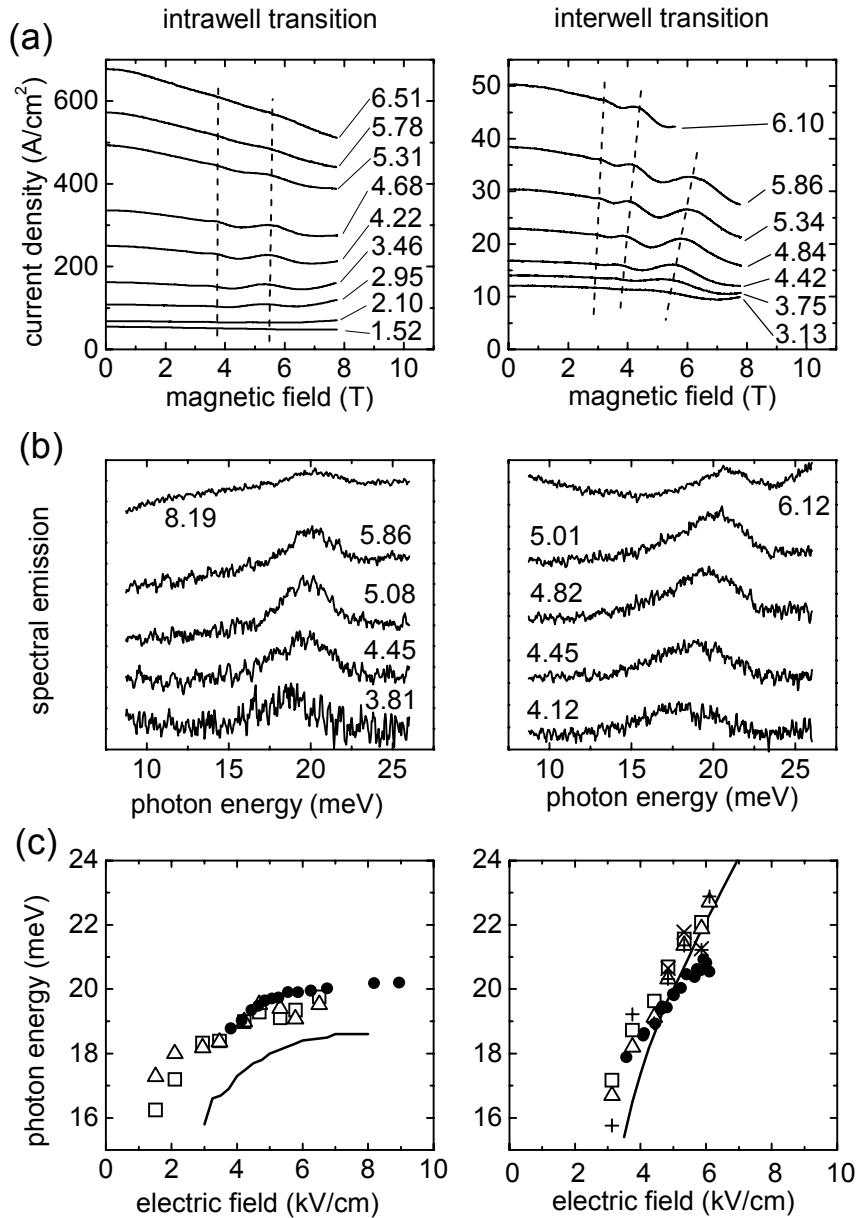


Fig. 2: (a) Current density versus magnetic field for various values of the electric field given in kV/cm. The dashed lines mark the magneto-intersubband resonances. (b) Electroluminescence spectra at electric fields as indicated in kV/cm. The spectra are plotted with arbitrary offsets. (c) Transition energy versus electric field extracted from the positions of the magneto-intersubband resonances for $M = 2$ (open squares), 3 (open triangles), 4 (+) and 5 (x); photon energy from the electroluminescence spectra (solid circles); and transition energy $E_i - E_f$ from Poisson-Schrödinger calculations (line).

3. Conclusion

Our comparison of an intrawell and an interwell quantum cascade structure yields: The interwell sample exhibits a Stark shift. This transition scheme could therefore form the basis of an electrically tunable source. The energy of the intrawell transition is also blue shifted in an electric field as the mixing of the transition subbands with those of the injectors is reduced. The lower current density of the interwell sample at an emission intensity, comparable to that of the intrawell sample, demonstrate the reduction of non-radiative scattering by spatial separation of the $|i\rangle$ and $|f\rangle$ subbands. A low scattering rate is an essential condition for population inversion and hence for lasing.

Acknowledgements

This work was supported by the Austrian Science Foundation (START Y47, Wittgenstein Award) and by the EU-TMR Program (INTERACT).

Reference

- [1] M. Rochat, J. Faist, M. Beck, U. Oesterle, M. Illegems: “Far-infrared ($\lambda= 88 \mu\text{m}$) electroluminescence in a quantum cascade structure” *Appl. Phys. Lett.*, vol. 73, pp. 3724 – 3726, 1998.
- [2] J. Ulrich, R. Zobl, N. Finger, K. Unterrainer, G. Strasser, E. Gornik: “Terahertz electroluminescence in a quantum cascade structure”, *Physica*, vol. B 272, pp. 216 – 218, 1999.
- [3] B. S. Williams, B. Xu, Q. Hu, M. R. Melloch: “Narrow-linewidth terahertz intersubband emission from three-level systems”, *Appl. Phys. Lett.*, vol. 75, pp. 2927 – 2929, 1999.
- [4] J. Faist, F. Capasso, D. L. Sivco, C. Sirtori, A. L. Hutchinson, A. Y. Cho: “Quantum cascade laser”, *Science*, vol. 264, pp. 553 – 556, 1994.
- [5] J. Ulrich, R. Zobl, W. Schrenk, G. Strasser, K. Unterrainer, E. Gornik: “Terahertz quantum cascade structures: Intra- versus interwell transition”, *Appl. Phys. Lett.*, vol. 77, 1928 – 1930, 2000.
- [6] J. Ulrich, R. Zobl, K. Unterrainer, G. Strasser, E. Gornik: “Magnetic-field-enhanced quantum-cascade emission”, *Appl. Phys. Lett.* vol. 76, pp. 19 – 21, 2000.

Sublithographische Siliziumoxid-Strukturen für die Phasenshifttechnologie

**H. Wanzenboeck¹, S. Gergov¹, U. Grabner², P. Pongratz², H. Störi³,
H. Hutter⁴, B. Basnar¹, J. Smoliner¹, E. Bertagnolli¹**

**¹ Institut für Festkörperelektronik, TU Wien,
Floragasse 7, 1040 Wien, Austria**

**² Institut für Angewandte und Technische Physik, TU Wien,
Wiedner Hauptstraße 8–10, 1040 Wien, Austria**

**³ Institut für Allgemeine Physik, TU Wien,
Wiedner Hauptstraße 8–10, 1040 Wien, Austria**

**⁴ Institut für Analytische Chemie, TU Wien,
Getreidemarkt 9, 1060 Wien, Austria**

Die Herstellung von Halbleiterbauelementen mittels optischer Lithographie bedient sich zur Erreichung der kleinen Strukturgrößen spezieller Methoden. In der State-of-the-art 180 nm-Technologie werden die klassischen Auflösungsgrenzen der optischen Lithographie unterschritten. Dies wird ermöglicht durch die Verwendung von kohärenten Lichtquellen und die Verwendung von Phasenshift-Masken. Die für Phasenshift-Masken typische Strukturierung des Quarzglas-Substrates selbst stellt eine wesentliche Fehlerquelle in der Maskenherstellung dar und verringern die Ausbeute deutlich. Eine Methode zur nachträglichen Reparatur von Phasenshift-Masken erlaubt eine signifikante Reduktion der Herstellkosten. Focused Ion Beam-Technologie stellt eine Methode zur lokalen Abscheidung von Siliziumoxid im sub- μm Bereich sowie zur lokalen Entfernung von Material durch Sputtern dar. In dieser Arbeit wurden die Möglichkeiten einer Maskenreparatur mittels Focused Ion Beam untersucht.

Mit einem rasterndem Ga^+ -Ionenstrahl wurde lokal auf einer Probenoberfläche eine chemische Gasphasenabscheidung (CVD) von Siliziumoxid induziert. Die Ga^+ -Ionen haben eine Energie von 50 kV und können zu einem Strahl bis zu 10 nm Durchmesser fokussiert werden. Der fokussierte Ionenstrahl induziert eine Zersetzung und Abscheidung von auf der Substratoberfläche adsorbierten Vorläufersubstanzen. Als Substrat dienen lithographische Masken, Quarz- oder Silizium-Wafer. Vorläufersubstanzen für die Siliziumabscheidung ist eine Gasmischung aus Tetramethylcyclotetrasiloxan und Sauerstoff. Die abgeschiedenen Teststrukturen haben eine laterale Ausdehnung zwischen 200 nm und 100 μm und Dicken im sub- μm Bereich.

Zur Untersuchung der optimalen Prozessführung wurde eine Variation der komplexen Abscheideparameter wie Gaszusammensetzung, Rastergröße und Scangeschwindigkeit durchgeführt. Es besteht eine Korrelation zwischen den Prozessparametern und der chemischen Zusammensetzung des abgeschiedenen Materials. Die optischen Eigenschaften des abgeschiedenen Siliziumoxides wurden ebenso charakterisiert wie die Oberflächenrauigkeit der hergestellten Strukturen. Mittels TEM Aufnahmen von Querschnitten von Siliziumoxid-Abscheidungen können Kantengeometrien sowie Interfaces zwischen Materialien detailliert untersucht werden.

Die durchgeführten Untersuchungen zeigen, dass die Focused Ion Beam-Technologie für die Maskenreparatur im sub- μm Bereich gut geeignet ist. Die Gallium-Kontamination durch den Ionenstrahl bedingt jedoch eine wesentliche Degradation der optischen Eigenschaften des abgeschiedenen Siliziumoxids. Es wird gezeigt, dass durch geeignete Prozessführung der Galliumgehalt signifikant reduziert werden kann.

GMe Presentations – Posters Cleanroom Linz

Fabrication of AlGaAs Nanostructures

T. Berer, G. Pillwein, G. Brunthaler

Institut für Halbleiter- und Festkörperphysik, Johannes Kepler Universität,
Altenbergerstraße 69, 4040 Linz, Austria

G. Strasser

Institut für Festkörperelektronik, TU Wien,
Floragasse 7, 1040 Wien, Austria

In order to investigate the electrical conductivity of nanostructures at low temperatures, different types of nanostructures were fabricated in the AlGaAs material system. The narrow lateral regions were either defined by deep etched grooves or by split gate structures on top of the samples. The electron density in the structures were additionally changed either by illumination or a large top gate Schottky contact. The formation of a 1D electron gas channel was observed.

1. Introduction

The driving force behind the investigation of solid state nanostructures is twofold. On the one hand side, the continuing miniaturization in microelectronics calls for investigation of the lower size limits for devices, on the other hand, nanostructures allow access to new fields in basic physics.

Today's miniaturization in microelectronics can be characterized by Moor's law – every 3 years, the single-chip memory size is increased by a factor of 4. The smallest structure size in this type of semiconductor devices is the gate length, which is 0.18 μm nowadays. This development in miniaturization is expected to continue at least for several years. But finally some hard physical limits will be reached. At least, when one memory unit would have the size of a single atom, a further continuation of miniaturization in the common way is hard to imagine. But other limits will be reached much earlier. If one continues to work with doped semiconductor structures, at much larger length scales one will reach the limit where only a few electrons will be in a single device, which makes the control of such a structure unreliable. Another limit is set by the wavelength of free electrons. As soon as the electrons wavelength becomes comparable with the structure size, interference and quantization effects will occur and strongly influence the functionality of such a device.

The latter limit is the starting point for a manifold of new physical phenomena. The confinement of electrons in nanostructures leads to a quantization in energies and wavefunctions. This allows, at least at low temperatures, the exact control of the state of the electrons and even allows to manipulate them individually. In quantum dots with two connecting tunneling contacts, single electron transmission due to Coulomb blockade can be achieved. Even the realization of quantum computation in solid state structures is considered nowadays.

In order to contribute to research and development in the above mentioned fields, we have established the techniques for the fabrication of nanostructures in the cleanroom facility in Linz. All necessary steps can be undertaken, including the critical electron

beam lithography and etching steps. We have chosen AlGaAs heterostructures as the starting point for the nanostructures fabrication. Figure 1 shows the internal layer structure of a typical sample. The high mobility two-dimensional (2D) electron gas is formed in the GaAs buffer layer at the interface towards the above lying AlGaAs spacer. The doping region is typically 20 nm away from the interface in order to reduce the scattering efficiency and increase accordingly the mobility of the 2D electron gas.

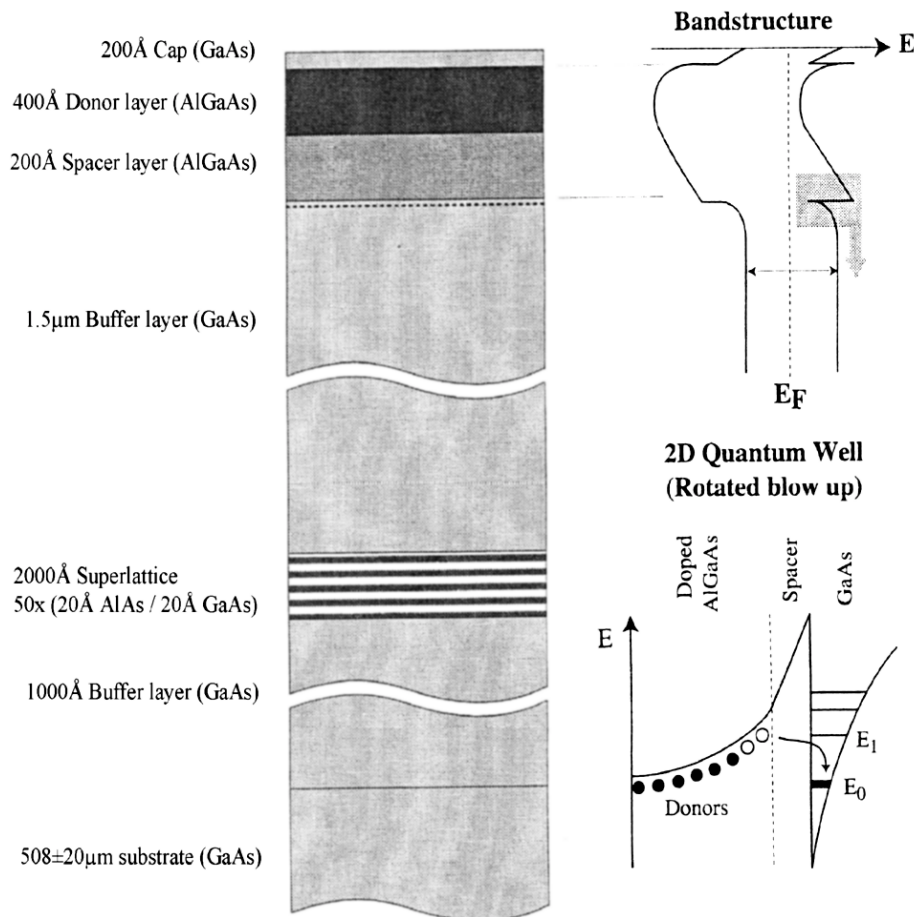


Fig. 1: The scheme on the left hand side shows a typical layer sequence of an AlGaAs heterostructure for achieving a high-mobility two-dimensional electron gas system. The upper diagram on the right hand side shows the band diagram of the heterostructure, the lower diagram displays the energy diagram in the vicinity of the electron gas on an expanded scale.

In order to be able to perform electrical measurements on nanostructures, some geometry for the electrical connections, the ohmic contacts and possible gates have to be prepared. We use a Hall bar geometry, which allows the determination of electron densities and mobilities on the same piece of heterostructure. The ohmic contacts are formed by a sequence of Cr/Ge/Au/Ni/Au which is evaporated onto the sample and annealed for 1.2 minute at 450°C. The Hall bar geometry was defined by a reversal photoresist AZ5218 and etched with CH₄ and H₂ in an “Oxford 80Plus” reactive ion etching system or in a wet chemical etch process. The different nanostructures are then prepared out of the Hall bar structures.

2. Etched Nanostructures

One kind of nanostructures is prepared by etching deep grooves into the heterostructure, which divide the 2D electron gas layer into different isolated regions. The groove structures were defined on the Hall bar by electron beam lithography with a JEOL 6400 microscope in a PMMA/MA photoresist. The etching of the structures was performed in the reactive ion etching system with CH_4/H_2 gas. The photoresist is then removed in a TEPLA asher. Wire structures with different widths between 100 and 1200 nm were produced, see Fig. 2a and 2b for 500 and 100 nm wide wires. In addition point contacts and ring structures were prepared (Fig. 2c and 2d).

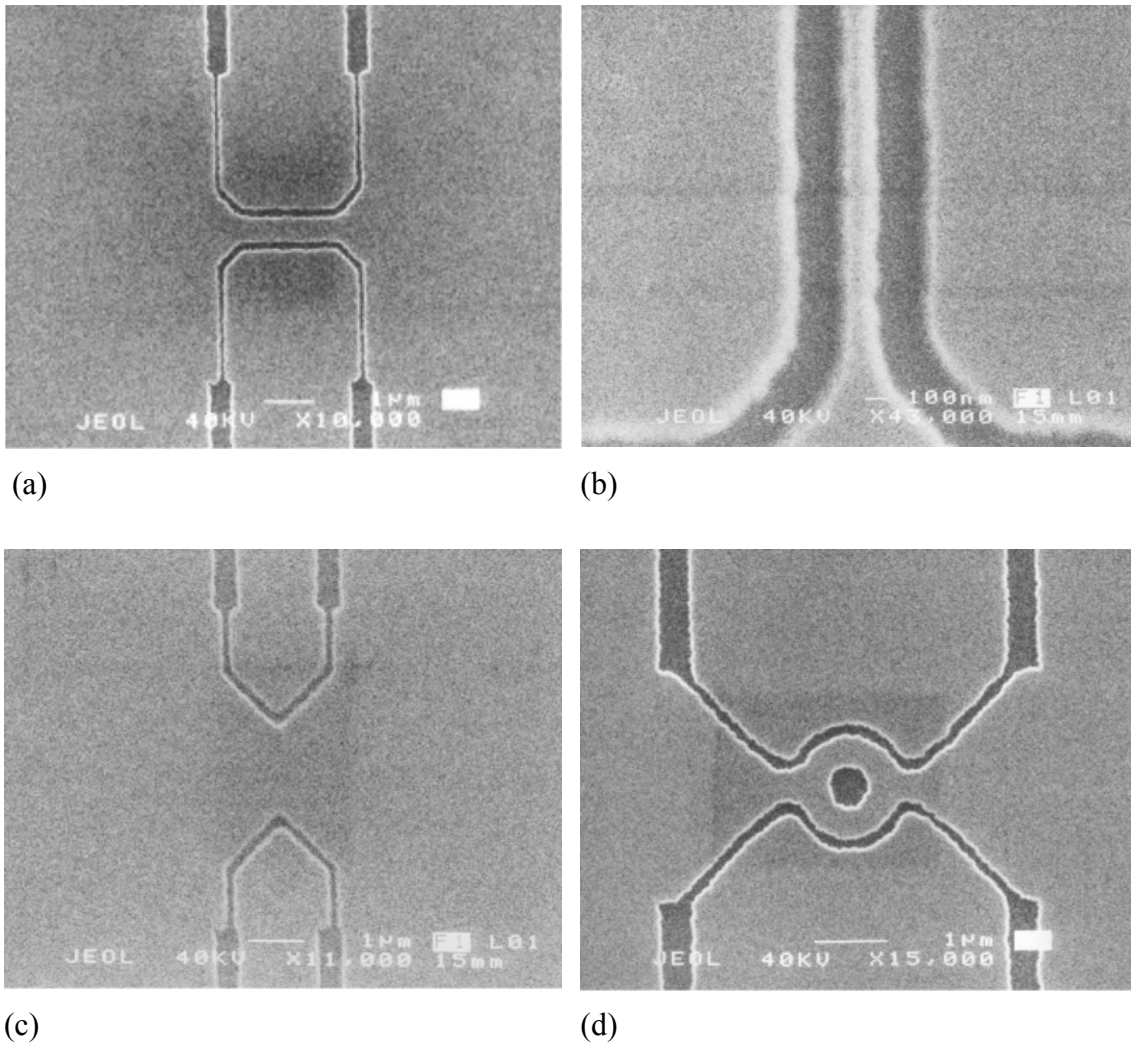


Fig. 2: (a) 2 μm long wire structure; (b) detail of a 100 nm wide wire; (c) etched point contact; (d) etched ring structure.

The electrical properties of these nanostructures were investigated. Most of the narrow structures were not conducting. This is caused by the defect states at the GaAs surface, which have a very high density close to midgap. Free electrons from the neighborhood go to those defect states leading to a depletion layer. Narrow etched nanostructure channels are thus usually not conducting in the GaAs material system. Only wider structures remain conducting despite the surface depletion.

Figure 3 shows resistivity measurements on a 400 nm wide, 2 μm long wire structure versus applied perpendicular magnetic field at a temperature of 1.5 K. As this sample had no gate, the electron density was varied via illumination with an infrared light emitting diode. Different curves in Fig. 3 correspond to different illumination intensities, where lower resistivity means higher intensity. Several curves show a step-like increase in resistivity at a magnetic field of about 0.6 T. The steps occur approximately between $1/10$ and $1/6$ of h/e^2 and between $1/6$ and $1/4$ h/e^2 and thus seem to correspond to transitions between different occupations of electron channels in the one-dimensional (1D) wire [1].

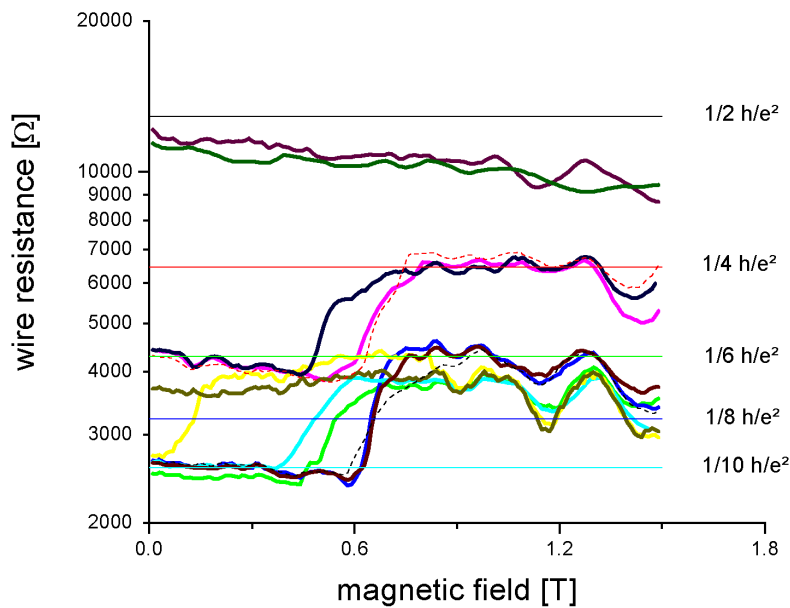


Fig. 3: Wire resistance versus magnetic field for a 400 nm wide, 2 μm long wire structure. Different curves correspond to different illumination intensities of the nanostructure with a infrared light emitting diode.

Due to the persistent photoconductivity effect, caused by DX-centers in AlGaAs structures [2], it is possible to increase the density of 2D electrons with illumination, but the density does not decrease to its previous value after switching off the illumination. Therefore it is difficult to change the density arbitrarily and the use of gated structures is desired.

3. Top Gate

By using a top gate, which covers the whole area of the 2D electrons gas together with the deep etched grooves, the electron density can be varied within a certain range. We have fabricated both a Schottky gate and an insulated metal gate on top of the structures. The area of the Schottky gate is defined in the usual way by photolithography, an Al metal layer is evaporated and the rest of the photoresist and the metallic layer is removed in the lift-off step. Figure 4 shows a sample where the surface is covered by an Al top gate. The Al layer forms itself a Schottky contact to the GaAs surface. With the

Schottky gate, the electron density n could be varied typically between 1.2×10^{11} and $4.2 \times 10^{11} \text{ cm}^{-2}$ before the leakage currents became too large. At low electron densities, where the resistivity is strongly increasing, we have observed several steps in the conductance versus gate voltage behavior, which can be attributed to transport in 1D channels.

As the Schottky gate starts to leak when the applied voltage becomes too high, we have also tested a metal gate on top of an insulating layer. As insulating layer, a PMMA/MA photoresist was used as this material is quite stable against thermal stress during cool down of the samples in a cryostat. A Ti/Au or Cr/Au layer was deposited on top of the insulation layer, the Ti (Cr) acts as an adhesive layer, the thicker Au is used as a contact layer for bonding beside the Hall bar. The samples with this kind of gate contact showed only a very small change of the electron density with applied voltage. It seems that lateral currents below the insulating layer shield the gate voltage, and the electron gas is nearly not affected.

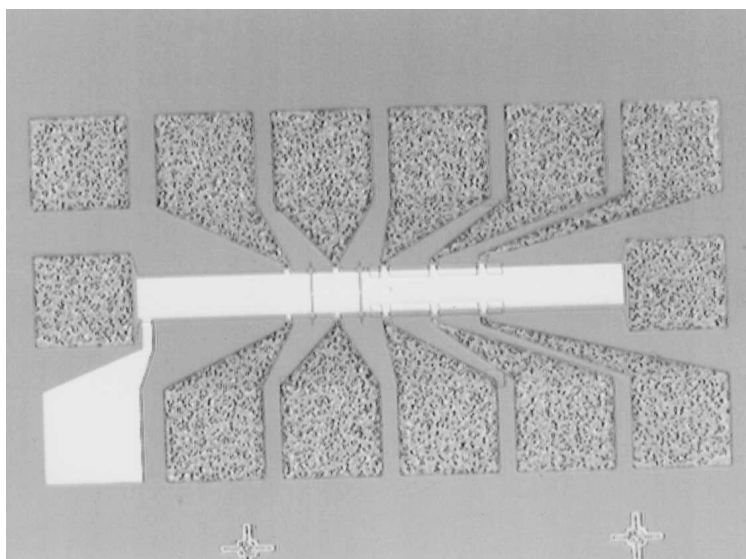


Fig. 4: Hall bar sample, where the 2D electron gas region together with the deep groove etched nanostructures is covered by an Al-Schottky gate.

4. Split Gate Nanostructures

Last but not least, split gate nanostructures were fabricated from the AlGaAs heterostructures. In these samples, a Schottky gate crosses the Hall bar from one side to the other, but leaving a narrow gap of several hundred nm width open. The narrow lateral gap in the gate was defined by electron beam lithography in the two-layer PMMA photoresist. The Al gate was produced in a lift-off step and is shown in a raster electron micrograph in Fig. 5(a).

By applying a negative voltage to both parts of the split gate, the electron density underneath can be reduced until the 2D electron gas is completely suppressed and the two conducting regions are separated. Only in the narrow restriction below the gap in the split gate, the two regions of the 2D gas are electrically connected via a 1D channel. This can be seen in Fig. 5(b) in the resistivity versus gate voltage curve as a plateau. By further increasing the negative gate voltage, also the lateral potential of the 1D channel

shrinks, and the resistivity increases further. Small steps, probably due to the quantized conductance in the 1D wire, can already be seen in Fig. 5(b). This resistivity range is most interesting as it contains the conduction through only a few 1D channels and will be investigated in more detail in the future.

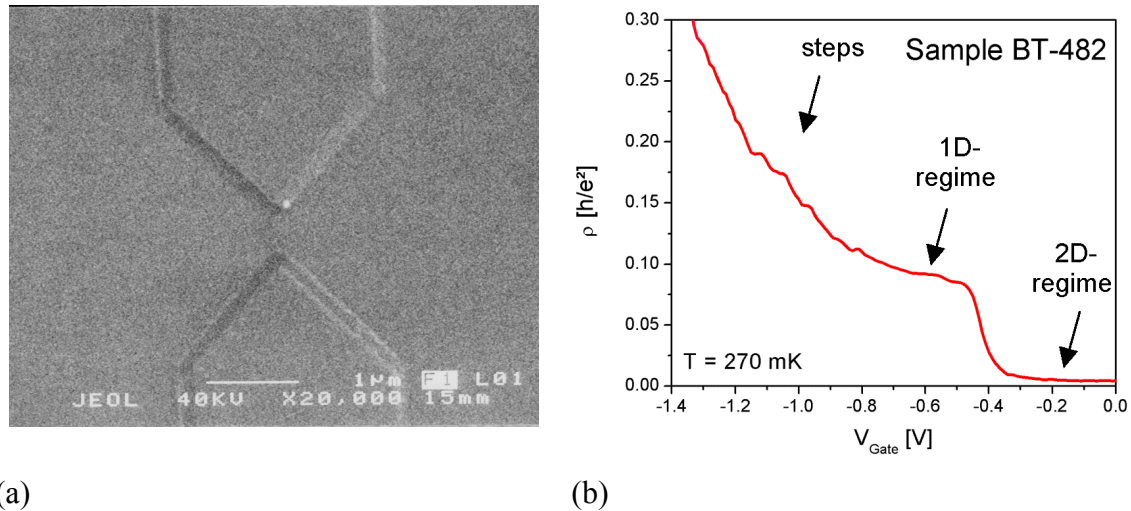


Fig. 5: (a) Split gate geometry formed by Schottky gate fingers on top of an AlGaAs heterostructure. The restriction has a lateral width of 400 nm. (b) Resistivity versus gate voltage behavior of the top gate structure.

5. Conclusion

We have fabricated several types of nanostructures on high mobility AlGaAs heterostructures. The samples with deep etched grooves suffer from the surface depletion of the GaAs material system, and it is difficult to control the conductivity for narrow lateral structures. Top gate structures worked, but the range in which the electron density can be varied is restricted due to the leakage of Schottky gates. Split gate structures were best suited to change the electron density in a narrow point contact.

Acknowledgements

We thank Poul Erik Lindelof and Rolf Haug for discussions concerning the fabrication and investigation of semiconductor nanostructures. The work was partly supported by the Austrian Science Foundation (FWF Project P13439-TPH).

References

- [1] T. Ando: "Quantum point contacts in magnetic fields", *Phys. Rev. B* **44**, 1991, pp. 8017 – 8027.
- [2] G. Brunthaler, M. Seto, G. Stöger and K. Köhler: "Influence of Coulombic broadened DX center energy levels on free electron concentration in δ -doped AlGaAs/GaAs quantum wells", *Appl. Phys. Lett.* **65**, 1994, pp. 3084 – 3086.

Strain Modulations in Si Underneath Patterned Oxide Stripes

A. Daniel, Y. Zhuang, J. Stangl, T. Roch, V. Holý, G. Bauer

Institut für Halbleiter- und Festkörperphysik, Johannes Kepler Universität,
Altenbergerstraße 69, 4040 Linz, Austria

We present a characterization method for lateral strain modulations in Si substrates underneath laterally patterned periodic SiO₂ stripes. For the investigations, the x-ray grazing incidence diffraction (GID) technique was applied to enhance the sensitivity to the interface near regions. Apart from a tensilely strained part below the oxide lines, we find two compressively strained regions close to the edges of the stripes. Furthermore, the experimental GID results clearly show the depth dependent in-plane strain distribution. These data are relevant for electronic transport, particularly in short channel structures.

1. Introduction

With the continuing miniaturization of electronic device structures, inhomogeneous strain distributions of various origins become more and more important for the electronic transport. Consequently, information on these surface-near strain distributions in nanostructures has to be obtained with sufficiently high resolution. Among the x-ray diffraction techniques, grazing incidence diffraction (GID) is particularly well suited for such investigations. Several groups [1] – [3] have employed this technique for the study of heterostructures and of buried nanostructures. However, the quantitative analysis of GID data requires the use of either the fully dynamical diffraction theory, which is barely treatable, or as a simpler approach, the distorted wave Born approximation (DWBA) [4] – [5]. As a suitable model system we have chosen a laterally periodic SiO₂ layer on a Si substrate, for the following reasons: (i) Silicon dioxide is widely used for the fabrication of high-density semiconductor integrated circuit devices. In particular, with their shrinking dimensions, the structure and the quality of the interface between the oxide and the Si substrate are crucial for the performance and reliability of the devices. Additionally, the evolution of internal stresses during the conversion of Si into SiO₂ becomes more and more important in these miniaturized structures. These stresses mainly originate from the thermal expansion mismatch created by the oxidation process. (ii) Due to the amorphous nature of the oxide, the scattered intensity distribution in an x-ray diffraction experiment results only from the strain distribution in the single crystalline Si substrate. This clear-cut situation allows to include not only transmission and specular reflection into the undisturbed wave fields in the DWBA-simulations, as it was done previously [2], but also diffraction. Coplanar high angle diffraction technique yields only information on the average strain in the Si substrate, whereas GID provides a depth sensitivity due to incidence and exit angles close to the critical angle of total external reflection [6].

2. Experiment

We started from a Si (001) wafer with a 100 nm thermal SiO₂. In order to estimate the value of the effective linear mismatch $\chi = (\langle a \rangle_{\text{SiO}_2} - a_{\text{Si}})/a_{\text{Si}}$ the curvature of the sample was measured using x-ray diffraction in transmission geometry. $\langle a \rangle_{\text{SiO}_2}$ is the mean distance of the Si atoms in the amorphous SiO₂, and a_{Si} the bulk lattice parameter of silicon. From the curvature we obtain a range of $3.4 \times 10^{-3} \leq \chi \leq 5.7 \times 10^{-3}$. The error of the curvature measurements is quite large and does not allow for an accurate determination of χ . After the curvature measurement, the oxide was structured into laterally periodic stripes by holographic lithography and an etching step. The stripes were oriented along the [-110] direction and had a period of about 800 nm. The height of the stripes, examined by atomic force microscopy, was about 100 nm, and the width of the stripes was 350 nm.

Quantitative strain calculations based on the finite element method were performed to obtain the strain distribution in the Si substrate. Since the effective mismatch χ depends sensitively on the particular growth parameters and can only be determined with some uncertainty from the curvature measurements, we use it as a fit parameter. We finally obtained the best correspondence with the x-ray measurements using a value of $\chi = 4.3 \times 10^{-3}$. Figure 1 shows the resulting contour plots for different components of the strain tensor $\boldsymbol{\epsilon}$. Directly underneath the SiO₂, a tensile force is exerted in the Si substrate which leads to a larger in-plane lattice constant compared to unstrained bulk Si. In between the SiO₂ stripes the Si in-plane lattice constant becomes smaller than that of unstrained bulk Si, corresponding to a compressed strain state.

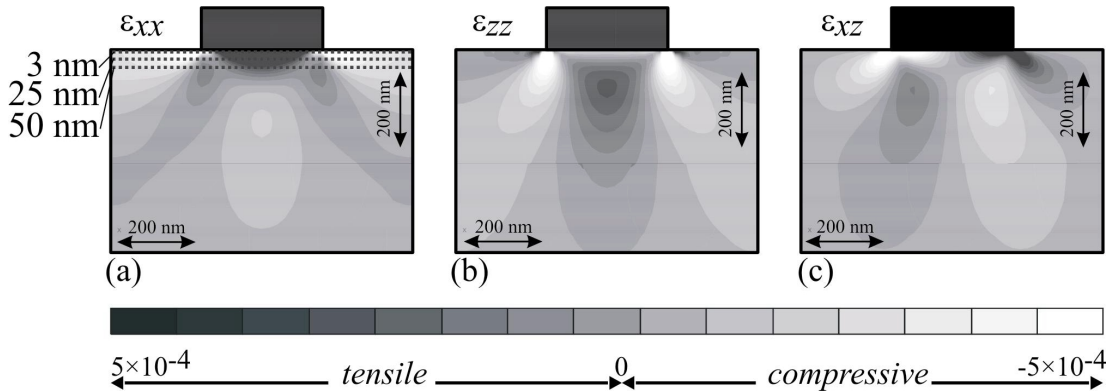


Fig. 1: Contour plots of the strain components (a) ϵ_{xx} , (b) ϵ_{zz} and (c) ϵ_{xz} based on finite element calculations for SiO₂ shadow mask and Si substrate.

Additionally, a compressively strained region appears in a larger depth > 100 nm below the center of the SiO₂ stripes. In the coplanar x-ray diffraction experiments, the whole region contributes to the detected signal, impeding a distinction between regions near and far from the Si–SiO₂ interface. In Fig. 2, ϵ_{xx} values for different depths in the Si substrate are shown, as indicated in Fig. 1(a).

For obtaining experimental information on such strain gradients in the Si substrate, GID experiments have been performed. In GID, the scattering plane is nearly parallel to the sample surface. If the angles of incidence α_i and exit α_f are close to the critical angle of the total external reflection α_c , the penetration depth of the x-ray beam depends very sensitively on α_i and α_f . It changes typically from 5 nm for $\alpha_i < \alpha_c$ to several μm for

$\alpha_i > \alpha_c$. Moreover, it is possible to choose the diffraction vector \mathbf{h} either parallel (2-20) or perpendicular (220) to the stripes. In the first case the diffracted intensity depends only on the shape of the stripes.

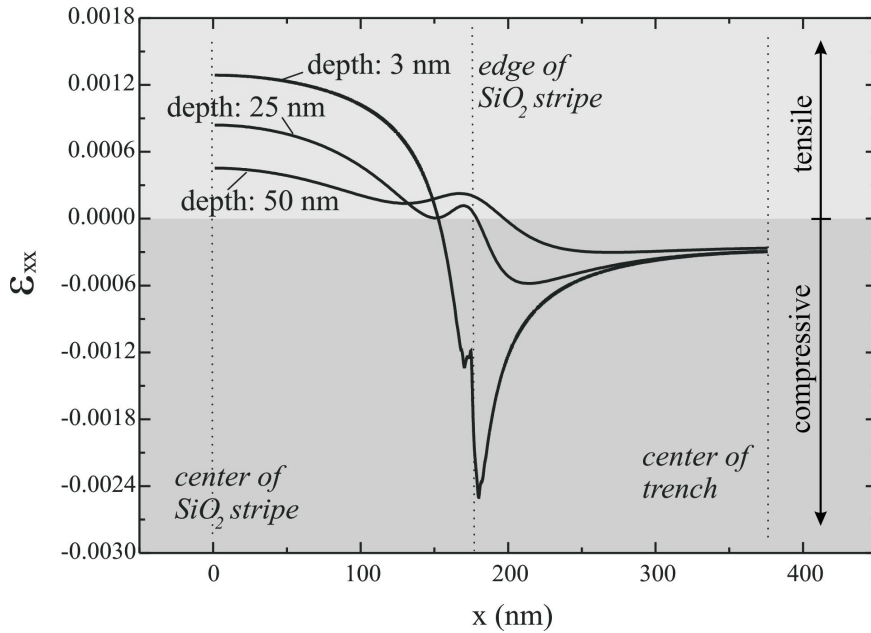


Fig. 2: Dependence of the strain tensor component ϵ_{xx} on lateral position in Si for three different depths below the interface.

In our case, the stripes are amorphous and thus in this geometry only a central peak at the position determined by the bulk Si lattice constant and no lateral peaks appear. This fact proves that the etching indeed stopped at the Si/SiO₂ interface and the Si substrate remains unpatterned.

In the second case, with the diffraction vector (220) perpendicular to the stripes, the intensity distribution depends both on shape and strain. However, in our case only the strain distribution in the crystalline Si accounts for the diffracted intensity distribution, reflecting both compressively ($q_x > 0$) and tensilely ($q_x < 0$) strained regions. Figure 3(a) shows longitudinal line scans measured around the (220) reciprocal lattice point for several angles α_i , keeping $\alpha_f = 0.20^\circ$. The appearance of the satellite peaks proves the presence of the lateral periodic strain modulation in the Si substrate with a period of 765 nm. The envelope of the intensity distributions exhibits a slight dependence on the incidence angle α_i . For the simulation of the measured data we have to solve the problem of GID from a periodically strained semi-infinite crystal with a flat surface, since the SiO₂ stripes act only as stressors and they do not contribute to the diffraction process.

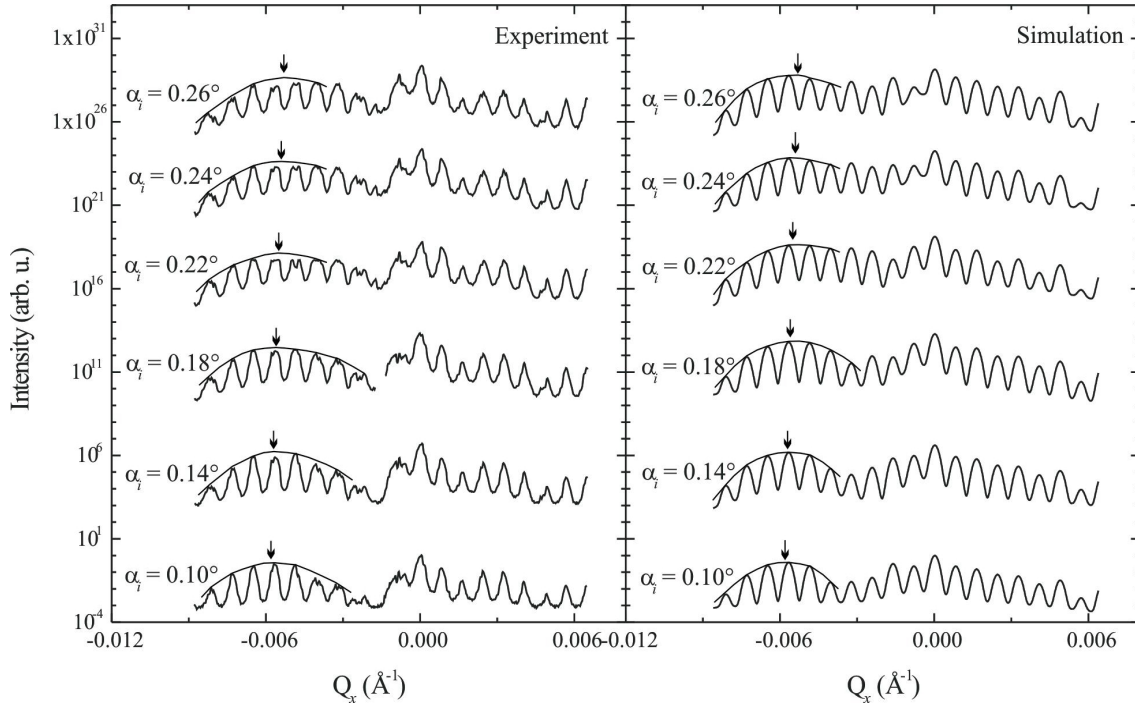


Fig. 3: Longitudinal line scans around the (220) reciprocal lattice point. (a) Experimental data, (b) simulations. For the tensilely strained regions, the envelope curve is indicated.

3. Results and Discussion

We calculated the dependence of the scattered intensity I on q_x using DWBA. A detailed description of the simulation model is given in Ref. [7]. The most significant influence of the effective mismatch χ on the simulations is found for values of $q_x < 0$ corresponding to the tensilely strained Si. Changing χ shifts the envelope curve and the best correspondence was found for $\chi = (4.3 \pm 0.2) \times 10^{-3}$ (see Fig. 3(b)). Furthermore, the experimental data demonstrate clearly the presence of compressively strained regions in Si near the interface to the stripes. While for the tensilely strained regions beneath the stripes the lateral period is the same as for the stripes, two compressively strained regions exist near the surface at each edge of the SiO₂ stripes. Thus the lateral peaks for $q_x > 0$ exhibit an additional modulation. This is qualitatively well reproduced by the simulations.

4. Summary

A periodic array of SiO₂ stripes on the Si surface exerts a periodic stress field on the surface that results in a deformation field periodic in the direction perpendicular to the stripes. We have investigated this deformation field by grazing-incidence x-ray diffraction. The deformation field in the plane perpendicular to the stripes has been calculated by the finite element method. Using this result, the x-ray diffraction patterns were successfully simulated. These simulations have been performed by means of the distorted-wave Born approximation assuming a perfect crystalline substrate as an undisturbed system.

References

- [1] T. Baumbach, D. Lübbert, M. Gailhanou, *J. Appl. Phys.* **87**, 3744 (2000).
- [2] A. Ulyanekov, N. Darowski, J. Grenzer, U. Pietsch, K.H. Wang, and A. Forchel, *Phys. Rev.* **B60**, 16701 (1999).
- [3] S. Tanaka, C.C. Umbach, Q. Shen, and J.M. Blakely, *Mat. Res. Soc. Symp. Proc.* **405**, 109 (1996).
- [4] S.K. Sinha, E.B. Sirota, S. Garoff, and H.B. Stanley, *Phys. Rev.* **B38**, 2297 (1988).
- [5] V. Holý, U. Pietsch, and T. Baumbach, *High-Resolution X-Ray Scattering From Thin Films and Multilayers*, (Springer Tracts in Modern Physics Vol. 149. Springer-Verlag Berlin, Heidelberg, New York, 1999).
- [6] U. Pietsch, T.H. Metzger, S. Rugel, B. Jenichen, and I.K. Robinson, *J. Appl. Phys.* **74**, 2381 (1993).
- [7] A. Daniel, V. Holý, Y. Zhuang, T. Roch, J. Grenzer, Z. Bochnicek, and G. Bauer, *J. Phys. D: Appl. Phys.*, (2000) in print.

Characterization of Si/Si_{1-x-y}Ge_xC_y Heterostructures for Device Applications

D. Gruber, M. Mühlberger, F. Schäffler

Institut für Halbleiter- und Festkörperphysik, Johannes Kepler Universität,
Altenbergerstraße 69, 4040 Linz, Austria

With the commercial introduction of the Si/SiGe heterobipolar transistor (HBT) into main-stream integration technologies, process compatibilities become an important issue. A basic problem is, for example, the transient enhanced diffusion (TED) of boron out of the SiGe base layer upon thermal activation of the poly-emitter implant. As a remedy, the use of a carbon co-doped base has been proposed, in which a carbon concentration of a few tenths of an atomic percent have been shown to very efficiently suppress TED. On the other hand, great effort has been dedicated in the past to reduce the carbon concentrations in Si ingots as far as possible, because of the propensity of C to form complexes and β -SiC precipitates. In contrast to substitutional C, some of these complexes are known to introduce electrically active states in the band gap. It is therefore important to characterize the microscopic configuration in which C is present after processing of SiGe:C HBTs.

We addressed this problem by a combination of Fourier Transform IR spectroscopy (FTIR), x-ray diffraction, and SIMS studies on MBE-grown HBT structures with implanted poly-Si emitter. With the FTIR technique we are sensitive to substitutional/interstitial C and different forms of C-C configurations. By proper calibration of the active and reference sample thicknesses we achieve very high sensitivities regarding substitutional C, β -SiC precipitates and some carbon complexes. From this, together with the chemical information we get from SIMS, we find that both complexes, C-C and SiC precipitates play a role in the process.

Magnetic Properties of Thin Iron Films

K. Himmelbauer, H. Sitter, H. Krenn

Institut für Halbleiter- und Festkörperphysik, Johannes Kepler Universität,
Altenbergerstr. 69, 4040 Linz, Austria

The incorporation of magnetic layers in semiconductor heterostructures is an increasingly active area of study. There is a great interest in the catalytic, electronic, and magnetic properties of transition metal overlayers on semiconductor substrates in thin film form. Since the metal-semiconductor interface plays an important role in thin film heterostructures, the initial stages of overlayer growth determine the morphology and crystalline structure of subsequent growth. Thin film properties often differ significantly from bulk properties due to surface and interface effects dominating the overall behavior of these films. Iron films show a broad range of magnetic properties depending on film thickness and deposition conditions. We investigate the influence of the initial substrate surface reconstruction on the magnetic behavior of iron films both on GaAs substrates as well as on ZnSe epilayers. Surface reconstruction leads to magnetic anisotropies dominated by an in-plane uniaxial component. We study the growth of ferromagnetic iron to determine the mode of film growth, the interface formation, and the magnetic film properties. Films are characterized by various methods: surface reconstructions are determined by Reflection High Energy Electron Diffraction (RHEED) and magnetic properties by Superconducting Quantum Interference Device (SQUID) measurements with the magnetic field applied along different in-plane directions.

1. Introduction

The growth of single-crystal ferromagnetic films on semiconductor substrates and the incorporation of metal layers in semiconductor heterostructures has attracted considerable attention due to its compatibility with planar electronics (e.g. for inducing magnetic fields in dilute magnetic semiconductors) and due to its potential for spin-sensitive heterostructure devices.

Body-centered cubic (bcc) α -iron is preferentially deposited on GaAs and ZnSe due to the slight lattice mismatch (1.5 % and 1.1 %, respectively). By variation of film thickness and deposition conditions iron films show a broad range of magnetic properties. In this paper we present the influence of the surface reconstruction of the substrate and the influence of the film thickness on the magnetization curves obtained by superconducting quantum interference device measurements.

2. Experimental

A new ultrahigh vacuum chamber, designed for the growth of bcc α -iron and described earlier [1], has been attached to an existing MBE-system allowing us to grow iron directly on (001) GaAs substrates or on ZnSe epilayers.

Prior to growth the (001) GaAs substrates are heated up to 720 °C and kept at that temperature till a streaky RHEED pattern indicates deoxidation of the substrates, usually for a few seconds.

The ZnSe epilayer is grown by ALE (Atomic Layer Epitaxy) [2] in the following way: The shutter of the Zn effusion cell is kept open for 3 sec. After a delay time of 0.5 sec, in which all shutters are closed, the shutter of the Se effusion cell is open for 3 sec. Another delay time of 0.5 sec finishes one growth cycle during which one monolayer of ZnSe is grown. Therefore the substrate with a temperature of 300 °C is exposed to only one kind of source material at one time. The ALE-growth of ZnSe starts with Zn and finishes with Se leading to a Se-terminated surface. The thickness of the ZnSe epilayer is chosen to be 500 Å, which is below the critical thickness at which dislocations start to form.

Figure 1 shows a typical RHEED pattern observed after growth of ZnSe. The distance between the streaks corresponds to a (2x4) reconstruction.

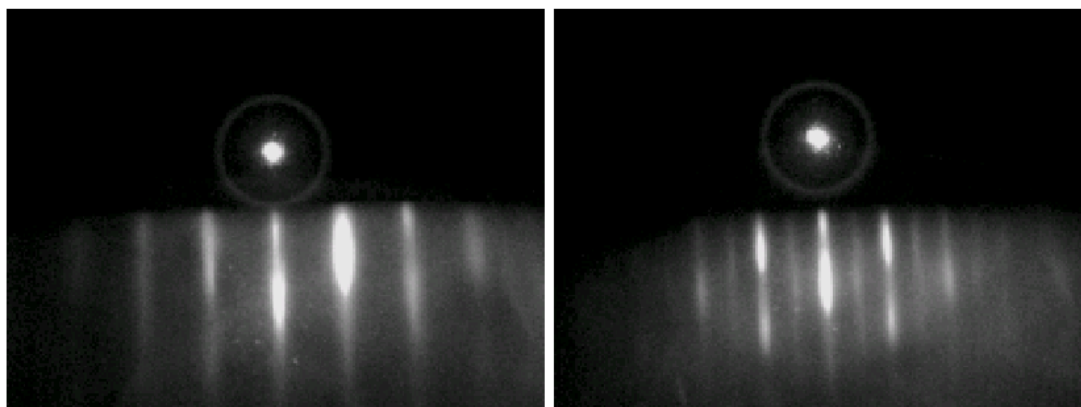


Fig. 1: RHEED pattern along the two [110] directions observed after growth of 500 Å ZnSe in ALE-mode on (001) GaAs.

After ZnSe growth the sample is cooled down to 150 °C and then transferred to the iron chamber via an UHV tunnel without breaking the vacuum. The iron chamber is equipped with an electron beam evaporation source due to the low vapor pressure of iron and the high source temperature required. For details see [1].

The iron layer is grown at a substrate temperature of 165 °C and with a growth rate of approximately 10 Å/min. The thicknesses of the iron films are in the range of 20 – 120 nm. After growth of iron RHEED patterns are taken still in UHV without the effects of oxidation. Then the iron samples, which are not covered with a capping layer, are exposed to air and oxidize. The films are characterized by SQUID measurements with the magnetic field applied along the [100] and [110] in-plane directions.

3. Results and Discussion

Figure 2 shows the results of SQUID measurements taken on a 60 nm thick Fe film on a ZnSe epilayer. There is a shift in horizontal direction due to an offset of the SQUID magnetometer. (Without offset the curves are symmetric with respect to the vertical axis.) For all measurements the magnetic field is applied in the plane of the Fe film.

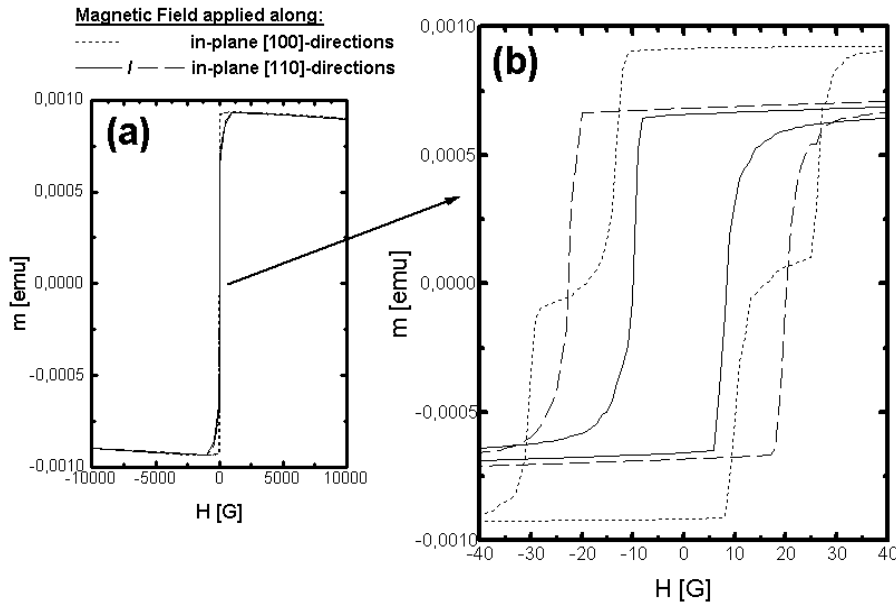


Fig. 2: Magnetic moment, m , versus applied magnetic field, H , obtained from SQUID measurements. (a) Iron film (60 nm thick) on a ZnSe epilayer; (b) magnification of (a) for low magnetic fields.

The curves of magnetization versus applied magnetic field indicate a saturation of magnetization at low magnetic fields (at 50 G and 750 G for the [100] and [110] direction, respectively). It is clearly visible that the [100] axis is the easy axis of magnetization while the [110] axis is the intermediate axis of magnetization as it is expected for a 60 nm thick film [3].

3.1 Magnetic Field Applied Along In-Plane [100] Directions

By taking a closer look at the magnetic behavior for low applied fields (see Fig. 2) we observe no rectangular hysteresis with one jump in magnetization, but a hysteresis containing two irreversible jumps of the magnetization when increasing/decreasing the magnetic field.

This behavior strongly depends on the thickness of the iron layer: For Fe films with a thickness between 20 and 30 nm we observe a hysteresis with only one jump, whereas the Fe films with a thickness between 60 and 120 nm show the two-jump-behavior.

This can qualitatively be explained by evaluating the energy density E of a magnetic thin film with the in-plane magnetization vector \vec{M} :

$$E = -\vec{M} \cdot \vec{H} + K_1 \cdot (\hat{a}_1^2 \hat{a}_2^2 + \hat{a}_2^2 \hat{a}_3^2 + \hat{a}_3^2 \hat{a}_1^2) + K_u \cdot \sin^2 \theta$$

where \vec{H} is the applied magnetic field, K_1 is the fourth-order cubic anisotropy, α_i are the direction cosines of the magnetization with respect to the cubic axes, K_u is a uniaxial in-plane second-order anisotropy, and θ is the angle between the magnetization and the in-plane [110] axis.

The ratio K_u/K_1 is crucial for determining the hysteresis. For the magnetic field applied along the [100] direction the hysteresis shows one jump for $|K_u/K_1| > 1$ (range (1)), two jumps for $1 > |K_u/K_1| > 0,3$ (range (2)) and again one jump for $0,3 > |K_u/K_1|$ (range (3))

[4]. In range (1) the magnetic field, at which the irreversible jump in the magnetization occurs, decreases with decreasing ratio K_u/K_1 . In range (2) the value of the magnetic field at the first jump increases and for the second jump decreases with decreasing ratio K_u/K_1 .

The evolution of the hysteresis with film thickness for our samples exactly agrees with the behavior predicted by the model: Films with thicknesses of 20 and 30 nm show a hysteresis with one irreversible jump of the magnetization with decreasing jump-field for increasing film thickness, whereas films with thicknesses of 60 and 120 nm show two jumps in the hysteresis. By assuming a decreasing ratio K_u / K_1 with increasing film thickness the fields for the jumps behave according to the model described above. Apparently the ratio K_u/K_1 is larger than 1 for Fe films between 20 nm and 30 nm thick while for the thicker films (60 – 120 nm) K_u/K_1 is between 0,3 and 1.

From this thickness behavior we conclude that the uniaxial anisotropy resulting in the inequivalence of the two in-plane [110]-directions is induced by the interface. Another important fact must be mentioned: We observe hysteresis curves with two irreversible jumps only for the Fe films on a ZnSe epilayer, whereas the Fe films grown directly on GaAs show only one jump in the magnetization for the complete thickness range !

This behavior can be explained in the following manner: By deoxidizing the GaAs-substrate prior to growth of iron directly on GaAs, there is no specific background pressure. Therefore after deoxidation we find Ga- and As-dimers at the surface, which are oriented along the $[110]$ and $[\bar{1}10]$ directions [5].

On the contrary by the insertion of a ZnSe epilayer, deposited by atomic layer epitaxy as described in the previous section, we have a Se-terminated surface due to the finishing epitaxy step with the Se shutter open, where the Se-dimers are oriented along the $[\bar{1}10]$ -direction [6].

For a (2x4)-reconstruction the dimer bond is parallel to the $[\bar{1}10]$ -axis as a result of the orientation of the dangling bonds, and the (2x4)-surface has a pronounced rowlike structure along $[\bar{1}10]$ due to the missing Se-dimer rows. Therefore, the axis perpendicular to the missing dimer rows, which characterize the surface reconstruction of the ZnSe, is an easy axis, whereas the axis parallel to the missing dimer rows is a hard one [5]. Due to the (2x4) surface reconstruction the two in-plane [110]-directions become inequivalent, expressed by the last term in Eq. 1 where θ is the angle between the magnetization and the [110] direction.

The uniaxial anisotropy originates in the interface between ZnSe and Fe and decreases with increasing film thickness, whereas the cubic anisotropy due to the crystal stays independent of the film thickness. This leads to a decreasing ratio K_u/K_1 with increasing film thickness, which has also qualitatively been determined from the evolution of the hysteresis curves.

3.2 Magnetic Field Applied Along In-Plane [110]-Directions

By comparing the hysteresis curves for the magnetic field applied along the two [110] in-plane directions (see Fig. 2), we notice that the magnetic fields of the irreversible jump of the magnetization are different for the two [110] directions by a factor of approximately 2.4. This also clearly indicates that one of the two in-plane [110] directions

is an easy axis for the magnetization, while the other one is a hard axis. This confirms the discussion given above.

In summary there are two contributions determining the hardness of the different in-plane axes: The cubic anisotropy, which distinguishes the [100] (easy) from the [110] (hard) axis, and the uniaxial axis, which leads to the inequivalence of the [110] and the $\bar{[110]}$ axis. These two contributions combine in a way as theoretically predicted in [7].

4. Conclusion

In summary we have presented (001) iron films with different thicknesses deposited both directly on GaAs as well as on ZnSe epilayers. While the iron films on GaAs show a rectangular hysteresis in the M versus H curves (magnetic field parallel [100]) with one irreversible jump of the magnetization for the whole thickness range, the iron films on the ZnSe epilayer exhibit a different magnetic behavior: The hystereses of thin films (20 – 30 nm) contain only one irreversible jump, but thicker films (60 – 120 nm) lead to hysteresis curves with two irreversible jumps.

This behavior originates in the Fe – ZnSe interface. The ZnSe epilayers are grown by atomic layer epitaxy, where the Se-terminated surface contains a rowlike composition of dimers resulting in inequivalence of the two [110] in-plane directions.

Measurements of M versus H curves with the magnetic field applied along the in-plane [110]-directions are in agreement with the results of the [100]-measurements.

References

- [1] K. Bierleutgeb, H. Sitter, H. Krenn, and H. Seyringer: *Phys. Status Solidi B*, 220, 2000, 41.
- [2] H. Sitter, and W. Faschinger: *Thin Solid Films* 225, 1993, p. 250.
- [3] J. J. Krebs, F. J. Rachford, P. Lubitz, and G. A. Prinz: *J. Appl. Phys.* 53, 1982, p. 8058.
- [4] C. Daboo, R. J. Hicken, D. E. P. Eley, M. Gester, S. J. Gray, A. J. R. Ives, and J. A. C. Bland: *J. Appl. Phys.* 75, 1994, p. 5586.
- [5] E. M. Kneedler, B. T. Jonker, P. M. Thibado, R. J. Wagner, B. V. Shanabrook, and L. J. Whitman: *Phys. Rev. B* 56, 1997, p. 8163
- [6] A. Ohtake, T. Hanada, T. Yasuda, K. Arai, and T. Yao: *Phys. Rev. B* 60, 1999, p. 8326.
- [7] C. Daboo, R. J. Hicken, E. Gu, M. Gester, S. J. Gray, D. E. P. Eley, E. Ahmad, and J. A. C. Bland: *Phys. Rev. B* 51, 1995, p. 15964.

Reflection Difference Spectroscopy on II- VI Semiconductors; A Tool to Investigate Surface Processes *in situ* During Growth

Kurt Hingerl

Institut für Halbleiter- und Festkörperphysik, Johannes Kepler Universität,
Altenbergerstraße 69, 4040 Linz, Austria

As the materials and structures of semiconductor technology become more complex, interest in developing real time process monitoring techniques during crystal growth is rapidly increasing. Optical Probes are best suited to be applied simultaneously with crystal growth, because they are non-invasive and non-destructive. A technique currently strongly used is *Reflectance Difference Spectroscopy* (RDS), which can monitor *in situ* surface processes in real time under UHV (MBE, ALE) as well as under atmospheric pressure (CBE, OMCVD) conditions. The measured signal is the difference between the near normal incidence reflectances of light linearly polarized along the two principal axes is investigated as a function of time, photon energy, and/or surface condition. For cubic materials the uninteresting bulk reflection cancels in subtraction, leaving the signal from the lower symmetry surface. However, there are also identified sources for bulk anisotropy for zincblende (001) surfaces which break the 4-fold rotational symmetry. We mention spontaneous ordering, the linear electro-optic effect, dislocations, and quantum confinement.

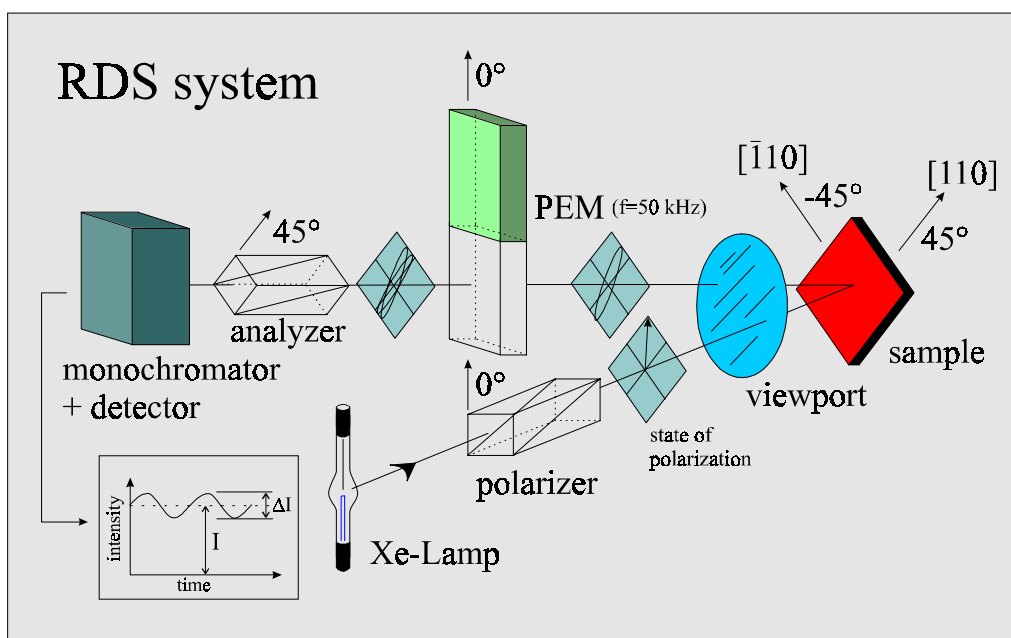


Fig. 1: The alignment of the optical components of the RDS system

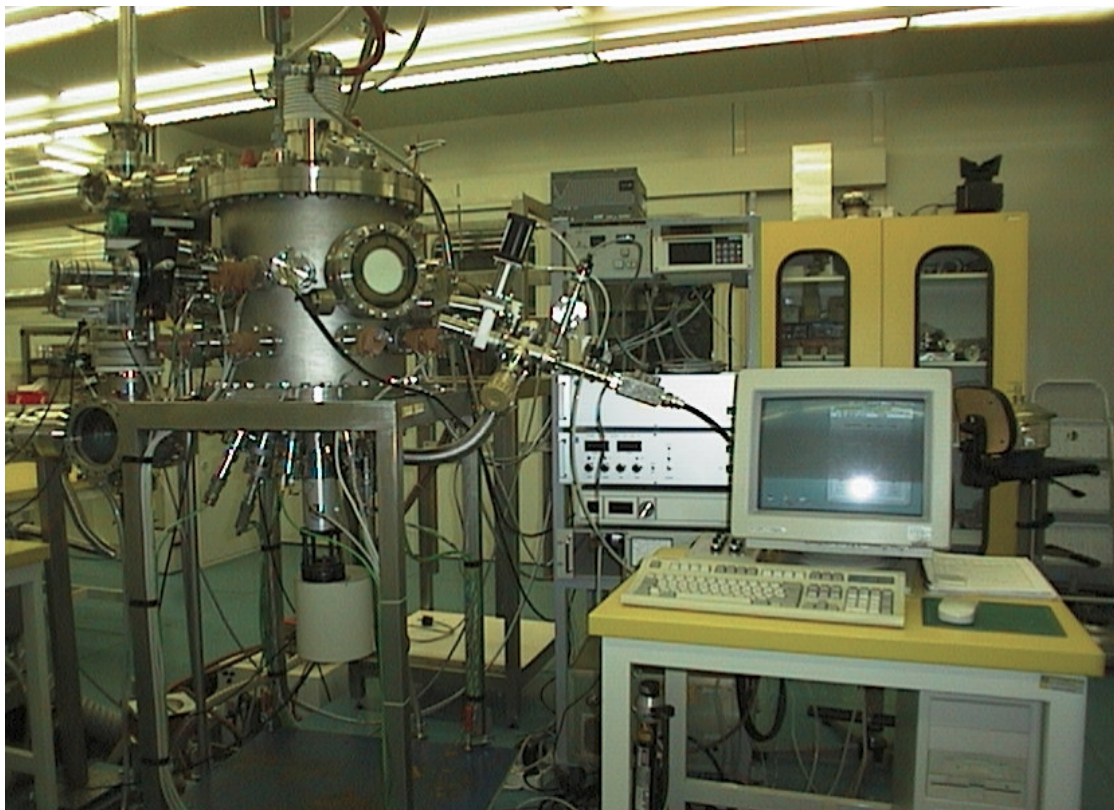


Fig. 2: A photo of the experimental setup of the UHV MBE chamber with the attached RDS in the cleanroom at Linz University (arrow).

Within the last years the understanding of information delivered by RDS and of kinetic RD data has grown considerably, however full exploitation of the power of these optical techniques needs further investigations, particularly when heteroepitaxial systems are concerned. Therefore, since the beginning of the work in February 1997, the major effort was directed onto these topics in II-VI semiconductors:

1. *In situ* determination of in plane stress and strain anisotropy in ZnSe/ZnTe/CdTe (001) Layers on GaAs.
2. On the origin of resonance features in RDS data of silicon.
3. *In situ* observation of stress relaxation in CdTe/ZnTe heterostructures by reflectance-difference spectroscopy at the critical thickness

ad 1) Is there an anisotropic in plane strain occurring due to dimerization for II-VI compounds? Furthermore we tried to find a theoretical description connecting the symmetry of the wave-functions and the polarization dependence of the optical transition matrix elements with the measured spectra (Bikus and Pir Hamiltonian) [6], [10]. Using reflectance difference spectroscopy we showed that Te surface termination on ZnTe induces, due to stress occurring from dimerization and the piezo-optic effect, a dichroism at the E_1 and $E_1 + \Delta_1$ critical points of the dielectric function of the ZnTe. The influence of Te dimers on the stress field in the epilayer was proven by comparing with *ex situ* measurements of anisotropically stressed ZnTe layers and *in situ* by enhancing the stress effect by inserting one atomic plane of Cd. Under Zn termination no stress was induced.

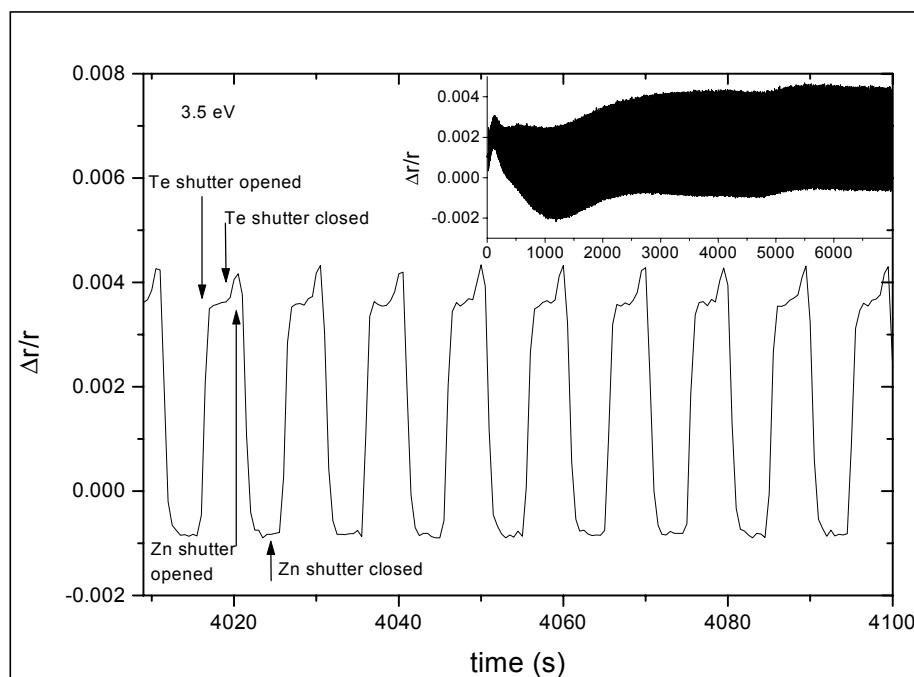


Fig. 3: Kinetic RD data taken during ALE growth of ZnTe (001) grown on GaAs at a photon energy of 3.5 eV. The inset displays RD data on a longer time scale.

ad 2) This also enabled us to shed light on the origin of sharp resonances in reflectance difference spectroscopy (RDS) data at the critical points of the dielectric function of bulk Si: The physical origin of sharp resonances in reflectance difference spectroscopy (RDS) data at the critical points of the dielectric function of bulk Si, previously assigned to surface-bulk transitions, to photon localization or to optical transitions from bound dimer states to excited dimer states was investigated. We show that uniaxial in-plane stress of bulk Si induces sharp resonances at exactly these critical points of Si via the piezo-optic effect. In the recent literature it was shown that surface reconstruction as well as dimerization exerts anisotropic stress, e.g. along the dimer direction, and the resulting strain is extending into the bulk. In our contribution we simulate this surface strain by externally stressing different Si faces and comparing *ex situ* measured RDS data of Si(001), Si(111), and Si(110) surfaces with RDS data measured *in situ* and density functional theory calculations.

ad 3) Understanding where the RDS features come from enabled us also for the first time to observe *in situ* the stress relaxation in CdTe/ZnTe heterostructures by reflectance-difference spectroscopy at the critical thickness. The first stages of epitaxial growth of CdTe on ZnTe and ZnTe on CdTe are monitored with reflectance difference spectroscopy. Spectroscopic reflectance difference data show strong optical anisotropy responses at the critical points of the bulk dielectric function at E_0 , E_1 and $E_1 + \Delta_1$ inter-band transitions of ZnTe, respectively CdTe, which indicate that anisotropic in-plane strain occurs during epitaxial growth. Applying a model it is possible to determine the in-plane strain due to the misbalance of 60° dislocations along the $[1\bar{1}0]$ and $[110]$ directions. Kinetic reflectance difference data taken at the E_1 transition of the respective material exhibit with an accuracy of one monolayer the onset of the formation of misfit dislocations for these material systems. An example of this kinetic behavior is shown in Fig. 5.

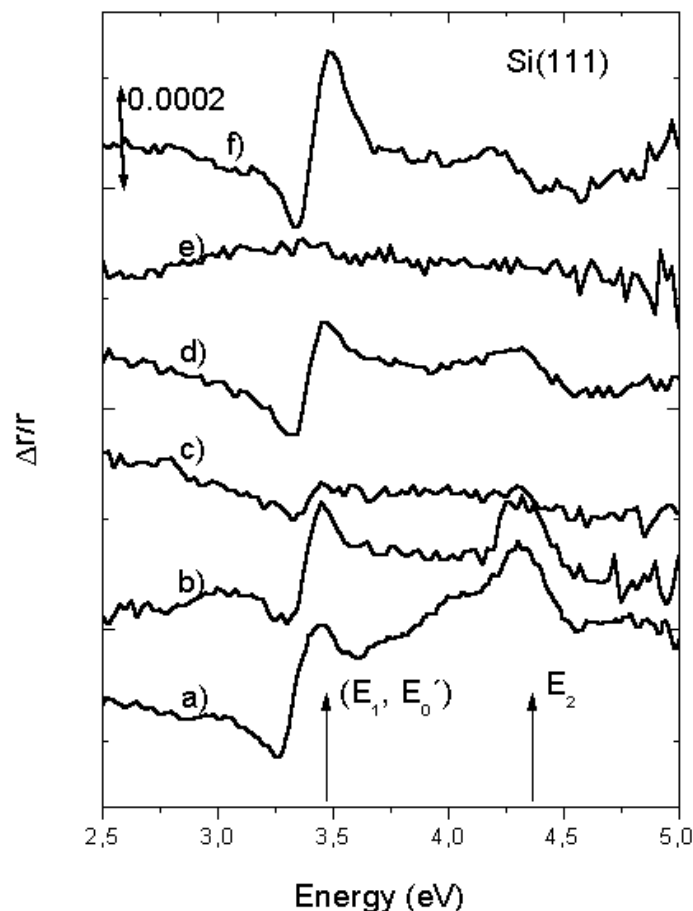


Fig. 4: Comparison between in situ RDS data obtained by other groups and our stress related features for example for the Si(111) surface: (a) displays the RD data of a Si(111): H surface 5° miscut towards the $[11\bar{2}]$ direction; (b) shows *ex situ* measured data on Si(111) surfaces covered with natural oxides and 2° miscut; (c) same as Fig. 4(b) with the RDS head rotated by 45° from the $[1\bar{1}0]$ direction towards the $[2\bar{1}\bar{1}]$ direction; (d) same as Fig. 4(c) with the application of 25 MPa compressive stress along the $[1\bar{1}0]$ direction; (e) the RD spectrum of a non miscut Si(111) sample; (f) same as Fig. 4(e) with the application of 25 MPa uniaxial stress along the $1\bar{1}0$ direction.

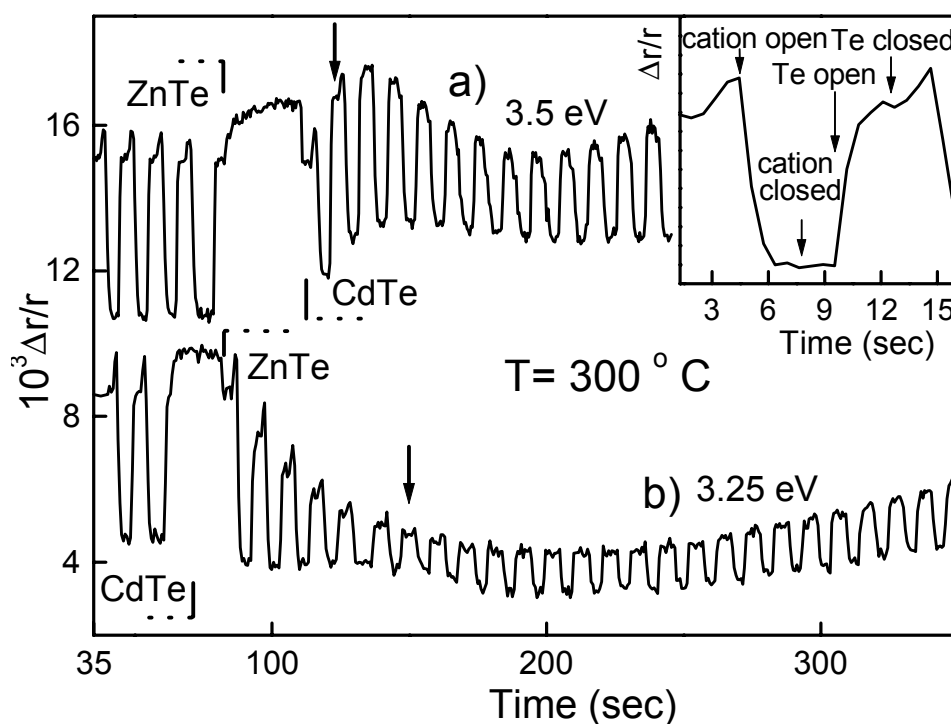


Fig. 5: In situ RD responses at the E_1 critical points during interfaces formation by atomic layer epitaxy growth: a) CdTe on ZnTe(001) and b) ZnTe on CdTe(001). Both curves have been displaced vertically for the sake of clarity. The inset shows the shutter sequences for anion (Te) and cation (Cd or Zn) fluxes prior to interface growth on a shorter time scale.

References:

- [1] A. Bonanni, H. Seyringer, H. Sitter, D. Stifter and K. Hingerl: "Control of morphology changes of self-assembled Mn-based nanostructures overgrown with mismatched material", *Appl. Phys. Lett.* 74, 3732, (1999)
- [2] D. Stifter, A. Bonanni, M. Garcia-Rocha, M. Schmid, K. Hingerl, H. Sitter: "In situ reflectance difference spectroscopy: Nitrogen-plasma doping of MBE grown ZnTe layers", *J. Cryst. Growth*, 201, 132 (1999)
- [3] A. Bonanni, D. Stifter, K. Hingerl, H. Seyringer, H. Sitter: "In-situ characterisation of the growth dynamics in MBE of Mn-based II-VI compounds: self-organised Mn structures on CdTe", *J. Cryst. Growth*, 201, 707 (1999)
- [4] D. Stifter, M. Schmid and K. Hingerl, A. Bonanni, M. Garcia Rocha and H. Sitter: "In situ reflectance difference spectroscopy of II-VI compounds: A real time study of N plasma doping during molecular beam epitaxy", *Jour. Vac. Sci. & Techn.* **B17**, 1697 (1999)
- [5] A. Bonanni, K. Hingerl, H. Sitter, D. Stifter: "Reflectance Difference Spectroscopy of Mn Intra Ion Transitions in p-doped diluted magnetic semiconductors", *phys. Stat. sol.* 215, 47 (1999)

- [6] T. Hanada, T. Yasuda, A. Ohtake, K. Hingerl, S. Miwa, K. Arai, and T. Yao: "In Situ Observation of Strain Induced Optical Anisotropy of ZnS_{1-x}Se_x/GaAs(110) during Molecular Beam Epitaxy", *Phys Rev. B* **60**, (8909) (1999)
- [7] D. Stifter, K. Hingerl, H. Sitter: "Zerstörungsfreie Messung dünner Schichten mit polarisationsoptischen Methoden", *e&i, ÖVE*, **116**, 315, (1999)
- [8] A. Bonanni, G. Pechtl, W. Heiss, F. Schinagl, S. Holl, H. Krenn, H. Sitter, D. Stifter and K. Hingerl: "Reflectance Difference Spectroscopy and magneto-optical analysis of digital magnetic heterostructures", *Jour. Vac. Sci. & Techn.* **B17**, 1722(1999)
- [9] K. E. Miller, K. Hingerl, C. Brabec, A. J. Heeger, and N. S. Sariciftci: "Reflectance Anisotropy Spectroscopy of Oriented Films of Semiconducting Polymers", submitted to *J. Chem. Phys.*, submitted
- [10] R. E. Balderas-Navarro, K. Hingerl, W. Hilber, D. Stifter, A. Bonanni, and H. Sitter: "In situ reflectance-difference spectroscopy of doped CdTe and ZnTe grown by molecular beam epitaxy", submitted to *J. Jour. Vac. Sci. & Techn.*, submitted

Collaborations

PROFACTOR GmbH, Wehrgrabengasse 5, A-4400 Steyr,

Joint Research Center for Atom Technology (JRCAT), Tsukuba 305-8562, Japan,

Institute for Materials Research, Tohoku University, Sendai 980-8577, Japan;

Defense Research Agency, UK,

Additional Funding: GME, ÖAW (APART), FWF, ÖAD, EC-Competitive and Sustainable Growth

Erbium in SiO_x Environment: Ways to Improve the 1.54 μm Emission

G. Kocher¹, H. Przybylinska^{1,2}, M. Stepikhova^{1,3}, L. Palmetshofer¹,
W. Jantsch¹

¹ Institut für Halbleiter- u. Festkörperphysik, Johannes Kepler Universität,
Altenbergerstr. 69, 4040 Linz, Austria

² Institute of Physics, Polish Academy of Sciences,
02-668 Warsaw, Poland

³ Institute Physics of Microstructures RAS,
603600 Nizhny Novgorod, GSP 105 Russia

Si:(Er,O) based light emitting diodes were developed and fabricated, emitting at room temperature in breakdown regime at a wavelength of 1,54 μm. We investigated doping profiles and electrical activity in order to optimize our structures for room temperature luminescence. We present data from SIMS and Hall effect investigations, which demonstrate significant deviations from TRIM simulations of the implantation profiles and the hitherto assumed electrical activity of Er in such environment.

1. Introduction

It is known that electroluminescence (EL) of erbium in silicon can be achieved by impact excitation with hot electrons injected in a reverse biased (r.b.) diode. Obviously, various Er centers can be excited in the impact excitation process. They can be distinguished by their characteristic luminescence line patterns. It was found, however, that the centers responsible for room temperature luminescence are contained in SiO_x precipitates. Their dominance at high temperature EL becomes apparent in the transformation of the emission spectra from the characteristic sharp line spectra to a less structured band with 20 nm width. The incorporation of Er in SiO_x clusters is achieved by Er and O implantation and subsequent annealing above 950 °C. The latter is necessary in order to initiate the formation of SiO₂:Er precipitates.

Er electroluminescence at room temperature can be realized in diodes operating both in the tunneling and in the avalanche regimes. In tunneling diodes, the Er excitation occurs only at a very small volume, within 15 nm of the depletion edge [1]. Making use of an avalanche process allows us to increase the excitation volume considerably but it is still limited to the space charge region of a pn-junction only.

The fabrication of these diode structures requires accurate control of doping gradients and thus knowledge of the electrical activity and the distribution of the implanted dopants. We present data from SIMS and Hall effect investigations, which demonstrate significant deviations from TRIM simulations of the implantation profiles and the hitherto assumed electrical activity of Er in such environment.

2. Design and Realization of p-n Junctions

An important property of the Er centers is their electrical activity which has to be taken into account in the design of the diodes. For isolated centers a large portion can be electrically active. Electrical activity has been seen also for SiO₂ precipitates. Therefore we investigated the electrical activity of our SiO_{2-δ}:Er precipitates by means of Hall effect measurements on samples prepared by implanting Er into high resistivity Si substrates (Fig. 1). As a result, we estimate an electrical activity of less than 3% for this sample.

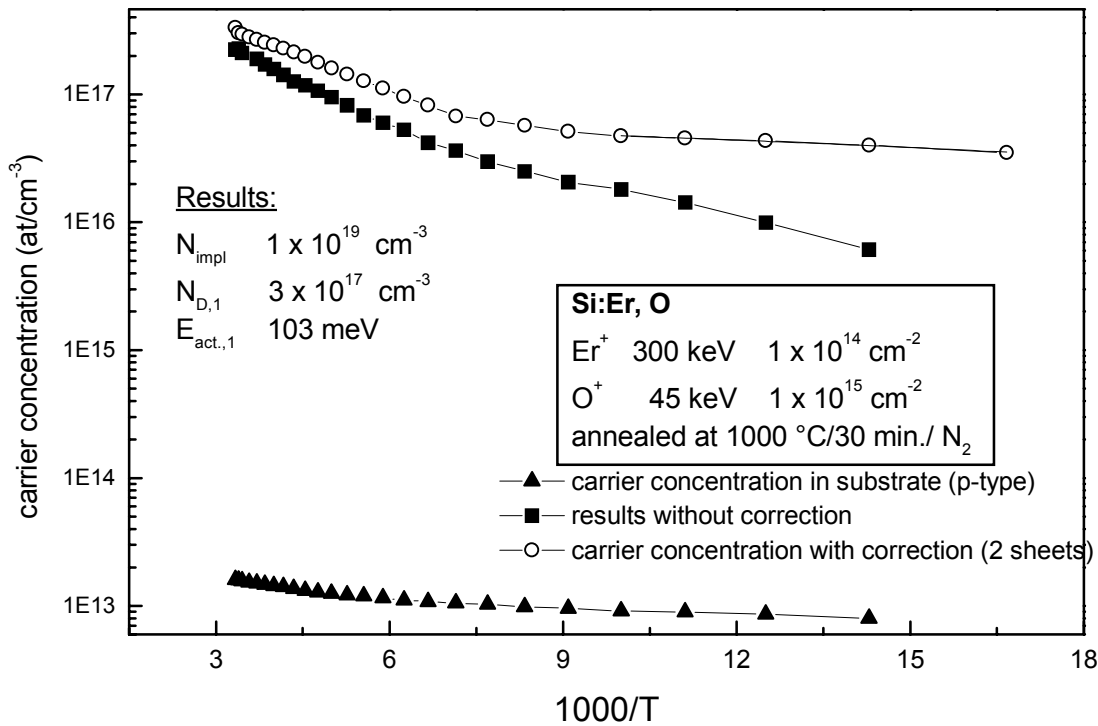


Fig 1: Arrhenius plot of the electron concentration measured by Hall effect on a sample of p-Si ($\rho > 1000 \text{ } \Omega \cdot \text{cm}$) implanted with Er+O. For the evaluation of the electron concentration a two sheet model was applied in order to correct for the substrate contribution.

The early successful attempts to obtain EL from *r.b.* p-n junctions were performed on diodes with large doping gradients that showed tunneling breakdown [2] – [4]. The problem with this kind of excitation is the short ballistic range of electrons with a energy of more than the 0.8 eV that are required to excite Er [1]. That way only a very small fraction of the incorporated Er can be excited and the total efficiency of such a device would be rather limited. An avalanche breakdown is expected to offer considerable advantages as it occurs in a much wider volume.

The most relevant parameter deciding about the two types of breakdown is the electric field strength which in turn is ruled by the doping gradient. According to Sze, for Si at room temperature the doping gradient must not exceed a value of 10^{23} cm^{-4} if avalanche conditions are desired [5]. This, together with the requirement of a large concentration of optically active Er centers in the avalanche region needs careful design of the implantation parameters and knowledge of the resulting implantation profiles.

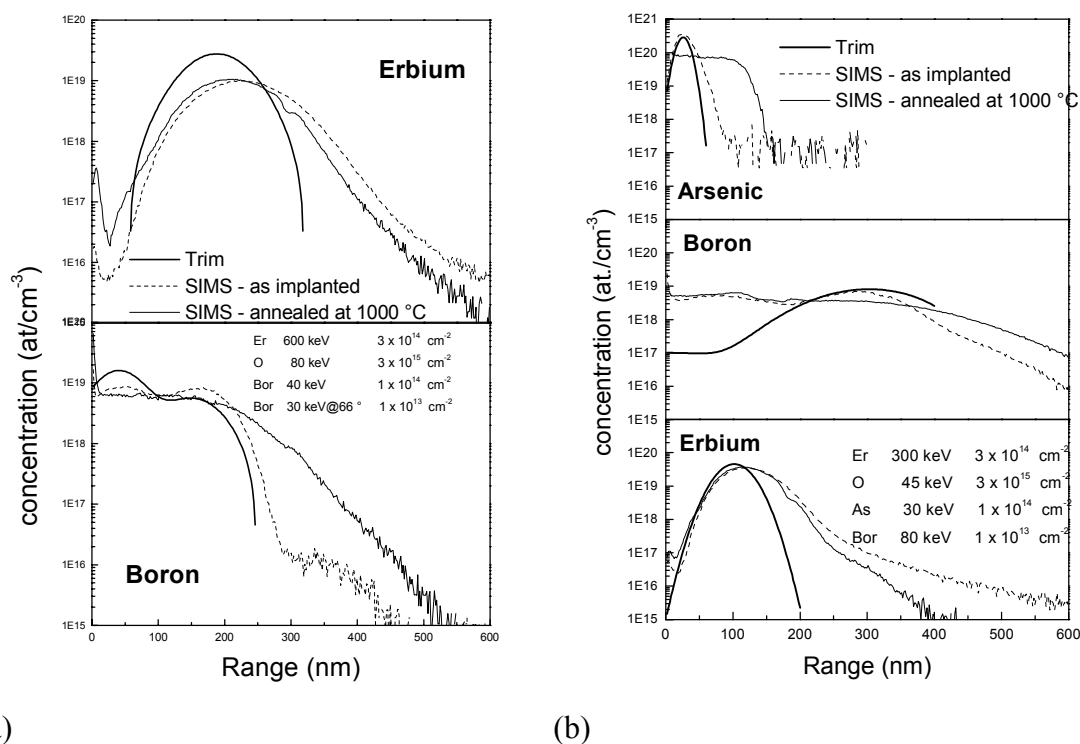


Fig. 2: Implantation profiles of Er and B into n-Si (a) and Er, As and B into p-Si (b) substrates.

Comparison of the implantation profiles measured by SIMS and those simulated by the TRIM code led to a surprise: the profiles of Er are substantially deeper than expected (see Fig. 2). Since the same discrepancy was found for Er implanted into amorphous SiO₂ [6], channeling effects can be excluded. Because of the low electrical activity of Er under the present preparation conditions this discrepancy may not be crucial for the electronic properties of a diode, but it is important for the optimal spatial overlap of the Er profile and the avalanche excitation volume. More important, however, is the fact that the shallow dopants also start to diffuse substantially at the annealing temperature of 1000 °C (s. Fig. 2). This diffusion has a strong influence on the doping gradient at the p-n junction and therefore realistic profiles have to be taken into account in the design of an avalanche breakdown diode.

Another important design consideration concerns the question of homogeneity of the field strength and thus of the generation rate in the avalanche regime across the diode cross section. It is well known that in an avalanche diode the field strength close to the edge of the contact may exceed the average field strength substantially. Consequently avalanche breakdown occurs already at lower voltage and excitation concentrates at the circumference of the diode whereas the center of the diode remains dark. This effect may lead to an early degradation of such a diode. In order to avoid this effect we apply a guard ring structure as it is also applied in the design of avalanche photon detectors.

3. Conclusion

At present, the only principle yielding stable emission at room temperature employs impact excitation of the Er in a reverse biased p-n junction. It has been shown that

thermal quenching of the luminescence can be avoided by producing a particular type of Er center. This type of center exhibits a single inhomogeneously broadened line with two characteristic asymmetrically arranged shoulders. There are several indications for an SiO₂-like surrounding of Er in this type of centers. The SiO₂:Er centers exhibit also larger excitation cross section for hot electrons than the isolated Er centers. We have shown that in the design of such a diode it is essential to control the doping gradient in order to achieve avalanche rather than tunneling breakdown in the diode. It turns out that TRIM simulations are insufficient to describe the Er implantation profile and either diffusion of the shallow dopants has to be taken into account at the necessary formation temperature for the SiO₂:Er clusters of 950 °C or a second implantation and annealing step at lower temperature is necessary. As a result, almost temperature independent emission of 1.54 μm can be achieved in a diode that can be produced in a way compatible with present Si technology. The shortcoming of this type of device is the rather low yield (mW/cm²), the low efficiency (10⁻⁴) and the relatively big linewidth (20 nm).

Acknowledgements

This work is supported by the GMe, FWF, ÖAD, and INTAS

References

- [1] S. Coffa, G. Franzo, F. Priolo, *Appl. Phys. Lett.* 73, 1998, 93.
- [2] G. Franzo, S. Coffa, A. Polman, A. Carnera, F. Priolo, *Appl. Phys. Lett.* 64, 1994, 17.
- [3] J. Stimmer, A. Reittinger, J.F. Nützel, H. Holzbrecher, Ch. Buchal, G. Abstreiter, *Appl. Phys. Lett.* 68, 1996, 23.
- [4] S. Coffa, G. Franzo, F. Priolo, *Appl. Phys. Lett.* 69, 1996, 2077.
- [5] S. M. Sze, "Physics of Semiconductor Devices", (J. Wiley, N.Y. 1981, 2nd ed.) p. 96 ff.
- [6] L. Palmetshofer, M. Gritsch, G. Hobler, *Material Science and Engineering B* 56, in print.

Molecular Beam Epitaxy of Self-Organized PbSe Quantum Dot Superlattices

R.T. Lechner¹, A. Raab¹, G. Springholz¹, M. Pinczolits¹, V. Holy¹, P. Mayer¹,
G. Bauer¹, H. Kang², L. Salamanca-Riba²

¹ Institut für Halbleiter- u. Festkörperphysik, Johannes Kepler Universität,
Altenbergerstraße 69, 4040 Linz, Austria

² Department of Materials and Nuclear Engineering,
University of Maryland, College Park, USA

Self-assembly of Stranski-Krastanow islands in lattice-mismatched heteroepitaxy has recently evolved as a novel tool for the fabrication of low-dimensional semiconductor nanostructures. In self-assembled quantum dots *superlattices*, the elastic interactions between the growing dots on the surface and those buried within the previous layers often lead to the formation of long range correlations within the dot ensembles. This can lead to a lateral ordering and size homogenization as well, which is of crucial importance for device applications. In contrast to other material systems, in IV-VI semiconductor quantum dot superlattices grown along the (111) growth directions, dot correlations *inclined* to the growth direction are observed. This leads to a unique *fcc*-like *ABC... ABC...* dot stacking sequence and a nearly perfect lateral ordering within the growth plane, and to the formation of *trigonal* self-organized 3D lattices of dots [1]. As shown by our previous work, this special type of ordering can be explained by taking into account the elastic anisotropy of the various materials systems [2].

In the present work, we have investigated how finite size effects affect the self-organization processes during PbSe superlattice growth. For this purpose we have fabricated several series of superlattice samples with (1) a variation of the thickness of the $\text{Pb}_{1-x}\text{Eu}_x\text{Te}$ spacer layers between the dots, and (2) with a variation of the PbSe dot sizes by adjustment of the PbSe thickness as well as the growth temperature. From cross sectional TEM as well as x-ray diffraction studies we find the occurrence of several different ordered dot phases due to abrupt changes in the type of vertical dot correlation at certain spacer thicknesses and dot sizes. For small spacer thicknesses and/or large dot sizes, the dots are vertically aligned with a weak hexagonal ordering in the lateral direction. For intermediate spacer thicknesses and/or medium sized dots, a well defined *fcc*-stacking is observed; and for large spacer thicknesses and/or small dot sizes no dot correlations are observed. For the different 3D dot arrangements, a qualitatively different scaling behavior of the lateral dot spacings versus spacer layer thickness is observed [3]. In addition, the different vertical correlations also result in a completely different evolution of dot sizes and shapes as a function of the number of superlattice periods. From finite element calculations it is shown that the different dot correlations are due to finite size effects, and the calculated spacer thicknesses for the transitions between the different dot phases are in good agreement with the experiments.

References:

- [1] G. Springholz, V. Holy, M. Pinczolits, and G. Bauer, *Science* **282**, 734 (1998).
- [2] V. Holy, G. Springholz, M. Pinczolits and G. Bauer, *Phys. Rev. Lett.* **83**, 356 (1999).
- [3] G. Springholz, *et al*, *Phys. Rev. Lett.* **84**, 4669 (2000).

In-Line Prozesskontrolle mit einem kompakten Echtzeit-FTIR-Spektrometer

W. Märzinger¹ and H. Krenn²

¹Upper Austrian Research GmbH, 4040 Linz, Austria

² Institut für Halbleiter- u. Festkörperphysik, Johannes Kepler Universität, Altenbergerstraße 69, 4040 Linz, Austria

Die In-line Überwachung von Prozessen in der Halbleitertechnologie (Epitaxie, PVD/CVD) wird nicht nur zur Überwachung von Prozessparametern wie Temperatur, Schichtdicke, Dotierung, sondern auch zur Garantierung enger Spezifikationen des gefertigten Produkts in der Qualitätskontrolle der Zukunft immer wichtiger werden. Die oftmals niedrigen Prozesstemperaturen ($< 500\text{ °C}$) in der Schichtabscheidung erfordern z.B. für eine berührungslose Temperaturmessung die breitbandige Auswertung der Strahlung im mittleren Infrarot. Der weite Wellenlängenbereich von $\lambda = 2.5 - 5.5\ \mu\text{m}$ kann aber auch dazu benützt werden, um das Temperaturprofil eines im RTP-Verfahren abgeschiedenen dünnen Films, seine Dotierung und Schichtdicke während des Prozesses zu bestimmen. Das vorgestellte FTIR-Spektrometer hat kleine geometrische Abmessungen ($18 \times 8 \times 13\text{ cm}$) und kann direkt an den Reaktor angeflanscht werden. Es wertet bis zu 80 Infrarot-Spektren (1024 Spektralkanäle) pro Sekunde durch eine spezielle auf einen SHARC Signalprozessor implementierte Software aus. Als Beispiele werden eine kontaktlose Temperaturmessung an TiN/TiCN-Vielfachschichten und eine simultane Temperatur- und Schichtdickenmessung an PbTe-Filmen auf BaF₂-Substraten vorgestellt.

Conduction Electron Spin Resonance in MBE-Grown Si/SiGe Quantum Wells

N. Sandersfeld¹, W. Jantsch¹, Z. Wilamowski^{1,2}, F. Schäffler¹

¹ Institut für Halbleiter- u. Festkörperphysik, Johannes-Kepler-Universität
Altenbergerstraße 69, 4040 Linz, Austria

² Institute of Physics, Polish Academy of Sciences,
Al Lotnikow 32/46, 0668 Warsaw, Poland

While electron spin is the most important parameter in magnetic storage devices, it has presently no relevance for commercial semiconductor devices. This is about to change, mainly due to the novel quantum computing concepts that emerged in recent years. If quantum computers can ever be realized in semiconductor materials with their superior miniaturization and integration technologies, spin will be of paramount importance. Because for such applications spin coherence times have to be as long as possible, the choice of semiconductors is limited to those that can be fabricated with a negligible amount of nuclear spins. Silicon is certainly the most prominent examples to fulfill that condition.

Here we report on the spin and transport properties of the 2-dimensional electron gases (2DEG) in modulation-doped Si/SiGe quantum wells. In a standard microwave absorption experiment we measured the conduction electron spin resonance (CESR), and simultaneously the cyclotron resonance (CR) signal of the 2DEG. The latter yields a large background signal extending over a broad magnetic field range, whereas the former appears as a very narrow signal at a Landé g-factor of 2. In high-quality samples the CESR signal is as narrow as 30 mG. By measuring the ESR signal as a function of incident microwave power the spin relaxation time can be derived. We find a longitudinal spin relaxation time of up to 30 μ s which is 6 – 7 orders of magnitude longer than the momentum relaxation times in these samples, and 3 – 4 orders of magnitude larger than the spin relaxation times in the quantum wells of III-V semiconductors.

A second prerequisite for quantum computing is the setting of a well-defined initial spin distribution. We show that this can be achieved in a rather simple gated structure which allows tuning of the g-factor. This way a spin-flip operation can be switched on and off in the microwave cavity of an ESR set-up by simply applying a gate voltage.

Modulation Doped Si/Si_{1-x}Ge_x-Field Effect Transistors

N. Sandersfeld, G.Lengauer, L.Palmetshofer, F. Schäffler

Institut für Halbleiter- und Festkörperphysik, Johannes-Kepler-Universität
Altenbergerstraße 69, 4040 Linz, Austria

Modulation doped Si/Si_{1-x}Ge_x samples show high electron mobilities because of the motion of the carriers along a crystalline heterointerface and the absence of ionized impurities in the conduction channel. We have developed a process sequence to implement n- and p-type MODFETs with 100 nm T-gates in the institute's cleanroom.

The modulation-doped layer sequences are grown by MBE and subsequently processed in a Schottky gate, mesa-isolation process with six lithographic steps. The ohmic contacts are ion implanted and activated by low-temperature rapid thermal annealing. Reactive ion etching is employed for mesa separation of the devices. The submicron gates are defined by e-beam lithography and lift-off. To minimize the series resistance along the gate finger, which can severely limit the achievable switching speed due to the parasitic R-C time constant, a new process was developed that results in a T-shaped cross section of the gates. For this purpose e-beam exposure of a three-layer resist is employed. With an appropriate stack of PMMA and co-polymer resists of different sensitivity the T-shape of the gates is defined in a self-aligned fashion, i.e. only one exposure run is required. Devices with 100 nm gate length show excellent I-V characteristics with complete pinch-off.

Mode Splitting and Lasing in Detuned Lead Salt Microcavity and Microdisk Resonances

T. Schwarzl, W. Heiss, G. Springholz

Institut für Halbleiterphysik, Johannes Kepler Universität Linz,
Altenbergerstraße 69, 4040 Linz, Austria

S. Gianordoli, G. Strasser

Institut für Festkörperelektronik, Technische Universität Wien,
Floragasse 7, 1040 Wien, Austria

M. Aigle, H. Pascher

Experimentalphysik I, Universität Bayreuth,
Universitätsstraße 30, 95447 Bayreuth, Germany

PbEuTe/EuTe microcavities and microdisks supporting strongly detuned resonances were fabricated by molecular beam epitaxy and reactive ion milling. For detuned cavity modes, we find a pronounced angle dependent relative polarization splitting of up to 1 % and vertical laser emission at 4.8 μm , for sample temperatures between 35 and 85 K. Furthermore, lateral confinement effects in circular microdisks with diameters below 20 μm are demonstrated.

1. Introduction

Microcavities have attracted immense interest in recent years due to their unique physical properties as well as their high potential for device applications. The very short cavities with lengths comparable to an optical wavelength require high reflectivity mirrors, which are realized by Bragg interference mirrors. Such Bragg mirrors exhibit a stop band with high reflectivity around a certain target wavelength. The width of this stop band is determined by the refractive index contrast between the mirror materials.

We have recently demonstrated PbEuTe/EuTe microcavities with Bragg mirrors having a very high refractive index contrast [1], which is more than four times higher than that of III-V [2] and II-VI [3] mirrors. In these cavities, the mirror stop band width is large enough to sustain Fabry-Perot resonances, which are highly detuned with respect to the stop band center wavelength. The range for this detuning is about six times larger than for III-V Bragg cavities.

In this work, we investigate the angle dependent polarization splitting between the TE and TM modes of detuned resonances (DRs) as well as mid-infrared vertical lasing [4], [5] from a DR. Furthermore, a splitting and a blueshift of resonances in laterally structured planar cavities into microdisks are shown.

2. Experimental

The microcavity samples were grown by molecular-beam-epitaxy (MBE) on (111) oriented BaF₂ substrates. They consist of two high reflectivity Pb_{0.95}Eu_{0.05}Te/EuTe Bragg

mirrors with only three layer pairs and with (2λ) and (4λ) $\text{Pb}_{0.95}\text{Eu}_{0.05}\text{Te}$ cavities in between. The samples intended for laser emission have inserted several 20 nm thick PbTe quantum wells in the cavity layer as active material. Circular microdisks with various diameters were formed by lateral structuring of the planar cavities by reactive ion milling. The optical characterization of the microcavities was performed with polarization dependent FTIR transmission measurements. For investigation of the microdisks, an IR microscope mounted on the FTIR spectrometer was used allowing spatially resolved reflectivity measurements with a resolution of 8 μm . The laser samples were optically pumped with a pulsed Nd:YAG laser [5].

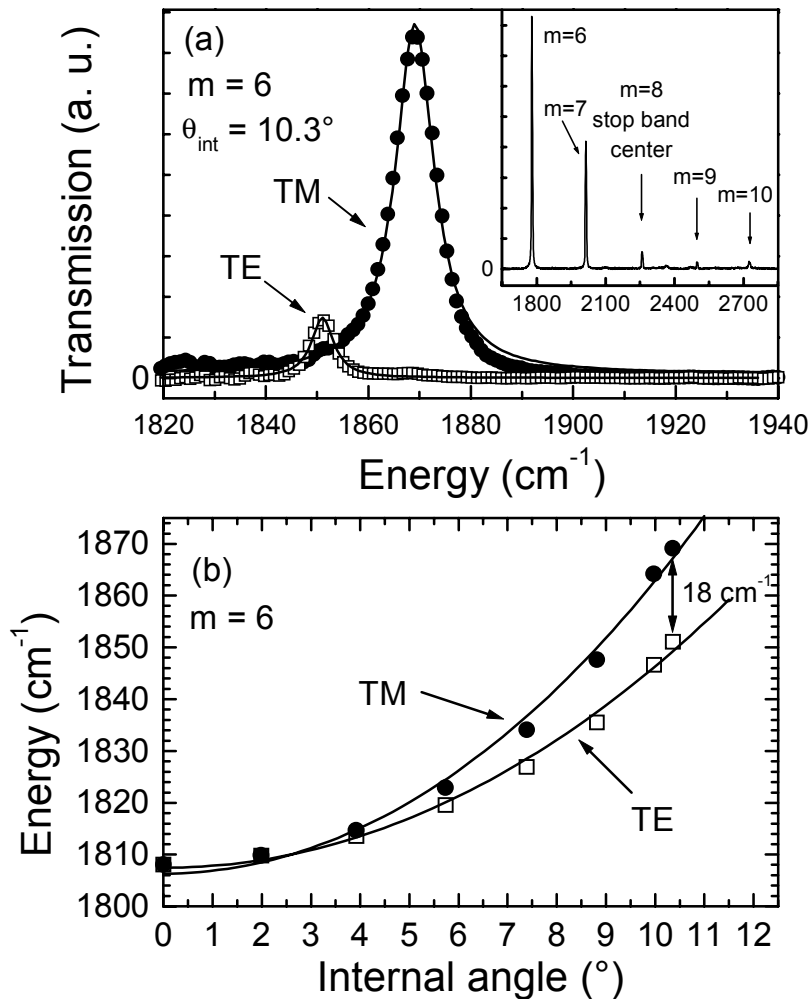


Fig. 1: (a) FTIR transmission of the $m = 6$ resonance of a 4λ microcavity for TE and TM polarization at an internal angle of 10.3° . Inset: FTIR transmission spectrum of the stop band region of the microcavity. (b) Angle dependent dispersion of the $m = 6$ mode for TE and TM polarization.

3. Polarization Splitting and Lasing in Microcavities

Our IV-VI microcavity with a length of 4λ supports five cavity resonances, as shown in the inset of Fig. 1(a) by the transmission spectrum of the cavity in the stop band region. The energy of the most detuned resonances with order $m = 6$ and $m = 10$ is about

450 cm^{-1} off from the mirror center. Figure 1(a) shows the polarization splitting of the $m = 6$ mode at 1860 cm^{-1} . At an internal angle of only 10.3° (64° external) it amounts 18 cm^{-1} yielding a relative splitting of 1 %. In comparison, in GaAs/AlAs cavities the tunability of the resonances is limited by the small stop band widths resulting in a polarization splitting of only 0.1 % at an external angle of 60° [6]. For the TE mode we observe, in addition, a considerable larger finesse than for the TM mode, which appears much higher and broader in the transmission spectrum. The difference of the finesse is due to a lower reflectivity for the TM polarization as predicted by the Fresnel formulas. The angular dispersion of the polarization modes of the $m=6$ resonance is shown in Fig 1(b). Both dispersions are fitted with the same equation [6] by using different values for the effective refractive index (3.55 and 4.25 for TM and TE mode, respectively).

The DRs have a lower quality factor than the central resonances, due to a about 3.5 % lower Bragg mirror reflectivity at the edges of the mirror stop band. Nevertheless, optically pumped lasing has been observed also at DRs, which is in particular important for IV-VI semiconductor lasers exhibiting a strong temperature dependence of the energy band gap. This enables vertical single mode laser operation over a large temperature range via mode hopping between central mode and DRs. This is observed indeed in the (2λ) laser cavity exhibiting three resonances. The sample shows narrow forward directed stimulated emission. At low temperatures around 4 K, emission is observed at the central $m = 4$ cavity mode at $5.87 \mu\text{m}$, whereas at 35 K the emission switches to the $m = 5$ DR at $4.82 \mu\text{m}$. Above 85 K the lasing quenches, because the band gap energy exceeds the energy of the DR [5].

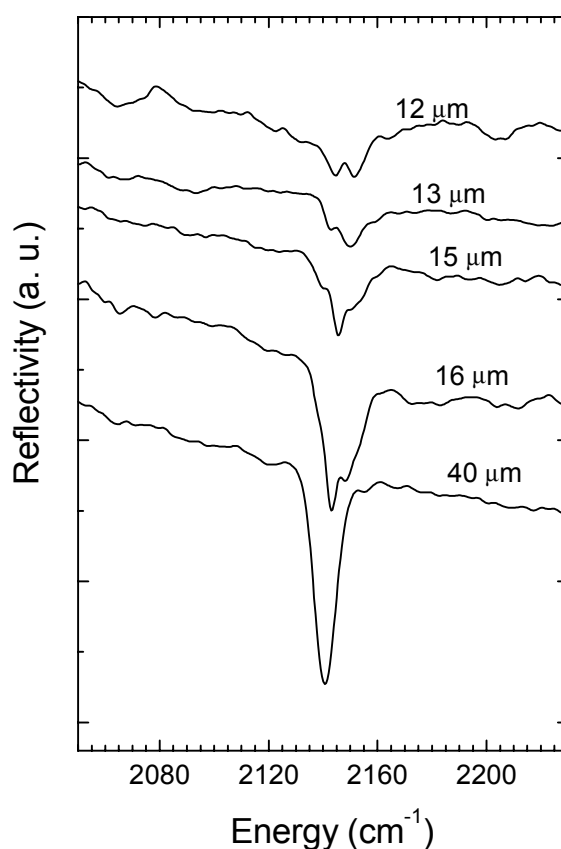


Fig. 2: Reflectivity spectra of circular microdisks with various diameters showing the $m = 5$ resonance dip.

4. Mode Splitting in Microdisks

The lower quality of the DRs can be improved by laterally structuring of the planar microcavities to obtain three dimensionally confined photonic states [7]. In Fig. 2, the reflectivity of one DR ($m = 5$) of circular microdisks with different diameters is shown. The disks were structured from a 2λ planar microcavity. For disks with diameters below $20\ \mu\text{m}$, the resonance dip shows a pronounced splitting into narrower modes.

The distance between the disk modes gets larger with decreasing diameter, as is expected from lateral confinement. Furthermore, the resonances shift to higher energies with decreasing diameter, also indicating lateral confinement. The narrow microdisk modes are attributed to radial-like modes as well as whispering-gallery-like modes [8].

5. Conclusion

In conclusion, we have demonstrated microcavities with strongly detuned resonances with respect to the mirror stop band center. These resonances exhibited a pronounced angle dependent polarization splitting and enable vertical laser emission despite low cavity finesse. Furthermore, circular microdisks showing lateral confinement effects were fabricated by laterally structuring planar microcavities.

Acknowledgements

We thank W. Krepper and O. Fuchs for technical assistance. This work is supported by the FWF P 13330 – TPH, Vienna.

References

- [1] T. Schwarzl, W. Heiß, and G. Springholz, *Appl. Phys. Lett.* **75**, (1999) 1246.
- [2] R. P. Stanley, R. Houdre, U. Oesterle, M. Gailhanou, and M. Ilegems, *Appl. Phys. Lett.* **65**, (1994) 1883.
- [3] E. Hadji, J. Bleuse, N. Magnea, J. L. Pautrat, *Appl. Phys. Lett.* **68**, (1996) 2480.
- [4] T. Schwarzl, W. Heiß, G. Springholz, M. Aigle, and H. Pascher, *Electron. Lett.* **36**, (2000) 322.
- [5] G. Springholz, T. Schwarzl, M. Aigle, H. Pascher, and W. Heiss, *Appl. Phys. Lett.* **76**, (2000) 1807.
- [6] D. Baxter, M. S. Skolnick, A. Armitage, V. N. Astratov, D. M. Whittaker, T. A. Fisher, J. S. Roberts, D. J. Mowbray, M. A. Kaliteevski, *Phys. Rev.* **B 56**, (1997) R10032.
- [7] J. P. Reithmaier, M. Röhner, H. Zull, F. Schäfer, A. Forchel, P. A. Knipp, and T. L. Reinecke, *Phys. Rev. Lett.* **78**, (1997) 378.
- [8] D. Labilloy, H. Benisty, C. Weisbuch, T. F. Krauss, C. J. M. Smith, R. Houdre, and U. Oesterle, *Appl. Phys. Lett.* **73**, (1998) 1314.

Kristalline dünne Filme aus Para-Hexaphenyl hergestellt mit Hot-Wall-Epitaxie

H. Sitter, A. Andreev

Institut für Halbleiter- und Festkörperphysik, Johannes-Kepler-Universität
Altenbergerstraße 69, 4040 Linz, Austria

In Zusammenarbeit mit dem Institut für Physikalische Chemie, dem Forschungsinstitut für organische Solarzellen und dem Christian Doppler-Laboratorium für Plastik-Solarzellen wurde die an unserem Institut entwickelte Hot-Wall-Epitaxie zur Herstellung sehr dünner Schichten auf organische Materialien angewandt. Dabei konzentrierten wir uns auf kleine Moleküle von Farbstoffen, zum Beispiel Para-Hexaphenyl (PHP). Diese Moleküle bestehen aus sechs aneinandergereihten Sechseringen von Kohlenstoff, und zeigen daher eine bevorzugte Orientierung entlang ihrer langen Achse.

Die Hot-Wall-Epitaxie ist ein Wachstumsverfahren, welches möglichst nahe am thermodynamischen Gleichgewicht arbeitet. Damit ist es möglich die Van der Waals-gebunden PHP Moleküle in eine geordnete Struktur zu bringen, die durch das Substrat, in unserem Fall Glimmer, vorgegeben wird. Die Moleküle ordnen sich dabei in Reihen, wobei sie mit der Längsseite aneinander liegen und arrangieren sich parallel zur Substratoberfläche. Diese Strukturanalyse wurde aus umfangreichen Untersuchungen mit Röntgenbeugung, Elektronenbeugung und optischen Untersuchungen gewonnen, die alle in Übereinstimmung die gleiche Anisotropie der Struktur zeigen.

Besonders auffallend ist die polarisationsabhängige Absorptions- und Lumineszenzeigenschaft der PHP-Filme. Diese Anisotropie sollte sich auch in der Emission von Licht zeigen, wenn derartige Schichten als aktives Material in Leuchtdioden verwendet werden. Damit könnte ein blau leuchtendes Display hergestellt werden, bei dem kein Polarisationsfilter mehr notwendig ist, um einen Kontrast zu erzielen.

***In situ*-Kontrolle der Herstellung von Galliumnitrid-Schichten**

H. Sitter, K. Hingerl, A. Bonanni, K. Himmelbauer, D. Stifter

**Institut für Halbleiter- und Festkörperphysik, Johannes-Kepler-Universität
Altenbergerstraße 69, 4040 Linz, Austria**

Im Rahmen eines EU-Projekts ist es gelungen, die entsprechenden finanziellen Mittel bereitzustellen, um eine „Metal-Organic-Vapor-Deposition“ (MOCVD)-Anlage anschaffen zu können, mit deren Hilfe GaN-Schichten hergestellt werden sollen. Mit Unterstützung des BMWV und der Landesregierung von Oberösterreich wurde die notwendige Infrastruktur geschaffen, um diese aufwendige Herstellungsmethode betreiben zu können.

GaN- und GaAlN-Schichten werden in der Halbleiterindustrie hauptsächlich für optoelektronische und Hochfrequenz-Bauelemente eingesetzt. Es besteht daher von Seiten der Industrie sehr großes Interesse, den Herstellungsprozess sehr genau überwachen zu können, um den Ausschuss bei der Produktion zu minimieren. Unsere Aufgabe in diesem EU-Projekt liegt daher in der Entwicklung einer Untersuchungsmethode, mit der bei laufendem Wachstum, das bei einer Temperatur von rund 1000 °C erfolgt, die Schichtzusammensetzung und die Dicke mit einer Auflösung von Nanometern gemessen werden können. Dafür wurde von uns ein spezieller Reaktor entworfen, der mit optischen Fenstern versehen ist, um während des Wachstums spektral aufgelöste Ellipsometrie und „Reflection Difference Spektroskopie“ betreiben zu können.

Das Interesse an dieser Methode ist von Seiten der Industrie sehr groß. Dies spiegelt sich auch in der Zahl der Firmen wieder, die mit im Konsortium des EU-Projekts mitarbeiten. Darunter sind: Aixtron – Aachen, Philips – Almelo, EPI – Cardiff und Thompson – Paris.

Strain and Composition of SiGe Islands on Si (001)

J. Stangl, A. Daniel, V. Holý, T. Roch, G. Bauer

Institut für Halbleiter- und Festkörperphysik, Johannes Kepler Universität,
Altenbergerstr. 69, 4040 Linz, Austria

We have investigated the strain and composition distribution in uncapped SiGe islands on Si (001) by x-ray diffraction. In order to be sensitive to the dot layer at the sample surface, and at the same time being able to measure in-plane strain and strain in growth direction, we utilized a scattering geometry at grazing incidence angles, but with high exit angles. The measured intensity distribution is compared to simulations based on the strain distribution calculated by the finite element method. It turns out that, although pure Ge has been deposited during island growth by molecular beam epitaxy, the Ge composition varies from 0.5 at the island base to 1.0 at the top of the islands. The elastic relaxation reaches only about 50% even at the island top.

1. Introduction

Recent years have seen a series of studies shedding light on the formation of so-called self-organized nanostructures during semiconductor heteroepitaxy. They are formed due to a growth instability in strained heterostructures. After a certain critical thickness of deposited material, in our case Ge on Si, three-dimensional islands form on top of a two-dimensional layer, the so-called wetting layer (WL). These islands can elastically relax and hence reduce their strain energy, which is the driving force of their formation. The main advantage of such islands as compared to nanostructures fabricated, e.g., by etching, is the high areal density and the virtually complete absence of defects [1].

However, it is difficult to control the size, strain and composition of self-organized structures because these quantities depend very sensitively on the growth conditions (substrate temperature, adatom flux, etc.). Transmission electron microscopy (TEM) has been used to investigate the strain distribution within such islands [2], [3]. Recently, also the Ge and Si distributions in uncapped SiGe islands have been investigated using TEM, showing that islands formed during the deposition of pure Ge onto a Si surface are alloyed [4]. On the other hand, TEM investigations on Ge islands grown by chemical vapor deposition of 11 ML of Ge at 600 °C have been interpreted as not giving evidence for significant alloying [5].

X-ray diffraction (XRD) techniques have also been applied to tackle the question of strain and composition [6], [7]. In principle, XRD is the method of choice to measure strains, and often the strain state can be directly related to a composition. This is a standard technique for the investigation of, e.g., SiGe buffer layers with graded composition. However, for objects as small as self-organized islands, the correct spatial localization of a certain strain state is an ambitious task.

2. Experimental

Our investigations focus on a sample (S1183B4) with free-standing SiGe islands grown by MBE on [001]-oriented Si. After growth of a Si buffer layer and a buried SiGe island layer, a layer of Ge islands at the surface was formed by the deposition of 6 ML of Ge. The growth temperature was 600 °C. Here we are interested solely in the surface islands; the buried islands have no influence on the scattered signal due to the low incidence angle $\alpha_i = 0.15^\circ$ (below the critical angle $\alpha_c \approx 0.22^\circ$). With AFM two types of islands have been detected on the sample surface, larger ones with a base diameter of about 175 nm and a height of 30 to 70 nm, but with a low density of about $2 \times 10^7 \text{ cm}^{-2}$, and smaller ones with a high density of about $4 \times 10^9 \text{ cm}^{-2}$, and a height and base diameter of about 13 nm and 110 nm, respectively. Here, we consider only the smaller islands, and neglect the scattering from the larger islands because of their low density.

In order to distinguish between material composition and strain state, we measure not only the in-plane lattice parameter, as in grazing incidence diffraction studies, but also the lattice parameter in growth direction. This can be achieved by measuring reciprocal space maps (RSMs) with the momentum transfer component along growth direction $Q_z > 0$, as illustrated in Fig. 1(a) and (b). RSMs have been recorded around the (202) reciprocal lattice point (RLP) of Si, which is inaccessible in the conventional coplanar geometry at a wavelength of 1.55 Å, but can be accessed by rotating the scattering plane around the scattering vector \mathbf{Q} , out of the plane of the RSM, as is shown in Fig. 1(c). With this setup, it is possible to keep the incidence angle α_i and hence the penetration depth constant at a value below a_c for the entire RSM, in order to be sensitive to the dot layer at the sample surface.

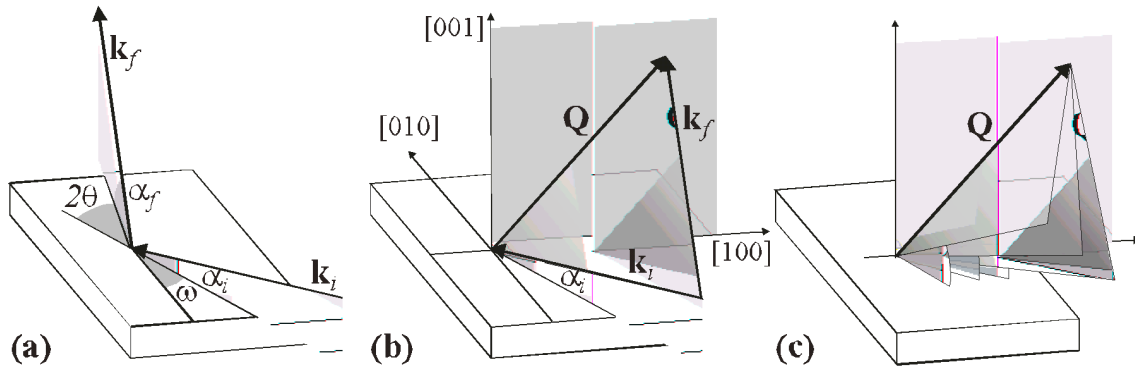


Fig. 1: Illustration of the scattering geometry in real space (a) and reciprocal space (b). (c) Tuning of the incidence angle by rotating the scattering plane around the scattering vector \mathbf{Q} .

For the determination of the Ge distribution within the islands, we use kind of a “fitting” procedure: we start with an assumption on the Ge distribution and calculate the strain distribution using the finite element method (FEM). With this result the XRD pattern is calculated, and compared to the experimental result. Repeating the procedure while varying Ge distribution and island shape until a good correspondence between experiment and simulation is reached, we are able to establish the distributions of Ge content and strain within the islands. We assumed islands with the shape of a rotational paraboloid. With the FEM data, RMSs have been calculated using a kinematic scattering theory, and as well assuming a cylindrical symmetry.

Figure 2(a) shows the measured intensity distribution. Taking simply the peak maximum position Q_{\max} and calculating the lattice parameters via the relation $a_{\parallel,\perp} = 2\pi/Q_{x,z}$, we would obtain values for the composition $x_{\text{Ge}} = 0.73$ and for the in-plane strain with respect to the substrate $\epsilon_{\parallel} = (a_{\parallel} - a_{\text{Si}})/a_{\text{Si}} = 0.011$. The results of our simulations are shown in Fig. 2(b) – (d). Using a constant composition of the SiGe islands, no good correspondence with the experiment can be obtained: assuming an island with the constant composition of $x_{\text{Ge}} = 0.73$, the simulation yields a peak at a different position than the measurement, at the correct value of Q_z , but at a too large value of Q_x (Fig. 2(c)).

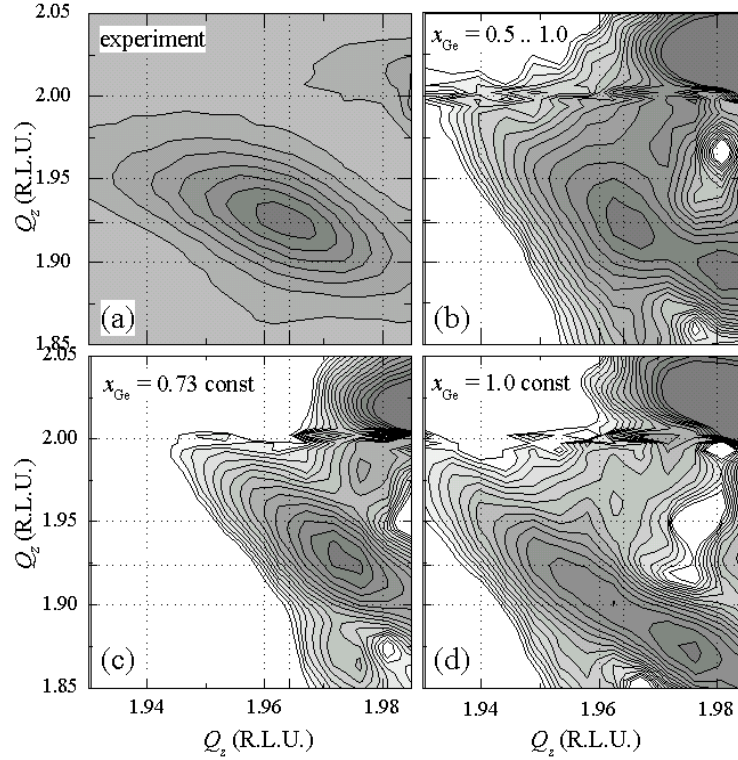


Fig. 2: (a) Reciprocal space map around the (202) Bragg reflection. (b) – (d) Simulations with different assumptions on the Ge distribution within the islands.

The reason for this difference is quite clear: the simple evaluation of the peak position assumes an island with homogeneous composition and homogeneous strain. As the island is grown pseudomorphically on the Si substrate, but relaxed towards the top, at least the latter cannot be true. We varied the composition of the island to obtain a smaller Q_x of the peak maximum. At $x_{\text{Ge}} = 1.0$ (Fig. 2(d)), the peak position is almost correct along Q_x , but now Q_z is too small. Hence it is clear that assuming a constant composition, no agreement with the experiment can be achieved. Thus we varied the Ge composition distribution within the island from a value $x_{\text{Ge},1}$ at the base to a value $x_{\text{Ge},2}$ at the top. Within the islands, the Ge content was assumed to be constant laterally, and only a vertical profile, either linear, or increasing like $z^{1/2}$ (i.e., the Ge content increases faster at the bottom of the island than on its top) or z^2 (Ge content increasing faster at the top of the island than on its base), was assumed. We found the best correspondence between simulation and experiment for a faster increase of the Ge content at the base of the islands. Figure 2(b) shows the calculated RSM for a Ge distribution which reproduces the peak position best, with a maximum content of $x_{\text{Ge},2} = 1.0$ at the top of the

island, and $x_{\text{Ge},1} = 0.5$. In contrast to, e.g., InAs Islands on GaAs [7], the maximum in-plane strain at the top of the islands reaches only about 0.02, i.e., the dot is only about 50% relaxed even at the top.

3. Conclusion

In summary, from our study it is evident that albeit pure Ge is deposited during MBE growth, the uncapped islands are alloyed, and the Ge content varies from about $x = 0.5$ at the base to $x = 1.0$ at the top (these particular values will depend sensitively on the growth parameters). We believe that the reduced elastic energy of an interdiffused island, [8] as compared to an island of pure Ge, is the main driving force for the alloying.

Acknowledgements

This project has been supported by SIGENET (EC). We thank D. Smilgies and the staff of TROİKA II beamline at the ESRF (Grenoble, France) for their support.

References

- [1] J.S. Sullivan, E. Mateeva, H. Evans, D.E. Savage, M.G. Lagally: "Properties of $\text{Si}_{1-x}\text{Ge}_x$ three-dimensional islands", *J. Vac. Sci. Technol.*, vol. A17, 1999, pp. 2345 – 2350.
- [2] S. Christiansen, M. Albrecht, H.P. Strunk, M.J. Maier: "Strained state of Ge(Si) islands on Si: Finite element calculations and comparison to convergent beam electron-diffraction measurements", *Appl. Phys. Lett.*, vol 64, 1994, pp. 3617 – 3619.
- [3] Chuan-Pu Liu, J.Murray Gibson, D.G. Cahgill, T.I. Kamins, D.P. Basile, R. Stanley Williams: "Strain Evolution in Coherent Ge/Si Islands", *Phys. Rev. Lett.*, vol. 84, 2000, pp. 1958 – 1961.
- [4] X.Z. Liao, J. Zou, D.J.H. Cockayne, Z.M. Jiang, X. Wang, R. Leon: "Composition and its impact on shape evolution in dislocatedGe(Si)/Si islands", *Appl. Phys. Lett.*, vol 77, 2000, pp. 1304 – 1306.
- [5] P.D. Miller, Chuan-Pu Liu, W.L. Henstrom, J. Murray Gibson, Y. Huang, P. Zhang, T.I. Kamins, D.P. Basile, R. Stanley Williams: "Direct measurement of strain in a Ge island on Si(001)", *Appl. Phys. Lett.*, vol. 75, 1999, pp. 46 – 48.
- [6] Th. Wiebach, M. Schmidbauer, M. Hanke, H. Raidt, R. Köhler, H. Wawra: „Strain and composition in SiGe nanoscale islands studied by x-ray scattering“, *Phys. Rev. B*, vol. 61, 2000, pp. 5571 – 5578.
- [7] I. Kegel, T. H. Metzger, A. Lorke, J. Peisl, J. Stangl, G. Bauer, J. M. García, P. M. Petroff: „Nanometer-Scale Resolution of Strain and Interdiffusion in Self-Assembled InAs/GaAs Quantum Dots“, *Phys. Rev. Lett.*, vol. 85, 2000, pp. 1694 – 1697.
- [8] S.A. Chaparro, J. Drucker, Y. Zhang, D. Chandrasekhar, M.R. McCatney, D.J. Smith: "Strain-Driven Alloying in Ge/Si(100) Coherent Islands", *Phys. Rev. Lett.*, vol. 83, 1999, pp. 1199 – 1202.

Nano-Scale Dislocation Patterning in PbTe on PbSe (100) Heteroepitaxy Studied by Scanning Tunneling Microscopy

K. Wiesauer and G. Springholz

Institut für Halbleiter- und Festkörperphysik, Johannes Kepler Universität,
Altenbergerstr. 69, 4040 Linz, Austria

Heteroepitaxial growth of PbTe on 5.2% lattice mismatched (100) oriented PbSe is investigated using UHV-scanning tunneling microscopy. A 2D growth mode is found, and it is shown that strain relaxation occurs by pure edge type misfit dislocation formation. The early stages of strain relaxation show a lateral injection of dislocation half loops from monolayer step edges on the surface. A rapid increase of the dislocation density with PbTe layer thickness indicates a very effective strain relaxation mechanism with a critical layer thickness below 1 monolayer (ML). At PbTe layer thicknesses above 4 ML we observe the formation of a highly regular network of misfit dislocations with a dislocation spacing of around 10 nm, and a smallest variation of the dislocation separation of only $\pm 12\%$. Thus, this nano-scale dislocation patterning can serve as template for the fabrication of self-assembled, ordered nanostructures.

1. Introduction

Strain relaxation is a critical process in lattice-mismatched heteroepitaxy. For highly mismatched heteroepitaxial systems, two different strain relaxation mechanisms exist, namely (1) the spontaneous formation of strain-induced coherent 3D islands on the surface, or (2) by misfit dislocation formation at the layer/substrate interface. For the latter, recent work has shown that the formation of interfacial dislocations strongly modifies surface morphology of the epitaxial layers, due to long-range elastic deformations of the lattice and in many cases due to monolayer surface glide steps [1]. In semiconductors, misfit dislocations are usually distributed in an irregular way within the layers, but for special growth geometries highly periodic dislocation arrays occur [2], [3]. This dislocation pre-patterning has been demonstrated as a tool for spatial manipulation of the nucleation sites of self-assembled quantum dots [4], [5], based on the local perturbation of the total free energy of the surface by the subsurface misfit dislocations.

In the present work, we have studied the strain relaxation mechanisms of PbTe on 5.2% lattice-mismatched (100) oriented PbSe substrates, using UHV scanning tunneling microscopy (STM). The non polar (100) surface has the lowest surface free energy in the rocksalt crystal structure, other than the polar (111) surface, where strain relaxation is found to occur by Stranski-Krastanow growth.

2. Experimental

The samples were grown by molecular beam epitaxy using compound sources for PbSe and PbTe. On polished PbSe (100) substrates, a several μm thick PbSe buffer layer was deposited at a temperature of 380 °C, followed by a PbTe layer, where the PbTe layer

thickness was varied from 0.3 to 22.5 ML. After growth, the samples were rapidly cooled down to room temperature and transferred to a separate UHV-STM chamber without breaking ultra-high vacuum conditions.

3. Results

In contrast to (111) oriented growth we find for the growth of PbTe on (100) oriented PbSe substrates a 2D growth mode that persists throughout the heteroepitaxial growth process (Fig. 1). Strain relaxation occurs purely by the formation of misfit dislocations that appear as dark surface depression lines in large-scale STM images (Fig. 1(b) – (d)). Studies of layers with varying PbTe layer thicknesses give a critical layer thickness h_c for the onset of misfit dislocation formation of only 0.8 ML, and STM images of very early relaxation stages show that misfit dislocation half loops are injected laterally from monolayer step edges on the surface (Fig. 1(b)). With increasing PbTe layer thickness the misfit dislocation density increases rapidly, and above about 4 ML PbTe a highly regular, square grid of misfit dislocations with a spacing of the order of 10 nm develops. By measuring the dislocation line density in STM images the relaxed strain in the layers was determined as a function of layer thickness, indicating a very rapid strain relaxation with more than 90% of the 5.2% misfit strain already relaxed at a PbTe layer thickness of 9 ML.

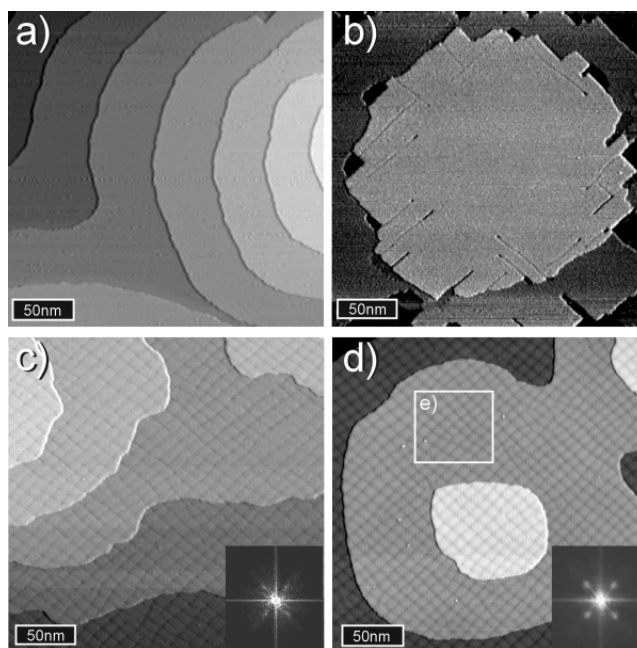


Fig. 1: STM images of PbTe layers on PbSe (100) for different layer thicknesses of (a) 0.3, (b) 0.8, (c) 4.5 and (d) 9 ML. Insert in (c) and (d): FFT power spectra of the STM images. The marked area (e) is shown in Fig. 2 (a) on an enlarged scale.

Atomically resolved STM images of an endpoint of a misfit dislocation (see Fig. 2(b)) show that the Burgers vector \mathbf{b} is of $\frac{1}{2}\langle 011 \rangle$ type, as expected for the rocksalt crystal structure of PbSe and PbTe. The Burgers vector is parallel to the heterointerface, and thus, the misfit dislocations cannot be formed by glide but only by climb processes. In addition, \mathbf{b} is perpendicular to the misfit dislocation lines that run along the fourfold $\langle 1-10 \rangle$ directions. Therefore the misfit dislocations are of pure edge character.

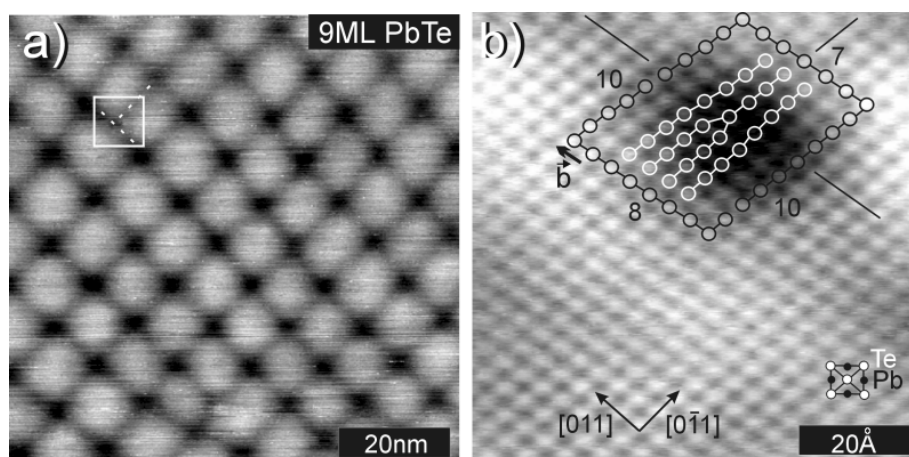


Fig. 2: STM images of a 9 ML PbTe layer on PbSe (100). As shown in (a) a very regular quadratic dislocation array is formed. The atomically resolved STM image of the area in (a) is shown in (b). As indicated by the Burgers circuit, the Burgers vector is equal to $\frac{1}{2}\langle 011 \rangle$ and the dislocations are formed along the $\langle 0-11 \rangle$ directions.

The remarkable regularity of the dislocation network is evidenced by the appearance of satellite peaks in the FFT power spectra of the STM images (insert in Fig. 1(c) and (d)). A statistical analysis of the dislocation spacings for the 4.5 and 9 ML PbTe samples (Fig. 3) indicates a narrowing of the distribution of the dislocation spacings, i.e. a higher regularity of the dislocation network with a variation of the dislocation separation of only $\pm 12\%$ for the 9 ML sample. This is less than the typical variations in size and spacing of self-assembled quantum dots formed by the Stranski-Krastanow growth mode. The high regularity of the dislocation network is explained by the repulsive force between the dislocations and the high dislocation mobility within the heterointerface.

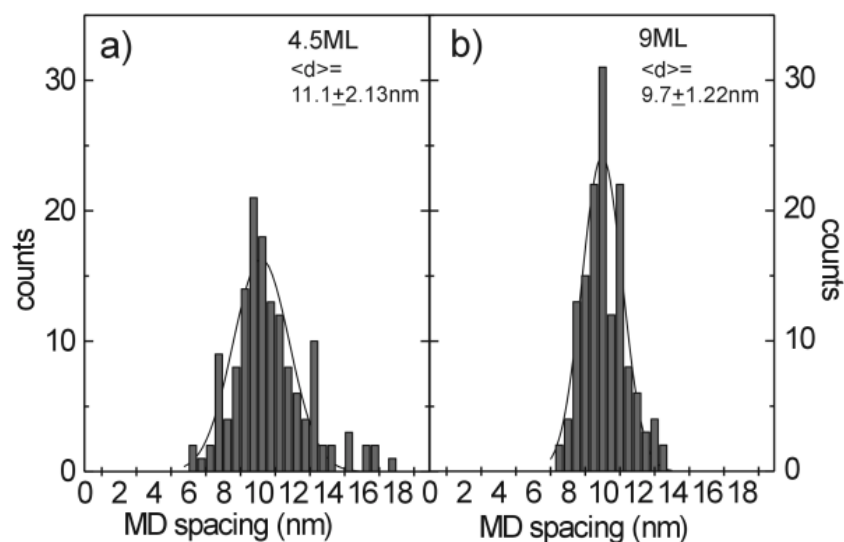


Fig. 3: Histograms of the lateral misfit dislocation spacings for PbTe layer thicknesses of (a) 4.5 ML and (b) 9 ML, indicating that the distributions narrow with increasing layer thickness.

4. Conclusions

For the growth of PbTe on (100) oriented substrates we find a 2D growth mode and a very effective strain relaxation process by the formation of pure edge type misfit dislocations that are formed by a climb process. With increasing PbTe layer thickness, the dislocations form a highly regular, square grid along the fourfold $\langle 1-10 \rangle$ directions with a period of the order of 10 nm. Due to the high uniformity of the dislocation network, this dislocation patterning can serve as template for the fabrication of self-organized ordered nanostructures. Because the interaction between dislocations depends strongly on the dislocation separation, similar results can be expected for other highly mismatched heteroepitaxial systems.

Acknowledgements

This work was supported by the *Fonds zur Förderung der wissenschaftlichen Forschung* and the *Österreichische Akademie der Wissenschaften*.

References

- [1] G. Springholz, V. Holy, and G. Bauer: “Local surface deformations induced by interfacial dislocations in lattice-mismatched heteroepitaxy of EuTe on PbTe (111)”, *Surf. Sci.*, Vol. 365, 1996, pp. 453 – 460.
- [2] J. G. Belk, J. L. Sudijono, X. M. Zhang, J. H. Neave, T. S. Jones, and B. A. Joyce: “Surface Contrast in Two Dimensionally Nucleated Misfit Dislocations in InAs/GaAs(110) Heteroepitaxy”, *Phys. Rev. Lett.*, Vol. 78, 1997, pp. 475 – 479.
- [3] A. Trampert, E. Tournié, and K. H. Ploog: “Defect control during growth of highly mismatched (100) InAs/GaAs-heterostructures”, *J. Cryst. Growth*, Vol. 146, 1995, pp. 368 – 373.
- [4] S. Yu. Shiryayev, F. Jensen, J. Lundsgaard Hansen, J. Wulff Petersen, and A. Nylandsted Larsen: “Nanoscale Structuring by Misfit Dislocations in $\text{Si}_{1-x}\text{Ge}_x/\text{Si}$ Epitaxial Systems”, *Phys. Rev. Lett.*, Vol. 78, 1997, pp. 503 – 506.
- [5] R. Leon, J. O. Okuno, and R. A. Lawton, M. Stevens-Kalceff, and M. R. Philips, J. Zou, and D. J. H. Cockayne, C. Lobo: “Dislocation-induced changes in quantum dots: Step alignment and radiative emission”, *Appl. Phys. Lett.*, Vol. 74, 1999, pp. 2301 – 2303.

ISBN: 3-901578-07-2